Universität Hamburg
DER FORSCHUNG | DER LEHRE | DER BILDUNG

CHyN
Centre for Hybrid Nanostructures

Noble metal nanoclusters for electrocatalysis, catalysis, enzyme-mimicking, and photoelectrochemistry analysis

DISSERTATION

Submitted in partial fulfillment of the requirements for the degree of Doctor of Natural Sciences

(Doktor der Naturwissenschaften, Dr. rer. nat)

Department of Chemistry

Faculty of Mathematics, Computer Science and Natural Sciences University of Hamburg

Submitted by

M.Sc. Lizhen Chen

from

Guangdong, China

Hamburg, 2021

The presented work conducted under the supervision of Dr. Indranath Chakraborty and Prof. Dr. Wolfgang J. Parak at the Center for Hybrid Nanostructure (CHyN) of the University of Hamburg (from September 2018 to December 2021).

Thesis Committee:	Prof. Dr. Wolfgang J. Parak
	Prof. Dr. Alf Mews
Evaluation Committee:	Prof. Dr. Wolfgang J. Parak
	Prof. Dr. Carmen Herrmann
	Prof. Dr. Dorota Koziej

Disputation Date: 18.02.2022

Declaration of Authenticity

I hereby declare upon oath that I have written the present dissertation independently without assistance from external parties and have not used further resources and aids than those stated. The ideas, materials and the included work in the dissertation have not been previously submitted for grading at this or any other academic institution.

Hamburg, 01.12.2021

_____

Lizhen Chen

Place, Date

Lizhen Chen

Bibliography

Personal information			
Name	Lizhen	Family name	Chen
Birthplace	Zhanjiang, Guangdong, China	Nationality	Chinese
Education			
09.2018-12.2021	University of Hamburg, AG Biophotonics (Prof. Dr. Wolfgang J. Parak), Germany		
	Doctor of Natural Sciences		
09.2012-06.2015	Changchun Institute of Applied Chemistry (CIAC), University of Chinese Academy of Sciences (UCAS), China		
	Master of Science		
09.2008-06.2012	Xiangtan University, China		
	Bachelor of Science		

List of publications:

[1] Chen, L.; Azeem, S.; Ruan, M.; Xu, W.; Barck, A.; Kornowski, A.; Parak, W.J.; Chakraborty, I.,[*] **Rapid Template-Guided Ligand-Free Synthesis of Ultrasmall Pt Nanoclusters with Efficient Hydrogen Evolution Reaction Activity and their Versatile Release.** Nano Select *2020, 2, 758-767.* **(Cover page)**

[2] Chen, L.; Black, A.; Parak, W.J.; Klinke, C.;[*] Chakraborty, I.,[*] **Metal Nanocluster-Based Devices: Challenges and Opportunities.** Aggregate *2021, doi: 10.1002/agt2.132.* **(Review)**

[3] Zhu, L.;[#] Gharib, M.;[#] Becker, C.; Zeng, Y.; Ziefuß, A.R.; **Chen, L.**; Alkilany, A.M.; Rehbock, C.; Barcikowski, S.; Parak, W.J.; Chakraborty, I.,[*] **Synthesis of Fluorescent Silver Nanoclusters: Introducing Bottom-Up and Top-Down Approaches to Nanochemistry in a Single Laboratory Class.** Journal of Chemical Education *2019*, *97 (1), 239-243.*

[4] Chen, L.; Ruan, M.; Klemeyer, L.; Koziej, D.; Werner, S.; Xu, W.;[*] Koeppen, A.; Bücker, R.; Gonzalez, M.G.; Parak, W.J.; Chakraborty, I.,[*] **Intrinsic Versatile Enzyme Mimicking of PtAg Alloy Nanoclusters and its Mechanism Study.** (In preparation)

[5] Chen, L.; Zierold, R.; Blick, R.H.; Werner, S.; Parak, W.J.;[*] Lisdat, F.;[*] Chakraborty, I.,[*] **Plasmon Enhancement of Au nanoclusters sensing with photoelectrochemical platform.** (In preparation)

[6] Chen, L.;[#] Gharib, M.;[#] Zeng, Y.; Parak, W.J.; Chakraborty, I.,[*] **The Biological Significance of Au@BSA Nanoclusters**. (In preparation)

Conference contributions:

[1] Chen, L.;[#] Azeem, S.;[#] Ruan, M.; Xu, W.; Barck, A.; Kornowski, A.; Parak, W.J.; Chakraborty, I.,[*] *A* **Facile and One-pot Synthesis of Ligand-free Noble Metal Nanoclusters Catalysts on Zeolitic Imidazolate Frameworks Supports**. Nanoscience with Nanocrystals 9 (**NaNaX9**), 17-20 September *2019*, University of Hamburg, Hamburg, Germany.

(Website: https://www.chemie.uni-hamburg.de/fachbereich/veranstaltungen/nanax9/welcome.html)

[#] Both authors contributed equally

Abstract

In recent years, noble metal nanostructures, especially nanoclusters (NCs) have gained increasing attention in nanomaterial science. They are used in a variety of applications, for example, electrocatalysis, photoelectrochemical, biosensing, bioimaging and more. Due to their unique physiochemical properties of NCs excel in comparison with nanoparticles (NPs) as their counterpart. Numerous efforts have been devoted to the preparation of the noble metal NCs and their further applications. In my thesis, the content is focused on the synthesis of noble metal NCs and their applications in catalysis, electrocatalysis, enzyme mimics as well as photoelectrochemical analysis. The work was split into three parts which shall be introduced in the following section:

Noble metal Platinum (Pt) is considered to be the most common catalyst among any other catalysts. However, the high cost and shortage of Pt resources have impeded the wide applicability of Pt-based catalysts for commercially used. To improve the Pt usage for fuel cell and electrocatalytic water splitting as well as to understand the electrocatalytic mechanism of the active site that existed in the Pt-based catalysts, I synthesized ultrasmall, ligand-free PtNCs based on the template of zeolitic imidazolate framework-8 (ZIF-8), denoted as PtNCs@ZIF-8. The structural information was confirmed by transmission electron microscopy (TEM), Fourier transform infrared spectroscopy (FTIR), X-ray photoelectron spectroscopy (XPS), and powder X-ray diffraction (PXRD). Furthermore, the catalytic performance of this catalyst was evaluated upon the reduction of 4-nitrophenol (4-NP) to 4-aminophenol (4-AP). Its electrocatalytic performance of oxygen reduction reaction (ORR) and hydrogen evolution reaction (HER) was tested, resulting in activities that are comparable to those of commercially 20 wt.% Pt/C catalysts. Moreover, these PtNCs can be extracted from their substrates to both aqueous and non-aqueous solvents, providing a fundamental system for a variety of applications. This study and its findings provide a rapid synthesis method to prepare efficient catalysts and offer avenues to obtain ligand-free homogenous PtNCs for further applications.

For the second part, to improve the catalytic efficiency of PtNCs-based nanozymes and to evaluate a multi-enzyme system, PtAg alloy NCs were prepared, based on the previous template. Two different protocols were applied to obtain PtAg@ZIF-8 materials. The first one uses the principle of co-reduction whereas the second one applies Pt-guided methods. The characterizations by TEM, Brunauer-Emmett-Teller (BET) surface area analysis, XPS, FTIR, and Thermogravimetric analysis (TGA) confirm the obtained nanocomposites. The enzyme mimicking properties of these catalysts were investigated. Therefore, the oxidation of o-phenylenediamine (OPD) in the presence of H_2O_2, the decomposition of H_2O_2, and the oxidation of 3,3′,5,5′-tetramethylbenzidine (TMB) in the presence of dissolved oxygen (O_2) were evaluated for the peroxidase (POD)-, catalase (CAT)- and oxidase (OD)-like activities, respectively. Further

mechanism studies regarding the enzyme-mimicking were performed to reveal the behaviors of PtAg@ZIF-8 in the presence of the substrates and H_2O_2 or dissolved O_2.

3. In this part, I show a strategy to enhance the photocurrent of the photoelectrochemistry (PEC) sensor by introducing a plasmonic metal. Here, an enhanced PEC sensor (ePEC) was fabricated consisting of a traditional PEC sensor based on AuNCs and an enhancer layer of thin-silica-coated Au nanorods (AuNRs@SiO$_2$). First, the photocurrent of the ePEC in PBS buffer solution without any oxidizer or reducer was tested and results indicated that the photocurrent was greatly enhanced after the AuNRs introduction. The photocurrent response to the illumination power shows a super-linear dependence at high illumination intensity. Futhermore, the enhancement is related to the absorption of the AuNRs, confirming a mechanism where the energetic charge transfer dominates the whole photoelectrochemical process. More importantly, to further examine the sensing potential and performance of this ePEC sensor, the ePEC platform was used to probe H_2O_2. The result shows a 9.3-time higher limit-of-detection (LOD) toward sensing H_2O_2 after AuNRs introduction, indicating a design strategy for enhancing the sensitivity of a traditional PEC sensor.

Keywords: nanoclusters, catalysis, electrochemistry, enzyme mimics, photoelectrochemistry

Zusammenfassung

In den letzten Jahren haben Edelmetall-Nanostrukturen, insbesondere Nanocluster (NCs), in der Nanomaterialwissenschaft eine zunehmende Aufmerksamkeit erlangt Sie werden in einer Vielzahl von Anwendungen eingesetzt, beispielsweise in der Elektrokatalyse, Photoelektrochemie, Biosensorik, Bioimaging und mehr. Dies ist auf ihre einzigartigen physikalisch-chemischen Eigenschaften im Vergleich zu Nanopartikeln (NPs) als ihren Gegenstücken zurückzuführen. Zahlreiche Anstrengungen wurden der Herstellung der Edelmetall-NCs und ihren weiteren Anwendungen gewidmet. Der Inhalt meiner Dissertation konzentriert sich auf die Synthese von Edelmetall-NCs und deren Anwendungen in der Katalyse, Elektrokatalyse, Enzymmimetik sowie photoelektrochemischen Analytik. Die Arbeit gliederte sich in drei Teile, die im folgenden Abschnitt vorgestellt werden sollen:

Edelmetall Platin (Pt) wird als der am weitesten verbreitete Katalysator unter allen anderen Katalysatoren angesehen. Doch die hohen Kosten und der Mangel an Pt-Ressourcen haben die kommerziellen Anwendungen von Pt-basierten Katalysatoren eingeschränkt. Um die Verwendung von Pt in Brennstoffzellen und photokatalytischer Wasserspaltung zu verbessern, und um den elektrokatalytischen Mechanismus des aktiven Zentrums in Pt-basierten Katalysatoren zu verstehen, synthetisierten wir ultrakleine, ligandenfreie PtNCs basierend auf dem Templat eines zeolithischen Imidazolatgerüst-8 (ZIF-8), die als PtNCs@ZIF-8 bezeichnet werden. Strukturelle Informationen wurden durch Transmissionselektronenmikroskopie (TEM), Fourier-transformierte Infrarot-Spektroskopie (FTIR), Röntgen-Photoelektronen Spektroskopie (XPS) und Pulverröntgendiffraktometrie (PXRD) bestätigt. Darüber hinaus wurde die katalytische Leistung dieses Katalysators anhand der Reduktion von 4-Nitrophenol (4-NP) zu 4-Aminophenol (4-AP) bewertet. Seine elektrokatalytische Leistung von ORR und HER wurde getestet, die in ihrer Aktivität mit kommerziellen 20 wt.% Pt/C-Katalysatoren vergleichbar ist. Zusätzlich können diese PtNCs sowohl in wässrigen als auch in nichtwässrigen Lösungsmitteln aus dem Netzwerk extrahiert werden, womit sie ein fundamentales Systemen eine breite Anwendung darstellen. Diese Studie und die Ergebnisse bieten eine schnelle Synthesemethode zur Herstellung effizienter Katalysatoren und Möglichkeiten zur Herstellung ligandenfreier homogener PtNCs für weitere Anwendungen.

Für den zweiten Teil galt: Um die katalytische Effizienz von PtNCs-basierten Nanozymen zu verbessern und ein Multienzym-System zu evaluieren, wurden PtAg-Legierungs-NCs basierend auf dem vorherigen Templat hergestellt. Zwei verschiedene Protokolle wurden angewendet, um PtAg@ZIF-8-Materialien zu erhalten. Das Erste nutzt das Prinzip der Co-Reduktion wohingegen das Zweite verschiedene Pt-gestützte Methoden bietet. Um die nach diesen beiden Methoden erhaltenen Produkte zu differenzieren, wurden Die Charakterisierungen mittels TEM, Brunauer-Emmett-Teller (BET) Oberflächenanalyse, XPS, FTIR und

thermogravimetrische Analyse (TGA) bestätigten, dass wir die beiden Nanopartikeltypen erhalten haben. Die enzymimitierenden Eigenschaften dieser Katalysatoren wurden untersucht. Daher wurden die Oxidation von o-Phenylendiamin (OPD) in Gegenwart von H_2O_2, die Zersetzung von H_2O_2 und die Oxidation von 3,3′,5,5′-Tetramethylbenzidin (TMB) in Gegenwart von gelöstem Sauerstoff (O_2) bewertet für die Peroxidase (POD)-, Katalase (CAT)- bzw. Oxidase (OD)-ähnlichen Aktivitäten. Weitere Mechanismusstudien bezüglich Enzymnachahmung wurden durchgeführt, um das Enzymnachahmungsverhalten von PtAg@ZIF-8 in Anwesenheit von den Substraten und H_2O_2 oder gelöstem O_2 zu offenbaren.

Im letzten Abschnitt stelle ich eine Strategie vor, um den Photostrom des Photoelektrochemie (PEC)-Sensors durch die Einführung eines plasmonischen Metalls zu verbessern. Hier wurde ein verbesserter PEC-Sensor (ePEC) hergestellt, der aus einem traditionellen PEC-Sensor auf Basis von Au-NCs und einer Enhancer-Schicht aus dünnen silikabeschichteten Au-nanorods ($AuNRs@SiO_2$) besteht. Zuerst wurde der Photostrom des ePEC in PBS-Pufferlösung ohne Oxidationsmittel oder Reduktionsmittel getestet und die Ergebnisse zeigten, dass der Photostrom nach der Einführung von Au-NRs stark erhöht wurde. Die Photostromantwort auf die Beleuchtungsleistung zeigt bei hoher Beleuchtungsintensität eine superlineare Abhängigkeit. Darüber hinaus hängt die Verstärkung mit der Absorption der Au-NRs zusammen, was einen Mechanismus bestätigt, bei dem der energetische Ladungstransfer den gesamten photoelektrochemischen Prozess dominiert. Um das Erfassungspotenzial und die Leistung dieses ePEC-Sensors weiter zu untersuchen, wurde die ePEC-Plattform zur Sondierung von H_2O_2 verwendet. Das Ergebnis zeigt eine 9,3-fach höhere Nachweisgrenze (LOD) für die H_2O_2-Erfassung nach der Einführung von Au-NRs, was auf eine Designstrategie zur Verbesserung der Empfindlichkeit eines herkömmlichen PEC-Sensors hindeutet.

Stichwörter: Nanocluster, Katalyse, Elektrochemie, Enzymmimetik, Photoelektrochemie

Table of Contents

List of Abbreviations

NPs	nanoparticles
NCs	nanoclusters
NRs	nanorods
SPR	surface plasmon resonance
HOMO	the highest occupied molecular orbital
LUMO	the lowest unoccupied molecular orbital
BSA	bovine serum albumin
CTAB	cetyltrimethylammonium bromide
'ad' subscript	a reaction site on the catalyst surface
AA	ascorbic acid
SiO_2	silica
MOFs	metal-organic frameworks
ZIF-8	zeolitic imidazolate framework-8
SR	thiol ligands
PET	2-phenylethanethiol
FTP	4-fluorothiophenol
Au	gold
Ag	silver
Pt	platinum
Pd	palladium
Ru	ruthenium
Cu	copper
ORR	oxygen reduction reaction
Pt/C	platinum/carbon
HER	hydrogen evolution reaction
DFT	density functional theory
PEC	photoelectrochemical
ICP-MS	inductively coupled plasma mass spectrometry
WE/CE/RE	working/counter/reference electrode
VB	the valence band
CB	the conduction band
PBS	phosphate buffered saline

$e^- - h^+$	electron-hole
A/D	acceptor/donor molecule
QDs	quantum dots
AChE	acetylcholinesterase
OPs	organophosphorus pesticides
TMB	3,3′,5,5′-Tetramethylbenzidin
4-NP	4-nitrophenol
4-AP	4-aminophenol
4-NPA	4-nitrophenylacetate
Y_{AP}	conversion yield of 4-AP
UV-vis	ultraviolet−visible
TEM	transmission electron microscopy
HRTEM	high-resolution transmission electron microscopy
FTIR	fourier transform infrared
DLS	dynamic light scattering
PXRD	powder X-ray diffraction
HAADF-STEM	high-angle annular dark-field scanning transmission electron microscopy
SEM	scanning electron microscopy
EDS	energy-dispersive X-ray spectroscopy
XPS	X-ray photoelectron spectroscopy
k	rate constant
A'	the pre-exponential factor
T	temperature T (in Kelvin)
R	the universal gas constant
m	total mass of the catalyst
E_a	the activation energy for the reaction
E'	the applied potential versus the Ag/AgCl reference electrode
E	the potential converted to RHE based on the Nernst equation
$E^0_{Ag/AgCl}$	the standard electrode potential of the Ag/AgCl electrode
H_{UPD}	H- adsorption/desorption peaks
Q_H	the charge for H_{UPD}
q_H	the charge required for a monolayer of hydrogen adsorption on Pt
POD	peroxidase
CAT	catalase

OD	oxidase
DMF	N, N-dimethylformamide
MeOH	methanol
2-MeIM	2-methyl imidazole
fcc	face-centered cubic
OPD	o-phenylenediamine
CVs	cyclic voltammetrys
LSV	linear sweep voltammetry
RHE	reversible hydrogen electrode
E_η	overpotential
α	the symmetry coefficient
j	the current density
β	the Tafel slope
SA	specific activity
ECSA	electrochemically active surface area
MA	mass-activity
ADT	accelerated durability test
RRDE	rotating ring-disk electrode
K-L	Koutecky-Levich
J_L	diffusion-limiting current density
J_K	kinetic current density
ω	electrode rotation speed
n	the overall number of electrons transferred in ORR
F	the Faraday constant
C_0	the bulk concentration of O_2
D_0	the diffusion coefficient for O_2 in solution
v	the kinetic viscosity of solution
i_D	the disk current density
i_R	the ring current density
N	the current collection efficiency of the Pt ring disk
GSH	glutathione
DDT	dodecanethiol
DCM	dichloromethane
DMSO	dimethyl sulfoxide
DMK	acetone (dimethyl ketone)

THF	tetrahydrofuran
SOD	superoxide dismutase
BET	Brunauer-Emmett-Teller
S_{BET}	the BET specific surface area
HK	Horvath-Kawazoe
V_{micro}	the micropore volume
d_p	the pore diameter
TGA	thermogravimetric analysis
K_m	the Michaelis constant
v_{max}	the maximum velocity
TA	terepthalic acid
HE	dihydroethidine
$\cdot OH$	hydroxyl radical
$\cdot O_2^-$	superoxide radical
SAM	self-assembled molecule
APTMS	(3-aminopropyl) trimethoxysilane
LOD	low of detection
$LSPR_T$	transverse localized surface plasmon resonance
$LSPR_L$	longtitudinal LSPR
SNR	signal to noise
I_{light}	light intensity
EET	excited energy transfer

List of Figures

xvi

1 Introduction

The innovation for new catalysts, a substance that accelerates chemical reaction rates approaching equilibrium and that remains intact after reaction, has been a central research field for the past 200 years. In the last few decades, one of the most significant breakthroughs in catalysts is the discovery of noble metal nanocatalysts. In 1987, a novel Au nanocatalyst for efficient carbon monoxide oxidation at low temperature was disclosed by Haruta and coworkers. This finding is a landmark to overwrite the traditional view of noncatalytic metal gold, leading to tremendous studies on nanocatalyst.[1] In general, noble metal nanoparticles (NPs) with a typical size diameter of 2 - 100 nm exhibit unique physical and chemical properties compared to their bulk counterparts. For instance, free electrons in noble metal NPs' surface layer become the collective oscillation upon the incidence of light, known as the surface plasmon resonance (SPR) effect.[2, 3] This endows noble metal NPs with enhanced properties that are used in catalysis, in addition to other biomedical, sensing, and bioimaging applications.

The ultrasmall (< 2 nm) NPs, also called nanoclusters (NCs), consisting of several to a few hundred of atoms, are of both fundamental and applied importance, as they bridge the regimes between single atoms and large NPs.[4-12] These noble metal NCs have been explored as another novel class of efficient nanocatalysts, displaying appealing catalytic activity and selectivity thanks to their fascinating geometric and electronic properties.[13-19] Firstly, the **surface-to-volume effect**: one NC has a lower number of atoms and diverse packing structure in comparison to the larger NPs, and thus exhibits related larger surface area and more unsaturated coordination sites are exposed. Secondly, the **quantum size effect**: ultrasmall NCs possess molecular-like behaviors, such as the discrete highest occupied molecular orbital (HOMO)-the lowest unoccupied molecular orbital (LUMO) gaps, strong luminescence, and unusual redox properties. Thirdly, **dynamic structural properties**: upon working conditions, the geometric and electronic features of NCs varyunder the activated NCs during the reaction process, thusing lead to specific reaction pathways. This enables NCs to explore novel catalytic processes.

Alloy metal NCs have gained increasing attention due to their enhanced physicochemical properties (such as improved stability, optical performance, and catalytic activity) compared to their corresponding homo-metal NCs. They thus are used for further electronic, optical and catalytic applications.[2, 20] The discovery of the alloying-induced improvement of performance dates back to the Bronze Age.[2] A strightforward example, reported by Wang's group, is the "Ag effect" in AuNCs; the group obtained the bovine serum albumin (BSA) capped Au-AgNCs with slightly enhanced fluorescence.[21] The "Ag effect"

was further examined by Shi *et al.*, which largely improved the catalytic performance in the Au-Ag bimetallic NCs.[22] The usage in catalysis of the more catalytic active platinum metal groups (Pt, Pd, and Ru) usage in catalysis is limited by the cost of these materials. In contrast, alloying these metal catalysts would reduce the costs, while also enhancing their catalytic efficiency. In addition, a salient improvement in controlling the properties of alloy metal NCs can be achieved by single-atom doping to form a single-atom alloy, and the enhanced mechanism has been proposed to the synergistic effects among the host metal and the dopant atom.[23, 24]

In recent years, a plethora of research has been reported to use noble metal NCs (*e.g.* Au, Ag, Pt, Pd, and their alloys) in catalysis, attributed to sophisticated synthesis methodologies by scientists, who are researching simplest and gentlest means to obtain NCs of high quality.[3, 25, 26] Nonetheless, the precisely-controlled synthesis of NCs with well-defined size, structure and composition is usually not easy. One solution to settle this problem is by introducing thiol-ligands, serving to protect and stabilize the NCs. The noble metal NCs presented by Chini's group was disclosed in the late 1950s, pioneering in the fields related to noble metal NCs.[27] Afterward, new methods have been investigated of which the most commonly used are the following.

1) **Direct synthesis method**, which has been used to obtain Ag, Au, Cu and alloy NCs.[5, 14, 28-31] It is worth mentioning that thiol-capped noble metal NCs are usually developed with this method in both organic and aqueous solution. For example, Zhu *et al.* proposed uniform AuNCs via organic-phase, including two key steps of the thermodynamic selection and the kinetic control.[32]

2) **Ligand-exchange method**, in which precursor NCs were etched with an excess of a different ligand, thus producing a new type of NCs. This method typically produces uniform NCs with intact metal core structures.

3) **Size-focusing method**, the same excess added thiol was employed later to the thiolate ligand of the presynthesized NCs, which is different from the ligand-exchange method. This is relatively time-consuming, and complicated.

4) **Template-assisted method**, for example, uniform noble metal NCs can be formed inside porous templates, such as metal-organic frameworks (MOFs), metal oxides, or other carbon-based supports.[33-36] Huang and co-authors proposed a strategy of "bottle around ship" for synthesizing PtPd bimetallic NCs by using ZIF-8 template.[37]

5) **Chemical etching method**, a typical top-down method, in which excess thiol etches large-scale NPs

2

producing monodisperse NCs. This method can be used for both monometallic and alloy NCs.[38]

6) **Reduction method** is the most common approach to synthesize alloy metal NCs, divided into galvanic and anti-galvanic types. This method depends on the redox potential difference between the two kinds of metals.

7) **Metal-exchange method**, different from the reduction method;[39] the added doping agent is a metal complex rather than an inorganic metal salt. Zhu *et al.* first introduced a metal-exchange method for a series of bimetallic NCs and further exploited it for trimetallic NCs.[40]

8) **Intercluster reaction method**, a new synthesis protocol for alloy NC related to the mutual interaction among two different stable NCs. Pradeep's group produced $(Au_{25-x}Ag_x)(SR)_{18}$ (x = 0 - 20) by exchanging the metal atoms and ligands from two different $[Au_{25}(PET)_{18}]^-$ (PET = 2- phenylethanethiol) and $[Au_{44}(FTP)_{30}]^{4-}$ NCs (FTP = 4-fluorothiophenol).[41]

Electrocatalysis and photocatalysis had significant research and application prospects in the last few decades.[36, 42-51] Due to the rapid development of the social economy, the exhaustive consumption of unrenewable energy sources (*e.g.* fossil, coal, and oil) has contributed to the urgent energy crisis and environmental pollution. To this end, electrocatalysis and photocatalysis can be applied for green, alternative, and sustainable energy sources generation, which is a key challenge. They are frequently utilized for the detection and degradation of environmental pollutants[52, 53] and intensive ongoing studies are devoted to applying noble metal NCs for these applications due to their distinct features.[2, 12]

Fuel cells have been suggested to be one of the new and green energy sources thanks to their advantageous features, such as low noise, high energy conversion efficiency and only produce water as waste.[54, 55] In fuel cells, oxygen reduction reaction (ORR) is a cathode reaction, which is the determining reaction, while the oxidation of fuel reaction occurs at the anode. In general, there are two different reaction mechanisms (direct four-electron and indirect two-electron processes) of ORR (**Table 1-1**).[56]

Table 1-1. ORR pathways under acidic and alkaline conditions.

pathway	acidic	alkaline
four-electron	$O_2 + 4H^+ + 4e^- \rightarrow 2H_2O$	$O_2 + 2H_2O + 4e^- \rightarrow 4OH^-$
two-electron	$O_2 + 2H^+ + 2e^- \rightarrow H_2O_2$	$O_2 + H_2O + 2e^- \rightarrow HO_2^- + OH^-$
	$H_2O_2 + 2H^+ + 2e^- \rightarrow 2H_2O$	$HO_2^- + H_2O + 2e^- \rightarrow 3OH^-$

3

Based on the theoretical calculation, the direct four-electron pathway is expected to have a higher efficient energy conversion than the indirect two-electron pathway in the fuel cell.[57] To date, Pt is still considered as the most catalytic active for both electrocatalytic anode and cathode reactions in fuel cells. Due to the high cost and low abundance of Pt sources, using low-Pt-based or non-Pt nanocatalysts for the maximum catalytic performance is highly desirable.[58, 59] Fischer *et al.* produced atom-precise Pt carbonyl NCs in zeolitic imidazolate framework-8 (ZIF-8) via thermal-oxidative decarboxylation method. The obtained Pt@ZIF-8, with an average diameter of ca. 1.1 nm, exhibited superior ORR properties compared to those of the commercial 20 wt.% platinum/carbon (Pt/C) catalysts.[58, 59] Chen *et al.* synthesized Au_nNCs (n = 11, 25, 55, 140) for the ORR evaluation and Au_{11} exhibited the best ORR activity.[60] The theoretical calculations further illustrated that the smaller Au_{11} NCs show narrower d bands, energies closer to the Fermi level, thus contributing to the easier O_2 adsorption.

Another potential alternative green energy is hydrogen (H_2). The water splitting by electrolysis or photolysis is promising as a strategy to generate high-purity H_2 and O_2 simultaneously. The whole water splitting process consists of the cathode- and anode-half reactions, named as hydrogen evolution reaction (HER) and oxygen evolution reaction, respectively. In terms of the HER process, there are two different Volmer-Heyrovsky and Volmer-Tafel mechanisms[61]. Generally, the kinetic processes of HER in both acidic and alkaline media consist of three possible reactions at 25 °C, indicated in **Table 1-2**.

Table 1-2. HER reactions in acidic and alkaline media.

reaction	acidic	alkaline
Volmer	$H_3O^+ + e^- \leftrightarrow H_{ad} + H_2O$	$H_2O + e^- \leftrightarrow H_{ad} + OH^-$
Heyrovsky	$H_{ad} + H^+ + e^- \leftrightarrow H_2$	$H_{ad} + H_2O + e^- \leftrightarrow H_2 + OH^-$
Tafel	$2H_{ad} \leftrightarrow H_2$	$2H_{ad} \leftrightarrow H_2$

Here, the "ad" subscript represents a reaction site on the catalyst surface. Many research has been performed in the HER activities of noble metal NCs and their alloys. NCs with smaller sizes can expose more active sites, while alloys help achieve the improved catalytic activity. Teranishi *et al.* reported the influence of the ligand structure on the HER performance by porphyrin-coordinated AuNCs.[62] Decreasing the distance between the porphyrin-ring and the surface of AuNCs leads to the increase of the HER activity. Besides, they also illustrated that the smaller $Au_n(SR)_m$NCs show higher HER properties. To date, Pt is still considered to be the state-of-the-art material with increased activity in HER. Due to the scarcity and expense of Pt metal. Numerous attempts are devoted to the miniaturization of the

Pt metal and theoretically predicting their activity by density functional theory (DFT) calculation and mechanisms.[63, 64] For example, Kwak *et al.* presented $Pt_1Au_{24}(SC_6H_{13})_{18}$ NCs with more efficient catalytic activity for HER compared to Au_{25} NCs, and showed higher onset potential of - 0.89 V than that of Au_{25} NCs with - 1.10 V.[62]

Photoelectrochemical (PEC) sensing is a newly emerged strategy which consist of innovative integration of excitation light response with electrochemical analysis. As opposed to PEC, conventional-applicable approaches such as inductively coupled plasma mass spectrometry (ICP-MS), atomic fluorescence spectroscopy, high-performance liquid chromatography coupling with MS, and gas spectrometry for chemical pollutants tracing, demand vast and expensive instruments and sophisticated detection processes. Moreover, the PEC sensor employs light as the excitation source and photocurrent as a readout signal, which enable portable and real-time on-site testing. All PEC working electrodes (WE) depend on the linkage of light-sensitive entities to trigger electron transfer upon light excitation, thus concomitantly generating a photocurrent. In a typical PEC sensing process, the photoactive material on the WE can induce the generation of electron-hole (e^-- h^+) pairs under illumination **(Figure 1-1)**.[65, 66] Here, we use semiconductors as an example. Trapping the photo-induced electrons from the conduction band (CB) with an acceptor molecule (A) would contribute to cathodic photocurrent (Process a). On the contrary, electrons from a donor molecule (D) to the light-sensitivity entity to neutralize the photo-induced holes from the valence band (VB), then would form an anodic photocurrent (Process b). Particular focus has been paid to various photoactive nanomaterials to fabricate PEC sensors, including quantum dots (QDs), NPs, nanowires, nanorods (NRs) and dyes, and their influence on the sensing performances. For example, Liu *et al.* fabricated acetylcholinesterase (AChE) modified CdSe@ZnS QDs/graphene nanocomposite on the Indium tin oxide glass as a photoactive electrode for the sensitive detection of organophosphorus pesticides (OPs). Under light irradiation, the photoactive electrode generated a stable photocurrent, which is inversely dependent on the concentration of OPs. Recently, noble metal NCs have become a research centre for the PEC sensing of pollutants, mainly because of their discrete bandgap and size-dependent optical features analogous to those of QDs. In addition, these noble metal NCs exhibit excellent photostability and capacity for photocatalysis. Xiao *et al.* reported an enhanced performance in the degradation of pollutants by Au_xNCs (where x indicates that the number of Au atoms is not accurately known) decorated TiO_2 nanotube arrays.[67] This suggested NCs would play specific roles in the photocatalysis and are thus promising potential to be a photoelectrical entity for PEC sensors.[68-70]
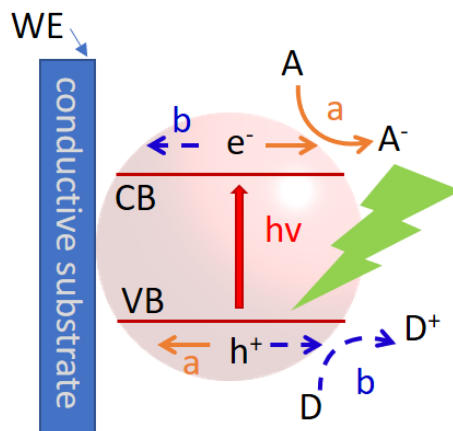
Figure 1-1. *Schematic demonstration of photocurrent generation in a typical PEC sensing process.*

Apart from the catalysis of nanomaterials, nanozyme of the nanomaterials have increasingly received attention in very recent years.[71, 72] The term "nanozymes" is used to define the nanomaterials with size in nanometer scale (1-100 nm) and with intrinsic enzyme-like activities, for example, peroxidase, catalase, oxidase and urease activities, and which are artificial enzymes that mimic natural enzymes. The nanozymes are promising substitutes as they overcome the shortcoming of natural enzymes, such as high cost, low stability and durability, which have been widely applied in industry, medicine and biology.[71] Since Gao *et al.* in 2007 discovered intrinsic horseradish peroxidase-like catalytic property of ferromagnetic NPs, a substantial amount of work with regards to nanozymes were found in biological analysis, environmental treatment and even target cancer therapy.[73] Up to now, various kinds of nanomaterials, such as metal NPs, metal oxide, metal sulfide, and carbon-based nanomaterial, are demonstrated with inherent enzyme-like features. In very recent, ultrasmall noble metal NCs have become a novel research interest in the area of nanozymes because of their higher catalytic properties and better biocompatibility compared to their larger counterparts. The first AuNCs-based nanozyme was investigated by Wang *et al.* in 2011.[74] They discovered BSA-protected AuNCs with higher peroxidase enzymatic activity as compared to natural peroxidase (POD), a class of enzymes that can catalytically induce the reduction of hydrogen peroxide or lipid peroxide in the presence of a/the substrate, whereas trigger the oxidation organic substances, for instance, 3,3′,5,5′-tetramethylbenzidine (TMB) to the color oxidized TMB (oxTMB). Moreover, this work provides a great promise of noble metal NCs nanozymes in analytical analysis in the future.

My work is divided into three chapters. In the first and second chapters, a facile template-assisted approach has been used to synthesize ligand-free ultrasmall PtNCs and PtAg alloy NCs, respectively.

6

The ligand-free PtNCs exhibit higher catalytic activity in the reactions of the reduction of 4-nitrophenol (4-NP), ORR and HER. Also, we evaluated the long-term stability of PtNCs for ORR and HER. Moreover, the PtNCs in ZIF-8 can be released into both aqueous and non-aqueous conditions via suitable ligands, providing possibilities for these PtNCs for further use in other systems. The bimetallic PtAg alloy NCs show their potential in the enzymatic mimicking as nanozymes, including the (POD)-, catalase (CAT)- and even oxidase (OD)-like activities. These PtAg alloy NCs were demonstrated with higher enzymatic performance over a wide range of pH compared to natural enzymes. In the third chapter, we introduced a strategy to enhance the sensing ability of traditional PEC sensors by introducing a plasmonic metal. Furthermore, we demonstrate that the enhanced PEC sensor we proposed here could be used to probe H_2O_2.

2 Template-based synthesis of ligand-free PtNCs for efficient catalysis and their versatile release studies[1]

2.1 Introduction and aim of the work

A new class of noble metal NPs with ultrasmall size (< 2 nm), known as metal NCs, has been a promising interest among nanomaterials thanks to their fascinating properties applicable for biological applications, catalysis, sensing and many more. In particular, their large surface-to-volume ratios and molecular-like activity contribute to their high catalytic activities. Thus noble metal NCs, such as Au and Ag NCs, have been intensively investigated due to their high stability. On the contrary, there is very little research on PtNCs, even with more catalytical activities. For instance, Wang and coworkers presented a successful in-situ synthesis of PtNCs protected by polyelectrolyte multilayers, demonstrated as excellent nanoreactors for NCs.[75] In another report, Chakraborty and coworkers proposed a paste-based route for synthesizing blue-emitting eleven-atom PtNCs by 4-(tert-butyl)benzyl mercaptan.[9] These PtNCs are synthesized and protected by suitable ligands, namely, thiols,[9, 76, 77] dendrimers,[78-80] phosphines,[81] and polymers,[75, 82, 83] which are essential to achieve the stable and atomically precise structure of NCs in solution. Besides, other molecules like N, N-dimethylformamide (DMF) are also reported to stabilize the PtNCs. These ligand-aided approaches are practical to obtain noble metal NCs; on the other hand, they may prevent the accessibility of the reactants to the NCs' surface, and thus occurs the blockage of the catalytic sites on the NCs surface and reduce the catalytic properties.

One of the standard methods, as mentioned in the introduction section, is a template-assisted method. Various porous materials have been reported to be used to synthesize noble metal NCs, such as MOFs, metal oxides, and carbon-based supports.[33-35] Up to now, MOFs with well-ordered nanopores have gained increasing interest owing to their high porosity and super thermal stability in the last two decades.[84-86] Besides, they promise various applications such as clean energy storage, gas separation, drug delivery and catalysis.[87] In recent years, MOFs have been suggested as excellent support for various nanomaterials.[88] For example, many researches reported various noble metal NPs, such as Ag, Pt, Au, Au-Ag alloy, synthesized successfully in different kinds of MOFs templates.[89-91] These NPs@MOF nanocomposites show more catalytic activities not only because of the highly accessibility of MOF template for the specific active sites to the NPs' surface, but also the synergistic effect between the MOFs and metal NPs. Among these MOFs, ZIFs, for example, ZIF-8, become one of the interests due to their

---

superior physical and chemical properties and thermal stabilities. Therefore, many works utilized ZIF-8 as the template for the size-controlled synthesis of NPs or NCs. For example, in 2018, Fu and coworkers synthesized NiPt@ZIF-8 nanocomposites *via* a two-step method, with good dispersion of the NiPtNCs in the ZIF-8 structure.[92] Fischer *et al.* prepared ~ 1.1 nm PtNCs with atom-precise Pt carbonyl NCs using ZIF-8 as templates. $[Pt_9(CO)_{18}][NBu_4]_2$ was reported to form ligand-free PtNCs inside ZIF-8 through a thermal-oxidative decarboxylation approach, and also Pt_{12}NCs can be achieved from $[NBu_4]_2[Pt_3(CO)_6\}_4]$ NCs based on the sample synthesis mechanism.

As mentioned in the introduction, Pt metal is suggested to be the most common catalyst for many catalytic reactions, including HER, ORR, and other organic reactions. Decreasing the PtNPs' size is one of the effective strategies to increase the Pt dispersion and catalytic activity sites. For HER, theoretical calculation have estimated that Pt metal with the size of ca. 1.8 nm exhibiting the best catalytic properties.[93] Few reports were recorded for the synthesis of ligand-free PtNCs. Thus the production of ligand-free PtNCs with highly catalytic properties is still in high demand.[94, 95]

Apart from the catalysis applications, monodispersed metal NCs would contribute to other possible applications. Hence, it is highly desired to release the NCs from MOFs templates to expand the applicable possibility of NCs. The surface modification would be one of the methods to stabilize the NCs for further use in the absence of MOFs and easily achievable.

In the present work, ligand-free PtNCs anchored on the outer defects of ZIF-8 were synthesized via a rapid template-assisted method in methanol solvent, and the obtained products were denoted as PtNCs@ZIF-8. The as-prepared PtNCs in ZIF-8 exhibit superior catalytic activity in the reduction of the 4-nitrophenol and electrocatalytic performance in ORR and HER. Moreover, these ligand-free PtNCs from PtNCs@ZIF-8 can be easily released from ZIF-8 with intact structure and diameter into both aqueous and non-aqueous conditions. This would provide a versatile approach to creating and functionalizing NCs according to the application demands.

2.2 Results and discussion

2.2.1 Characterization of PtNCs@ZIF-8

The PtNCs@ZIF-8 nanocomposites were prepared by a facile synthesis approach, whose schematic illustration was shown in **Figure 2-1**. First of all, we dropwise added 2-methyl imidazole (2- MeIM)/methanol (MeOH) solution into zinc nitrate hexahydrate $(Zn(NO_3)_2 \cdot 6H_2O)$/MeOH to

synthesize template ZIF-8, which is milky color (more details are shown in Experimental Design in **6.3.1.1**). Next, the H_2PtCl_6 aqueous solution was introduced to the as-synthesized ZIF-8/MeOH solution. In this step, four different volumes (0.333, 1.332, 1.998, and 2.664 mL, separately) of Pt precursors solution were added, and thus the obtained PtNCs@ZIF-8 are denoted as Pt-1, Pt-2, Pt-3 and Pt-4@ZIF-8, respectively. Following is the fast addition of the freshly prepared reducing agent sodium borohydride ($NaBH_4$) aqueous solution under constant stirring. Subsequently, the mixture color obviously changed from light yellow to dark brown in approximately 3 min, which may indicate the PtNCs formation in the mixture. After the synthesis process, the product was washed with methanol by centrifugation several times. Then, the PtNCs@ZIF-8 precipitate was collected and left drying in the air for at least 24 h, and the obtained powder product was kept for further use.

The morphology of the above as-synthesized PtNCs@ZIF-8 was investigated by transmission electron microscopy (TEM). The TEM images indicated the rhombic dodecahedral shape of the hybrid materials for all as-synthesized PtNCs@ZIF-8 of Pt-1, Pt-2, Pt-3 and Pt-4@ZIF-8 (**Figure 2-3** and **Figure 2-4**), respectively, which are in good agreement with pure ZIF-8 (**Figure 2-2**).[96] The TEM images of Pt-2@ZIF-8 displayed a more homogeneous distribution of PtNCs in the outer layer of the ZIF-8 structures (**Figure 2-4, b-c**) compared to Pt-1, Pt-3 and P-4@ZIF-8 (**Figure 2-3**). Notably, the enlarged TEM image of Pt-2@ZIF-8 in **Figure 2-4c** revealed that the PtNCs are densely populated near the edge side of the ZIF-8. On the other hand, the population of PtNCs per ZIF-8 was very low in Pt-3 and Pt-4@ZIF-8 with some aggregated dots as shown in corresponding TEM images (**Figure 2-3, b-c**), while extremely low PtNCs could be found in Pt-1@ZIF-8 (**Figure 2-3a**). This data set demonstrates that the ratio of Pt content/ZIF-8 may play a decisive role in controlling the homogeneity and spatial distribution of PtNCs in ZIF-8. Due to the better homogeneity of PtNCs in ZIF-8 of Pt-2@ZIF-8, further investigation was carried out only for this nanocomposite. The inorganic core diameter of PtNCs in Pt-2@ZIF-8 was calculated to be $d_c = 1.86 \pm 0.20$ nm (**Figure 2-4e**). The high-resolution TEM (HRTEM) image reveals the single-crystalline nature of the PtNCs in Pt-2@ZIF-8 with the highlighted lattice distances of 0.225 nm, which matches well with (111) facets of a typical face-centred cubic (*fcc*) Pt structure (**Figure 2-4d**).[97]

Figure 2-4a displays the powder X-ray diffraction (PXRD) patterns of Pt-2@ZIF-8 nanocomposites, confirming the unalter structure of ZIF-8 after the formation of PtNCs compared with those of the simulated ZIF-8 (blue curve). The PXRD patterns of diffraction peaks in the 2Ө range of 10 - 38 degrees for Pt-2@ZIF-8 (red curve) can be well indexed to those for the corresponding parent ZIF-8 (black curve), indicating that the ZIF-8 structure keeps intact after the formation of PtNCs in ZIF-8. It can be

found that a broad peak appeared near at $2\Theta = 40°$ of Pt-2@ZIF-8, which is indexed to (111) of the Pt with *fcc* structure (green curve).[98] Its large width is most likely resulting from the ultrasmall nature of the particles size, whose diffraction peak shape is not as obvious as that of the simulated bulk Pt material.
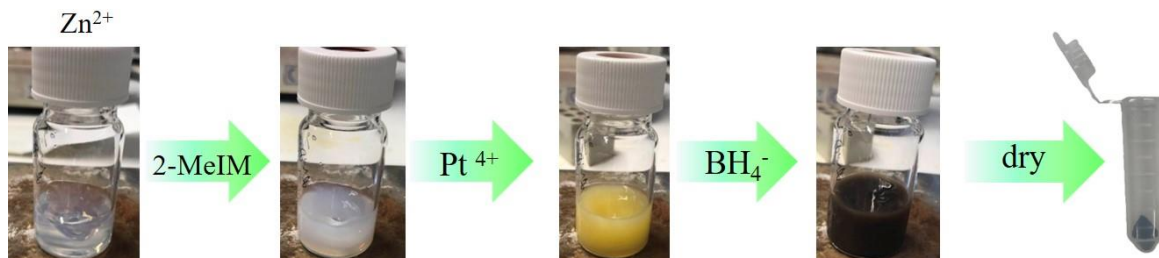
Figure 2-1. *Schematic illustration of PtNCs@ZIF-8 synthesis.*
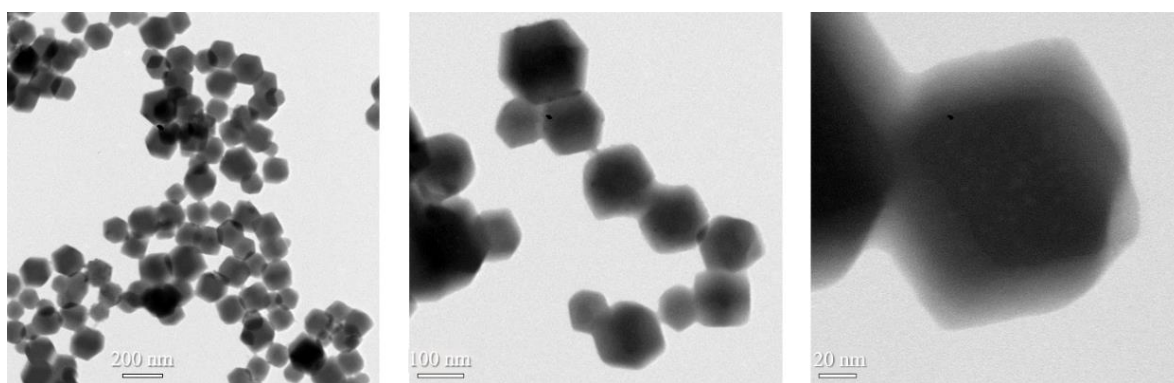
Figure 2-2. *Representative TEM images of parent ZIF-8. The TEM images of this figure were recorded by Mr. Andreas Kornowski.*
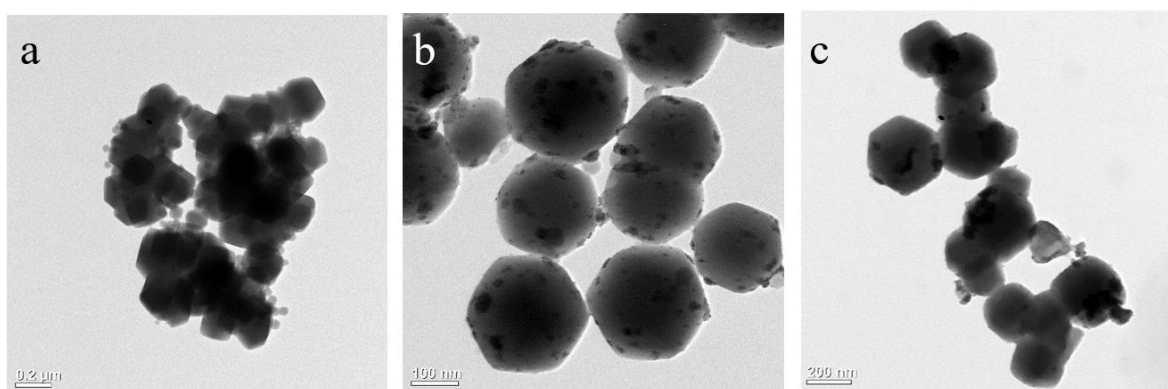
Figure 2-3. *Representative TEM images of PtNCs@ZIF-8. (a) Pt-1@ZIF-8, (b) Pt-3@ZIF-8, and (c) Pt-4@ZIF-8.The TEM images of this figure were recorded by Mr. Andreas Kornowski.*
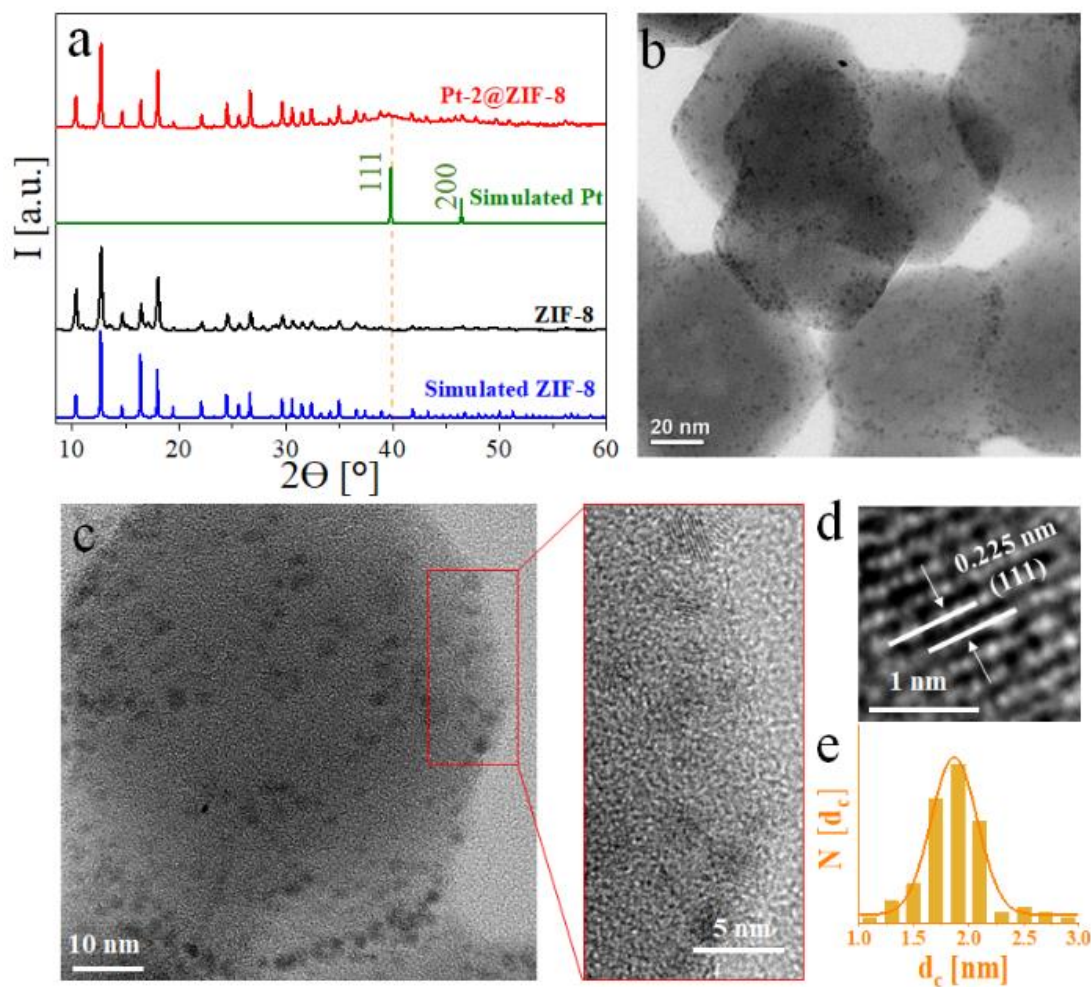
Figure 2-4. *PRXD patterns and TEM images of ZIF-8 and Pt-2@ZIF-8. (a) PXRD patterns of as-synthesized ZIF-8 and Pt-2@ZIF-8 compared with simulated ZIF-8 and simulated Pt bulk (fcc). (b-c) Representative TEM images of Pt-2@ZIF-8. (d-e) Representative HRTEM image of a PtNC (d) and the corresponding size distribution histogram of the core diameter (e, $d_c = 1.86 \pm 0.20$ nm). The PXRD patterns of this figure were recorded by Ms. Almut Barck, and TEM and HRTEM images of this figure were recorded by Mr. Andreas Kornowski.*

High-angle annular dark-field scanning transmission electron microscopy (HAADF-STEM) images of PtNCs in Pt-2@ZIF-8 nanocomposites (**Figure 2-5**, **a-b**) and the corresponding energy-dispersive X-ray spectroscopy (EDS) elemental mapping analysis (**Figure 2-5**, **c-d**) confirm that Pt has homogeneous distribution in Pt-2@ZIF-8. The presence of the Zn and N indicated the formation of the ZIF-8 structure. Further, X-ray photoelectron spectroscopy (XPS) spectra confirmed the presence of Pt element in addition to Zn, C, N and O elements in Pt-2@ZIF-8 compared to those in the ZIF-8 shown in survey spectra of **Figure 2-6a**. After Pt formation, the XPS spectra of Zn and N in Pt-2@ZIF-8 is distinct from in the pure ZIF-8 (**Figure 2-5**, **e-f**). One noticeable difference is that the peaks for N 1s and Zn 2p shifted

12

to higher binding energy (0.5 eV for N element and 1 eV for Zn element) after PtNCs formation, implying the existence of an interaction between Pt with N and Zn.[99, 100] As a comparison, the peaks for C 1s do not shift after PtNCs loading (**Figure 2-6b**). The peak intensity of the N 1s peak (responsible for the nitrogen with a double bond with C) is considerably decreased (**Figure 2-5e**) in Pt-2@ZIF-8, which might be arising from the reduction after the addition of the reducing agent $NaBH_4$.[101] The increasing percentage of Zn^{2+} in Pt-2@ZIF-8 may be attributed to the formation of a Zn-Pt bonding interaction (**Figure 2-5f**).[100]
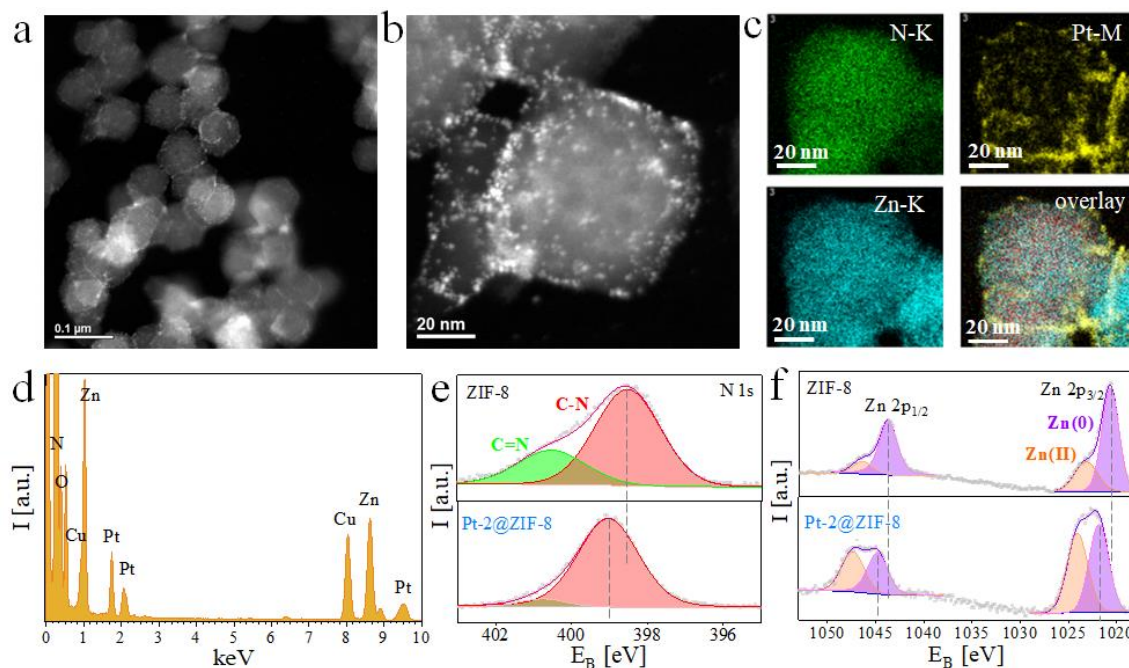
Figure 2-5. HAADF-STEM images, EDS spectra and high-resolution XPS spectra of Pt-2@ZIF-8. (a-b) HAADF-STEM images and (c) corresponding element mapping images, displaying the uniform distribution of Pt (yellow). (d) EDS spectra of Pt- 2@ZIF-8, showing the presence of PtNCs in ZIF-8. (e-f) High-resolution XPS spectra of N1s and Zn2p of ZIF-8 and Pt-2@ZIF-8. EB is the binding energy. The HAADF-STEM and EDS spectra data of this figure were recorded by Mr. Andreas Kornowski, and XPS spectra was recorded in CIAC, CAS.

The interaction of N with Pt in Pt-2@ZIF-8 was further confirmed by the Fourier transform infrared (FTIR) spectroscopy. A change in the C=N stretching peak (near 1584 cm^{-1}) was observed in the FTIR spectra of Pt-2@ZIF-8 compared to the corresponding ZIF-8 (**Figure 2-7**). The spectral broadening at this regime might result from the proximity or bonding interactions of PtNCs with the nitrogen group of ZIF-8.[102] Based on this structural characterization, the PtNCs formation mechanism on ZIF-8 can be explained. The unsaturated Zn and free N^- extremities on the external surface of ZIF-8 or at defects[103] can hold the Pt precursor $(PtCl_4^-)$[104] where NC nucleation initiates during the *in situ* reductions. Moreover, the STEM

images demonstrated that the PtNCs are distributed mostly within the outer layer of the ZIF-8 structure but not inside the ZIF-8, which can be attributed to the outer defect structure of ZIF-8.[105-107] The surface pore defects[108, 109] in ZIF-8 worked as the template for PtNC growth and restricted the NC's overgrowth. The formation of PtNCs inside the pores of ZIF-8 is ruled out as the internal pore diameter (1.16 nm) of ZIF-8 is much smaller than the size of PtNCs (1.86 nm in diameter).
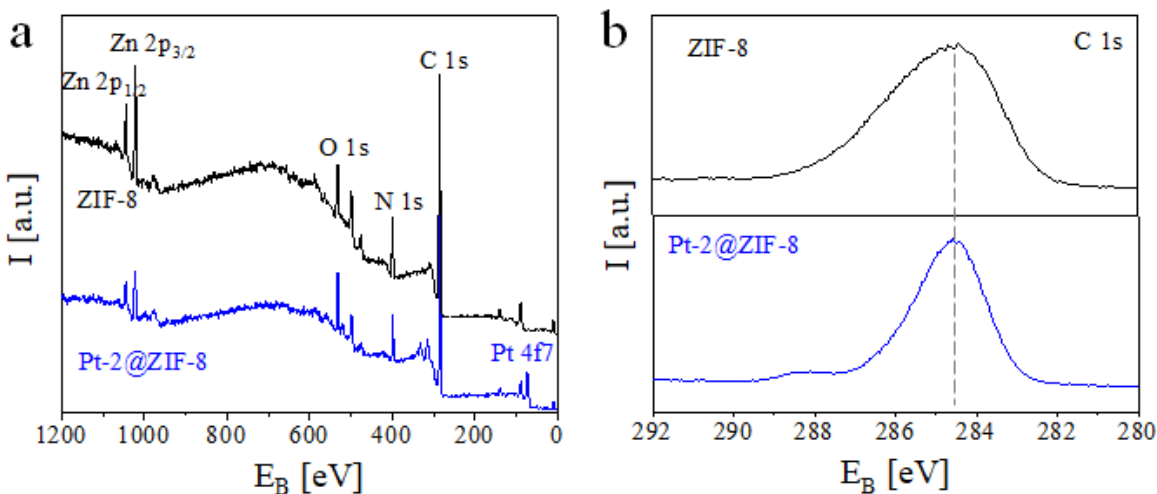
Figure 2-6. *XPS spectra of ZIF-8 and Pt-2@ZIF-8. (a) XPS spectra survey of ZIF-8 and Pt-2@ZIF-8. (b) High-resolution XPS spectra of C1s of ZIF-8 and Pt-2@ZIF-8. No peak shift was observed. XPS spectra was recorded in CIAC, CAS.*
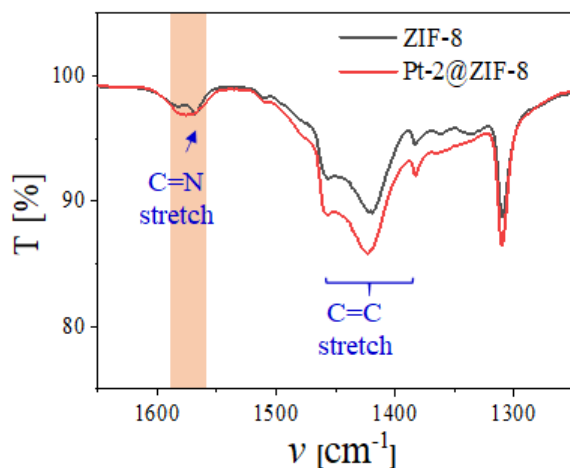
Figure 2-7. *FTIR spectra of ZIF-8 and Pt-2@ZIF-8 ZIF-8 (black line) and Pt-2@ZIF-8, respectively(transmission mode T (v), i.e., transmission T versus wavenumber v). The FTIR spectra of this figure were recorded at University of Marburg.*

2.2.2 Catalytic reduction of 4-nitrophenol (4-NP)

The catalytic activity of Pt-2@ZIF-8 was first assessed with the standard reduction reaction on catalyzing 4-NP reducing to 4-aminophenol (4-AP) by sodium borohydride (NaBH$_4$).[110-114] The underlying mechanism is shown in **Figure 2-8a**. This catalytic reduction reaction of 4-NPA anion at 400 nm can be easily monitored by UV-vis absorption spectroscopy (**Figure 2-8b**, inset). It should be noted that in the absence of BH$_4^-$, the absorption peak of 4-NP was at 317 nm (**Figure 2-8b**, inset, black trace), which is shifted to 400 nm (A$_{400}$) because of the formation of 4-NPA anion in the presence of BH$_4^-$ (**Figure 2-8b**, inset). The continuous decrease of the absorption peak of A$_{400}$ and the corresponding increase of the absorption peak at λ = 232 nm indicated the reduction of 4-NPA and the formation of 4-AP.[33]

Figure 2-8b shows the dramatic conversion in the presence of Pt-2@ZIF-8 (red trace), while no reduction reaction was observed in the absence of catalyst (black trace), indicating the catalytic property of Pt- 2@ZIF-8 on the reduction of 4-NP. The corresponding image (**Figure 2-8b**, inset) further visibly illustrate the reduction reaction that the solution color of yellow (4-NPA) changed to colorless due to the formation of 4-AP.

Concentration-dependent experiments were carried out to gain further insight into the kinetics of Pt-2@ZIF-8 nanocatalysts (**Figure 2-9**). Different concentrations of platinum C$_{Pt}$ (0.579 0.959, 1.904, 3.246, and 4.474 mg/L, respectively) were investigated. The platinum concentrations were calculated by ICP-MS. For all these reduction experiments, the initial concentration of 4-NP and NaBH$_4$ was maintained at 0.08 mM and 0.024 M, respectively. Because the concentration of NaBH$_4$ is much higher than that of 4-NP, its concentration can be considered as constant throughout the reduction process. Hence, the whole reduction reaction is taken as a pseudo-first-order kinetic mechanism on 4-NP. As expected, a linear relationship of k with concentration was observed (**Figure 2-9g**). For relatively low Pt concentration (C$_{Pt}$ = 1.904 mg L^{-1}), the rate constant k was calculated to be 5.18×10^{-3} s^{-1}. The mass activity parameter (k' = k/m) of Pt-2@ZIF-8 was calculated to be 1.29×10^2 s^{-1} g^{-1}.[115] Those values indicate that the catalytic efficiency of the as-synthesized Pt-2@ZIF-8 on the reduction of 4-NP is higher than those of many previously reported metal@MOF hybrid catalysts (**Table 2-1**).[90, 91, 116, 117]

Moreover, the dependence of reaction rate constant on temperature was also investigated. As shown in **Figure 2-10**, the k under four different temperatures of 290, 295, 300 and 305 K were obtained. The activation energy of E$_a$ = 15.1 kJ mol^{-1} (**Figure 2-10e**) was received by the linear fitting of ln k versus 1/T with the Arrhenius equation. This activation energy is much lower than that of previous reports,[118] further indicating the high catalytic activity of Pt-2@ZIF-8.

It is assumed that the superior catalytic performance of Pt-2@ZIF-8 could be probably ascribed to the following factors: first, the structural properties of ZIF-8 plays an important role. The high porosity is beneficial for the fast transport of 4-NP reactant and 4-AP products.[119] Also the organic ligands of ZIF-8 should facilitate the adsorption of 4-NP via π–π stacking interactions with the aromatic rings of 4-NP, which might improve the contact probability between the 4-NP and the catalyst.[120] Second, the high catalytic performance might be attributed to the morphology, size, and spatial distribution of PtNCs.[121] The increased surface area makes the active sites more accessible, and as a result, the catalytic performance could be enhanced. Third, the strong interaction between the PtNCs and the ZIF-8 framework could efficiently protect the PtNCs from agglomerating, and based on ZIF-8 support, the dispersion of PtNCs could be preserved.[119] The synergistic effect of PtNCs and ZIF-8, thus, is of significance to enhance the catalytic activity of 4-NP with NaBH$_4$.
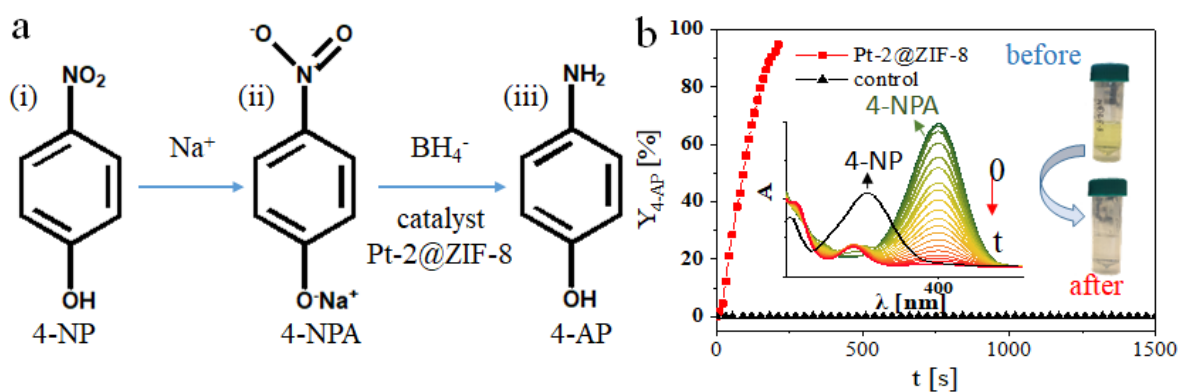
Figure 2-8. *Conversion of 4-NP to 4-AP by Pt-2@ZIF-8 in the presence of NaBH$_4$. (a) Mechanism of the reduction of 4-NP to 4-AP catalyzed by Pt-2@ZIF-8 upon the addition of NaBH$_4$. (b) Conversion yield of 4-NP (Y$_{4-AP}$) to 4-AP in presence (red trace) and absence (black trace) of Pt-2@ZIF-8 catalyst. The inset UV−vis absorption spectra show the corresponding reduction of 4-NP from 4-NPA to 4-AP by NaBH$_4$ catalyzed by Pt-2@ZIF-8, from which the conversion has been calculated. The inset images illustrate the reduction reaction of 4-NPA (yellow) to 4-AP (colorless).*

16
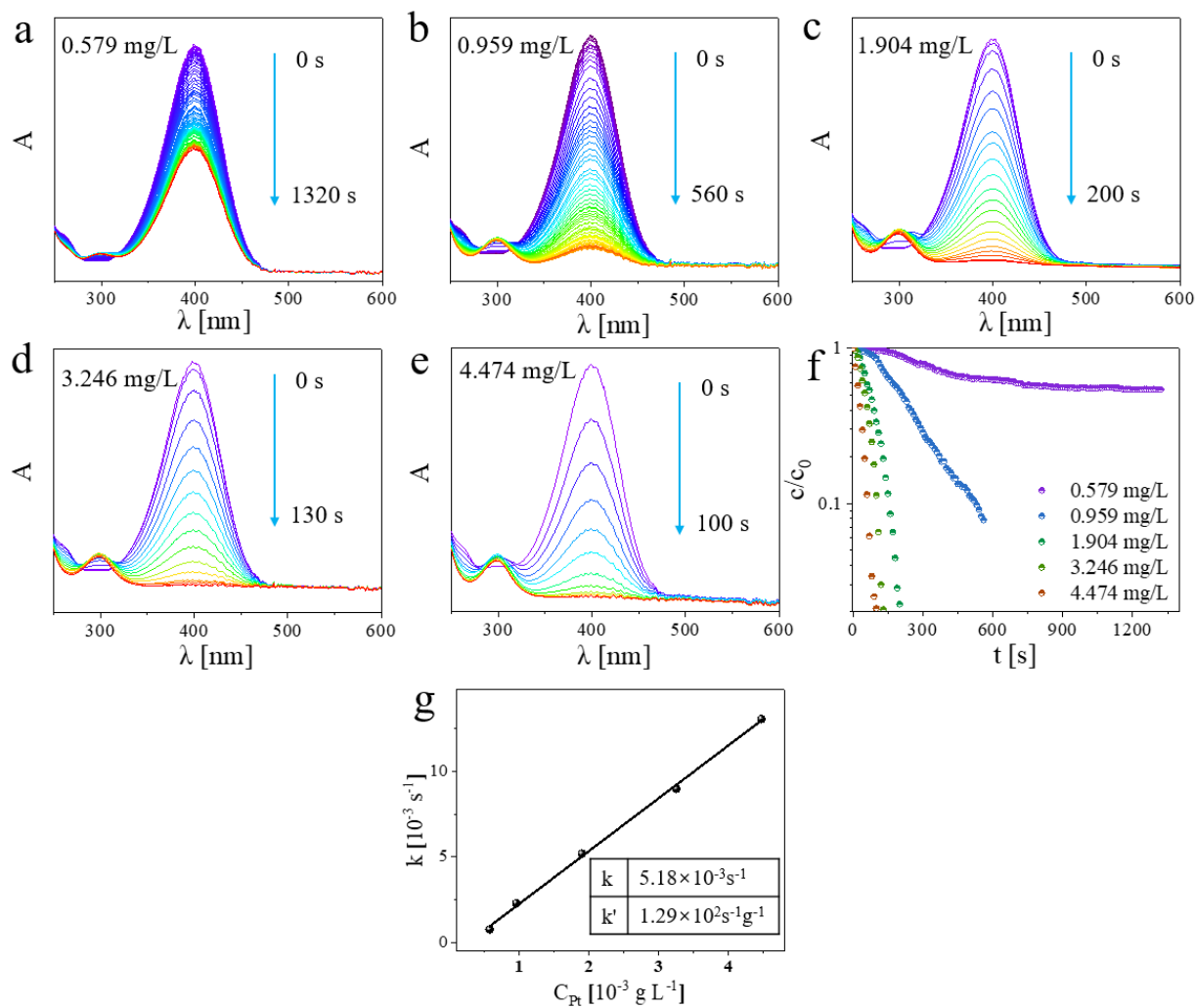
Figure 2-9. *Conentration dependence on Pt-2@ZIF-8 upon the reduction of 4-NP. (a-e) UV-vis spectral data for the concentration-dependent experiment on the reduction rate of 4-NP. (f) Corresponding linear plots of the 4-NP concentration c (which is proportional to A) in terms of ln (c/c₀) versus t (c₀ is proportional to A₀ (at λ = 400 nm) at t = 0 s), as obtained from UV-vis spectra (a-e). (g) Plot of k versus C_{pt} for the 4-NP reduction by NaBH₄ catalyzed by different concentration of Pt-2@ZIF-8 at 22 °C.*
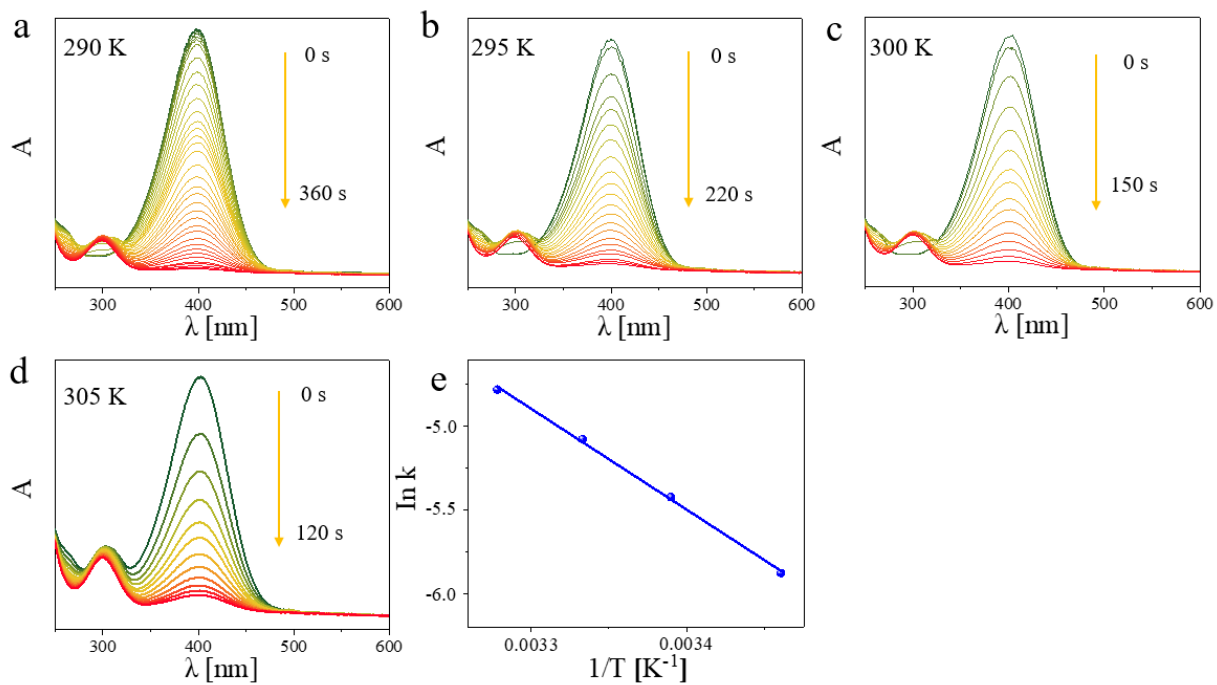
Figure 2-10. *Temperature dependence on the reduction of 4-NP. (a-d) UV-vis absorption spectra representing the temperature-dependent kinetics of the 4-NP reduction. (e) Plot of In k versus 1/T for the 4-NP reduction by NaBH4 with $C_{Pt} = 1.628$ mg/L.*

Table 2-1. *Comparison with diverse noble metal@MOF catalysts on the reported 4-NP reduction reaction.*

	catalyst	d_c *[nm]*	k *[10^{-3} s^{-1}]*	k' *[10^2 s^{-1} g^{-1}]*	*Reference*
1	*1 kGy Ag@HKUST-1*	*1.4 ± 0.7*	*14*	*0.0723*	[122]
2	*1000Au$_{25}$(SG)$_{18}$@ZIF-8*	*1.5*	*-*	*-*	[116]
3	*2Ag/MIL-101(Cr)*	*1.9 ± 0.6*	*2.89*	*-*	[123]
4	*PtNCs@ZIF-8*	*1.91 ± 0.37*	*5.18*	*1.29*	*This work*
5	*Au$_{0.4}$Pt$_{0.6}$/HKUST-1*	*2.0 ± 0.4*	*6.23*	*-*	[90]
6	*Ag@CTGU-1*	*2*	*25.7*	*0.25*	[117]
7	*Au(III)@Cu(II)-MOF*	*2.0*	*-*	*-*	[124]
8	*Pd/HKUST-1*	*2.1 ± 0.4*	*4.48*	*-*	[90]
9	*Au−Pd@BIF-39-Cd*	*2.12*	*-*		[97]
10	*Au$_{0.3}$Pt$_{0.3}$Pd$_{0.4}$/ HKUST-1*	*2.2 ± 0.2*	*7.96*	*-*	[90]
11	*Au$_{0.4}$Pd$_{0.6}$/HKUST-1*	*2.3 ± 0.3*	*5.21*	*-*	[90]
12	*Pd@MIL-101*	*1.5 - 2.5*	*1.89*	*0.0019*	[91]
13	*Au/HKUST-1*	*2.6 ± 0.6*	*3.73*	*-*	[90]
14	*Pt/HKUST-1*	*2.8 ± 0.5*	*3.03*	*-*	[90]
15	*Pt/UiO-66*	*2.9*	*-*	*-*	[125]
16	*ZIF-8@Au*	*2 - 3*	*-*	*-*	[126]
17	*ZIF-8@Au@mSiO$_2$*	*2 - 3*	*-*	*-*	[127]
18	*2%Au@2%Ag/ZIF-8*	*2 - 6*	*4.97*	*0.014*	[89]
19	*Au@Ag/MIL-101-S*	*2 - 10*	*4.58*	*-*	[120]
20	*Ag@BIF-20*	*3.0*	*370*	*0.74*	[128]
21	*Au@BIF-20*	*4.0*	*220*	*0.44*	[128]
22	*Ag@CTGU-3*	*4 ± 2*	*8.64*	*0.086*	[34]
23	*Pd/MPC*	*5*	*12*	*4.00*	[129]
24	*Au/MPC*	*5 - 8*	*10*	*0.33*	[129]
25	*Ag@CTGU-4*	*6 ± 2*	*3.03*	*0.03*	[34]
26	*Ag/HKUST-1*	*8.7 ± 2.8*	*2.9*	*-*	[90]
27	*UiO-66-NH2/TTACP/Ni@Pd*	*10*	*0.014*	*0.14*	[115]
28	*MagNP@PDA@AuNPs@ZIF-8*	*15*	*0*	*-*	[130]

29	MagNP@PDA@AuNPs@UiO-66	15	-	-	[130]
30	Pd-0.5Br@1P@MOF	-	-	-	[35]
31	Pd-0.5Br@2P@MOF	-	-	-	[35]
32	Pd-0.5Br@3P@MOF	-	-	-	[35]
33	Pd-NH2-UiO-66	-	-	-	[35]
34	Au@ MIL-100(Fe)	-	5.5	0.016	[131]
35	Au/MIL-101-S	-	0.008	-	[120]
36	Ag/MIL-101-S	-	1.527	-	[120]
37	Ag(I)-MOFs	-	3.3	-	[132]

2.2.3 Electrochemical catalytic activity study

2.2.3.1 Hydrogen evolution reaction (HER) analysis

The HER performance of Pt-2@ZIF-8 catalyst and commercial 20 wt.% Pt/C catalyst was evaluated in N_2-saturated 0.1 M $HClO_4$ with a sweep rate of 50 mV s^{-1}. **Figure 2-11** shows the cyclic voltammetrys (CVs) of Pt-2@ZIF-8, and the typical H*/O*-adsorption/desorption peaks for the Pt are observed, indicating the PtNCs supported on the non-conductive ZIF-8. The increased peaks become steady after 20 cycles because all PtNCs are exposed due to the dissolving of ZIF-8 structures under acidic conditions. This further demonstrated that the PtNCs are not placed inside of ZIF-8; otherwise, no characteristic peaks of Pt can be observed in the first cycle due to the non-conductive property of ZIF-8.[58] It should be noted that that for electrochemical processes, the applied potential E' of the working electrode is converted into the potential (hereafter noted as E) in reference to a reversible hydrogen electrode (RHE) for better comparison.

Figure 2-12a illustrated the corresponding linear sweep voltammetry (LSV) of HER measurement for Pt-2@ZIF-8 and the commercial 20 wt.% Pt/C catalysts. It can be found that Pt-2@ZIF-8 exhibited excellent HER performance in comparison with the commercial 20 wt.% Pt/C catalysts. In particular, to achieve a 10 mA cm^{-2} current density (the critical value for the conversion of solar fuel),[133] the Pt-2@ZIF-8 required a much small overpotential (E_η) of 1.4 mV, which is 16 mV lower than that of the commercial Pt/C (17.4 mV) under the same conditions (**Figure 2-12a**, inset).[134] Moreover, the kinetic current was utilized to further characterize the intrinsic electrocatalytic performance. The specific activity (SA) of Pt-based catalysts was introduced, which is calculated with the normalized current density to the electrochemically active surface area (ECSA) of Pt-based catalyst.[135] **Figure 2-12a** showed that Pt-2@ZIF-8 had achieved a current density of 33.9 mA cm^{-2} when E_η = 50 mV, which is slightly higher than that of the commercial 20 wt.% Pt/C catalyst with 30.2 mA cm^{-2}. In terms of SA, however, the as-prepared Pt-2@ZIF-8 catalyst exhibited the calculated SA of ca. 20.5 mA cm^{-2}, which is approximately 11-fold better than that of commercial 20 wt.% Pt/C catalyst of 1.9 mA cm^{-2} (**Figure 2-12b**, left Y-axis). On the other hand, the mass-activity (MA) of Pt in the commercial 20 wt.% Pt/C and Pt-2@ZIF-8 was further studied. Based on the ICP-MS results of the prepared inks, Pt-mass of commercial 20 wt.% Pt/C and Pt-2@ZIF-8 loaded on the electrode was approximately 32 and 4 µg cm^{-2}, respectively. Hence, the MA of Pt-loading was calculated to be 7.61 A mg^{-1}_{Pt} at E_η of 50 mV, which is about 8 times higher than that of the state-of-the-art commercial 20 wt.% Pt/C (0.95 A mg^{-1}_{Pt}) as presented in **Figure 2-12b**, right Y-axis.

Notably, both parameters of the lower overpotential E_η (at $j = 10$ mA cm^{-2}) and a small Tafel slope β are preferred for catalysts with high activity in the application, showing the better scaling of the kinetics with voltage.[136] As shown in **Figure 2-12c**, the resulting Tafel slope of Pt-2@ZIF-8 was calculated to be $\beta \approx 24$ mV per decade, which is equal to that of the commercial 20 wt.% Pt/C catalyst. This suggests that the mechanism of the Volmer-Tafel process was the same for both catalysts for HER under acidic conditions, while Tafel step was the rate-determining process.[61] Besides, the exchange current density (j_0) was evaluated according to the extrapolation of the Tafel plot. As shown in **Figure 2-12d** (inset), the j_0 value of Pt-2@ZIF-8 (11.6 mA cm^{-2}) was 4.3 times higher than that of the commercial 20 wt.% Pt/C catalyst (2.7 mA cm^{-2}), which suggests the outstanding electrocatalytic property of our Pt-2@ZIF-8 catalyst.
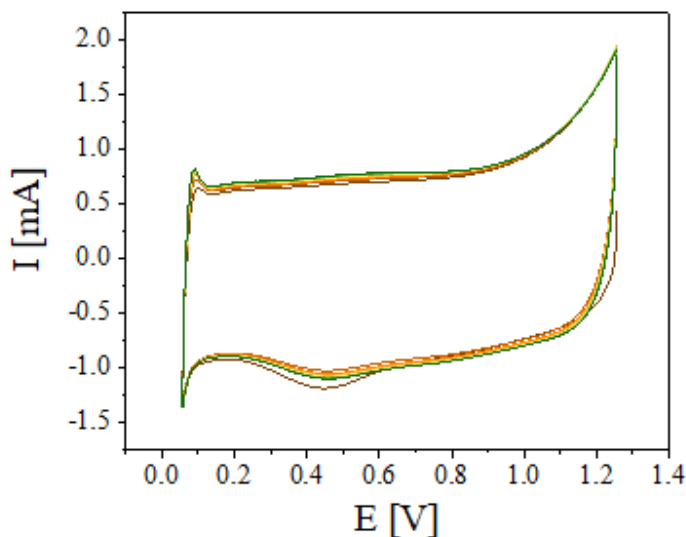
Figure 2-11. *CVs of the prepared electrode with Pt-2@ZIF-8 catalyst. The CVs data in this figure was recorded by Mr. Mingbo Ruan.*
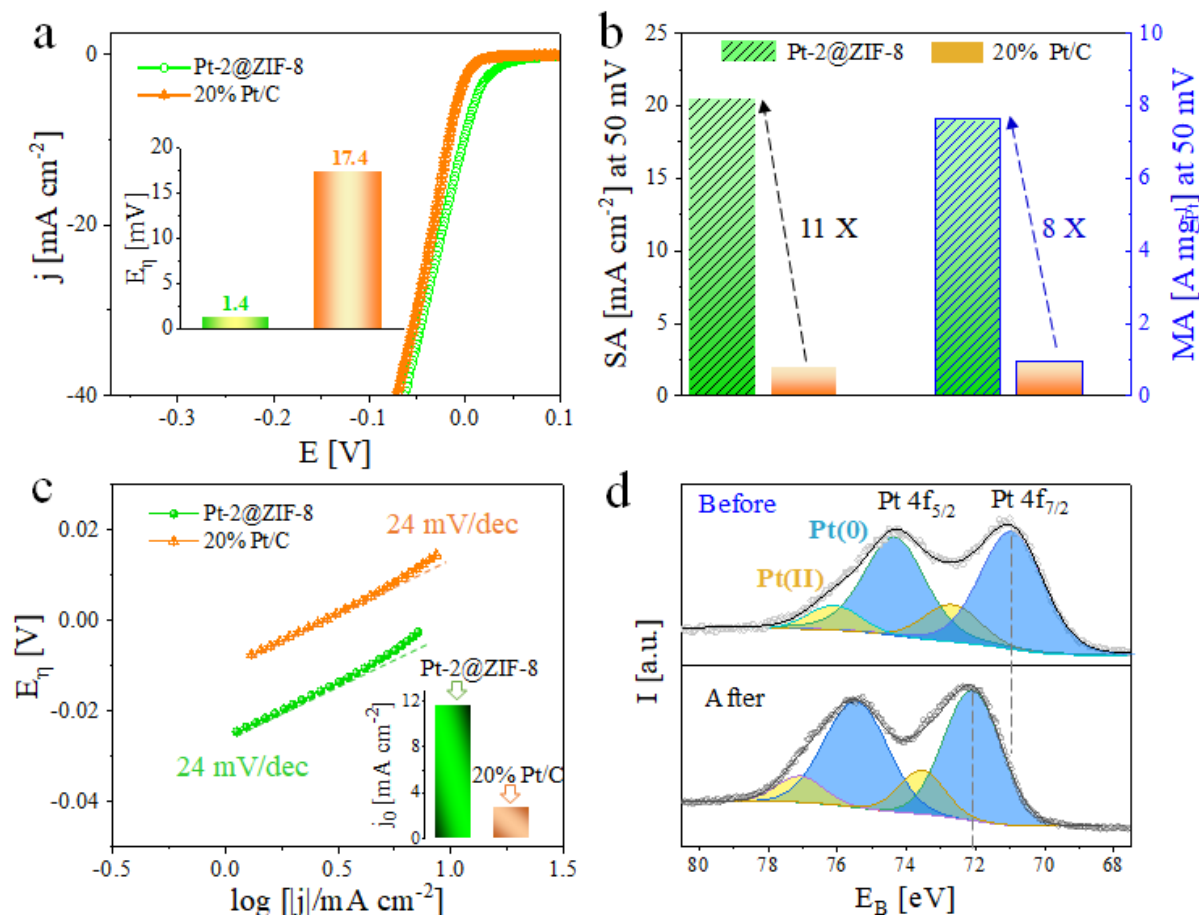
Figure 2-12. *Representative HER activities and XPS spectra of Pt 4f before and after HER measurements. (a) HER polarization curves of Pt-2@ZIF-8 and the commercial 20 wt.% Pt/C catalysts in N_2-saturated 0.1 M $HClO_4$. The inset shows the overpotential E_η at a current density of $j = 10$ mA cm^{-2}. The current density j is plotted versus the applied potential E, which has been converted in reference to the potential of an RHE (details are mentioned in SI). The scan rate was 5 mV s^{-1}. (b) The SA and MA of PtNCs compared with the commercial 20 wt.% Pt/C catalyst at overpotential 50 mV. (c) Corresponding HER Tafel plots derived from the data presented in 'a'. The inset shows the relative exchange current densities. (d) High-resolution Pt 4f XPS spectra of Pt-2@ZIF-8 before and after HER tests. The HER tests were recorded by Mr. Mingbo Ruan and XPS data of this figure were recorded in CIAC, CAS.*

Furthermore, the long-term stability of catalysts is another important parameter to evaluate the catalysts. To investigate the stability of the Pt-2@ZIF-8, accelerated durability test (ADT) of Pt-2@ZIF-8 catalyst was carried out. **Figure 2-13** revealed the negligible degradation in polarization curves of Pt-2@ZIF-8 in 4000 CV cycles, suggesting this promising material with excellent catalytic stability. For a straightforward comparison, all the above-mentioned parameters (η_{10}, j_0, SA, MA and Tafel slope, etc.) of our Pt-2@ZIF-8 together with other Pt-based HER catalysts are listed in **Table 2-2**, indicating the

better HER activity of our Pt-2@ZIF-8.

It could be speculated that the highly catalytic activity is probably attributed to the smaller size and ligand-free property, allowing the most surface atoms be accessible to the reactants. To gain further insight into the size-effect of HER, the catalytic activities of other Pt-based catalysts of low Pt loading (Pt-1@ZIF-8), larger Pt size (Pt-3@ZIF-8 and Pt-4@ZIF-8), and PtNPs (~ 5 nm in diameter) capped with ligands[137] were conducted, which showed much lower HER efficient than that of the Pt-2@ZIF-8 (as shown in **Figure 2-14**). This may be ascribed to the size of PtNCs (~ 1.86 nm), offering the optimal coordination number of the surface atoms for HER consistent with the previous report.[93] Moreover, XPS spectra was further applied to clarify the catalytic stability of the Pt-2@ZIF-8 catalyst by analyzing the chemical state of Pt 4f before and after HER measurements. In **Figure 2-12d**, it could be found that the Pt 4f peak position of PtNCs exhibited similar binding energies before and after HER test, which indicates good stability of PtNCs during catalysis in good agreement with ADT result. Notably, a peak shift of ~ 1 eV to lower binding energy was observed, which could be due to the PtNCs environment changing because of the ZIF-8 structure was destroyed under the acidic test conditions.[138] Furthermore, **Figure 2-15** showed the XPS spectra of Zn 2p, indicating that trace Zn element were still left after the test. The trace Zn element left maybe form Pt-Zn alloy, which may also contribute to the high catalytic performance and stability of PtNCs.[139, 140] Furthermore, no agglomeration of PtNCs were observed in TEM images after HER experiments. The corresponding size distribution of the diameter is highly consistent with the Pt-2@ZIF-8 before HER measurements, as shown in **Figure 2-16**.
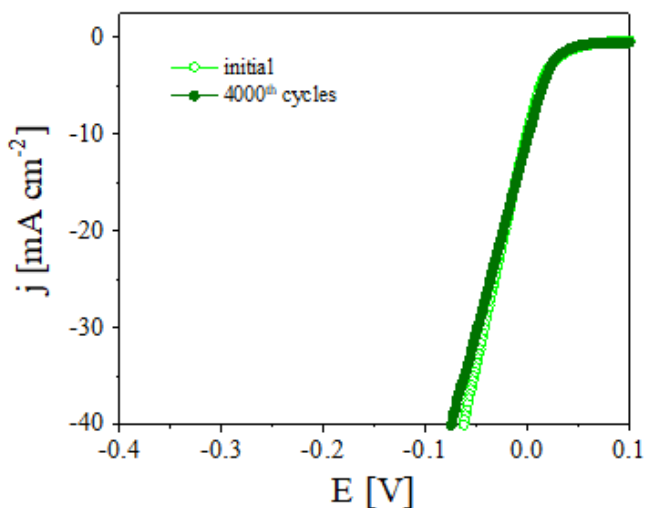
Figure 2-13. *Polarization curves of Pt-2@ZIF-8 catalyst initially and after 4000 CVs cycles. The LSV data of this figure were recorded by Mr. Mingbo Ruan.*
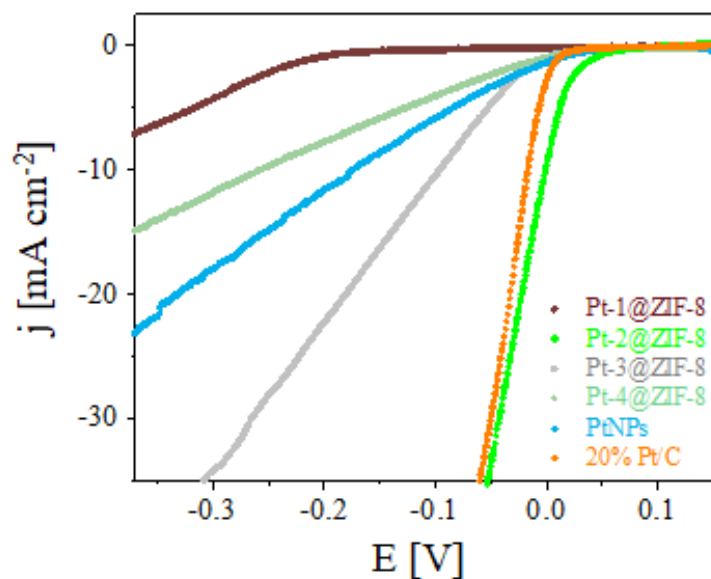
Figure 2-14. *HER of other catalysts in N₂-saturated 0.1 M HClO₄. The LSV data of this figure were recorded by Mr. Mingbo Ruan.*
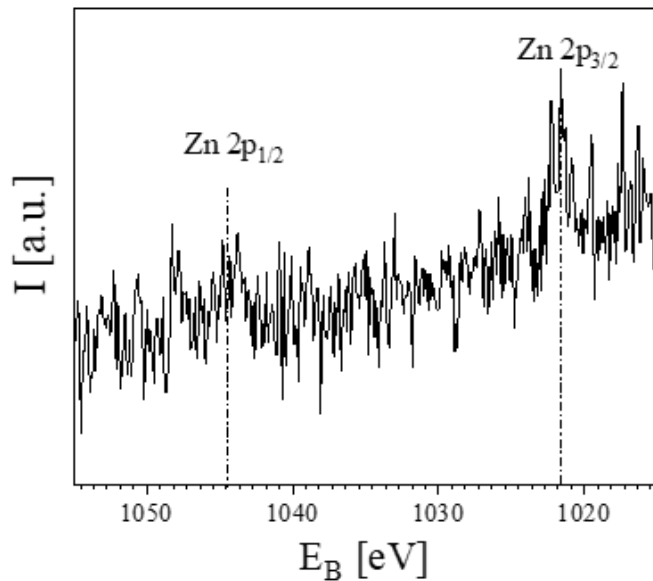
Figure 2-15. *XPS spectrum of Zn 2p of the catalyst after HER measurements. The XPS data of this figure were recorded in CIAC, CAS.*
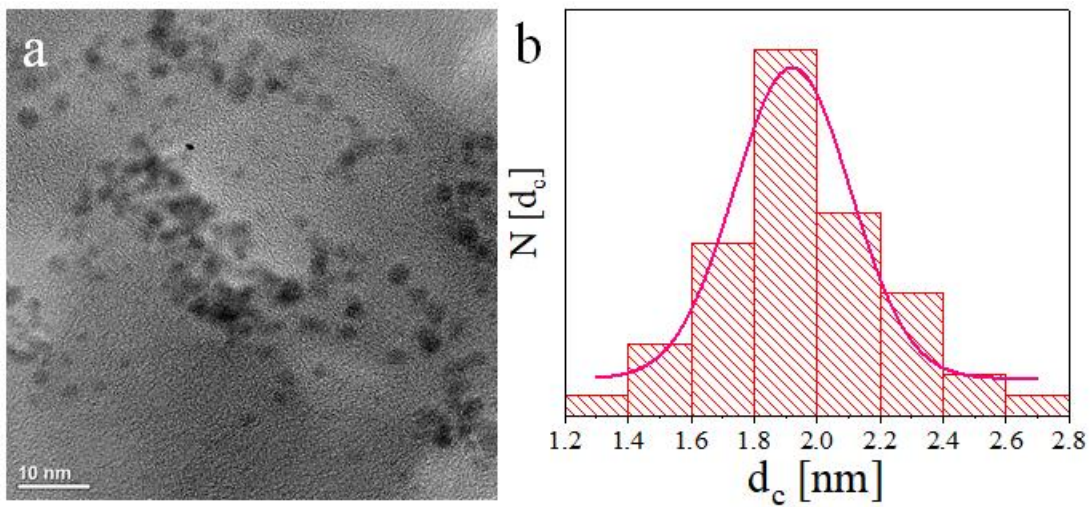
Figure 2-16. *TEM characterization of Pt-2@ZIF-8 after HER measurements. (a) TEM image and (b) the corresponding distribution of the inorganic core diameter with a mean value of 1.92 ± 0.36 nm. The TEM image of this figure was recorded by Mr. Andreas Kornowski.*

Table 2-2. *Comparison of the HER properties of PtNCs and Pt single atom-based catalysts from this work and references published in the last two years.*

Catalyst	Pt Loading /μg cm^{-2}	Electrolyte	η_{10} /mV	Dura-bility /Cycles	Mass activity /A mg$_{Pt}^{-1}$	specific activity /A mg$_{Pt}^{-1}$	Exchange current density (j$_0$)/ mA cm^{-2}	Tafel slope /mV dec^{-1}	Reference
Pt-2@ZIF-8	4	0.1 M HClO$_4$	1.4	4000	7.61 at − 50 mV	20.5 at − 50 mV	11.6	24	This work
20 wt.% Pt/C	24	0.1 M HClO$_4$	17.6		0.95 at − 50 mV	1.9 at -50 mV	2.7	24	This work
Pt@NHPCP	2	1 M HClO$_4$	57	5000	N/A	N/A	N/A	27	[141]
Pt/C	N/A	1 M HClO$_4$	69.6		N/A	N/A	N/A	32	
Pt5/HMCS	7.6	0.5 M H$_2$SO$_4$	20.7	N/A	12.8 at − 30 mV	30.9 at – 30 mV	N/A	28.3	[142]
Pt/C-20 wt.%	30	0.5 M H$_2$SO$_4$	24.1	N/A	1.12 at − 30 mV	4.16 at - 30 mV	N/A	28.4	
Pt/CNTs-ECR	140	0.5 M H$_2$SO$_4$	34	10000	N/A	N/A	N/A	26	[143]
20 wt.% Pt/C	N/A	0.5 M H$_2$SO$_4$	43		N/A	N/A	N/A	30	
Pt/f-MWCNTs	N/A	N/A	43.9	2000	18.16 at - 50 mV	N/A	0.834	30	[144]
20 wt.% Pt/C	N/A	N/A	45.2		0.245 at - 50 mV	N/A	0.582	31	
AC Pt-NG/C	5.66	N/A	35.28	4000	6.508 at − 50 mV	N/A	0.520	31	[145]
20 wt.% Pt/C	56.6	N/A	42.03		0.309 at − 50 mV	N/A	0.513	31	
Pt-AC/DG-300	2.06	1 M HClO$_4$	29	5000	15.55 at - 50 mV	N/A	1.48	38.4	[146]
20 wt.% Pt/C	N/A	1 M HClO$_4$	30		1.41 at - 50 mV	N/A	1.41	44.1	
Pt$_1$/hNCNC-2.92	2.87	0.5 M H$_2$SO$_4$	15		7.60 at − 20 mV	N/A	N/A	24	[147]
20 wt.% Pt/C	N/A	0.5 M H$_2$SO$_4$	~23		0.41 at − 20 mV	N/A	N/A	30	
1.08 wt.%	N/A	0.5 M H$_2$SO$_4$	8.3	10000	75 at	N/A	N/A	29.12	[148]

Pt/N-Mo2C					– 25 mV				
20 wt.% Pt/C	N/A	0.5 M H$_2$SO$_4$			7 at - 25 mV	N/A	N/A	30.52	
Pt/NMC-LT	10	0.5 M H$_2$SO$_4$	17	5000	N/A	N/A	N/A	26.2	[149]
20 wt.% Pt/C	10	0.5 M H$_2$SO$_4$	75.3		N/A	N/A	N/A	33.7	
Pt/defWO3@ CFC	6.75	0.5 M H$_2$SO$_4$	42		0.321 at – 50 mV	N/A	N/A	61	[150]
	51	0.5 M H$_2$SO$_4$	34		0.105 at – 50 mV	N/A	N/A	46	

28

2.2.3.2 Oxygen reduction reaction (ORR) analysis

To further investigate the ORR catalytic performance of Pt-2@ZIF-8, a rotating ring-disk electrode (RRDE) analysis of Pt-2@ZIF-8 was executed in O_2-saturated 0.1 M $HClO_4$. For comparison, the commercial 20 wt.% Pt/C was also measured as a control. **Figure 2-17a** showed that the onset potential of Pt-2@ZIF-8 was close to that of commercial 20 wt.% Pt/C catalyst, while the limit current density of the former was much higher than that of the latter one (**Figure 2-17a**, inset).

Figure 2-17b shows that the Tafel slope β for Pt-2@ZIF-8 was 146 mV/dec in acidic media, which is close to that of commercial 20 wt.% Pt/C catalyst with 145 mV/dec.[48, 151] Furthermore, the electron transfer kinetics was estimated from LSV curves at different rotating rates (**Figure 2-17c**, inset).[152] It is evident that the current density increased along with the increase of the rotation rate ranging from 225 to 1600 rpm. In addition, Koutecky-Levich (K-L) plots were applied to calculate the number of transferred electrons in the catalytic reactions (**Figure 2-17c**). The plots of the corresponding inverse current densities as obtained at five different electrode potentials E (0.50, 0.45, 0.40, 0.35 and 0.30 V versus RHE) against the inverse square roots of the rotation rates showed approximately a linear relation, revealing a similar electron transfer number (n) for the ORR at diverse potentials (**Figure 2-17c**).[153] The linearity and parallelism of the K-L plots elucidated first-order reaction kinetics with regard to the concentration of dissolved O_2 and a potential-independent electron transfer rate. The average value of n was calculated to be approximately 4.0, suggesting mainly a direct four-electron transfer pathway. Additionally, we accurately quantify the ORR electron transfer number by quantifying the amount of H_2O_2 generated at the disk electrode.[49] The results in **Figure 2-17d** show that the electron transfer number is ~ 4.0, and the H_2O_2 yield is only ~ 2.12% in a wide potential range, indicating mainly a high-efficient four-electron oxygen reduction process of Pt-2@ZIF-8, consistent with the above K-L analysis (**Figure 2-17c**). This illustrated that Pt-2@ZIF-8 had improved ORR activity and was able to reduce O_2 to H_2O directly.

Interestingly, compared with the huge response of commercial Pt/C for the electro-oxidation of methanol,[104] the Pt-2@ZIF-8 exhibited no redox response to methanol in O_2-saturated solution (**Figure 2-18**). This demonstrates that the micro-environment of PtNCs on Pt-2@ZIF-8 was largely different from that on commercial Pt/C. This probably was due to the nano-confinement effect of the ZIF-8 support, which inhibits the adsorption of relatively large methanol molecules rather than of small O_2 molecules on Pt. This result is in consistent with the observation of a small negative shift for onset potential of ORR after the addition of methanol (**Figure 2-18**).
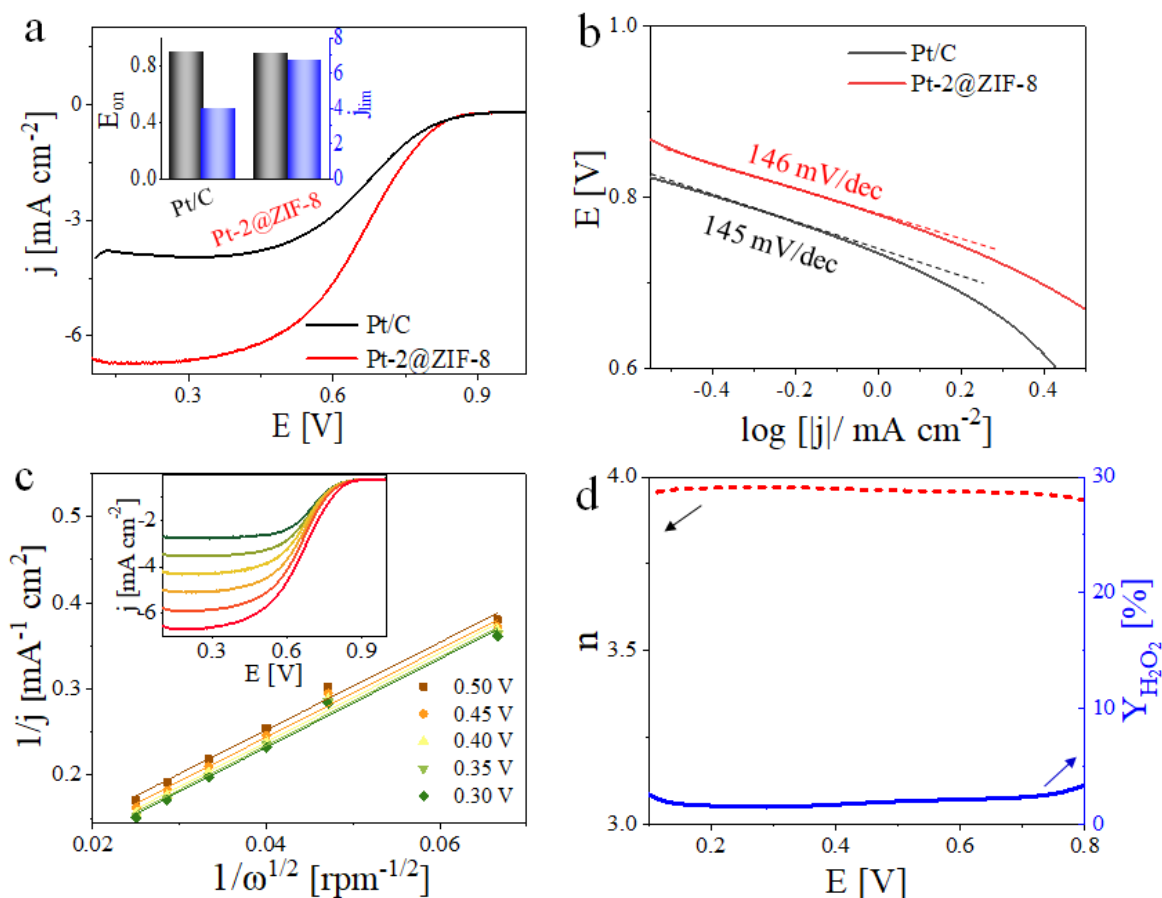
Figure 2-17. *ORR measurement of Pt-2@ZIF-8 and the commercial 20 wt.% Pt/C catalysts. (a) ORR polarization curves of Pt-2@ZIF-8 and the commercial 20 wt.% Pt/C catalysts in O_2-saturated 0.1 M $HClO_4$ at a scan rate of 5 mV/s under the rotation rate of 1600 rpm. The inset shows a corresponding comparison of the onset potential E_{on} and the limiting current density j_{lim}. (b) Tafel plots derived from LSVs are plotted for Pt-2@ZIF-8 and commercial Pt/C in acidic conditions and Tafel slope (β) was calculated (slopes are demonstrated by the dotted lines). (c) K-L plots derived from LSVs observed at different rotation speed (ω). The inset shows the corresponding LSVs of Pt-2@ZIF-8 in O_2-saturated 0.1 M $HClO_4$ at a scan rate of 5 mV s^{-1} at different RRDE rotation rates ω (from top to bottom: 225, 400, 625, 900, 1225, and 1600 rpm, respectively). (d) The electron transfer number n (left axle) and the H_2O_2 yield Y_{H2O2} (right axle) of the catalysts of Pt-2@ZIF-8 in O_2-saturated 0.1 M $HClO_4$. The ORR data of this figure were recorded by Mr. Mingbo Ruan.*

The durability assessment was performed by multiple CVs of the catalyst between 0.2 and 0.8 V at 200 mV s^{-1} in an O_2-saturated solution of 0.1 M $HClO_4$.[104] Based on the previously reported results, a ~ 40 mV negative shift of half-wave potential ($E_{1/2}$) is shown for the commercial Pt/C after 10,000 (10 k) continuous CV cycles, illustrating that deterioration of Pt occurred on the commercial Pt/C catalyst.[48, 153] However, Pt-2@ZIF-8 exhibited a much better durability as indicated by a small negative shift (~ 9 mV)

of $E_{1/2}$ after cycling of 10 k repeats of CVs (**Figure 2-19**). Similarly, this high-efficient four-electron ORR pathway and outstanding durability could be due to the smaller size and ligand-free property, stability of the PtNCs in acidic conditions (**Figure 2-16**) as well as the synergistic effect of Zn in PtNCs under the acidic conditions due to the degradation of ZIF-8 template (**Figure 2-15**).
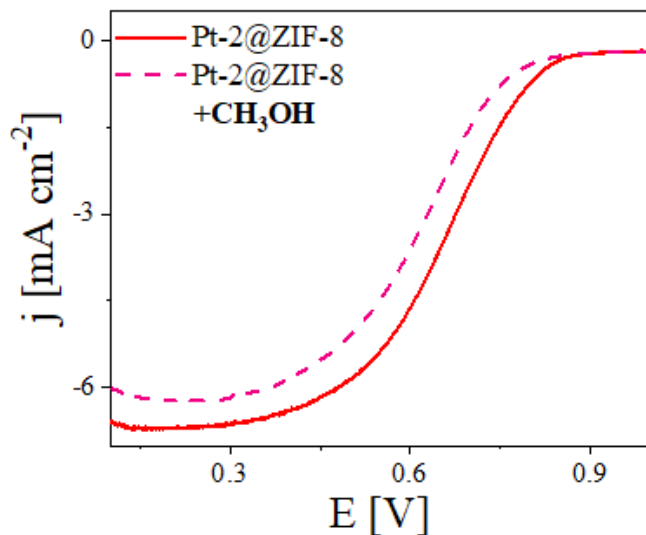
Figure 2-18. The response of Pt-2@ZIF-8 to methanol (0.5 M) in O₂-saturated 0.1 M HClO₄. The LSV data of this figure were recorded by Mr. Mingbo Ruan.
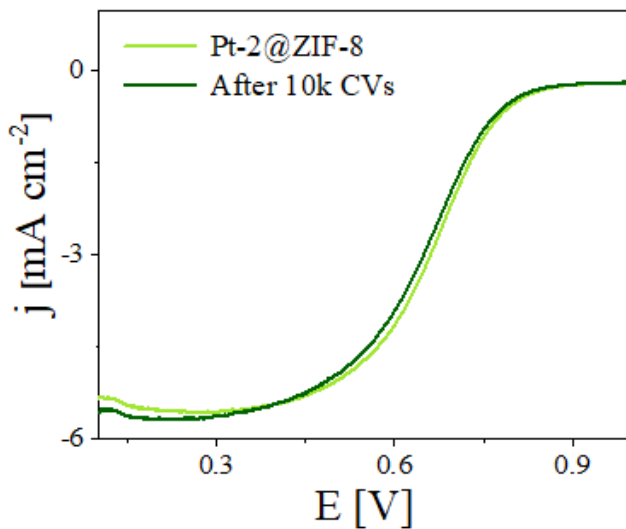
Figure 2-19. The long-term operation stability of PtNCs@ZIF-8 in O₂-saturated 0.1 M HClO₄. The data showed the 1ˢᵗ and the 10⁴ᵗʰ CVs. The LSV data of this figure were recorded by Mr. Mingbo Ruan.

2.2.4 Characterization of the releasing PtNCs from ZIF-8

The above discussion has shown that Pt-2@ZIF-8 catalyst exhibited high catalytic activity. Nonetheless, well-dispersed PtNCs are also promising in other applications like sensing or drugs delivery, which are still highly desired. As we mentioned above, the as-synthesized PtNCs in Pt-2@ZIF-8 is ligand-free as PtNCs were grown on the ZIF-8 template in the absence of any stabilizing ligands, which possess excellent merit of the tunability of their surface functionalization. This may potentially benefit other applications except for catalysis. Hence, in the following part, we aim to extract monodispersed PtNCs for the ZIF-8 template into both aqueous and non-aqueous conditions.

2.2.4.1 Under aqueous condition

Glutathione (GSH) ligand was utilized as a stabilizer to the surface of PtNCs in solution mainly owing to its biocompatibility and the strong affinity between the -SH group and Pt surfaces (as shown in **Figure 2-20a**, left). The experimental details for releasing the PtNCs from the ZIF-8 are described in **6.3.1.4**. In brief, a proper amount of GSH/NaOH solution was added into Pt-2@ZIF-8 to produce PtNC@GSH@ZIF-8 mixture. Next, the as-prepared PtNC@GSH@ZIF-8 precipitate was obtained by centrifuge, re-dissolved in the aqueous solution with different pH values (ca. 1, 3, 6.5, 8, 9, 10, 11, 12, 13, and 14, respectively). After centrifugation, the supernatant was collected for further study. Obviously, as shown in **Figure 2-20b** (left), the colored supernatant was obtained under alkaline conditions. It was found that the supernatant at pH 13 showed the most brownish color compared to those at other pH values, probably indicating that most of PtNC@GSH stayed in this part further confirmed by ICP-MS data. As shown in **Figure 2-21**, the bulk concentration of Pt in the supernatant varied along with the color change. And the highest bulk concentration of Pt in the supernatant was shown at pH 13 in comparison with those at other pH levels, which was calculated to be approximately 77 wt.% to that of parent Pt-2@ZIF-8. Moreover, the size distribution and morphology of the released PtNC@GSH was further characterized by TEM imaging. **Figure 2-20c** exhibited the TEM images of monodisperse PtNC@GSH, while the inset displayed the corresponding size distribution ($d_c = 1.92 \pm 0.40$ nm) in great agreement with the parent PtNCs in Pt-2@ZIF-8 (**Figure 2-4, c-e**). In addition, the corresponding HRTEM showing latticing space of PtNC@GSH is consistent with that of Pt-2@ZIF-8 (**Figure 2-4d**). To further comment the existence of GSH ligands on the surface of PtNC@GSH, the EDS spectra were conducted. The presence of the S element in **Figure 2-22** was found, indicating the successful preparation and releasing of PtNC@GSH in an aqueous solution. Meanwhile, to understand the role of a solvent on releasing the PtNC@GSH, the same amount of MeOH solution was used as solvent in the extraction process (I-III), however, only transparent supernatant was obtained in the photographs, indicating that MeOH cannot serve as an agent to release PtNC@GSH and

32

that PtNC@GSH@ZIF-8 is much stable in MeOH conditions (**Figure 2-23**).

To shed light into the releasing mechanism under aqueous conditions, a control experiment of releasing PtNCs into pH 13 aqueous solution in the absence of any ligands was also carried out. Interestingly, the results shown in **Figure 2-23** demonstrated that the brownish supernatant was obtained without GSH ligands when following the standard release protocol. This may suggest the successful extraction of PtNCs into the supernatant. Further TEM and HRTEM images of these released PtNCs are shown in **Figure 2-24a**. The size distribution of the core diameter of these PtNCs ($d_c = 1.87 \pm 0.37$ nm) was unchanged compared to parent PtNCs in Pt-2@ZIF-8 (**Figure 2-4e**). EDS spectra result further confirmed the existence of Pt element in the absence of S element, as shown in **Figure 2-24b**. In the absence of GSH ligands, the PtNCs could be extracted under basic condition (here at pH 13), but in such cases, the NCs were found to be less stable than PtNC@GSH ones. We can't exclude that in the absence of GSH, there might be some ligated 2-MeIM that protects the NCs in the solution. It should be noted that ZIF-8 exhibited outstanding chemical stability against the alkaline agent, as mentioned in the previous work.[154] In our work, TEM and PXRD data further evidenced that no apparent morphology and no PXRD peak position change of ZIF-8 upon treatment with pH 13 aqueous solution in **Figure 2-25** and **Figure 2-26**, respectively. By contrast, the TEM images of the precipitate PtNC@GSH@ZIF-8 after being treated with pH 6.5 solution were taken, showing aggregated PtNCs with some structure-broken ZIF-8 (**Figure 2-27**). Above all, it can be concluded that the optimal condition to release PtNCs without aggregating is under an alkaline solution (in this case is at pH = 13). As for the extraction mechanism of PtNCs from ZIF-8 in alkaline solution, which could be speculated to be the disruption of hydrophobic interaction of ZIF-8 triggered by sonication.[155-157]
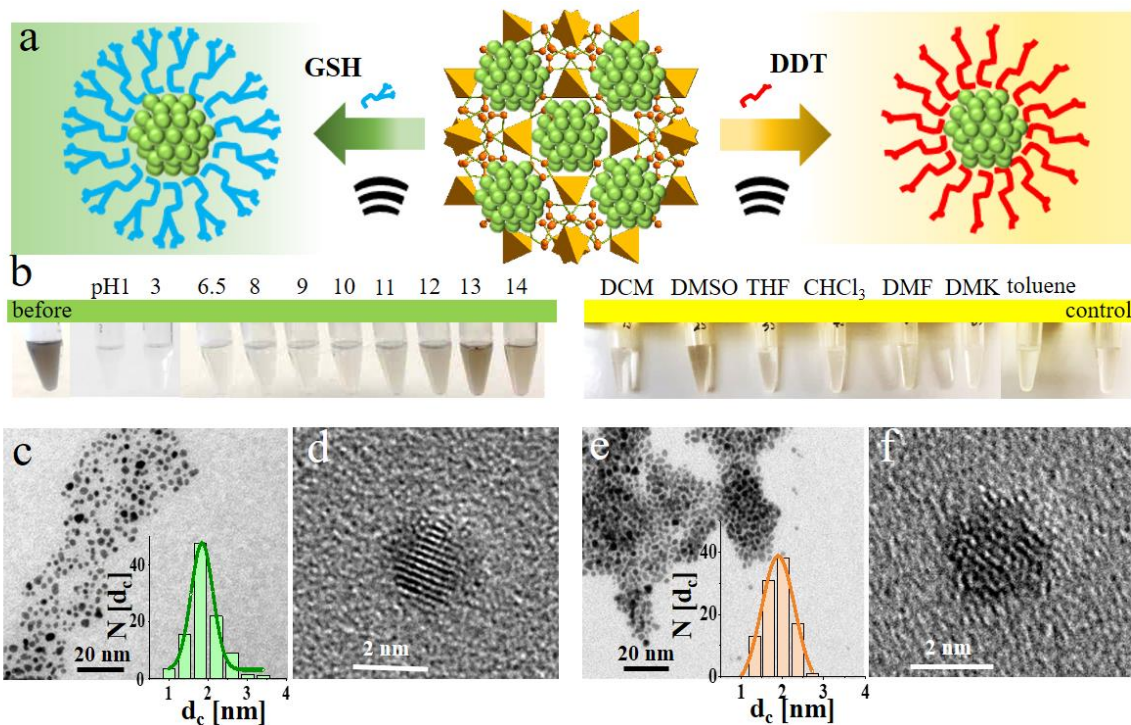
Figure 2-20. *Release of PtNCs into both aqueous and non-aqueous solution. (a) Schematic illustration of releasing PtNCs into the aqueous (left) and non-aqueous (right) solvent with proper ligands of GSH and dodecanethiol (DDT), respectively. (b) Representative photographs of the supernatant of PtNCs released from Pt-2@ZIF-8 solution with ligands in different solvents. (c-d) TEM and HRTEM images of PtNC@GSH. The inset shows the corresponding size distribution histogram of the core diameters (d_c = 1.92 ± 0.40 nm). (e-f) TEM and HRTEM images of PtNC@DDT. The inset shows the corresponding size distribution histogram (d_c = 1.90 ± 0.33 nm). The TEM and HRTEM images of this figure were recorded by Mr. Andreas Kornowski.*
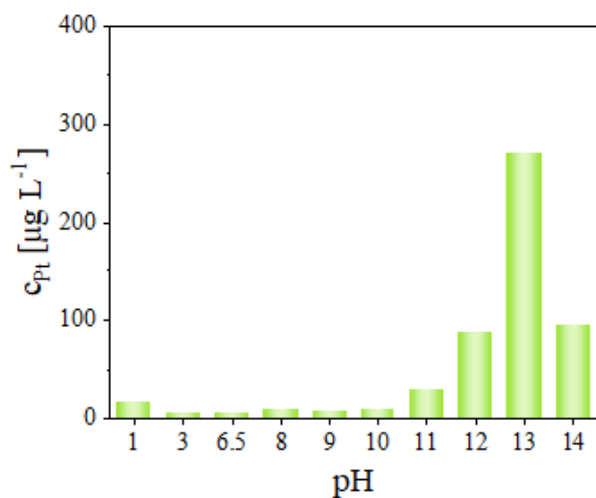
Figure 2-21. *ICP-MS data of the bulk concentration of Pt in the supernatant at different pH levels. This ICP-MS data were recorded by Dr. Indranath Chakraborty.*

34
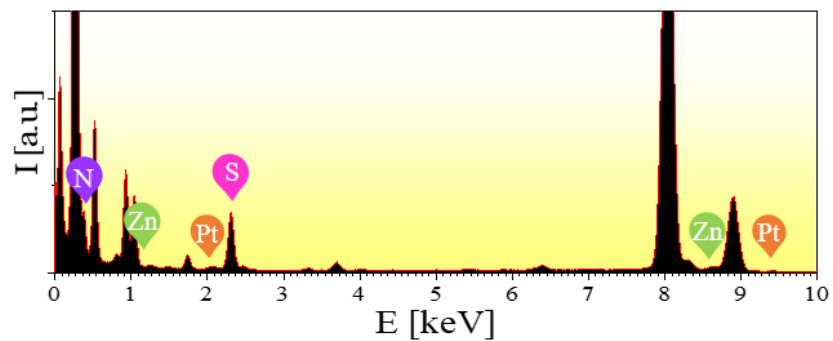
Figure 2-22. EDS spectra of the released PtNC@GSH. The EDS data of this figure were recorded by Mr. Andreas Kornowski.
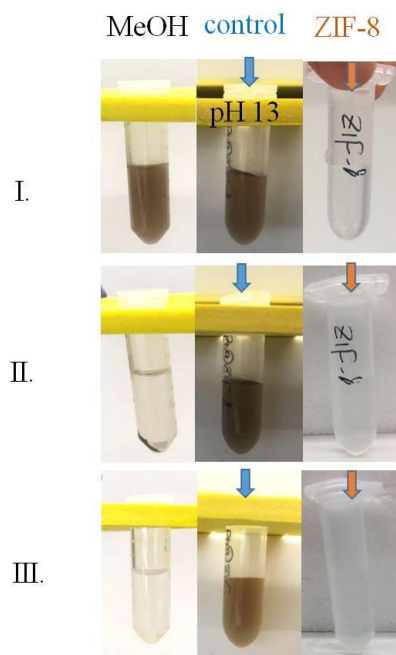
Figure 2-23. Photographs of the release experiment of PtNC@GSH@ZIF-8 in MeOH. (I) Pt-2@ZIF-8/ZIF-8 in pH 13 solution after sonication at 480 W for 5 min, (II) after centrifugation at 5000 rpm for 10 min, and (III) supernatant collected right after (II).
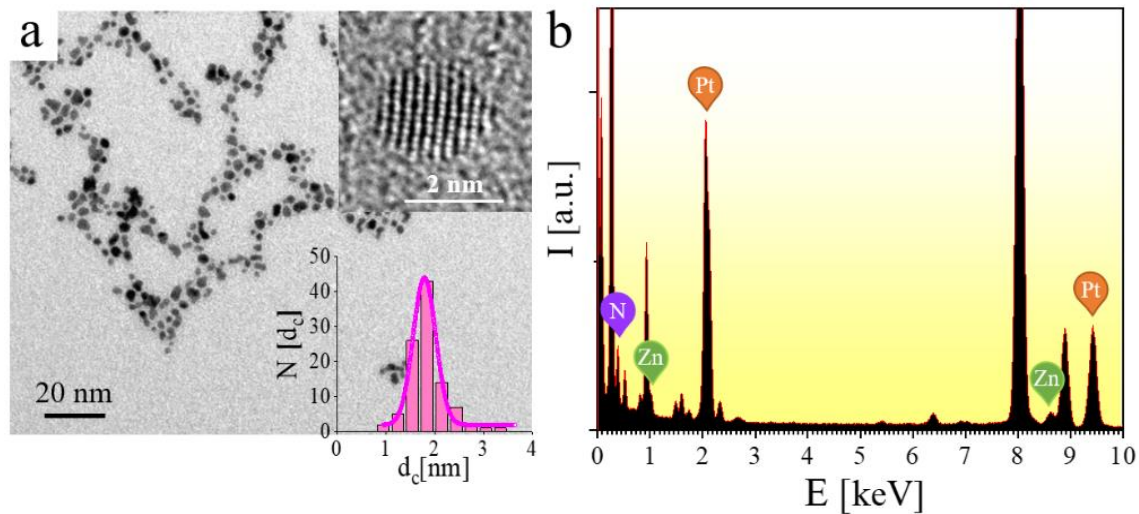
Figure 2-24. *TEM and EDS characterization of extracted PtNCs in absence of GSH ligands. (a) TEM image. The inset shows a representative HRTEM image (top) and the corresponding size distribution with a mean core diameter of $d_c = 1.87 \pm 0.37$ nm (bottom). (b) EDS spectra of PtNCs released in the absence of GSH ligands at pH 13. The TEM, HRTEM and EDS data of this figure were recorded by Mr. Andreas Kornowski.*
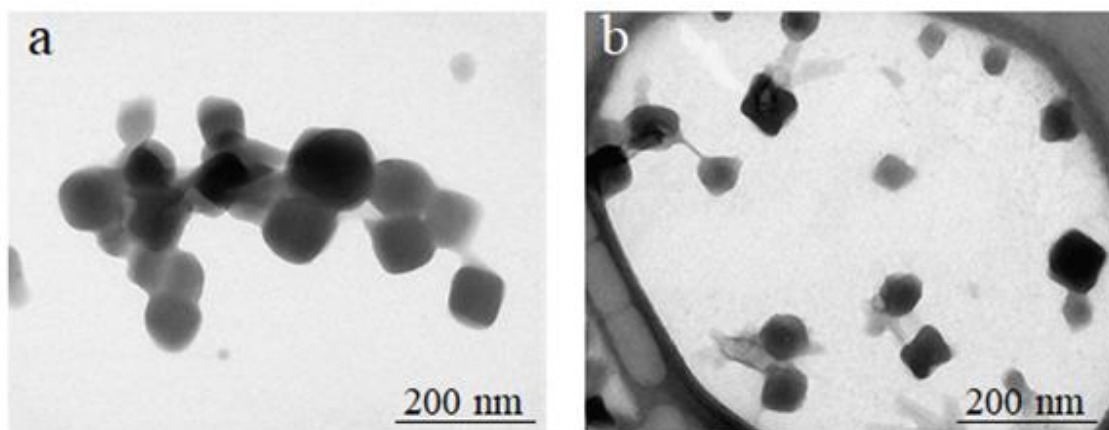
Figure 2-25. *TEM images of ZIF-8 after treated in aqueous solution at pH 13. (a) with and (b) without sonication. The TEM images of this figure were recorded by Mr.*
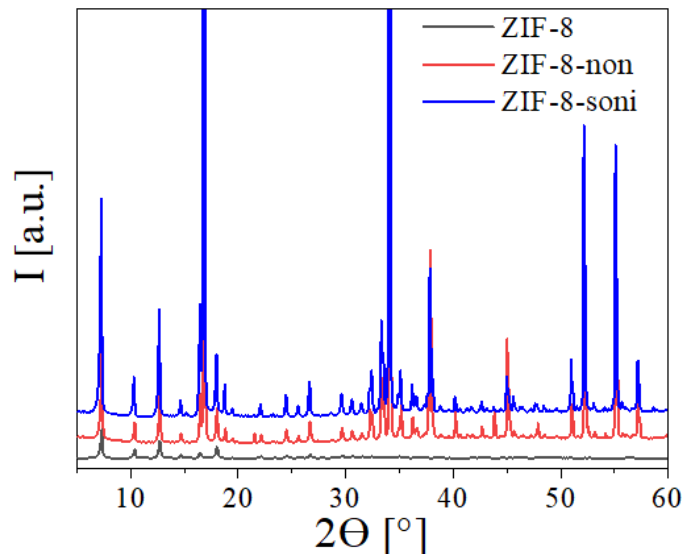
Figure 2-26. *Representative PXRD pattern of ZIF-8 in pH 13 solution. Having been treated with pH 13 solution with (marked as 'soni') and without (marked as 'non') sonication, as compared to parent ZIF-8. The PXRD patterns of this figure were recorded by Ms. Almut Barck.*
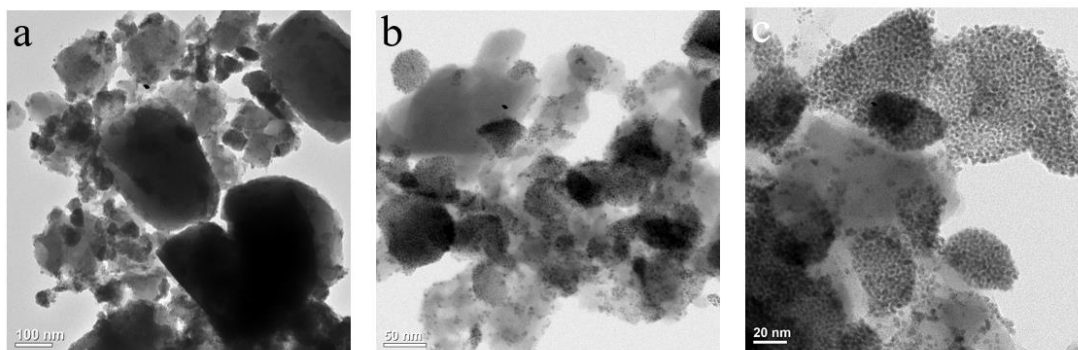
Figure 2-27. *TEM images of the precipitate of PtNC@GSH@ZIF-8 after treated at pH 6.5. The TEM images of this data were recorded by Mr.Stefan Werner.*

2.2.4.2 Under non-aqueous condition

To extend more possibility for the extraction of PtNCs under non-aqueous solvents in addition to the aqueous condition, DDT was used as ligands for non-aqueous extraction, and dichloromethane (DCM), dimethyl sulfoxide (DMSO), tetrahydrofuran (THF), chloroform (CHCl$_3$), DMF, acetone (dimethyl ketone, DMK) as well as toluene are chosen as solvents. Obviously, as shown in **Figure 2-20b** (right), the relative brownish supernatant is observed in DMSO solvent, which might indicate that the PtNCs@DDT is likely to release in DMSO in comparison with other supernatants, which present almost colorless solutions.

Furthermore, the morphology and lattice structure of the released PtNC@DDT in DMSO was characterized by TEM and HRTEM imaging (**Figure 2-20, e-f**), respectively, which was highly consistent with those of the parent PtNCs (**Figure 2-4**, **c-e**). However, the extraction yield was only ~ 20 wt.%, which is lower than that of extraction in the aqueous solution (at pH 13). Further, PXRD patterns show that the peak positions are unchanged after ZIF-8 treated with DMSO, demonstrating that no apparent structural variation of ZIF- 8 happened during the extraction process with DMSO (**Figure 2-28**). The extraction ability of DMSO for PtNCs with the help of DTT may be result from the high polarity index of DMSO as the DTT is also a high polar molecule. As can be seen in **Table 2-3**, DMSO has the highest polarity index.
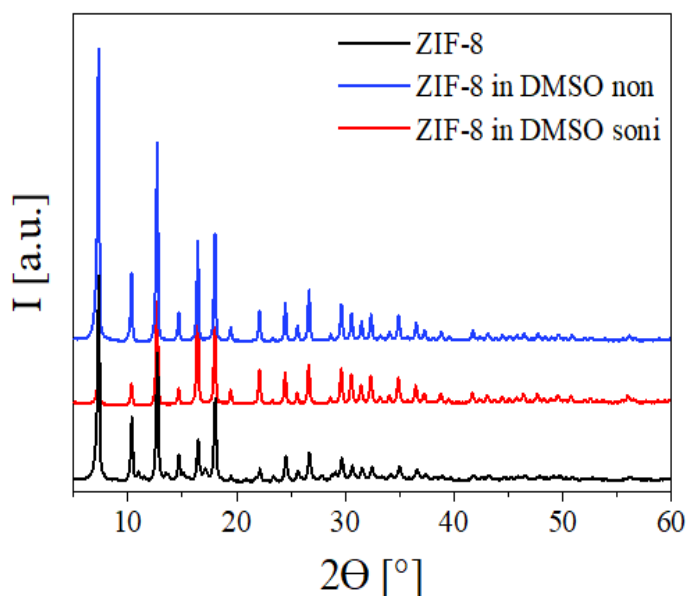
Figure 2-28. *Representative PXRD pattern of ZIF-8 after treated with DMSO. The PXRD patterns of this figure were recorded by Ms. Almut Barck.*

Table 2-3. *Polarity index of different solvent used to release PtNC@DDT.*

Solvent	*DCM*	*DMSO*	*THF*	*CHCl₃*	*DMF*	*DMK*	*toluene*
Polarity index	*3.1*	*7.2*	*4.0*	*4.1*	*6.4*	*5.1*	*2.4*

3 Different methodologies for the synthesis of alloy PtAg for multi-enzyme mimicking studies

3.1 Introduction and aim of the work

Natural enzymes, mainly consisting of proteins, exhibit highly specific catalytic efficiency, which plays a vital role in biochemistry, the food industry, and ecosystem protection.[71] However, high costs in preparation and purification, relatively low stability (easily denatured and digested), and environmental condition-dependent catalytic sensitivity have impeded the further applications of these natural enzymes from biosensing to biomedicine especially in harsh conditions. This stimulates the quick emergence, and fast growth of numerous enzyme mimics with various materials, which are denoted "artificial enzymes". The term "nanozyme", defined as "nanomaterials with enzyme-like properties", was first mentioned in 2013.[158] It was illustrated as one of the promising nanomaterials with advantages like robust stability, lower costs, flexibility in composition as well as structure design, durability, and versatile catalytic activities over natural enzymes.[71, 159] In recent years, intensive work dedicated to nanozymes have been emerged in various applications ranging from biosensors to therapeutics, attributing to rapidly well-developed regimes of nanotechnology, catalysis and computational design.[160, 161] A variety of nanomaterials, such as carbon nanomaterials, metal-based NPs or metal hybrid nanostructures, were reported to exhibit inherent peroxidase (POD), superoxide dismutase (SOD), as well as catalase (CAT) mimicking properties.[160, 162-165] For instance, some studies demonstrated that PtNPs – well-known excellent catalysts for many chemical reactions – exhibit efficient enzyme mimetic activities such as ferroxidase- and POD-like mimics.[166-170] Despite considerable progress have been made in the regime of nanozymes, the catalytic efficiency and a mimic multi-enzyme system for a nanozyme is still highly challenging.

Ultrasmall metal NCs as a new class of emerging nanomaterials have attracted tremendous attention due to their specific properties. In 2014, Wang *et al.* as a pioneer in this field proposed nanozymes based on AuNCs, which show high POD-like activity. This work paved the way for using noble metal NCs as enzyme mimic with excellent analytical potential in the following years.[21] To enhance the catalytic activity and selectivity, various methods have been proposed to prepare the NCs-based nanozymes. One of the strategies is doping or alloying synergetic materials for the effective catalytic activity.[171] Despite the success of previous reports in terms of nanozymes, developing catalytic efficient alloy metal NCs as multi-enzyme mimics is still challenging. Pt-based nanomaterials have obtained increasing attention as

fantastic nanozymes, attributed to the enhanced catalytic properties.[172-176]

In this work, I demonstrate a nanozyme, prepared from the ZIF-8 templated synthesis method, presenting high catalytic activity in multi-enzyme mimics. The alloy PtAg nanozymes with different metal core sizes were obtained via two different synthesis routes and further investigated their multi-enzyme mimicking properties. Additionally, the intrinsic enzyme mimicking mechanism was studied.

3.2 Results and discussion

3.2.1 Characterization of PtAgNCs@ZIF-8

Two different protocols, namely co-reduction and Pt-guided methods were applied to obtain nanocatalyst alloy PtAg in a ZIF-8 template based on a modified method (**Figure 3-1**).[36] In the co-reduction process, a total amount of 1.332 mL of 25 mM K_2PtCl_4 and 25 mM $AgNO_3$ aqueous solution was added to the as-obtained ZIF-8 mixture and stirred for 0.5 h, followed with the addition of 0.5 mL 500 mM $NaBH_4$. For the Pt-guided method, an aqueous K_2PtCl_4 solution was first injected into the ZIF-8 solution to produce monometallic Pt@ZIF-8, followed by the addition of the aqueous K_2PtCl_4 and $AgNO_3$ solution for the alloy formation. The K_2PtCl_4 at the second step was added to guide the formation of the respective PtAg alloy. The structure of the obtained PtAg nanocatalysts was characterized and confirmed by TEM, HAADF-STEM, HRTEM, and EDS mappings. TEM images (**Figure 3-2**) confirm that the ZIF-8 nanocrystal forms as a rhombic dodecahedral shape in all cases which is in good agreement with the naked ZIF-8 reported.[96] Interestingly, smaller homogenous PtAgNCs were obtained via the Pt-guided method in ZIF-8 template (**Figure 3-2**, **a-b**). The average size of PtAgNCs was $d_c = 1.78 \pm 0.12$ nm (**Figure 3-2b**, inset). A HRTEM image shows the lattice space of 0.230 nm which was ascribed to the fringes of the (111) plane in an individual PtAgNC (**Figure 3-2b**, inset), and is similar to that in the literature.[177-179] TEM images of obtained PtAgNCs exhibited a uniform shape and homogenous distribution. The average core diameter of PtAgNCs has a slight increase in comparison to that of the pure PtNCs@ZIF-8 with $d_c = 1.73 \pm 0.10$ nm (**Figure 3-3**). This may be the contribution of the PtNCs seeds to the formation of PtAgNCs alloy during the reaction. In contrast, bigger PtAgNPs were produced by the co-reduction method with an average core diameter of $d_c = 9.10 \pm 2.31$ nm (**Figure 3-2**, **e-f**). Additional HRTEM images confirm the crystallinity of PtAgNPs. The lattice fringes spacing of 0.223 and 0.240 nm were ascribed to the (111) crystal planes of *fcc* PtNPs and AgNPs, respectively (**Figure 3-2f**, inset).
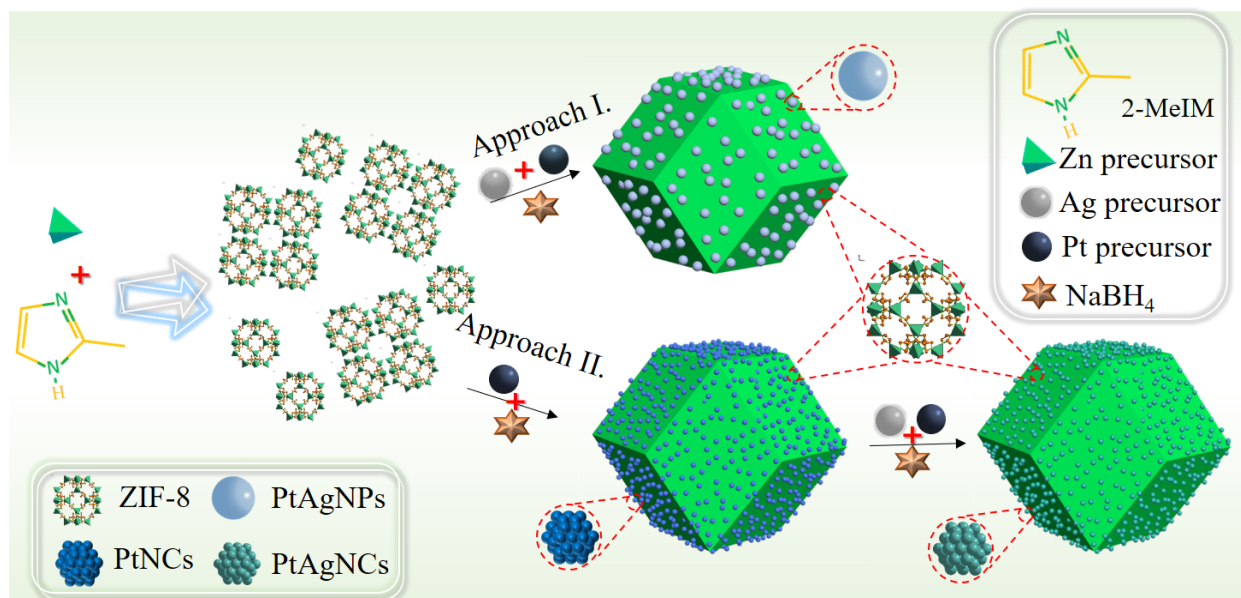
Figure 3-1. *Schematic illustration of the synthesis approaches of PtAg alloy. I) co-reduction and II) Pt-guided method.*

To specifically evaluate the composition of PtAg nanocatalysts, HAADF-STEM imaging and EDS elements mapping analyses were performed. The structure of the PtAg alloy nanocatalyst is particularly distinct in HAADF-STEM images (**Figure 3-2**, **c-d**, **g-h**) becauase PtAg alloy has a brighter contrast due to the larger atomic mass of Pt and Ag element. **Figure 3-2**, **c-d** implies the uniform formation of smaller PtAgNCs in ZIF-8, while **Figure 3-2**, **g-h** confirmed the formation of the bigger size PtAgNPs. As presented in **Figure 3-2i**, the Pt and Ag elements are evenly distributed in the crystal of ZIF-8. Evidence is given by the corresponding TEM element mapping of the Zn and N elements, indicating the successful formation of PtAg alloy. **Figure 3-2j** showed that the distribution of Ag ions is broader than Pt element, implying a composition with a large molar ratio of Ag to Pt. Corresponding EDS spectra of PtAgNCs-1 and PtAgNPs-1were shown in **Figure 3-4**, revealing the close relation of Pt and Ag together with Zn and N. To conclude, all the samples prepared by the above-mentioned methods consisted of both Pt and Ag atoms.
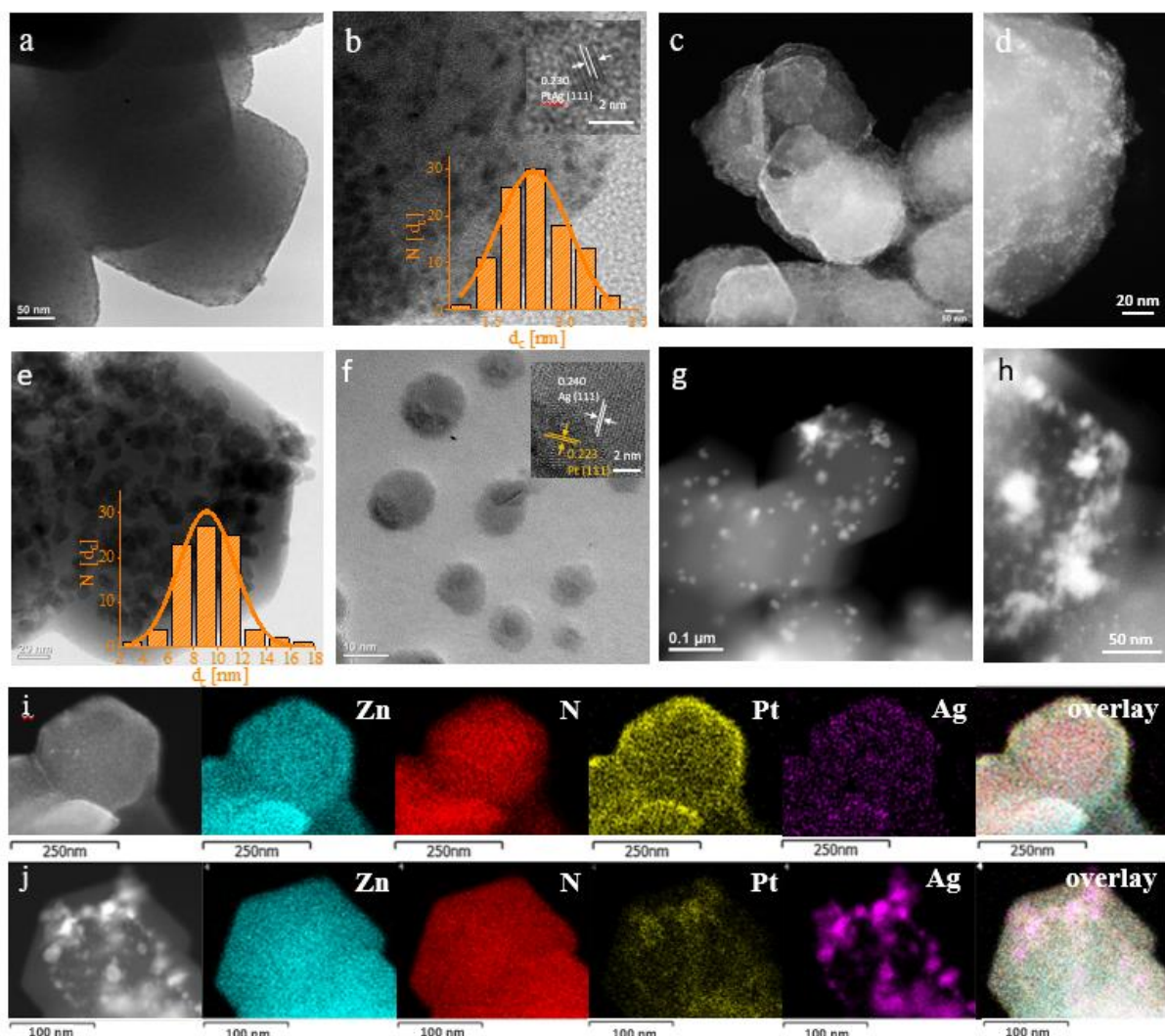
Figure 3-2. *TEM characterization of PtAgNCs and PtAgNPs.(a-b) TEM images and (c-d) HAADF-STEM images of PtAgNCs samples. The insets in b represent the corresponding size distribution histogram of the core diameter ($d_c = 1.78 \pm 0.12$ nm) and the HRTEM of a PtAgNC. (e-f) TEM images and (g-h) HAADF-STEM images of PtAgNPs samples. The inset in e, f is the corresponding size distribution histogram of the core diameter ($d_c = 9.10 \pm 2.31$ nm) and HRTEM image of a PtAg in PtAgNPs samples. (i-j) Corresponding element mapping images of PtAgNCs (i) and PtAgNPs (j).*
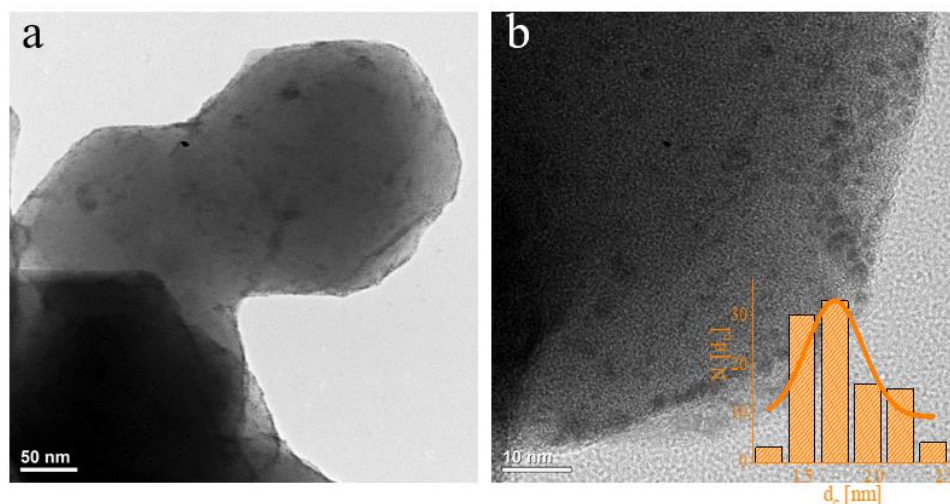
Figure 3-3. *TEM images of monometallic Pt@ZIF-8 samples. The inset in b is the corresponding size distribution histogram of the core diameter (d_c = 1.73 ± 0.10 nm). The TEM data of this figure were recorded by Mr. Stefan Werner.*
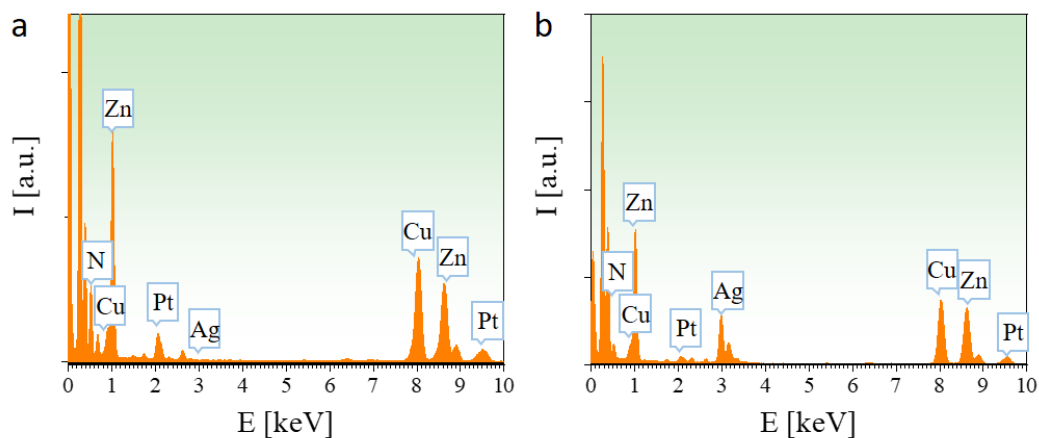
Figure 3-4. *EDS spectra of PtAgNCs (a) and PtAgNPs (b). The EDS spectra of this figure were recorded by Mr. Stefan Werner.*

The PXRD patterns (**Figure 3-5**) characterization indicated that the as-synthesized ZIF-8, PtAgNCs and PtAgNPs samples consist of distinct crystal structures, as the diffraction peaks matched well with the simulated PXRD patterns. It can be found that after the formation of PtAg alloy NCs and NPs, no apparent variation was observed in the PXRD patterns of PtAgNPs samples compared to that of the pure ZIF-8, which shows the negligible influence of PtAg formed on the ZIF-8 phase. Additional features were observed in the PXRD patterns of PtAgNCs, which are not visible, which was predicted due to the

incorporation of NCs and ZIF-8 contributing to the change of total structures of ZIF-8. The structural information of PtAgNCs-1 and PtAgNPs-1 was further analyzed with FTIR spectroscopy. In **Figure 3-6**, similar peaks of these PtAg alloy products were observed with respect to that of the ZIF-8 template. The peaks at 3135 and 2928 cm^{-1} resulted from the aromatic and the aliphatic C-H stretching of the imidazole ring, respectively.[102, 180] The bands at 1584, 1310 along with 1146 cm^{-1} are attributed to C=N and C-N stretching mode, respectively, whereas the peaks at 1350-1500 and 754 cm^{-1} are assigned to the entire ring stretching and Zn-O bending, respectively. It should be noted that the vibration at 1025 cm^{-1} was observed in PtAgNCs, suggesting the interaction of PtAgNCs with Pr-imidazole groups of ZIF-8, which is consistent with the PXRD result of PtAgNCs. The thermal stability of ZIF-8, PtAgNCs and PtAgNPs were analyzed by TGA under N_2 flow (**Figure 3-7**). A significant weight loss in ZIF-8 occurs approximately at ~ 580 °C similar to the previous reports, related to the framework collapse.[181-183] It is observed that a large amount of AgNPs in ZIF-8 structures influences the thermal stability of ZIF-8 compared to those of the ZIF-8 and PtAgNCs.[184]
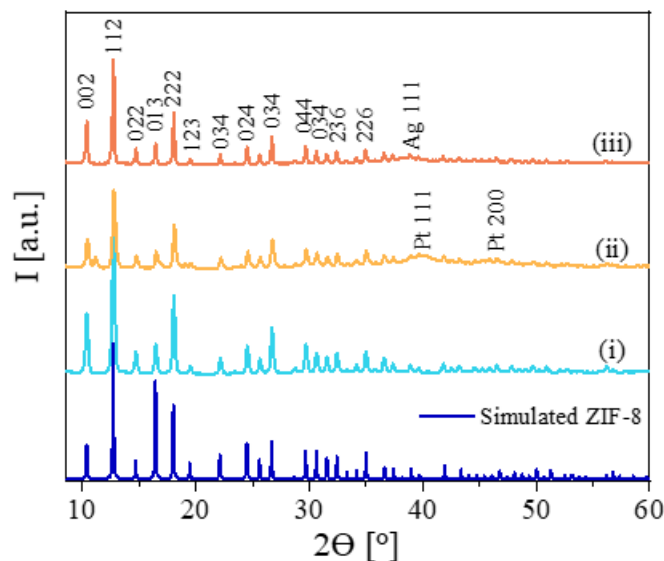
Figure 3-5. *PXRD patterns of ZIF-8 (i), PtAgNCs (ii) and PtAgNPs (iii). The PXRD patterns of this data were recorded by Mr. Stefan Werner.*

44
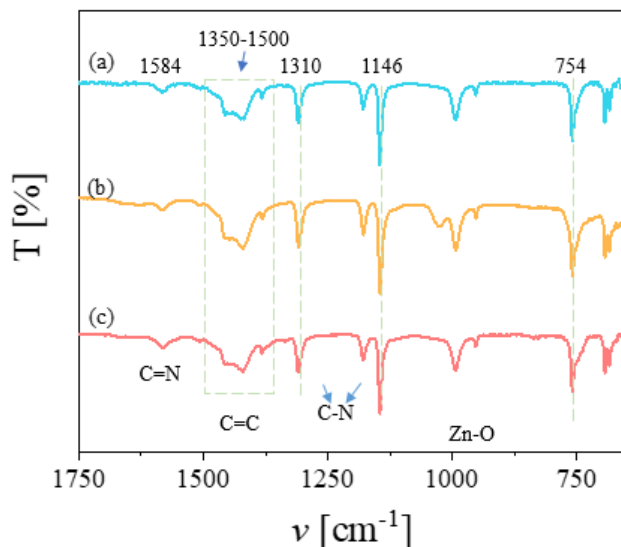
Figure 3-6. *FTIR spectra of ZIF-8 (a), PtAgNCs (b) and PtAgNPs (c), respectively.*
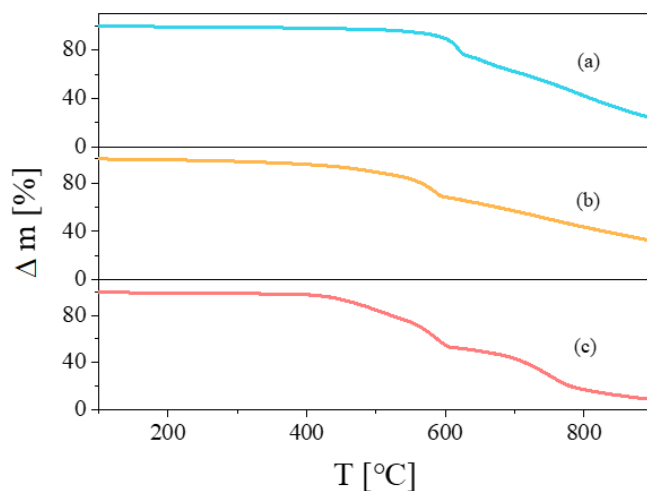
Figure 3-7. *TGA spectra of ZIF-8 (a), PtAgNCs (b) and PtAgNPs (c), respectively.*

The N_2 absorption-desorption isothermal of the as-obtained ZIF-8, PtAgNCs-1 and PtAgNPs-1 samples displayed type I isotherms, indicating typical microporous materials (**Figure 3-8a**). In comparison with the pristine ZIF-8, a slight decrease in both surface areas and pore volumes was shown in PtAgNCs-1 and PtAgNPs-1 samples. The Brunauer–Emmett–Teller surface areas (S_{BET}) of PtAgNCs-1 and PtAgNPs-1 was calculated as 1471 and 1412 $m^2\,g^{-1}$, the pore volumes as 0.5876 and 0.5124 $cm^3\,g^{-1}$, and compared to ZIF- 8 which has 1733 $m^2\,g^{-1}$ and 0.6525 $cm^3\,g^{-1}$, respectively (**Figure 3-8**, **Table 3-1**). It matches the expectations because the bimetallic PtAg in the ZIF-8 should be nonporous. No distinct difference of the pore size

45

distribution was observed for the PtAgNCs-1 and PtAgNPs-1 samples after the formation of thePtAg alloy via both approaches. In theory, the average core diameter of both PtAgNCs and PtAgNPs are too large to occupy the 1.16 nm cavities of ZIF-8 (**Figure 3-8c**).[185] This suggests that the PtAg alloys are not formed inside ZIF-8 but in the outerlayer of ZIF-8.[36, 37]
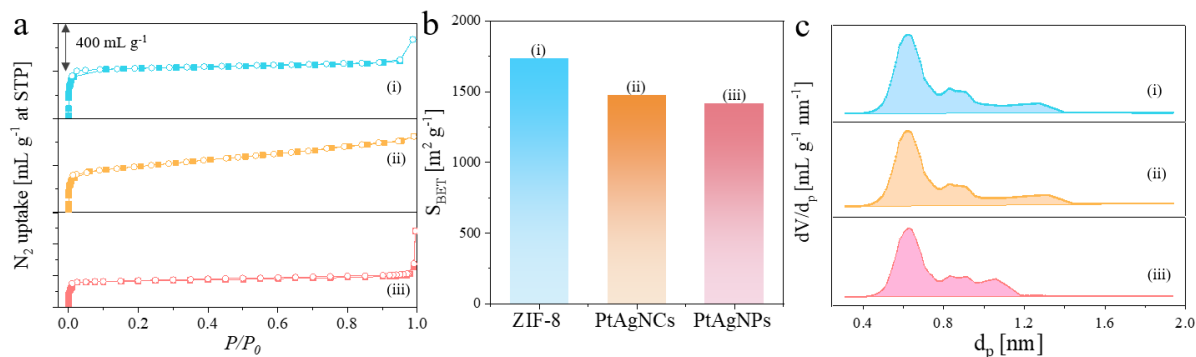
Figure 3-8. BET measurement of ZIF-8, PtAgNCs and PtAgNPs samples. (a) N_2 adsorption-desorption isotherms of ZIF-8 (i), PtAgNCs (ii) and PtAgNPs (iii) samples at 77 K up to 1 bar. Solid symbols represent the adsorption isotherms, whereas the empty symbols represent desorption isotherms. (b) comparison bar graph of the S_{BET} values. (c) Corresponding pore size distributions of ZIF-8 (i), PtAgNCs (ii) and PtAgNPs (iii), respectively. The BET data of this figure were recorded in CIAC, CAS.

Table 3-1. Porous structure analysis of ZIF-8, PtAgNCs and PtAgNPs.

Samples	S_{BET} ^{a} [m² g⁻¹]	V_{micro} ^{b}[cm³ g⁻¹]	d_p ^{c} [Å]
ZIF-8	1733	0.6525	0.6275
PtAgNCs	1471	0.5876	0.6225
PtAgNPs	1412	0.5124	0.6275

^{a} S_{BET} is the BET specific surface area, ^{b} V_{micro} is the micropore volume calculated by using the adsorption branch at the N_2 isotherm at $P/P_0 = 0.99$. ^{c} d_p is the pore diameter determined from the local maximum of the Horvath-Kawazoe (HK) pore size distribution obtained in the adsorption branch of the N_2 isotherm.

X-ray photoelectron spectroscopy (XPS) was applied for analyzing the surface compositions and valence states of both PtAg alloy NCs (ii) and NPs (iii) in comparison with pristine ZIF-8 (i). The survey spectra are presented in **Figure 3-9a**. The Zn 2p signal of (ii) and (iii) was deconvoluted into two components, the lower energy band (Zn 2p$_{3/2}$) at 1021.8 and 1023.5 eV for (ii), and 1021.5 and 1022.7 eV for (iii). And a high energy band (Zn 2p$_{1/2}$) was shown at 1044.5 and 1046.2 eV for (ii), and 1044.6 and 1045.9 eV for (iii),

46

respectively (**Figure 3-9b**). This indicated that Zn is present in two different oxidation states, Zn (0) and Zn (II). In comparison to those in pure ZIF-8, a positive shift to higher binding energy was observed after PtAg alloy formation and is similar to that in the literature.[96] The XPS spectrum of N 1s (ii) and (iii) showed a positive shift compared to that in ZIF-8 (i), as shown in **Figure 3-9d**. This implied the existence of an interaction between Pt, Ag with N and Zn after the introduction of PtAg alloy in ZIF-8. Notably, the Pt 4f spectra of (ii) and (iii) with strong doublets show characteristic peaks of Pt $4f_{7/2}$ and Pt $4f_{5/2}$ at 70.8 and 74.05 eV for (ii), along with 70.7 and 74.05 eV for (iii). A negative shift was observed in both samples compared to Pt4f spectra in PtNCs@ZIF-8 (**Figure 3-9c**). Together with the binding energy of Ag 3d spectrum peaks displayed in **Figure 3-9e**, in which positive shift in both (ii) and (iii) samples compared to standard Ag were shown, confirmed the successful formation of the PtAg alloy in ZIF-8 and the electron transfer from Ag to Pt due to the higher metallic electronegativity of Pt compared to that of Ag.[174, 186]
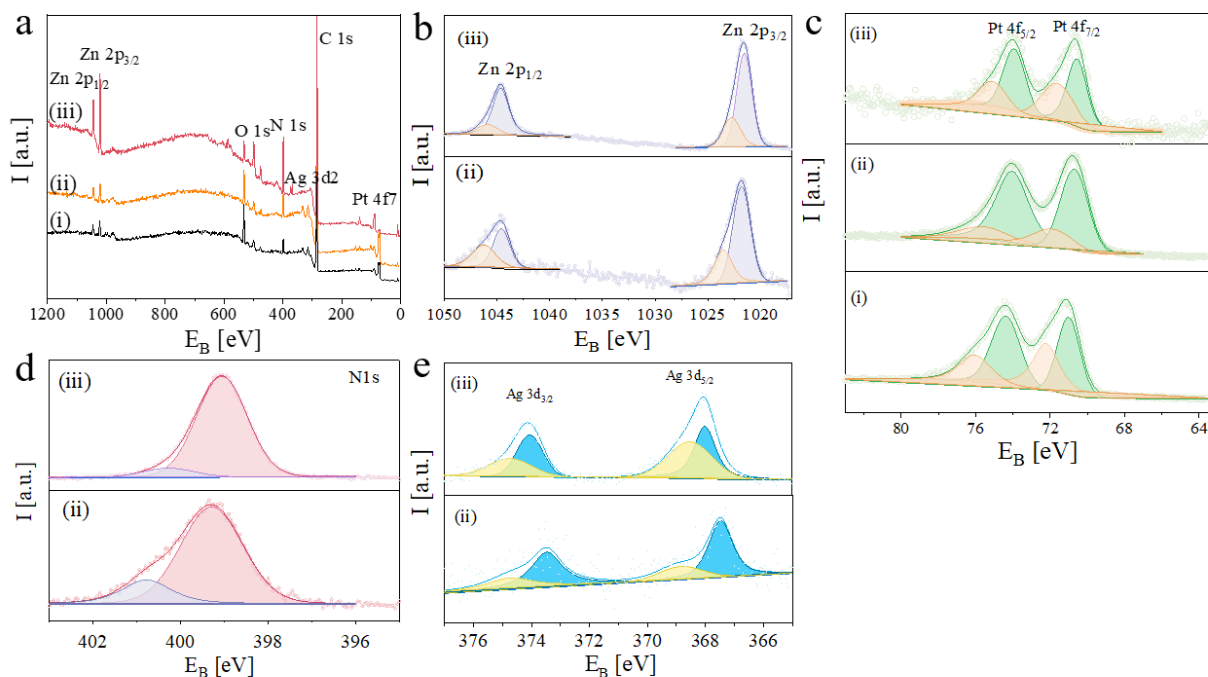
Figure 3-9. *XPS analysis of (i) Pt@ZIF-8, (ii) PtAgNCs, and (iii) PtAgNPs. (a) XPS spectra survey. (b-e) High-resolution XPS spectra of (b) Zn 2p, (c) Pt 4f, (d) N 1s, and (e) Ag 3d. The XPS spectra data of this figure were recorded in CIAC, CAS.*

3.2.2 Characterization of multi-enzyme mimics of PtAgNCs@ZIF-8

3.2.2.1 Peroxidase (POD)-like activity of PtAgNCs@ZIF-8

Different enzyme mimics activities were investigated after the successful preparation of PtAg alloy, as illustrated in **Figure 3-10**. To evaluate the POD-like catalytic activities of PtAgNCs and PtAgNPs, one of the typical peroxidase substrates of OPD was selected as the chromogenic substrate. As shown in **Figure 3-11h**, PtAgNCs could induce the oxidation of OPD to the yellow product DAP in the presence of H_2O_2, confirming the catalysts with POD-like properties. The oxidation of OPD was evaluated at different pH values with PtAgNCs nanozymes in sodium acetate buffer. UV-vis absorption spectra were used to study OPD-like activities with the characteristic maximum absorption at 450 nm, which originates from the production of DAP (**Figure 3-11**). Similar to HRP, the catalytic activity of PtAgNCs was pH-dependent, and the optimal pH was observed at pH 4 (as shown in **Figure 3-11h**).
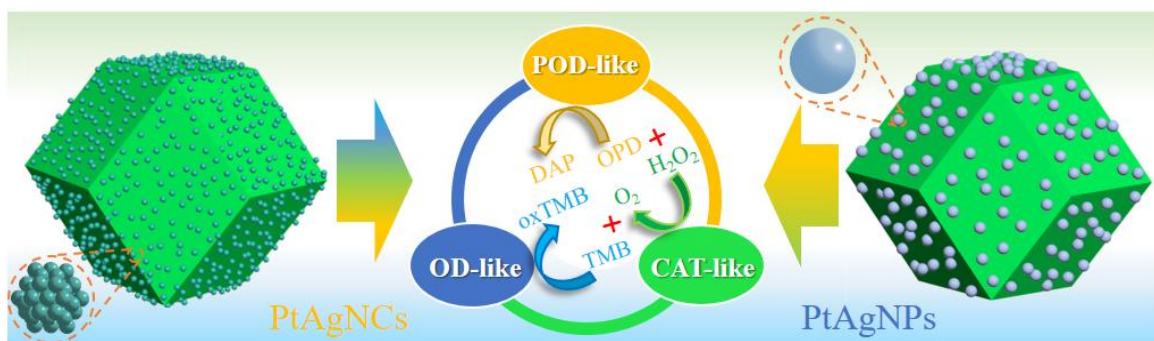
Figure 3-10. *Schematic illustration of the enzyme mimicking process. POD-like, CAT-like and OD-like activities by PtAgNCs (left) and PtAgNPs (right).*
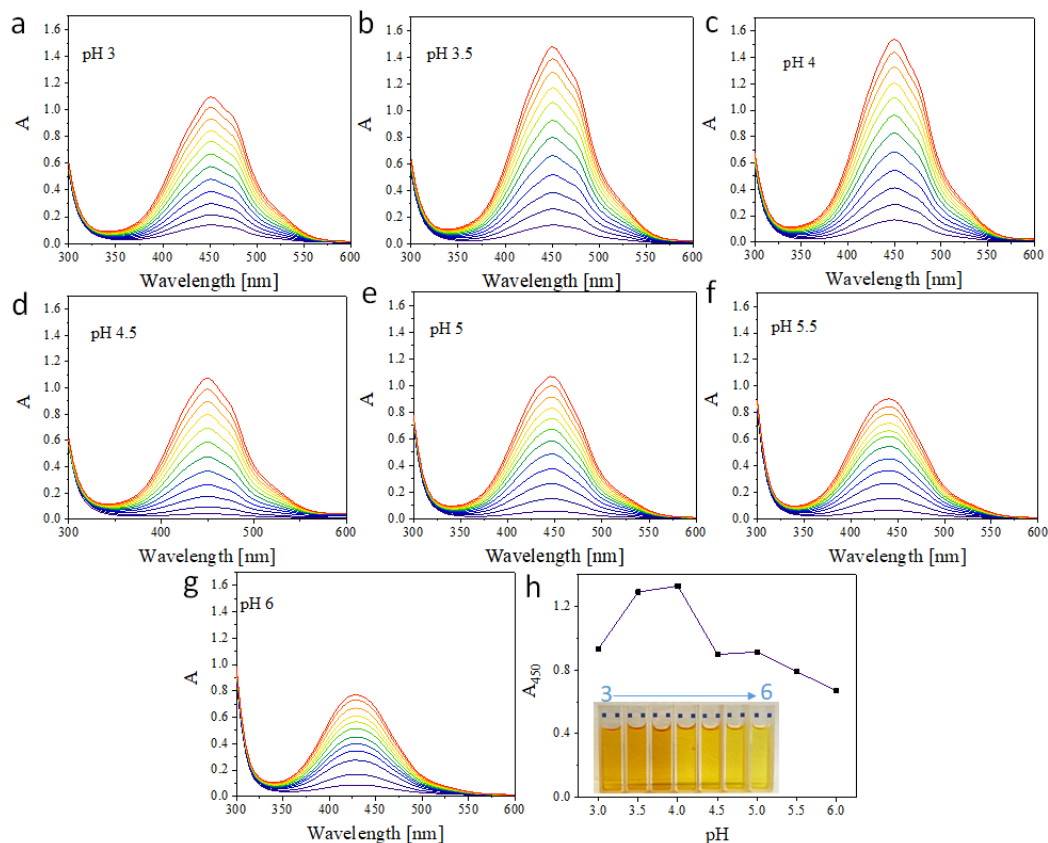
Figure 3-11. pH-dependent activities of oxidation of OPD by PtAgNCs. (a-g) Time-dependent absorption spectra A(λ) of oxidation of OPD by PtAgNCs in buffer solution at varying pH levels. (h) Comparison of PtAgNCs' intrinsic POD-like activity at different pHs after 24 min. The inset shows the corresponding photographs after reaction.

Considering the composition of PtAgNCs, samples with different Pt/Ag ratios were investigated. As shown in **Figure 3-12**, PtAgNCs exhibited superior POD-like activity than the monometallic Pt@ZIF-8 whereas Ag@ZIF-8's activity is negligible. For further investigation, seven PtAgNCs were prepared with 2, 4, 8, 16, 32, 40 and 80 μL AgNO₃, respectively. The obtained PtAgNCs products were thereafter numerated from 1 to 7. The ICP-MS data of the samples was shown in **Figure 3-13a**, and the corresponding absorption at 450 nm in pH 4 buffer were shown in **Figure 3-13b**. The results indicate that an increasing Ag content in PtAg alloy reduces the enhancement in OPD-like catalytic performance down to a certain levle. The POD-like activity of this PtAgNCs showed a composition dependence. In comparison, PtAgNPs also displayed the pH- and composition-dependent properties with a superior catalytic performance at pH 4 and a lower Pt content in PtAg alloy nanocomposites (**Figure 3-14** and **Figure 3-15**). Different Pt/Ag ratios were 1:0.5, 1:1, 1:2, 1:3, 1:3.5, 1:4, 1:4.5 and 1:5, denoted as PtAgNPs-1 to -8, respectively.
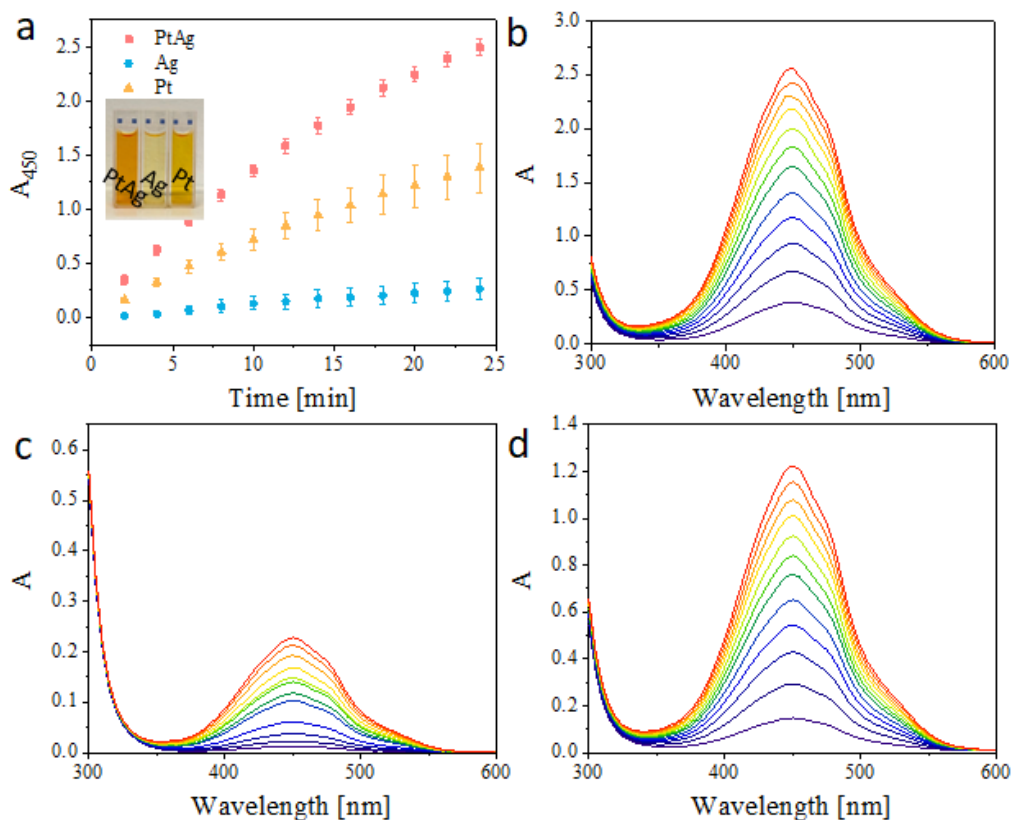
Figure 3-12. *Comparison of OPD-like activieties catalyzed by PtAg, Pt and Ag@ZIF-8, respectively. (a) Time-dependent absorption spectra A (λ = 450 nm) of the oxidation of OPD by PtAg, Pt and Ag@ZIF-8, respectively. The image shows the reaction solution after 24 min by PtAgNCs, Ag and Pt@ZIF-8, respectively. (b-c) Time-dependent absorption spectra (λ) of the oxidation of OPD by PtAg, Pt and Ag@ZIF-8, respectively.*
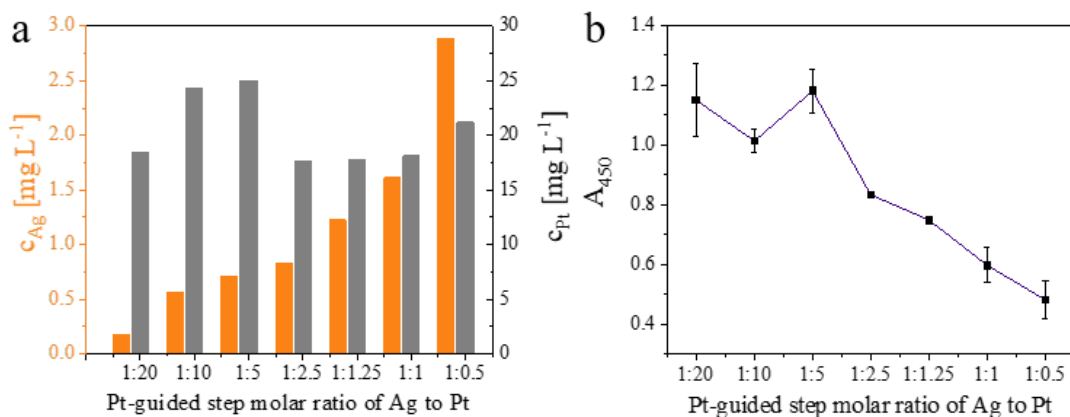
Figure 3-13. *ICP-MS results and absorption at 450 nm with PtAgNCs catalyst. (a) ICP-MS results and (b) corresponding absorption at 450 nm of the oxOPD in buffer at pH 4 by PtAgNCs with different molar ratio of Ag to Pt. The ICP-MS data of this figure were recorded by Dr. Indranath Chakraborty.*

50
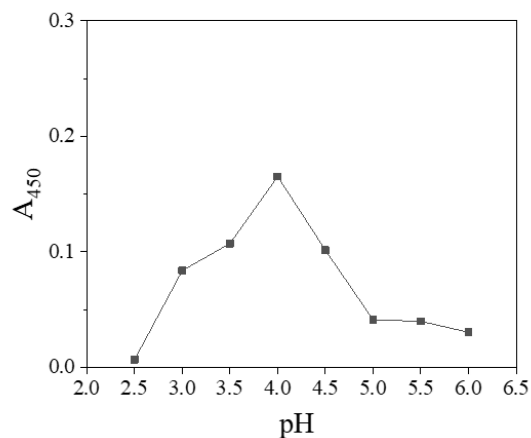
Figure 3-14. Comparison of PtAgNPs' intrinsic POD-like activity in relation to the pH after 24 min.
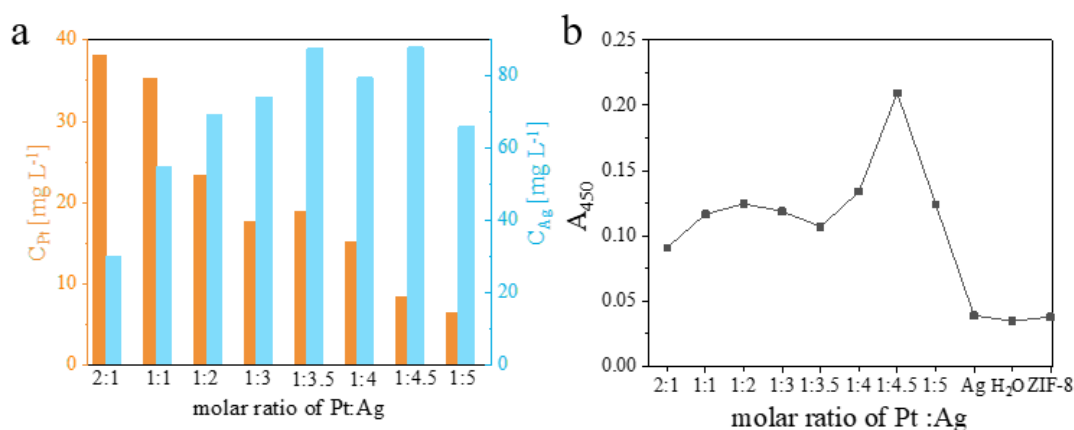
Figure 3-15. ICP-MS results and absorption at 450 nm with PtAgNCs catalyst. (a) ICP-MS results and (b) corresponding absorption at 450 nm of OPD in buffer at pH 4 oxidized by PtAgNPs with different molar ratio of Ag to Pt. The ICP-MS data of this figure were recorded by Dr. Indranath Chakraborty.

Steady-state kinetics studies for POD-like catalytic activities of PtAgNCs and PtAgNPs were further investigated according to the Michaelis-Menten model using H_2O_2 and OPD as substrates. Here the kinetic parameters for the PtAgNCs-1 and PtAgNPs-7 were investigated. The data were recorded by increasing one substrate concentration while keeping the other one constant. The time-dependent absorbance changes in absorbance at 450 nm were measured, as shown in **Figure 3-16** to **Figure 3-21**. To emphasize in **Figure 3-16** and **Figure 3-19**, the oxidation reaction of OPD calculated by both PtAgNCs-1 and PtAgNPs-7 fit the typical Michaelis-Menten behavior towards both H_2O_2 and OPD substrates. The linear fits are plotted in **Figure 3-22** and listed in **Table 3-2**. 56.5 and 0.231 mM as the K_m values for the H_2O_2 and OPD systems of PtAgNCs-1 were smaller than those for PtAgNPs-7 (1714 and 0.284 mM, respectively). Control

experiments were carried out with monometallic Pt@ZIF-8 and Ag@ZIF-8 (**Figure 3-23** and **Figure 3-24**). It was found that PtAgNCs-1 exhibited much lower K_m and v_{max} than those for Pt@ZIF-8 and Ag@ZIF-8. The K_m value in OPD system for HRP was shown much higher than that of PtAgNCs-1. Thus, PtAgNCs-1 seems to have stronger binding affinity towards OPD. This is probably due to more active sites on the surface of the PtAgNCs-1 than HRP and PtAgNPs-7. The K_m value for H_2O_2 of PtAgNCs-1 is lower than the as-synthesized PtAgNPs-7, Pt@ZIF-8 and Ag@ZIF-8, showing a higher affinity to H_2O_2.
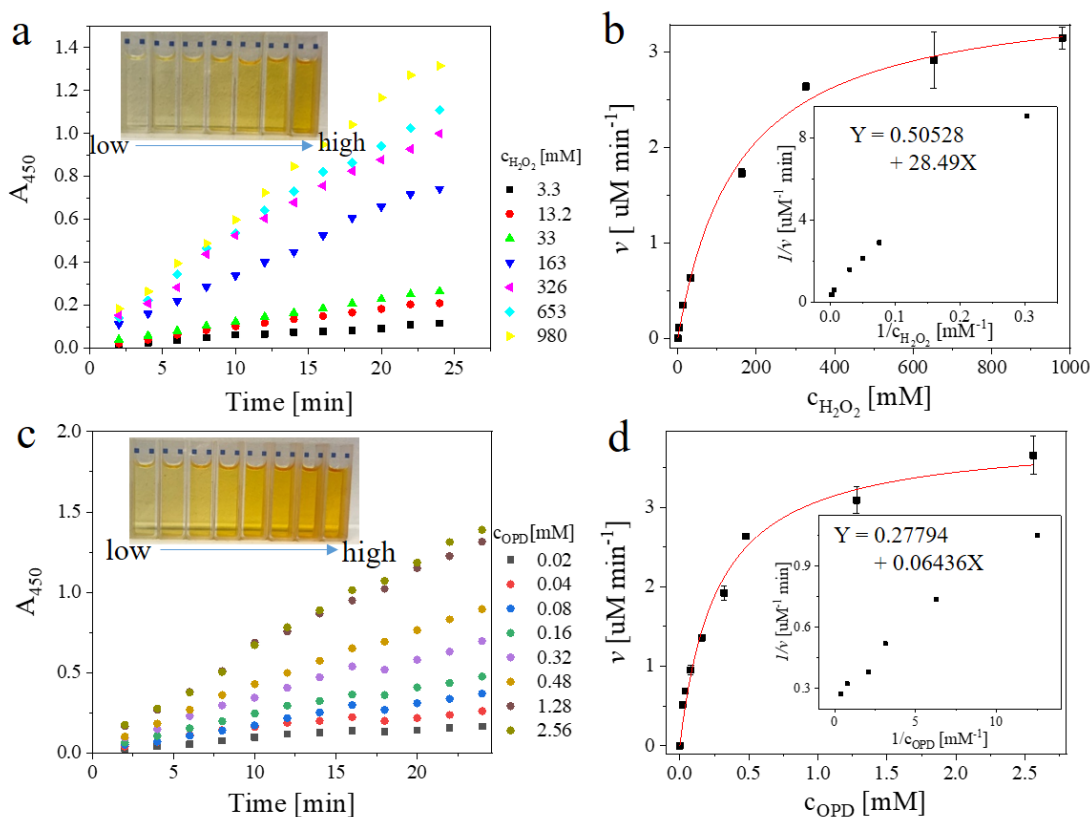
Figure 3-16. *Steady-state kinetic of POD-like activities of PtAgNCs-1. The oxidation of OPD in the presence of H_2O_2 with different concentration of substrate (a-b) H_2O_2 and (c-d) OPD at pH 4. Insets of a and c show the corresponding photo images after 24 min OPD oxidation reaction, and b and d are corresponding Lineweaver-Burk fitting.*
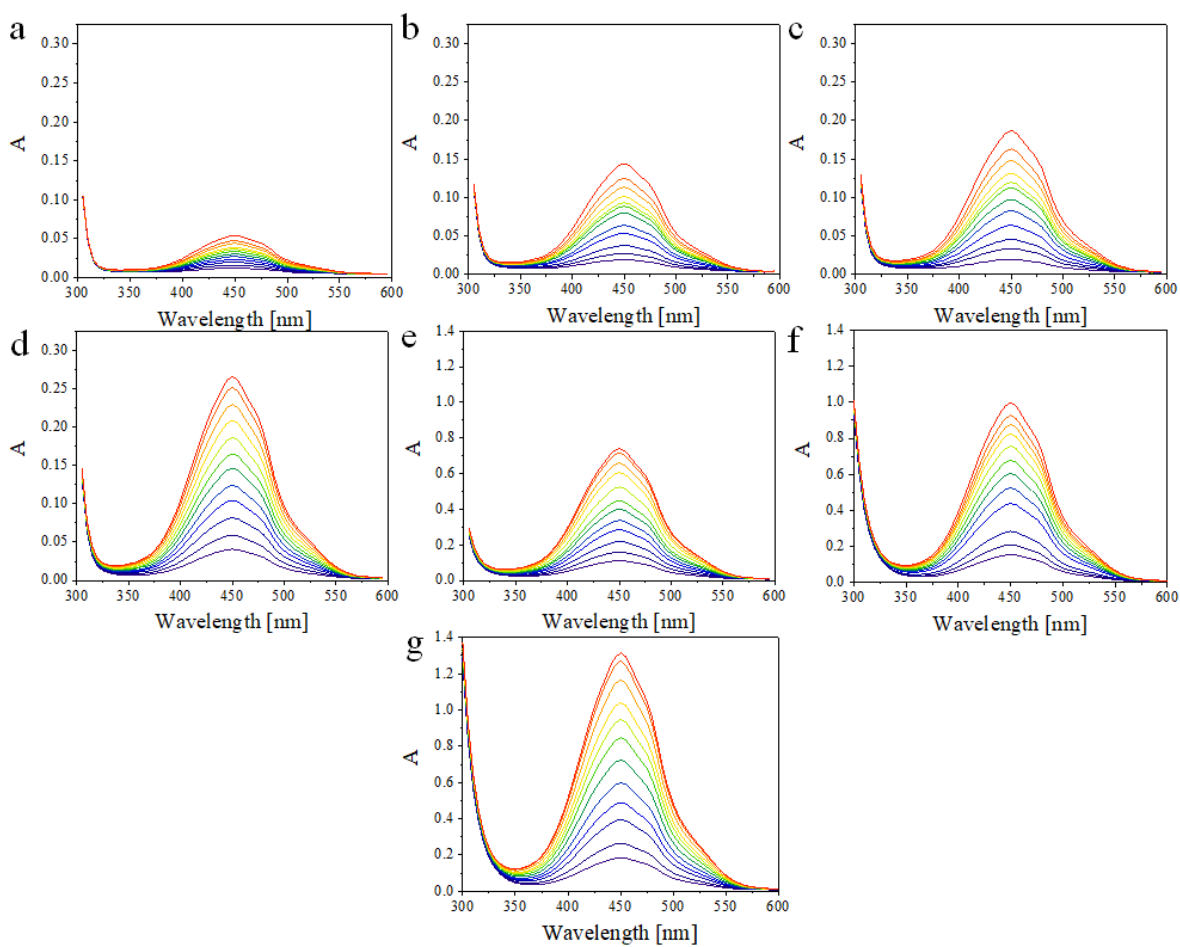
Figure 3-17. *Time-dependent absorption spectra A(λ) of the oxidation of OPD by PtAgNCs-1 with different concetration of H₂O₂. (a-g) Different concentration of H₂O₂ was used (c_{H2O2} = 3.3, 13.2, 33, 163, 326, 653 and 980 mM, respectively) while keeping the OPD concentration fixed.*
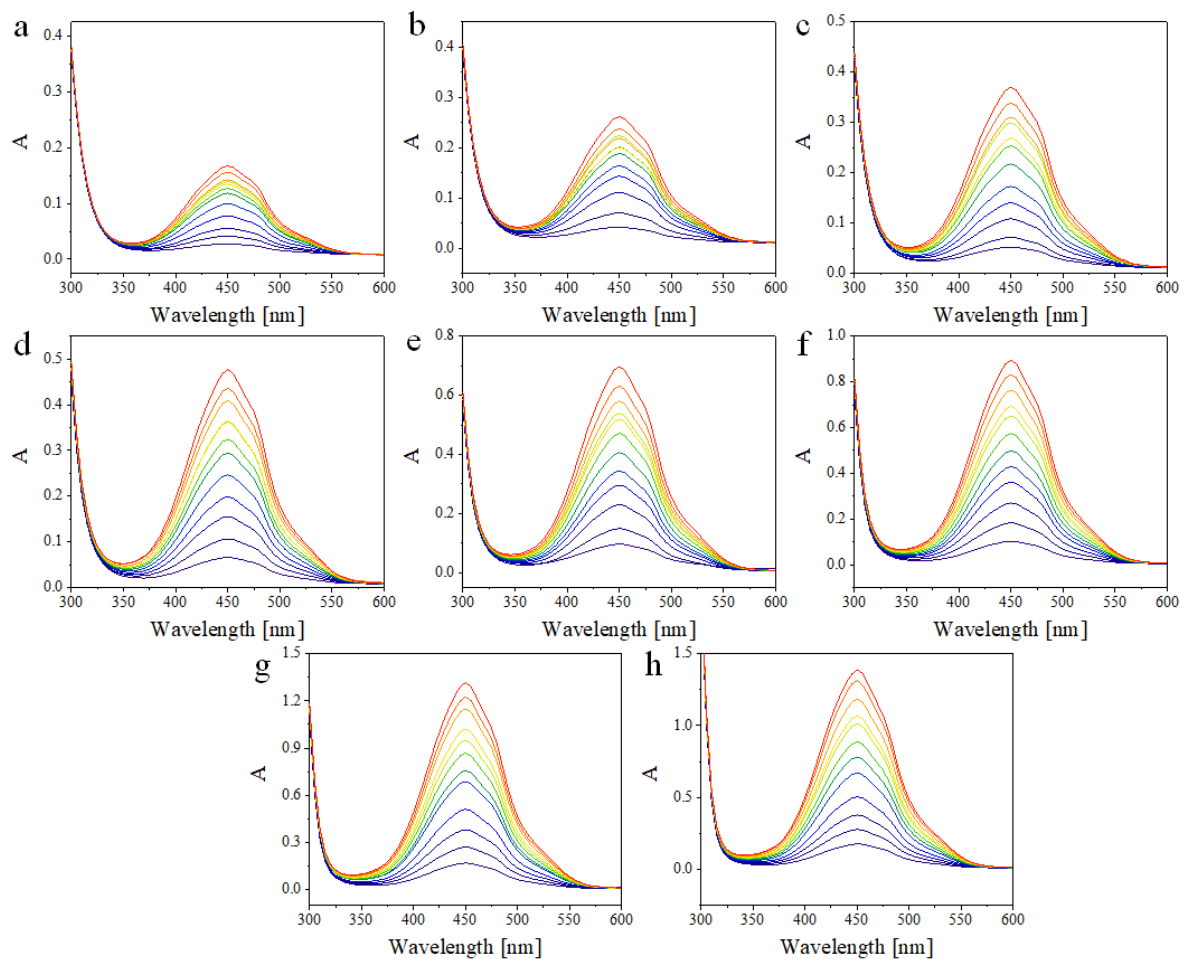
Figure 3-18. *Time-dependent absorption spectra A(λ) of the oxidation of OPD by PtAgNCs-1 with different concetration of OPD. (a-h) Different concentration of OPD was used (c_{OPD} = 0.02, 0.04, 0.08, 0.16, 0.32, 0.28, 1.28 and 2.56 mM, respectively, while the H_2O_2 concentration was kept constant.*
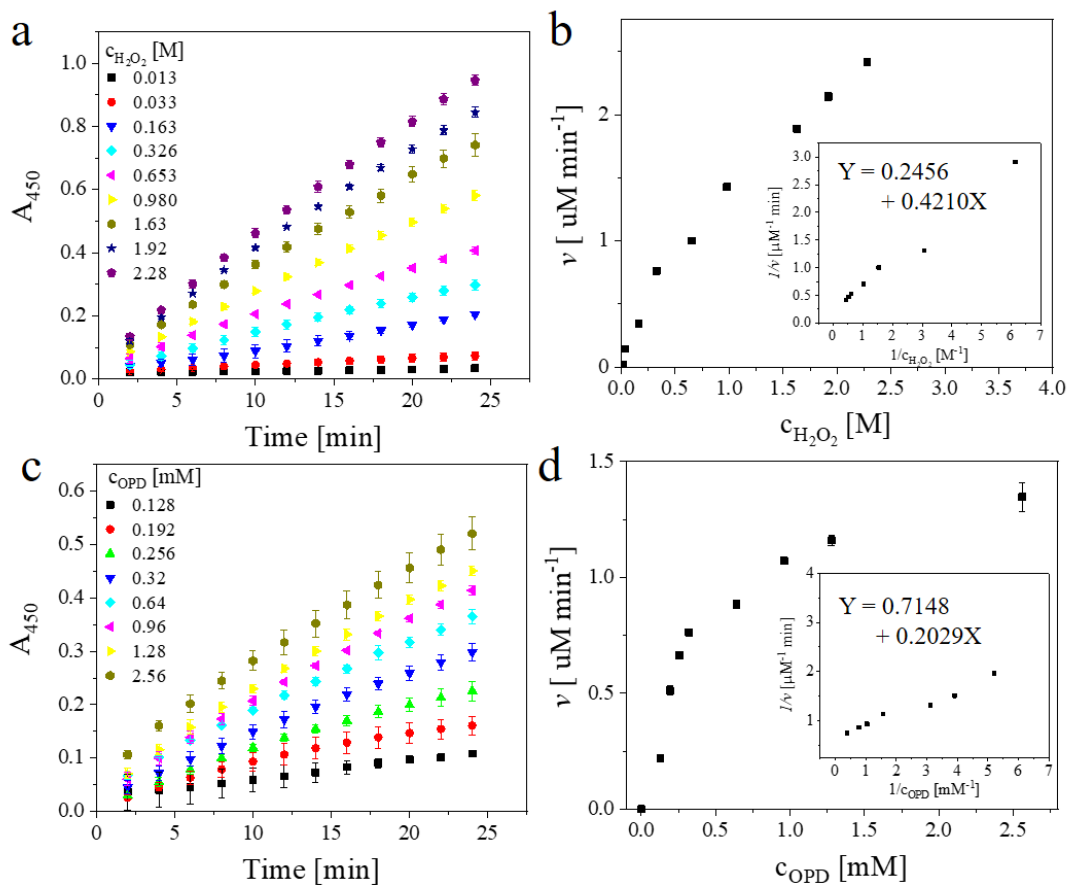
Figure 3-19. *Steady-state kinetic of POD-like activities of PtAgNPs-7 upon the oxidation of OPD in the presence of H₂O₂. Different concentration of substrate (a-b) H₂O₂ and (c-d) OPD at pH 4 were shown. Insets of and b and d are corresponding Lineweaver-Burk fits.*
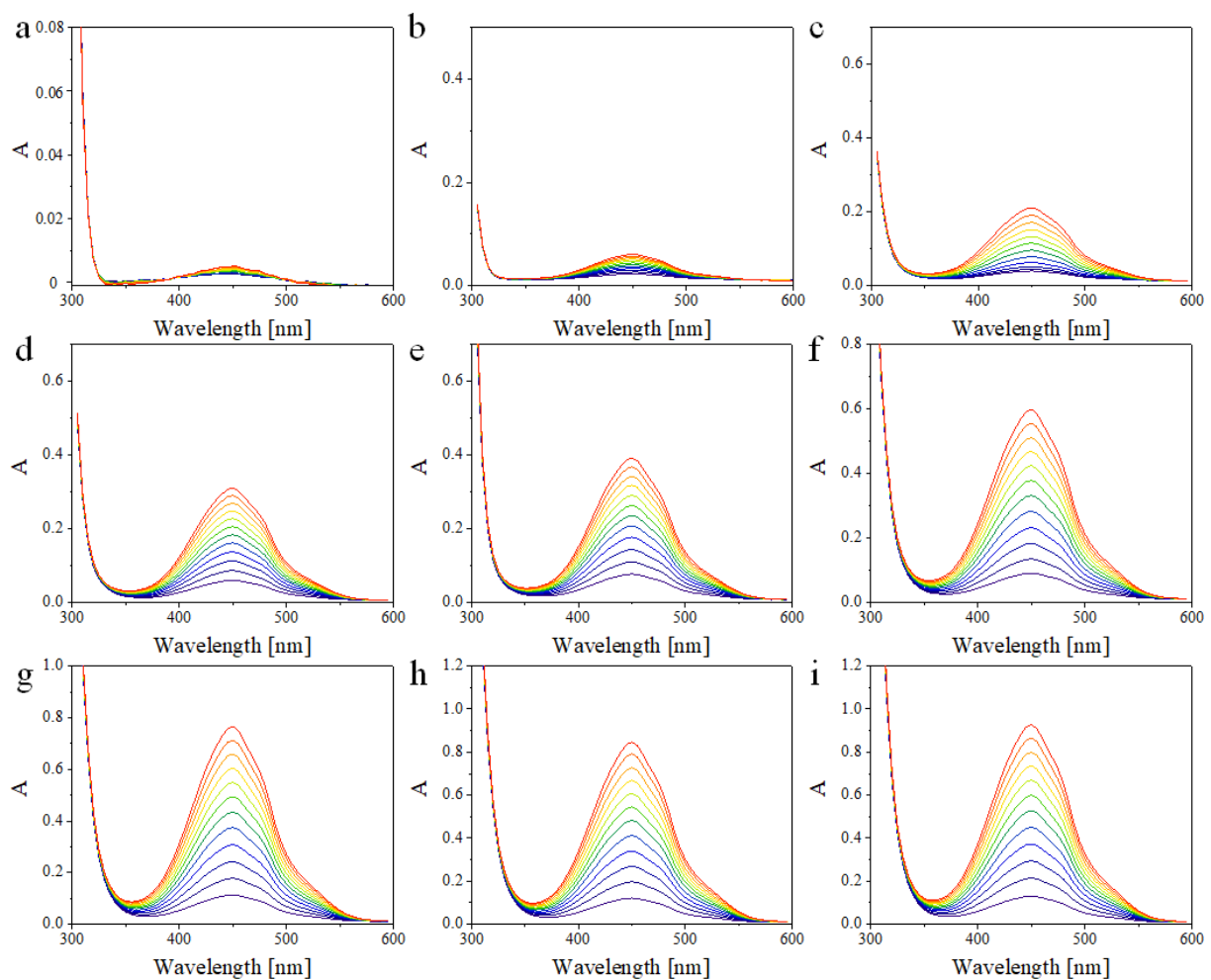
Figure 3-20. *Time-dependent absorption spectra A(λ) of the oxidation of OPD by PtAgNPs-7 with different concetration of H_2O_2. (a-g) Different concentration of H_2O_2 was used (c_{H2O2} = 0.013, 0.033, 0.163, 0.326, 0.653, 0.98, 1.63, 1.92 and 2.28 M, respectively) while keeping the OPD concentration constant.*
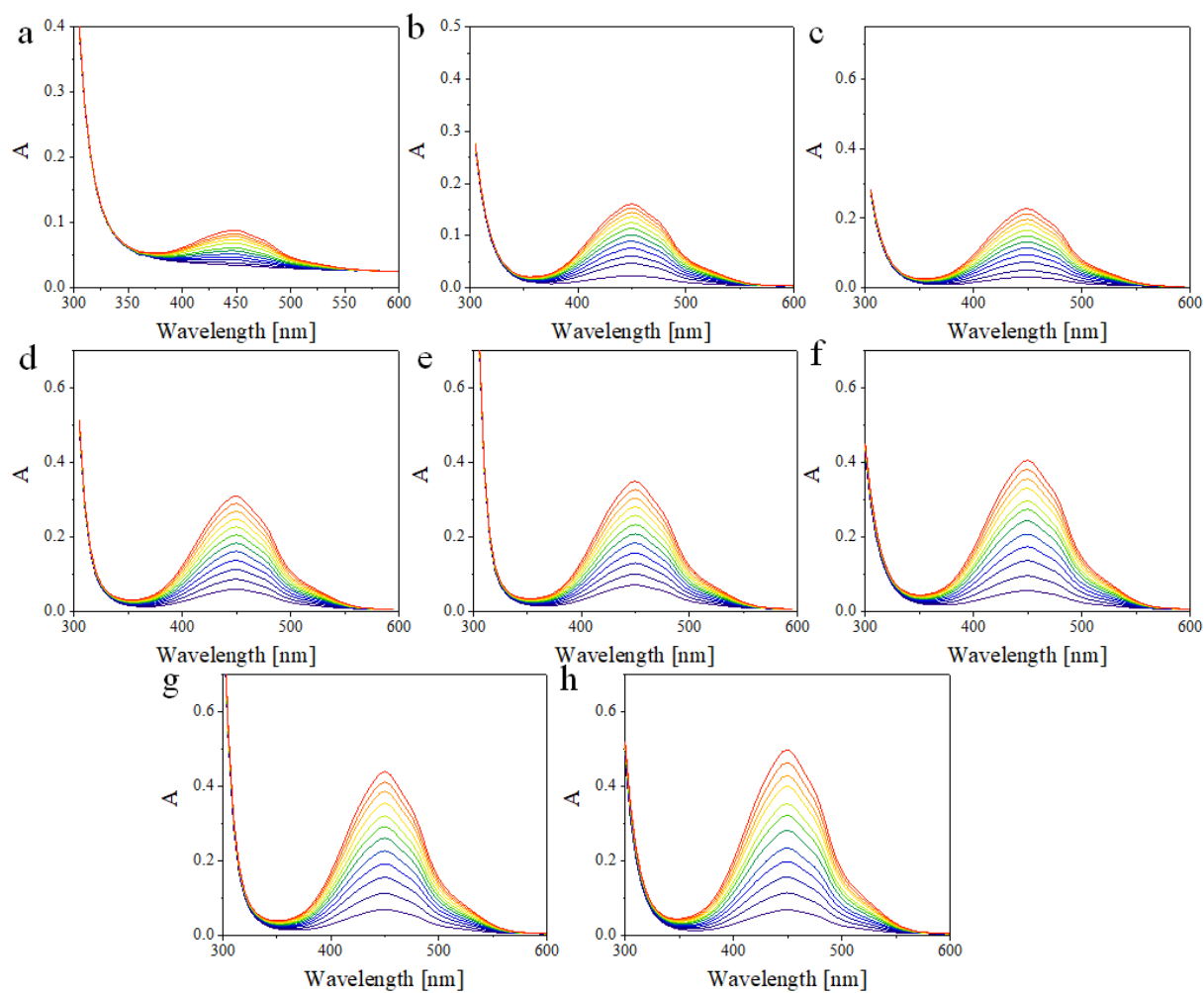
Figure 3-21. *Time-dependent absorption spectra A(λ) of the oxidation of OPD by PtAgNPs-7 with different concetration of OPD. (a-h) Different concentration of OPD (c_{OPD} = 0.02, 0.04, 0.08, 0.16, 0.32, 0.28, 1.28 and 2.56 mM, respectively, while the H_2O_2 concentration was kept constant.*
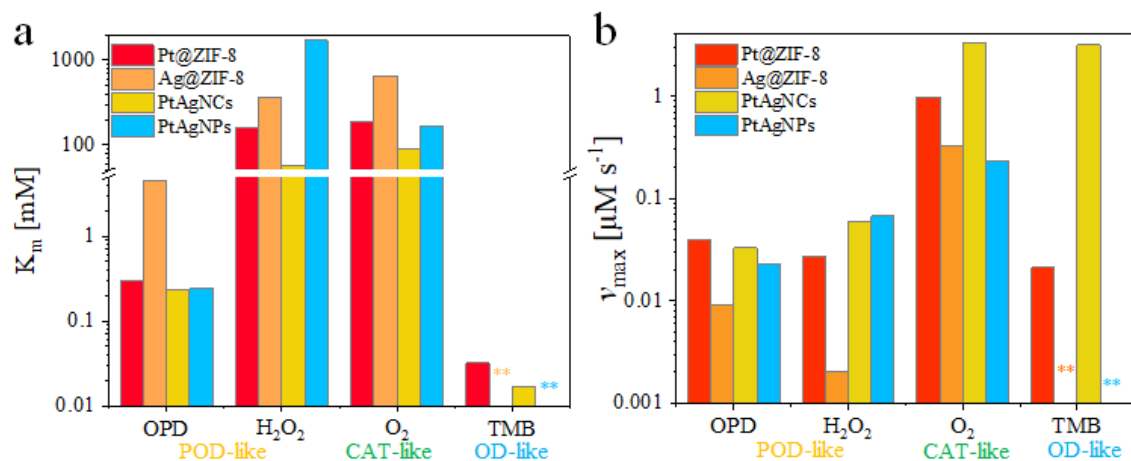
Figure 3-22. *Corresponding K_m and v_{max} analysis of Pt@ZIF-8, Ag@ZIF-8, PtAgNCs and PtAgNPs for the enzyme mimicking.*
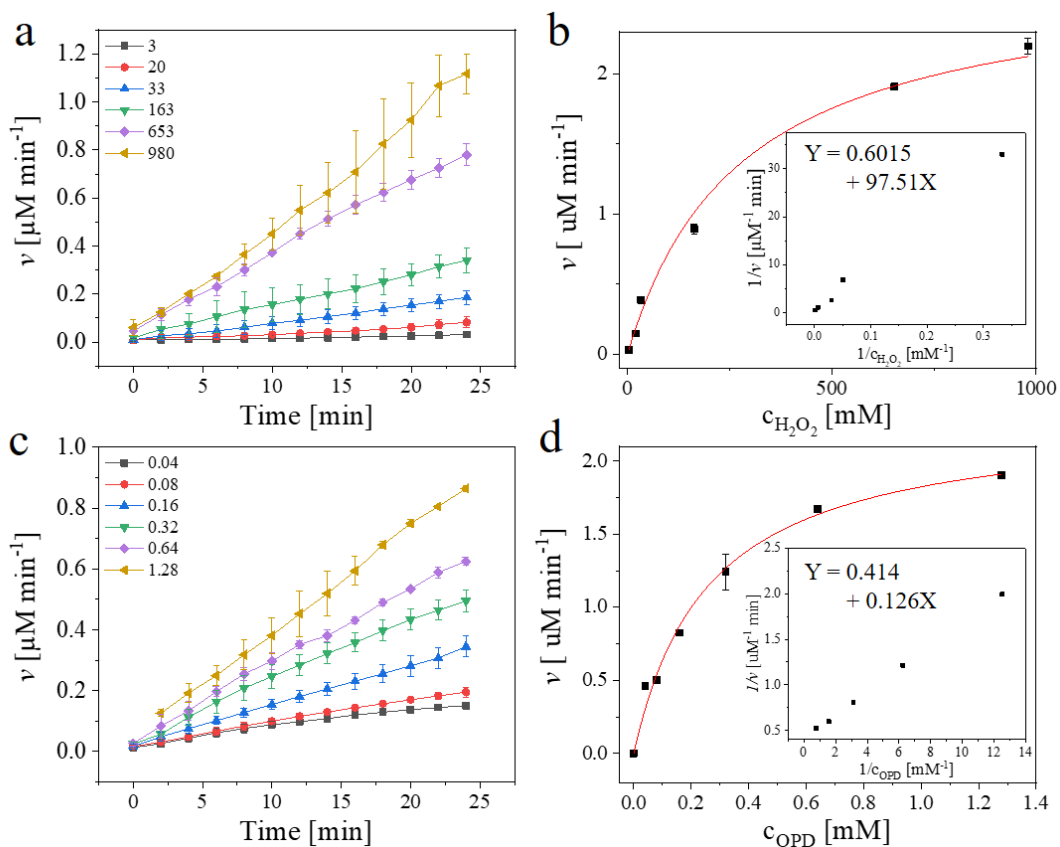
Figure 3-23. *Steady-state kinetic of POD-like activities of Pt@ZIF-8 upon the oxidation of OPD in the presence of H_2O_2. Different concentration of substrate (a-b) H_2O_2 and (c-d) OPD were recorded at pH 4. Insets of and b and d are corresponding Lineweaver-Burk fitting.*

58
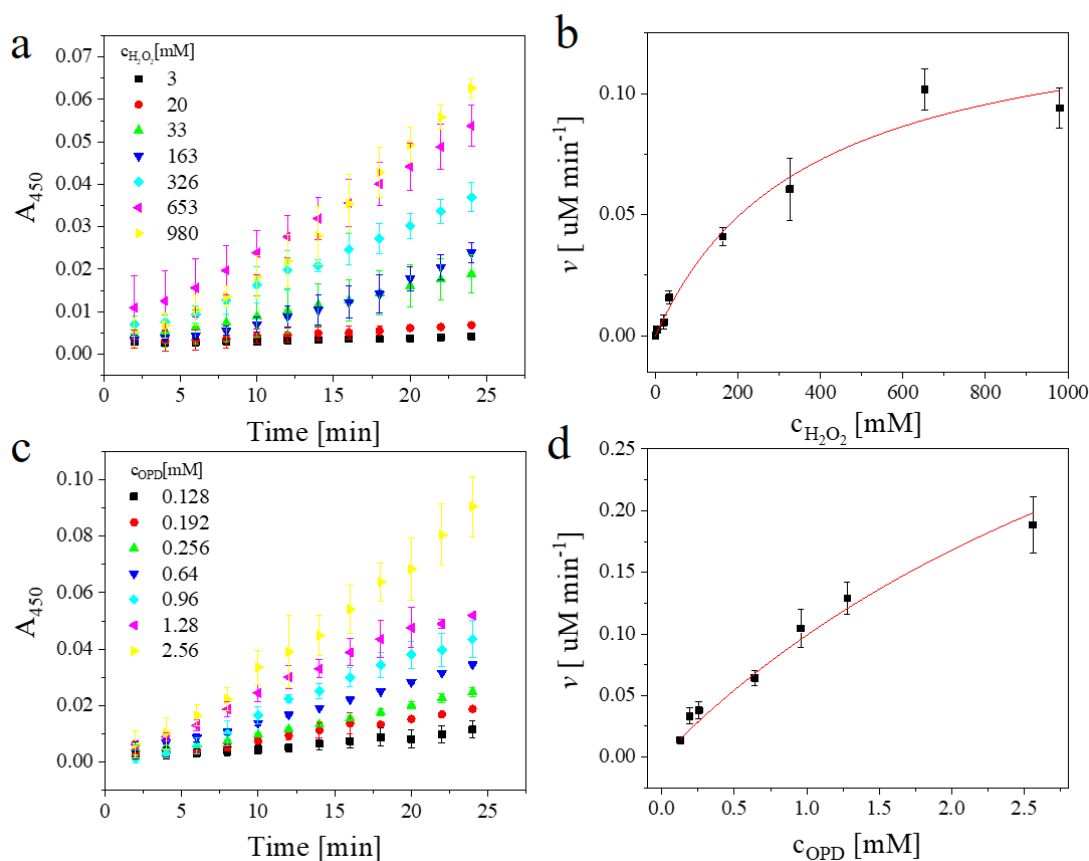
Figure 3-24. Steady-state kinetic of POD-like activities of Ag@ZIF-8 upon the oxidation of OPD in the presence of H_2O_2. Different concentration of substrate (a-b) H_2O_2 and (c-d) OPD were recorded at pH 4.

3.2.2.2 Catalase (CAT)-like activity of PtAgNCs@ZIF-8

Pt was illustrated as a better CAT mimic than other metals (like Ag, Au), what has been confirmed for the efficient O_2 generation accompanyied the decomposition of H_2O_2.[160, 169] The CAT-like activities of PtAgNCs were then investigated in 0.1 M PBS (pH 7). The generation of O_2 by the PtAgNCs-1 was evaluated in the presence and absence of H_2O_2 to detect the CAT-like performance of catalyst under neutral conditions. As shown in **Figure 3-25a**, the concentration of O_2 did not alter in the absence of H_2O_2 compared to the fast liberating of O_2 with H_2O_2. It indicates the ability of PtAgNCs -1 to decompose H_2O_2. The image showed obvious bubbles in the solution during the decomposition of H_2O_2 by PtAgNCs-1 (**Figure 3-25b**). Different pH values buffer solutions were also examined. Results show a lower O_2 liberation rate which implies better catalytic properties under neutral conditions consistent with previous studies (**Figure 3-26**). Control experiments were performed with ZIF-8, Pt@ZIF-8, and Ag@ZF-IF-8 with and without the addition of H_2O_2. The results exhibit the enhanced CAT-like activities for the liveration of

O_2 on the decomposition of H_2O_2 by alloyed PtAgNCs-1 when compared to monometallic Pt@ZIF-8 or Ag@ZIF-8. Moreover, different ratios of PtAgNCs catalysts were studied, demonstrating that the generation rate of O_2 is composition-dependent on the Pt/Ag ratio of PtAgNCs (**Figure 3-27**). It should be noted that the lower Pt: Ag ratios contribute to less CAT-like catalytic properties. A similar generation rate of O_2 was observed for PtAgNCs-1 and PtAgNCs-2 (**Figure 3-28**), which could be attributed to the high percent of Pt in both samples. In contrast, the series of PtAgNPs catalysts provided no strong enhancement with monometallic Pt@ZIF-8 as reference (**Figure 3-29**). This might be demonstrating that the smaller sizes PtAgNCs provide more catalytic sites on the surface than bigger PtAgNPs catalysts.
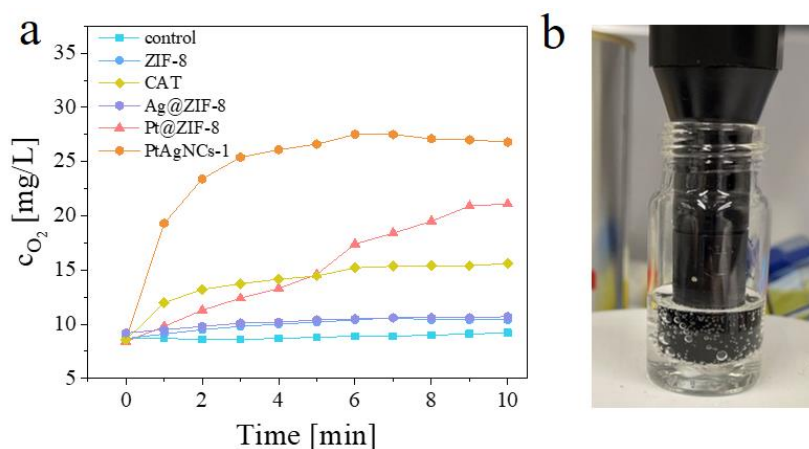
Figure 3-25. *CAT-like activities catalyzed by the PtAgNCs, ZIF-8, Pt@ZIF-8, Ag@ZIF-8 and CAT in the preasence of H_2O_2. (a) Time-dependent changes in the concentration of produced O_2 upon the catalytic decomposing of H_2O_2 in the PtAgNCs, ZIF-8, Pt@ZIF-8, Ag@ZIF-8 as well as CAT with the addition of H_2O_2 in comparison that in the absence of catalyst at PBS buffer pH 7. (b) Photo image of liberated O_2 in the solution.*
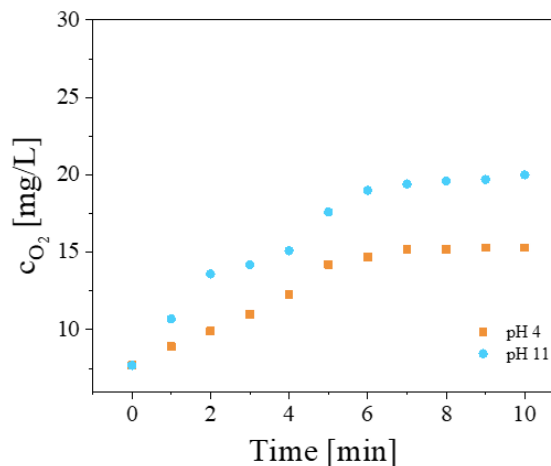
Figure 3-26. *Time-dependent changes in the concentration of liberated O_2 catalyzed by PtAgNCs-1 at different pHs.*
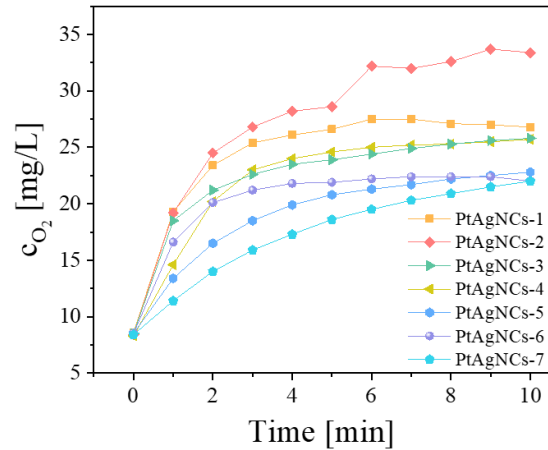
Figure 3-27. *Composition-dependent CAT-like activities of PtAgNCs. Time-dependent changes upon the generation of O_2 upon the catalytic decomposing of H_2O_2 in the PtAgNCs with different Pt to Ag ratio at PBS buffer pH 7.*
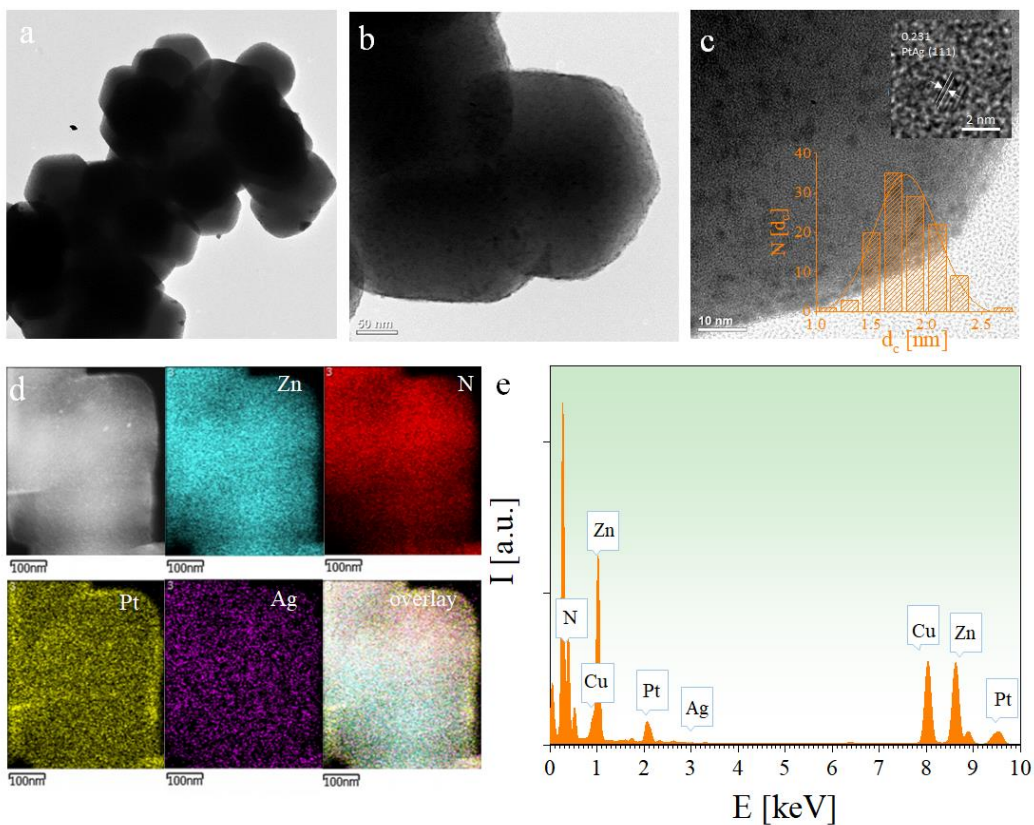
Figure 3-28. *TEM and EDS characterization of PtAgNC-2. (a-c) TEM images of PtAgNCs-2 samples. The insets in c represent corresponding size distribution histogram of the core diameter ($d_c = 1.80 \pm 0.15$ nm) and the HRTEM of a PtAgNC. (d-e) Corresponding element mapping images and EDS spectra of PtAgNCs-2. The TEM and EDS data of this figure were recorded by Mr. Stefan Werner.*
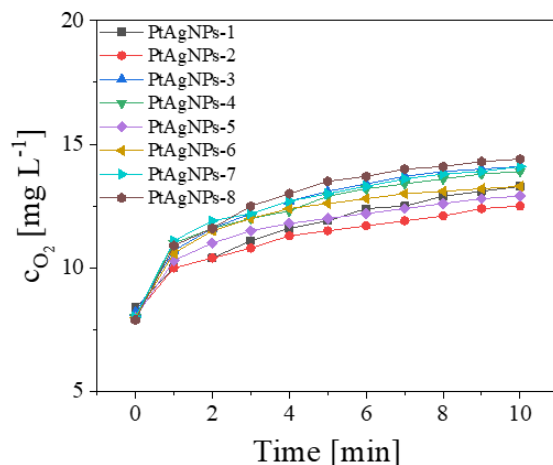
Figure 3-29. *Composition-dependent CAT-like activities of PtAgNPs. Time-dependent changes upon the generation of O_2 upon the catalytic decomposing of H_2O_2 in the PtAgNPs with different Pt to Ag ratio at PBS buffer pH 7.*

The CAT-like catalytic properties of PtAgNCs-2 was further investigated for the apparent steady-state kinetics. Time-dependent generation of O_2 in various H_2O_2 concentrations (0, 15, 37, 74, 360, and 750 mM) and corresponding data was plotted. The generation rate of O_2 as a function of H_2O_2 concentration was fitted to the Michaelis-Menten model, as shown in **Figure 3-30**. The correlation of the O_2 generation rate and H_2O_2 concentration could be confirmed by a double reciprocal plot. The linear fit according to the Lineweaver-Burk method resulted in $v_{max} = 3.3$ µM s^{-1} and $K_m = 88.89$ mM (**Figure 3-30b**, inset; **Table 3-2**). The K_m value for PtAgNCs-2 was similar to the catalase K_m, showing comparable affinity towards H_2O_2.[169] Furthermore, the higher K_m and smaller v_{max} values of PtAgNPs-7, Pt@ZIF-8, Ag@ZIF-8 catalysts were obtained, showing the high catalytic properties in smaller size alloy PtAgNCs-2 (**Figure 3-31**, **Table 3-2**).
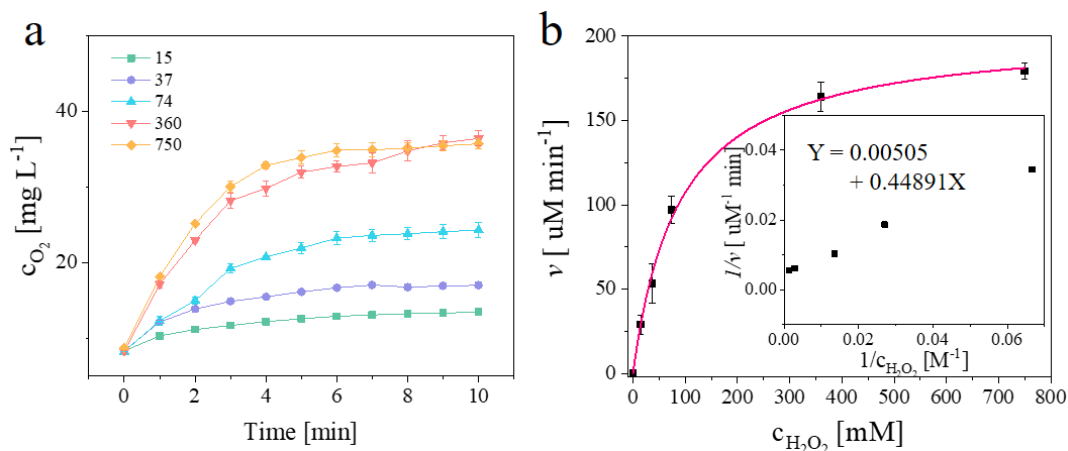
Figure 3-30. *Apparent kinetic of PtAgNCs-2 in catalase mimicking study. (a) Time-dependent changes in the concentration of produced O_2 upon the catalytic decomposing of H_2O_2 with different concentration (c_{H2O2} = 15, 37, 74, 360 and 750 mM, respectively). (b) Steady-state kinetic study of CAT-like activities upon the catalytic decomposition of H_2O_2 by PtAgNCs-2. Inset represents the corresponding Lineweaver-Burk fitting of CAT-like activity of PtAgNCs-2.*
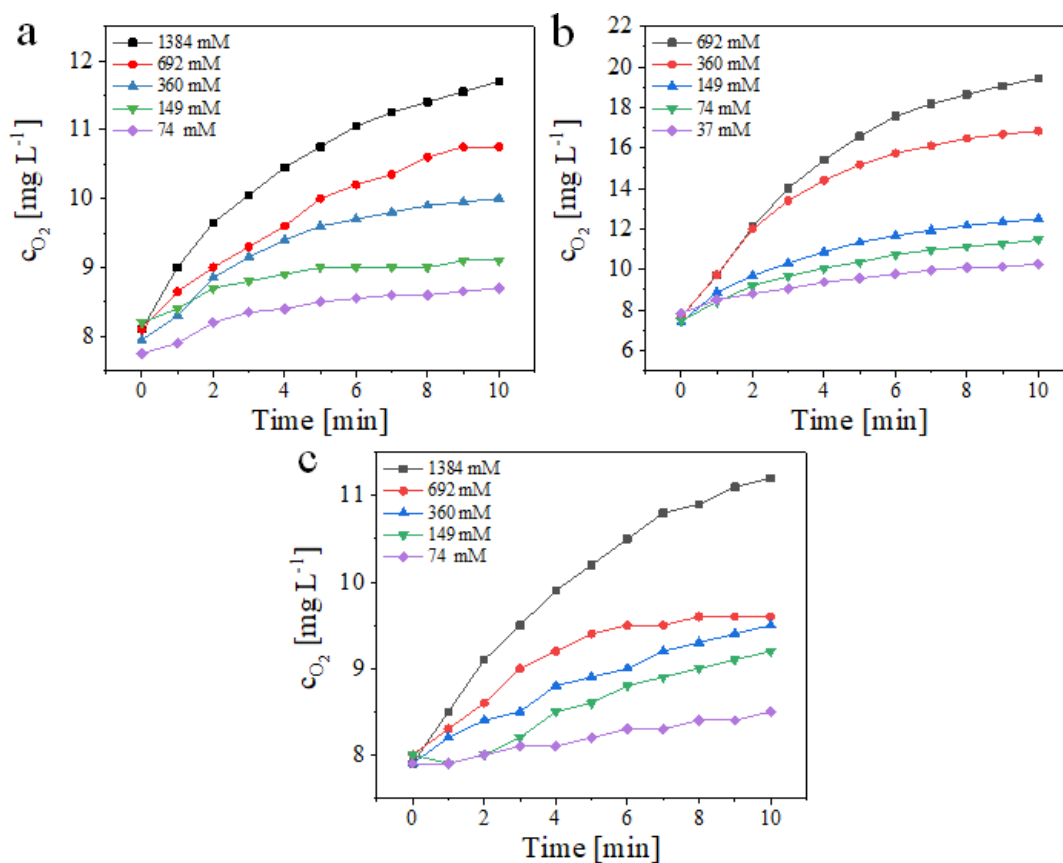
Figure 3-31. *Time-dependent changes in the concentration of liberated O_2 catalyzed by PtAgNPs-7 (a) Pt@ZIF-8 (b) and Ag@ZIF-8 (c). Different concentration of H_2O_2 at PBS buffer pH 7 were used.*

3.2.2.3 Oxidase (OD)-like activity of PtAgNCs@ZIF-8

More interestingly, PtAgNCs was found to be an OD mimic with TMB as chromogenic substrate in the presence of O_2. The O_2-dependent catalytic property was studied in the O_2- and N_2-saturated NaAc buffer solution (pH 4) in the presence of PtAgNCs-1. **Figure 3-32** shows the time-dependent absorption peak of the oxTMB at 652 nm. It could be found that PtAgNCs-1 can highly catalyze the oxidation of TMB to obtain blue color within 6 min whereas the presence of N_2 led to the nearly colorless solution, indicating that the O_2 is essential for the oxidation catalysis. Additionally, it proves that the oxTMB by PtAgNCs-1 originated from their catalytic ability in reducing dissolved O_2, confirming their oxidase-like activity, instead of being an oxidant. The pH-dependent performance of the PtAgNCs-1 catalytic activity was further examined at different pH values mainly to ensure optimal properties of previous reported nanozymes and native enzymes (most at pH 4).[187] As shown in **Figure 3-33** and **Figure 3-34**, PtAgNCs-1 tend to be inactivated at neutral and even alkaline conditions. After 6 min, no corresponding absorption peaks in the UV-vis spectra were observed at 652 nm, and for the rest of the time the final reaction buffer remained colorless. On the contrary, the high catalytic efficiency of PtAgNCs-1 was observed in acidic conditions. Optimal conditions were present at pH 4 according to the pH-dependent absorption at 652 nm after reaction for 6 min. It should be noted that the optimal pH for both the OPD (in peroxidase mimics) and TMB substrates at about 4 might be due to the similar diamine structure in both substrates which cause poor solubility under week alkaline conditions. Along with the O_2-dependency, PtAgNCs-1 were confirmed as oxidase mimics rather than an oxidant. Control experiments were conducted in the presence of Ag@ZIF-8, ZIF-8, Pt@ZIF-8 and H_2O, respectively. Replacing the PtAgNCs-1, Ag@ZIF-8, ZIF-8, and H_2O displayed negligible OD-like catalytic activity towards the oxidation of TMB, whereas Pt@ZIF-8 exhibited a minor OD-like catalytic property (**Figure 3-35** and **Figure 3-36**). Different Ag/Pt ratios for PtAgNCs were also investigated for the oxidation of TMB in the presence of O_2 (**Figure 3-37** and **Figure 3-38**). The oxidase-like catalytic efficiency decreased along with the increasing Ag/Pt ratios, probably because the tiny Ag-doping Pt contributes to the highest catalytic activities, and PtAgNCs-1 showed the best catalytic activity. In addition, the PtAgNPs exhibited negligible catalytic activity as oxidase mimics (**Figure 3-39**).

64
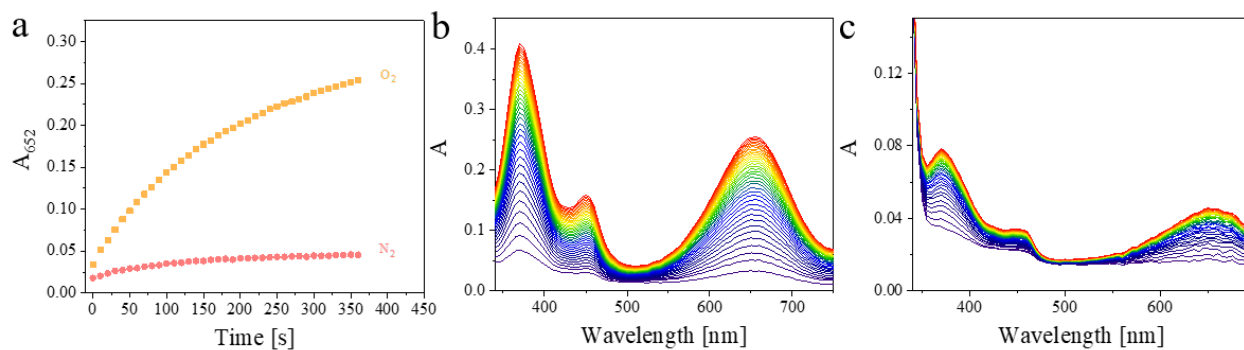
Figure 3-32. *Absorption spectra A(λ) of the oxidation of TMB by PtAgNCs-1 in the presence of dissolved O₂ and N₂. (a) Time-dependent absorbance changes at 652 nm upon the oxidation of TMB by PtAgNCs-1 in the presence of dissolved O₂ and N₂. (b-c) Corresponding UV-vis spectra of the OD-like of PtAgNCs-1.*
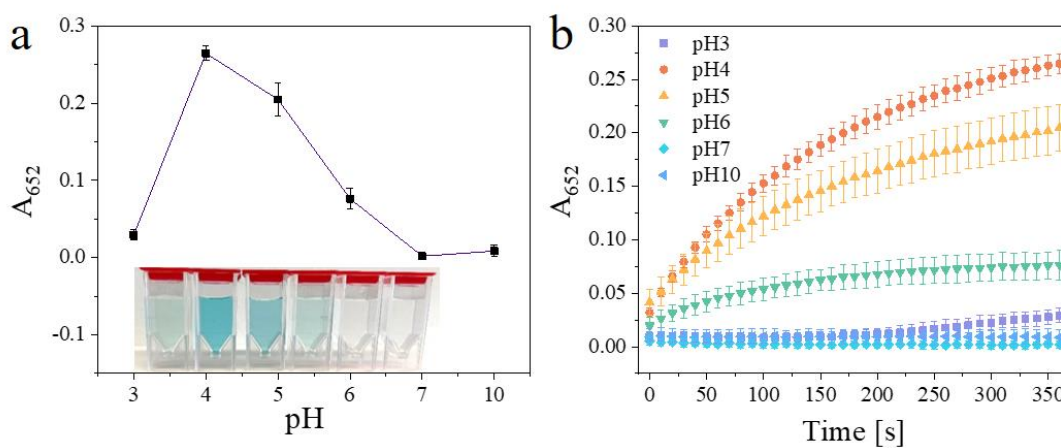
Figure 3-33. *pH-dependent OD-like activities of PtAgNCs-1 upon the oxidation of TMB. (a) pH-dependent OD-like activities of PtAgNCs-1 upon the generation of oxTMB (at 652 nm) in the presence of dissolved oxygen at different NaAc-HAc buffer pH (3, 4, 5, 6, 7, and 10) for 6 min. (b) Corresponding time-dependent absorbance changes at 652 nm upon the oxidation of TMB by PtAg@ZIF-8 for 6 min under different pH buffer.*
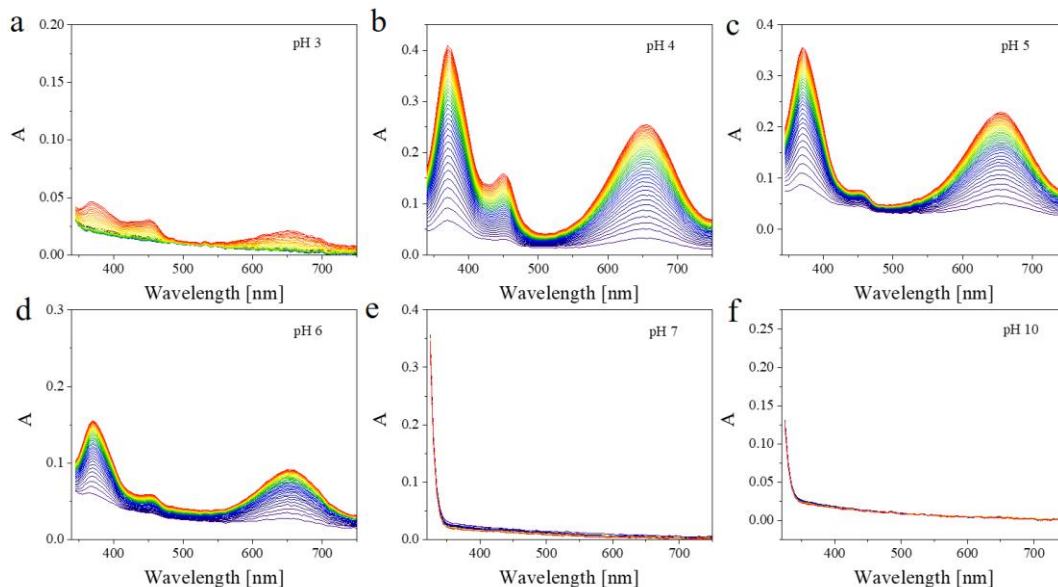
Figure 3-34. *Time-dependent absorption spectra of the oxidation of TMB by PtAgNCs-1 in the presence of dissolved O$_2$. Different NaAc-HAc buffer pH of (a) pH 3, (b) pH 4, (c) pH 5, (d) pH 6, (e) pH 7, and (f) pH 10 were recored for 6 min.*
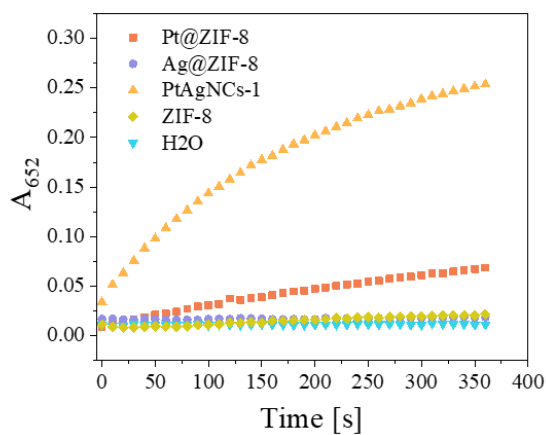
Figure 3-35. *Comparison of time-dependent absorbance changes at 652 nm upon the oxidation of TMB with different catalysts. Pt@ZIF-8, Ag@ZIF-8, ZIF-8, and PtAgNCs-1 catalysts were recorded in the absence of any catalysts in the presence of dissolved oxygen for 6 min.*

66
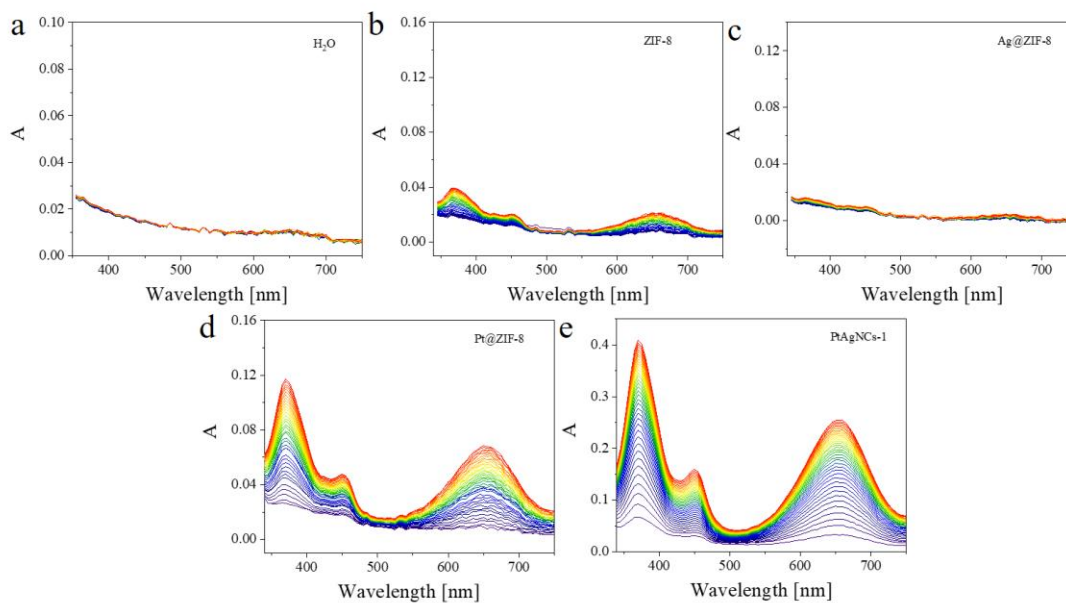
Figure 3-36. *Corresponding time-dependent absorption spectra of the oxidation of TMB by different catalysts added. (a) H₂O, (b) ZIF-8, (c) Ag@ZIF-8, (d) Pt@ZIF-8, and (e) PtAgNCs-1 in the presence of dissolved oxygen for 6 min.*
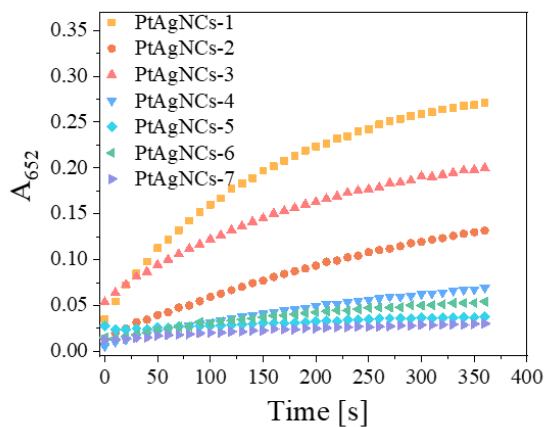
Figure 3-37. *Composition-dependent OD-like activities of PtAgNCs. Time-dependent absorbance changes at 652 nm of the oxidation of TMB by PtAgNCs with different ratios of Pt to Ag in the presence of dissolved oxygen for 6 min.*
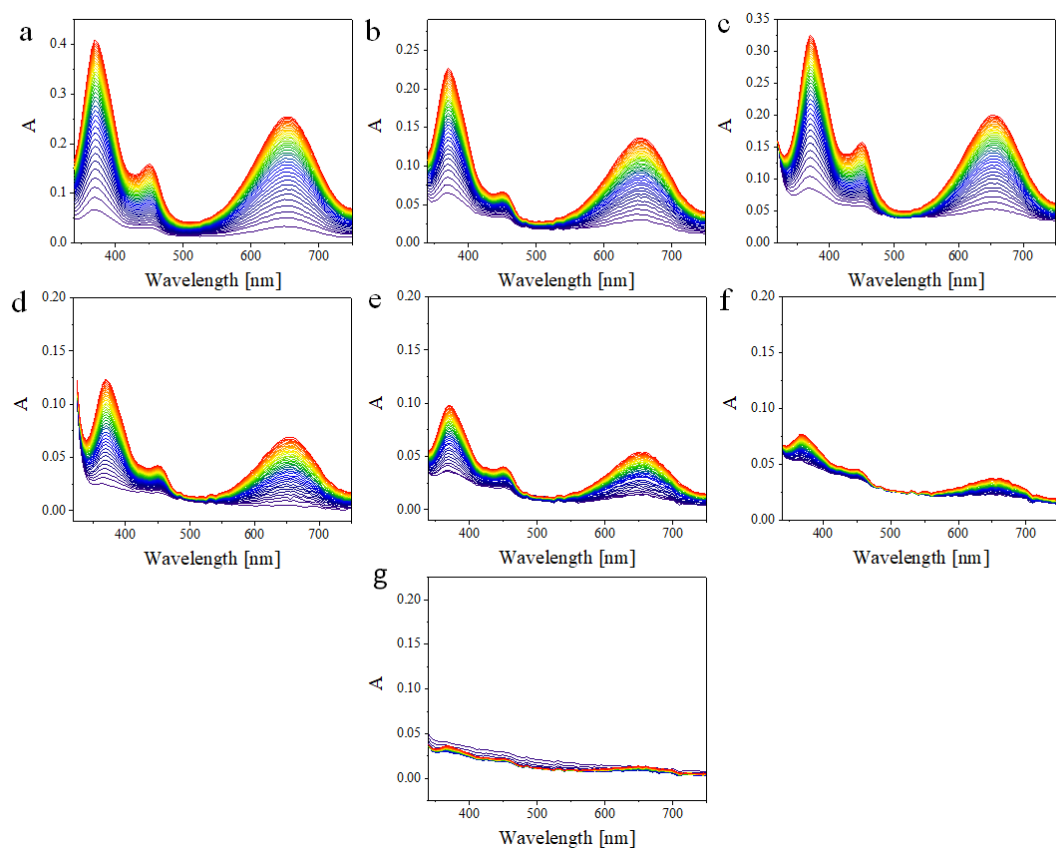
Figure 3-38. *Corresponding time-dependent absorption spectra of composition-dependent OD-like activities of PtAgNCs. The oxidation of TMB by PtAgNCs with different ratios of Pt to Ag in the presence of dissolved oxygen for 6 min.*
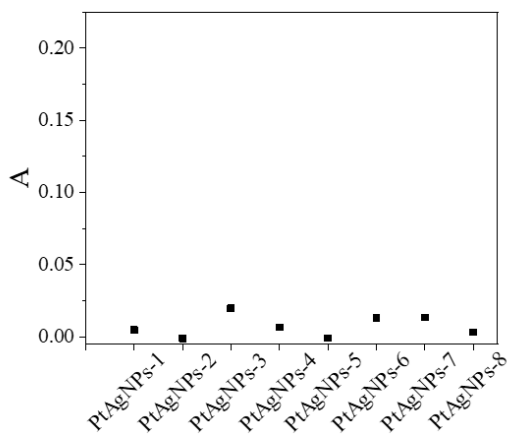
Figure 3-39. *Composition-dependent OD-like activities of PtAgNPs. UV-vis spectra at 652 nm of the oxidation of TMB by PtAgNPs with various Pt/Ag ratios in the presence of dissolved oxygen for 10 min at pH 4 NaAc-HAc buffer.*

Supplementary steady-state kinetic studies displayed that the oxidation of TMB catalyzed by PtAgNCs-1 in the presence of O_2 obeying the Michaelis-Menten kinetics (**Figure 3-40** to **Figure 3-42**). TMB solutions of 0.0039, 0.0079, 0.0118, 0.0393, 0.0786, 0.1179 and 0.2358 mM concentration were used under acidic conditions (0.1 M NaAc buffer, pH 4). **Figure 3-40b** presents a linear fit obtained by using the Lineweaver-Burk method. The obtained K_m and v_{max} values for PtAgNCs-1 catalyzing TMB were calculated as 0.017 mM which is smaller than those from monometallic Pt@ZIF-8 catalysts with 0.032 mM and other reported Pt-based oxidase (**Figure 3-41** and **Figure 3-43**, **Table 3-2**). It implies higher affinity of PtAgNCs to TMB, which is probably due to more active sites on the surface. It should be mentioned that the kinetic parameters for PtAgNPs and Ag@ZIF-8 were not obtained because even at high concentrations of TMB the signals were negligible (**Figure 3-44**). The kinetic parameters of this study are summarized in **Table 3-2**, compared to other reported nanozymes. The better catalytic performances are provided by PtAgNCs products.
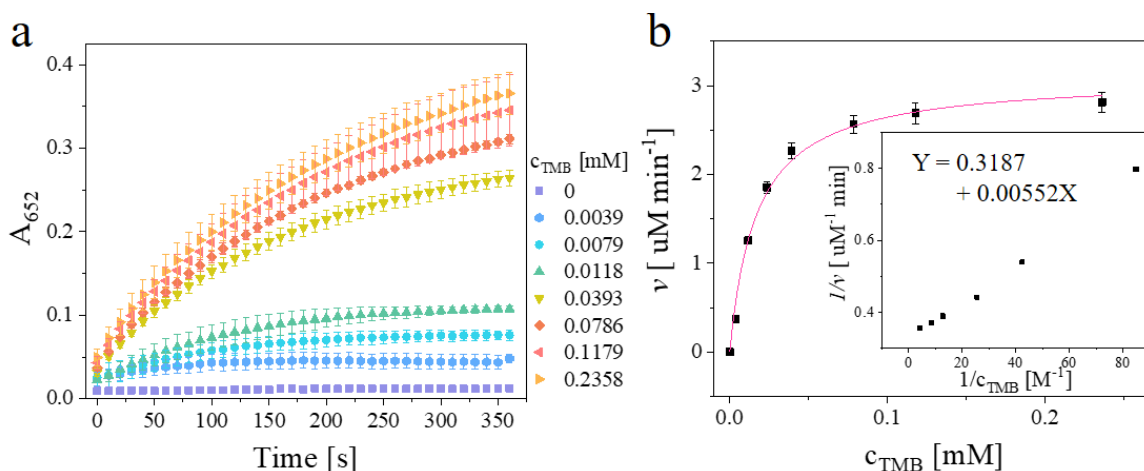
Figure 3-40. *Steady-state kinetic study of the OD-like activities of PtAgNCs-1. (a) Time-dependent absorbance changes of A_{652} upon the oxidation of TMB by PtAgNCs-1 under different concentrations of TMB. (b) Steady-state kinetic study of the OD-like activities upon the oxidation of TMB by PtAgNCs-1 in the presence of O_2 at pH 4. Inset is the corresponding Lineweaver-Burk fit.*
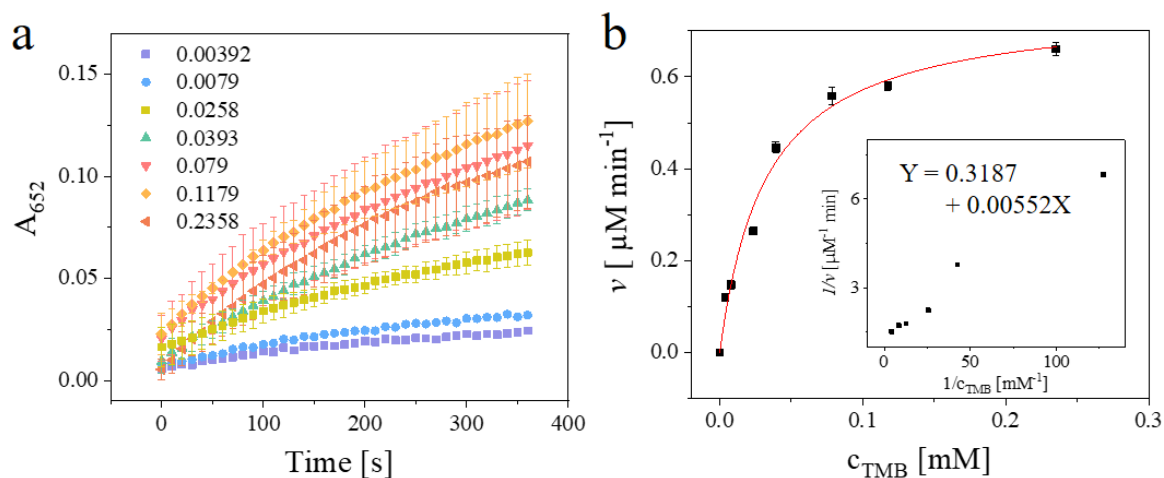
Figure 3-41. *Steady-state kinetic study of the OD-like activities of Pt@ZIF-8. (a) Time-dependent absorbance changes of A_{652} upon the oxidation of TMB by Pt@ZIF-8 under different concentrations of TMB. (b) Steady-state kinetic study of the OD-like activities upon the oxidation of TMB by Pt@ZIF-8 in the presence of O_2 at pH 4. Inset is the corresponding Lineweaver-Burk fit.*
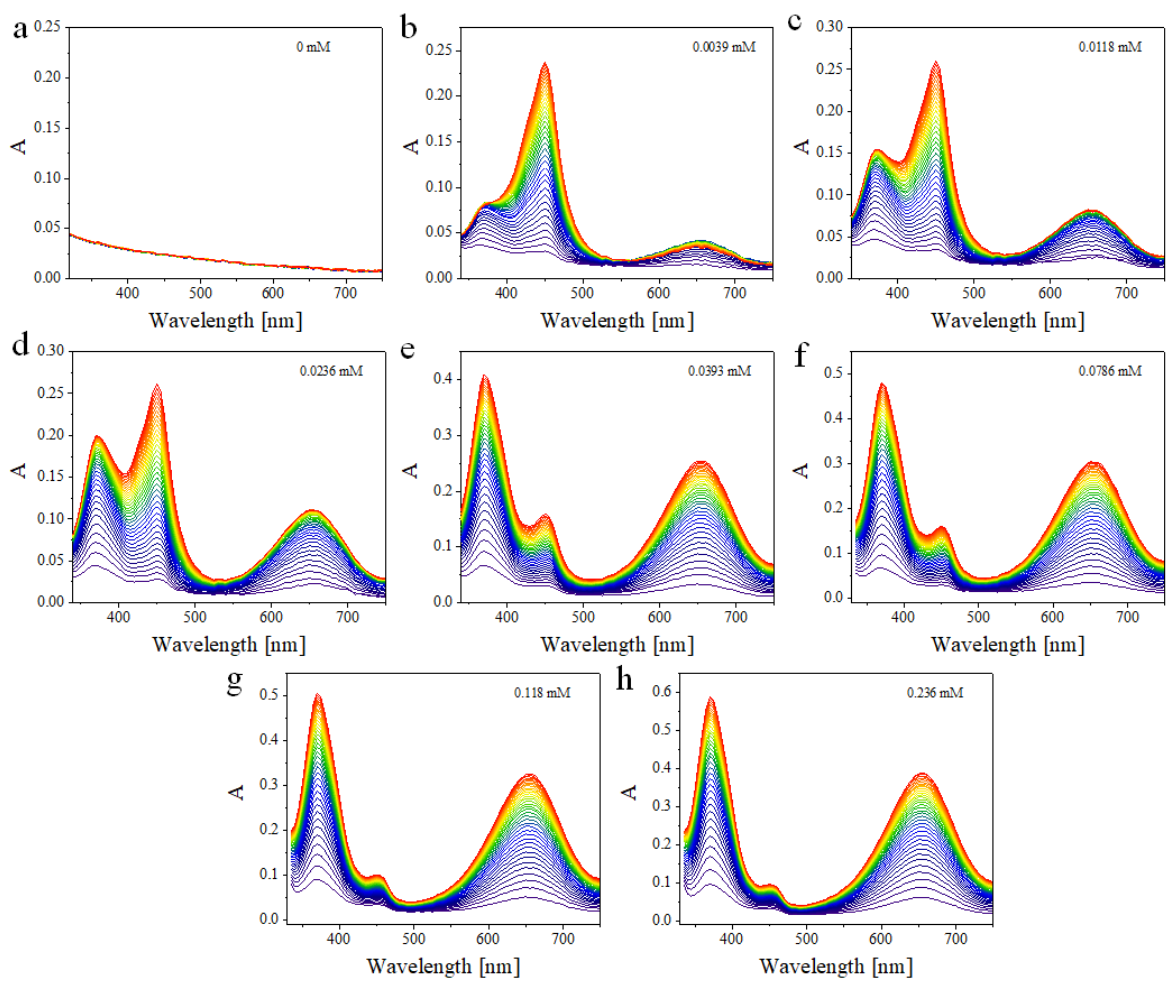
Figure 3-42. *Correpoonging of concentration-dependent absorption spectra of oxTMB by PtAgNCs-1.*
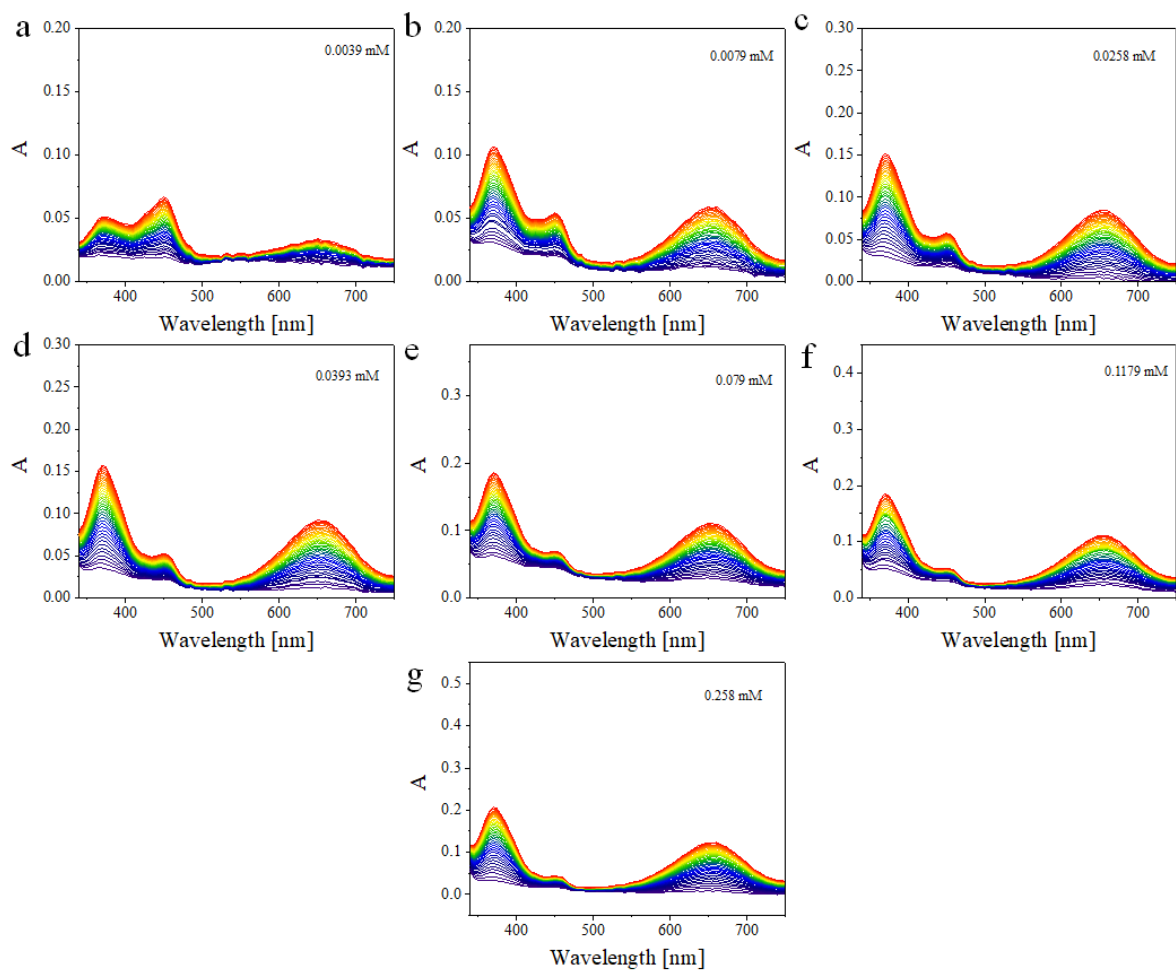
Figure 3-43. *Correpoonging of concentration-dependent absorption spectra of oxTMB by Pt@ZIF-8.*
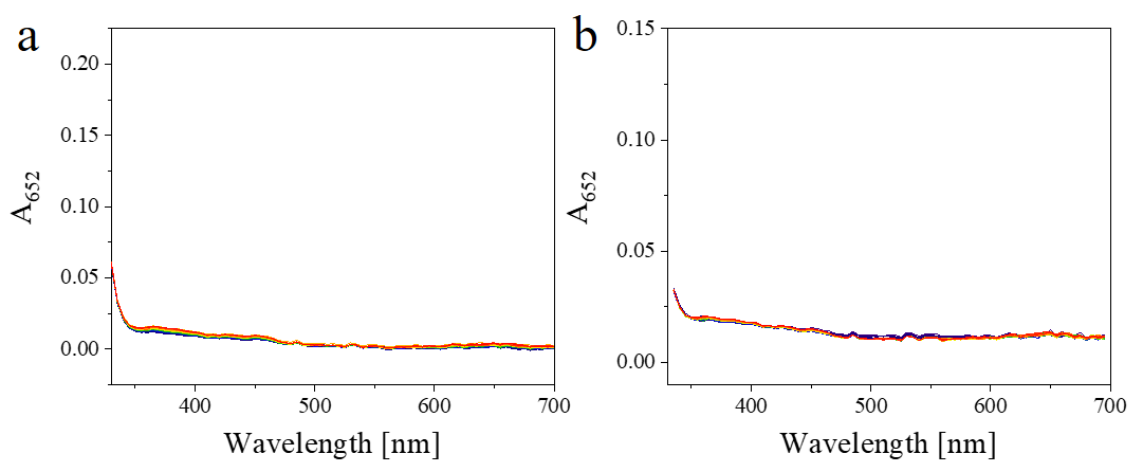
Figure 3-44. *Time-dependent absorption spectra upon the oxidation of TMB by Ag@ZIF-8 (a) and PtAgNPs-7 (b).*
The measurements were recorded in the presence of 0.236 mM TMB.

Table 3-2. *Comparison of the kinetic parameters among different nanozymes for various enzyme mimics.*

Enzyme mimicking	Nanozymes	Substrate	K_m [mM]	v_{max} [$\mu M\ s^{-1}$]	References
Peroxidase mimics	PtAgNCs-1	H_2O_2	56.5	0.060	This work
		OPD	0.231	0.033	This work
	PtAgNPs-7	H_2O_2	1714	0.067	This work
		OPD	0.284	0.023	This work
	Pt@ZIF-8	H_2O_2	162.5	0.027	This work
		OPD	0.304	0.040	This work
	Ag@ZIF-8	H_2O_2	364.7	0.002	This work
		OPD	4.60	0.009	This work
	HRP	H_2O_2	0.34	0.0948	[188]
		OPD	0.59	0.0465	[188]
Catalase mimics	PtAgNCs-2	H_2O_2	88.89	3.3	This work
	PtAgNPs-7	H_2O_2	163.62	0.232	This work
	Pt@ZIF-8	H_2O_2	186.72	0.98	This work
	Ag@ZIF-8	H_2O_2	652	0.33	This work
	catalase	H_2O_2	71.60	-	3
Oxidase mimics	PtAgNCs-1	TMB	0.017	3.14	This work
	PtAgNPs-7	TMB	**	**	This work
	Pt@ZIF-8	TMB	0.032	0.0121	This work
	Ag@ZIF-8	TMB	**	**	This work
	AuPtNPs	TMB	0.6	16.2	[189]
	Ch-PtNPs	TMB	0.018	-	[190]

3.2.3 Mechanism study

The catalytic mechanisms of noble metal-based nanozymes have been reported in many references, in which the two most possible mechanisms are the generation of radical intermediates ($\cdot$OH, $\cdot O_2^-$) and facilitating electron transfer.[176, 191] First, terephthalic acid (TA) was chosen as a fluorescence probe to detect $\cdot$OH. The reaction with $\cdot$OH yields a highly fluorescent product (2-hydroxy terephthalic acid).[192, 193] Gradual decrease of the fluorescence intensity at 425 nm was shown along with the increasing concentration of the PtAgNCs (**Figure 3-45**), indicating that the PtAgNCs consume the $\cdot$OH radical generated. The nature of the POD-like performance of the PtAgNCs did not due to the formation of $\cdot$OH radical. In addition, the PtAgNCs showed the ability to reduce the $\cdot$OH concentration by catalyzing the decomposition of H_2O_2, implying the CAT-like activities of PtAgNCs, as discussed above. Furthermore, another fluorescence probe, dihydroethidine (HE), was added into O_2-saturated buffer solution to detect $\cdot O_2^-$ for the OD-like activities of PtAgNCs. HE is a specific fluorescence probe for $\cdot O_2^-$ radicals, with an definite fluorescent emission wavelength at 610 nm (**Figure 3-46**). No distinct fluorescent emission at 610 nm was observed for both pH 4 and pH 7 buffer solutions, emphasizeing very limited $\cdot O_2^-$ formation under these conditions (**Figure 3-46**). Previous reports have presented the intrinsic OD-like activity of Pt-based materials serving as an enzyme, facilitating the electron transfer process when electron acceptor (here dissolved oxygen) and electron donor (here TMB) were adsorbed on the surface.[194] For this reason, the nature of the enzyme mimics catalytic behavior of PtAgNCs does not originate from the generation of $\cdot$OH or $\cdot O_2^-$ radical, and it most likely because of their ability to accelerate the electron-transfer process between the substrates and H_2O_2 or O_2.[195]
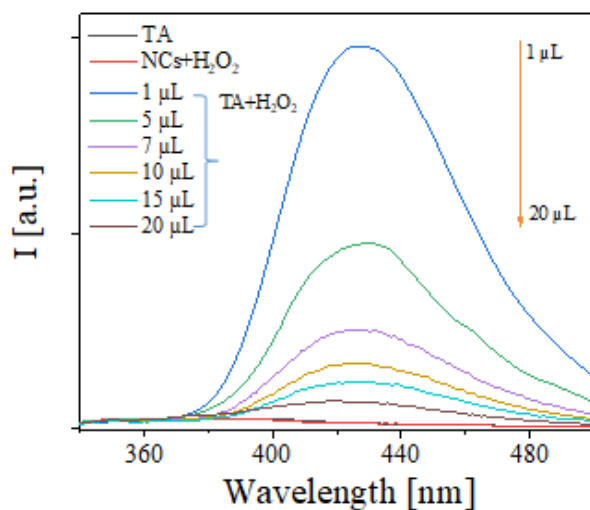
Figure 3-45. *The effect of the PtAgNCs on the formation of hydroxyl radical (·OH) with TA as fluorescence probe. The fluorescence spectra were recorded with excitation wavelength at 315 nm and emission wavelength at 425 nm.*
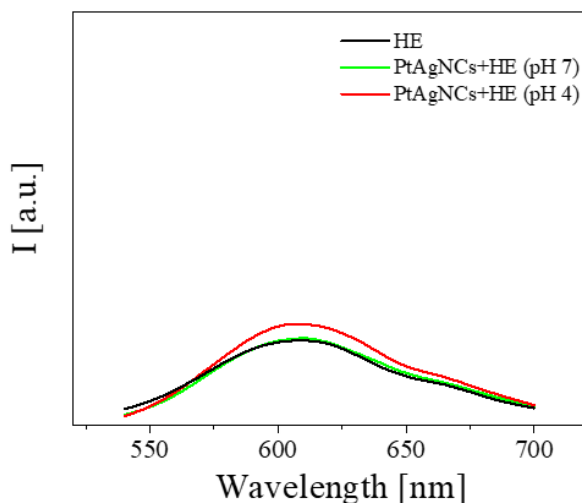
Figure 3-46. *Detection of superoxide radical (·O_2^-) with fluorescence probe HE, excited at 510 nm.*

Previous reports suggested that the surface defects were active sites regarding the catalysis of different nanomaterials (metal, metal oxides). Thus, possible mechanisms are illustrated in **Figure 3-47**. For POD-like mimetics, H_2O_2 molecules were first adsorbed on the surface defects of PtAgNCs, which were then split into two OH_{ad} (the subscript marks the surface-adsorbate species) as the H_2O_2 prefers base-like decomposition process under acidic conditions.[196, 197] Thereafter, ·OH intermediates can form H_2O and O_{ad} on the surface defects, and thus the direct oxidation of substrates (i.e., OPD) by these OH_{ad} and O_{ad} species occurred. In the end, the colored products could be confirmed by the UV-vis spectra. It should be

noted that most of the generated ·OH was consumed on the surface of nanozymes; thus terephthalic acid cannot react with the ·OH radical in the solution as discussed before. The CAT-like catalytic mechanism is based on the formation and accumulation of O_{ad} on the surface defects, yielding O_2 subsequently.[197] The mechanism for the OD-like mimicking activity of PtAgNCs is proposed to be the dissolved oxygen which was adsorbed onto the surface defect of PtAgNCs along with the substrate TMB. Dissolved oxygen acts as electron acceptor which was reduced to H_2O by a four-electron oxygen reduction process. Meanwhile, the electron donor TMB can be oxidized to form oxTMB. This result is in agreement with most other studies dedicated to OD-like mimics, as neither H_2O_2 (**Figure 3-48**) nor intermediates radicals could be detected during the reaction.[194, 198]
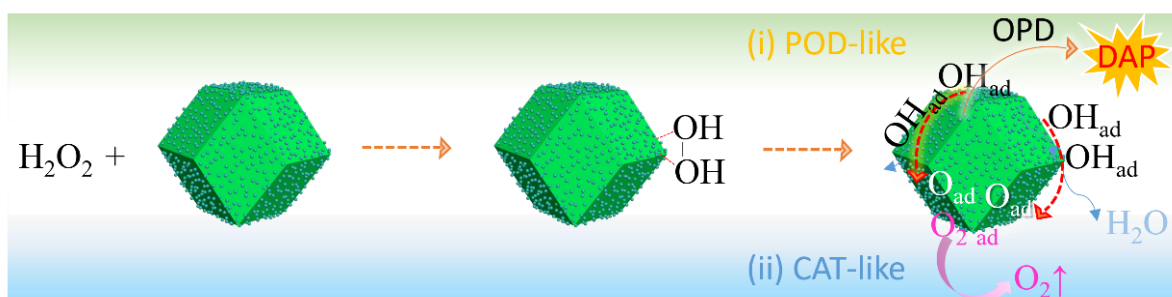
Figure 3-47. *Possible mechanisms proposed after evaluating the enzyme mimicking studies of PtAgNCs.*
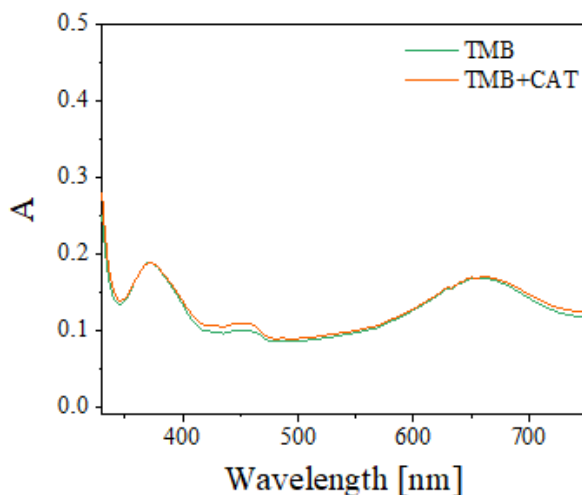
Figure 3-48. *UV-vis spectra of the oxTMB catalyzed by PtAgNCs-1 in O_2-NaAc-HAc buffer in the presence and absence of CAT.*

4 Plasmon enhancement of AuNCs sensing with photoelectrochemical (PEC) platform

4.1 Introduction and aim of the work

The PEC sensor has gained increasing attention because of its high sensitivity compared to traditional electrochemical process, due to its low background influence, and the ease, simplicity and affordablility of its apparatus. For the PEC, a photoactive catalyst is essential to couple to the electron transfer reactions at the photocatalyst-electrolyte interface. The properties of this photoactive catalyst is directly related to the photocurrent intensity. QDs have been extensively used as photoactive materials thanks to their unique electronic and optical features. Recently, low-toxic and biocompatible AuNCs with discrete energy levels have been found to possess many fascinating semiconductor-like characters. Similar to semiconductors or QDs, AuNCs have been proved to have good photostability and photocatalytic features, which demonstrated that AuNCs have promising potentials of replacing QDs in obtaining stable photocurrent for PEC bioanalysis.[68, 69] However, because the AuNCs only adsorbs light lower than 500 nm wavelength, pure AuNCs cannot offer enough photo-induced electrons due to the low charge separation efficiency under visible light. Hence, it is essential to enhance the photoelectric properties of AuNCs.

Recently, plasmonic metals (such as Au, Ag, and Cu) nanostructures have been coordinated with semiconductors to enhance PEC response,[199-201] mainly consisting of distance-dependent surface SPR, and excited energy transfer (EET) effects induced direct plasmon-improvement. It has been found that the strong plasmon resonances of plasmonic NPs can efficiently improve the catalytic activity of nearby catalysts. For example, it has been demonstrated that plasmonic NPs can enhance the activity of photocatalytic water splitting, the reduction of CO_2 for generating hydrogen fuels, and the degradation of organic molecules.[202] However, the underlying mechanism for enhancement is still unclear.[203] Currently, three potential but competitive enhancement mechanisms are discussed (**Figure 4-1**): Mechanism A: enhancement of electron-hole (e^- - h^+) pair generation rate by local heating of NPs; mechanism B: enhancement of e^- - h^+ pair generation rate by the NP-mediated strong electric field enhancement of NPs; mechanism C: hot electron injection from NPs to adjacent catalysts.[203-205] In this mechanism, the light-induced charge-carriers (electron or holes), formed on the surface of NPs, transiently occupy energetically accessible CB or LUMO of the adjacent catalysts before their energy is dissipated into phonon modes of NPs, thus the reaction is induced by the actions of these energetic charge-carriers.[204]
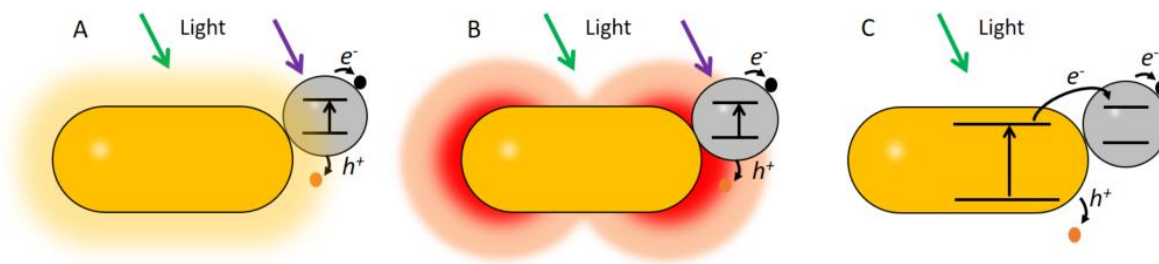
Figure 4-1. (A,B,C) Principal physical mechanisms of plasmon-assisted photocatalysis.

Recent experimental studies and theoretical calculations indicate that the formation of photo-induced energetic charge carriers is the probable main mechanism for reaction triggering and enhancement for semiconductors.[206-211] However, the enhancement mechanism is still open for discussion for bimetal nanostructures because charge transfer efficiency is very low due to the extremely short lifetime (fs) of energetic charges in a metal.[212, 213]

To date, few reports illustrated the plasmonic enhancement of the photoelectric properties of AuNCs. Systematic mechanism investigations upon the plasmon-enhanced photoelectric of AuNCs and further improved applications in the PEC-bioanalysis field are still challenging. In the last few decades, AuNRs have been paid attractive attention as plasmonic enhancers due to their modulatable optical properties. This endows AuNRs as interesting candidates for a variety of applications from photovoltaics to sensing.[214-217] Enormous efforts have been denoted to synthesize AuNRs with different length and width, as well as well-established methods offer opportunities to integrate them with other structures for further applications.[218, 219]

In this part, we demonstrated a plasmon-enhanced PEC sensing platform of AuNCs based on AuNRs as enhancer. We built the enhanced PEC platform (ePEC) in a layer-by-layer method and tested the photocurrent for revealing the enhancement phenomenon at different potential. Further, we focus on the enhancement mechanism of our ePEC platform by measuring the light power and wavelength-dependent photocurrent. More importantly, we show that our ePEC sensor is able to sense the H_2O_2 with good sensitivity.

4.2 Results and discussion

4.2.1 Characterization of nanomaterials

The Au NCs coated with glutathione (GSH) were prepared according to the previously reported method.[220]

The obtained absorption and fluorescence spectra of the Au@GSH NCs are shown in **Figure 4-2**. The UV-vis absorption spectra of the as-prepared AuNCs displayed a shoulder peak at ~ 400 nm, while no characteristic peak at ~ 520 nm of bigger AuNPs was observed (**Figure 4-2a**), which is in good agreement with the previous literature.[221] This molecular-like absorption of AuNCs might be due to their discrete electronic state. In addition, AuNCs exhibited strong orange fluorescence at ~ 605 nm with an excitation wavelength at 365 nm (**Figure 4-2b**), which is in agreement with the previous reports.[220]
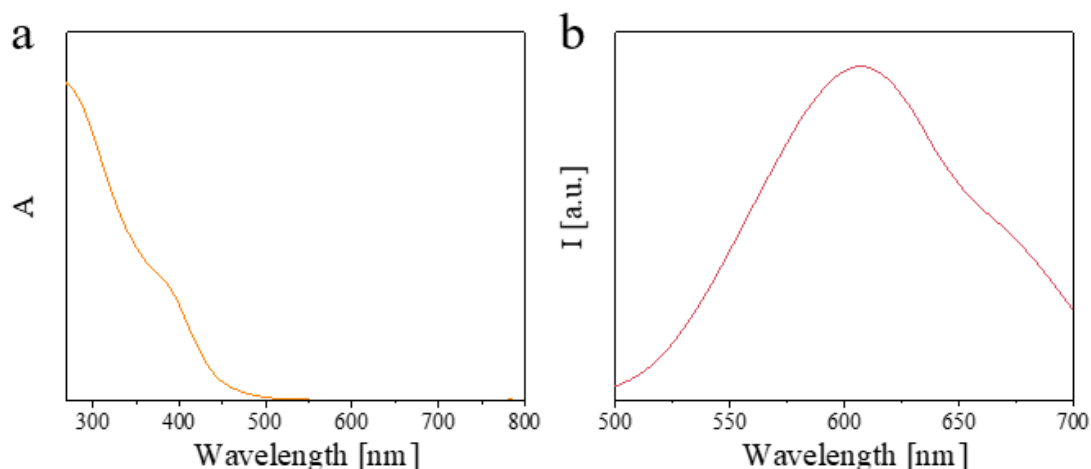
Figure 4-2. UV-vis absorption (a) and photoluminescence spectra (b, excited at 365 nm) of AuNCs.

The synthesis of AuNRs and AuNRs@SiO$_2$ is schematically illustrated in **Figure 4-3a**. The AuNRs were prepared via seed-mediated growth method according to a previous report.[219] The concentration of AuNRs used for the further SiO$_2$ coating were first measured by UV-vis absorption spectra and ICP-MS methods, showing a good agreement with both methods. For the SiO$_2$ coating, a (3-Aminopropyl) trimethoxysilane (APTMS) aqueous solution was added in the AuNRs solution for surface modification with -NH$_2$ group. After vigorous stirring for 10 min, Na$_2$SiO$_3$ aqueous solution was added and the mixture was left stirring overnight to obtain a thin silica shell. The morphology of the prepared AuNRs and AuNRs@SiO$_2$ was determined by TEM images. As shown in **Figure 4-3**, **b-d**, AuNRs with size of (39.46 ± 2.46 nm) × (20.27 ± 1.5 nm) and aspect ratio of ~1.95 were obtained. **Figure 4-3**, **e-f** represent Au NR with SiO$_2$ of 1.94 ± 0.31 nm. **Figure 4-3g** showed UV-vis absorption peaks of AuNRs at 525 and 611 nm, corresponding to the transverse localized surface plasmon resonance (LSPR$_t$) and longitudinal (LSPR$_L$) resonances, respectively. Because of the increase in the local refractive index of the surrounding medium after silica coating, it can be seen that the position of the longitudinal peak of AuNR@SiO$_2$ is broad.
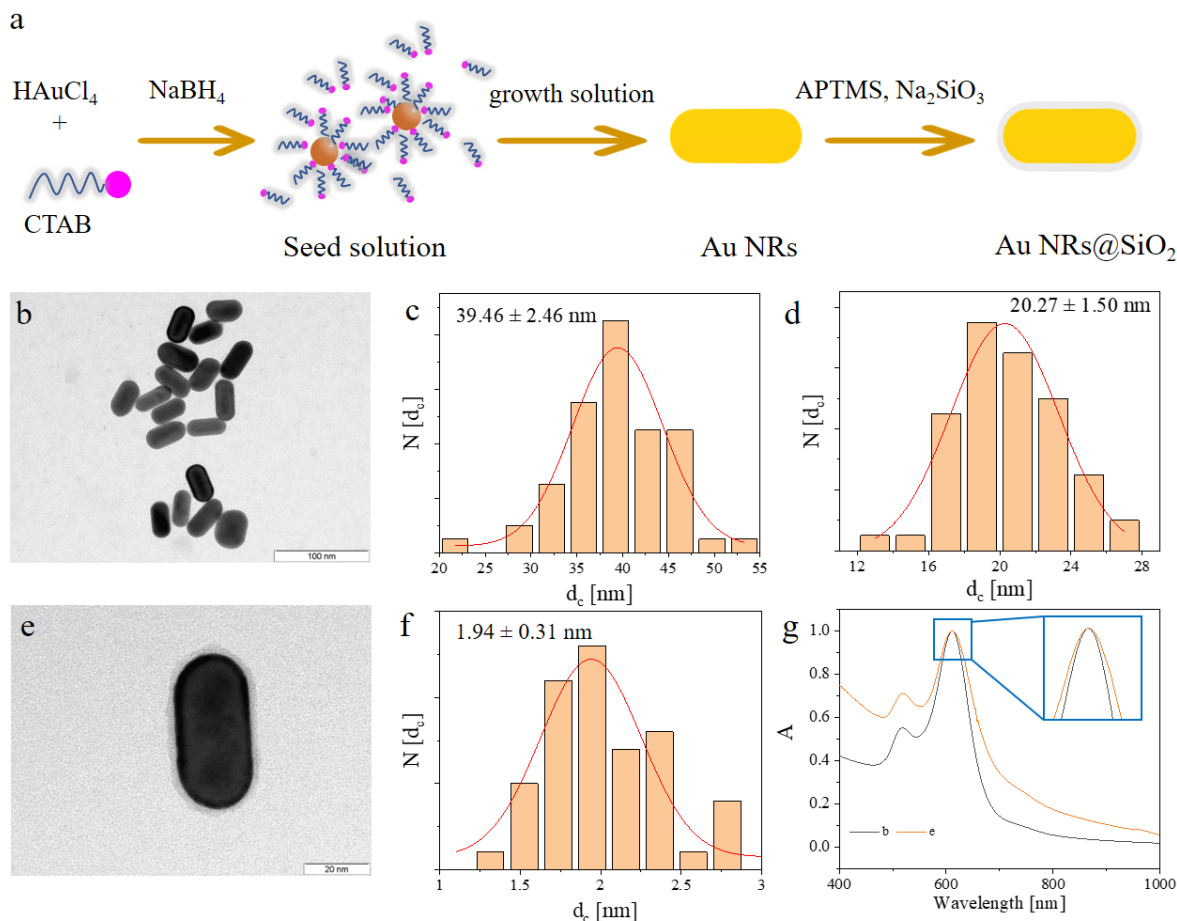
Figure 4-3. *Synthesis and characterization of AuNRs and AuNRs@SiO₂. (a) Schematic illustration of AuNRs and Au NR@SiO₂. (b-d) Typical TEM image and transverse and longitudinal size distributions of AuNRs. (e-f) TEM image of AuNR@SiO₂ and corresponding size distribution of silica with 1.94 ± 0.31 nm. (g) UV-vis absorption spectra of AuNRs and AuNRs@SiO₂. The TEM images of this figure were recorded by Mr. Stefan Werner.*

Furthermore, we used the zeta potential measurements to confirm the surface changes of our AuNRs and AuNCs, which can be used for further preparation of the PEC sensor. From the data in **Figure 4-4**, the as-synthesized CTAB-protected AuNRs exhibited a positive charge of 40.6 mV, which changed to a negative charge of - 30.0 mV originated from the silanol groups on the AuNRs surface. After -NH₂ functionalization, Au NR@SiO₂-NH₂ showed a positively charged potential of 20 mV because of the presence of amino groups on the surface. It can be seen that the zeta potential of Au NC@GSH was anegatively charged (- 12.9 mV), due to the carboxyl groups on the AuNCs surface.
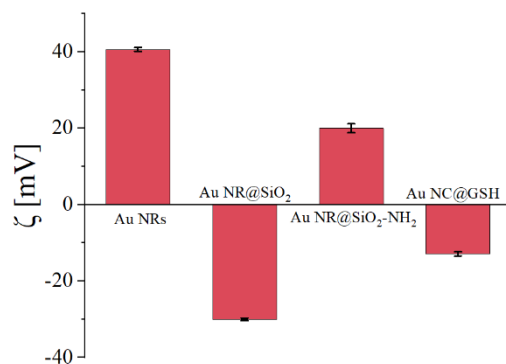
Figure 4-4. *Zeta potential (ζ) of AuNRs, Au NR@SiO₂, AuNRs@SiO₂-NH₂, and Au NC@GSH.*

4.2.2 PEC properties of AuNRs@SiO₂/AuNCs/SAM/Au electrodes

Figure 4-5 shows a schematic of the preparation process of ePEC platform. From bottom to up, we first modified the Au film electrode with a self-assembled molecule (SAM) layer by strong S-Au bonding. Here, a BDT molecule was introduced to be SAM as an insulator, which can hinter redox molecules to reach the gold electrode surface in the solution. Then a layer of AuNCs as catalyst was deposited on the SAM layer by spinning coating methods. At the end, the AuNRs@SiO₂ film was deposited on the AuNCs/SAM/Au-electrode surface through a floating transfer process to form the ePEC sensing platform, denoted as the AuNRs@SiO₂/AuNCs/SAM/Au sensor. In this ePEC system, the layer of AuNRs with spaces worked as enhancer to improve the photocurrent of the PEC property. The self-assembly AuNRs@SiO₂ monolayer was formed as follows: 1.5 mL of the as-prepared AuNRs@SiO₂ solution was first injected into a small plastic watch glass, and then 230 μL of hexane was added to form a liquid-liquid interface. Then, 1.8 mL methanol was injected to the mixture to capture the NRs between the two-phase interface. After the evaporation of hexane, the NRs spontaneously assemble into the golden monolayer film visible to the naked eye. To confirm the successful immobilization of AuNCs and AuNRs@SiO₂, the UV-vis absorption spectroscopy was used on the AuNCs and AuNRs@SiO₂ modified glass. The detailed method of this experiment is shown in **Figure 4-6a**. It can be seen that a typical absorption of AuNCs on glass was in good agreement with that in the aqueous solution (**Figure 4-6b**). The absorption spectra of solid-state AuNRs@SiO₂ show a slight difference with a broad peak compared to that in aqueous solution; this is due to the AuNRs@SiO₂ on the glass which was aggregated, unlike that in the solution (**Figure 4-6c**). These suggested the successful immobilization of AuNCs and AuNRs@SiO₂. **Figure 4-7** shows the SEM image of the ePEC sensor surface, indicating the distribution of AuNR@SiO₂ on the surface.
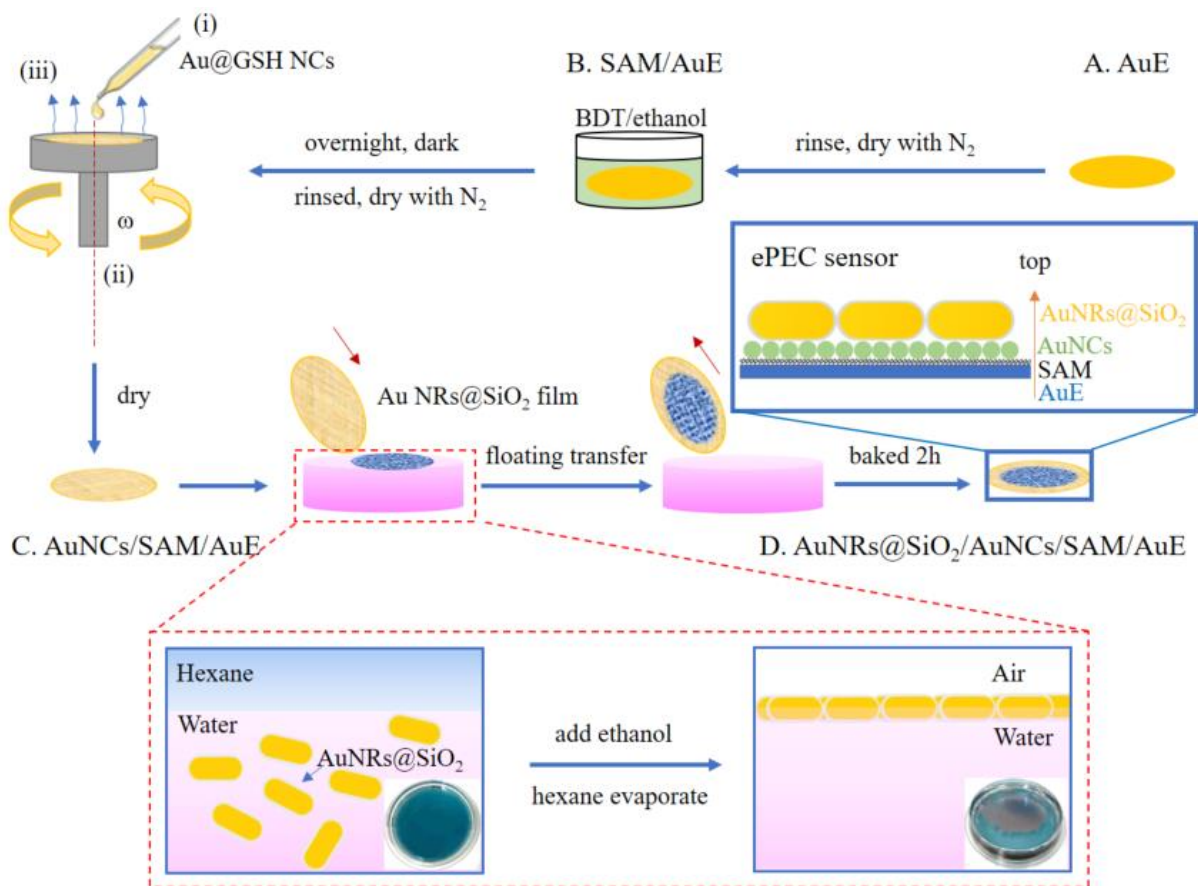
Figure 4-5. *Schematic illustration of the preparation of ePEC platform via a floating transfer process. The spinning coating process was used to immobilize the Au@GSH NCs, which consists of (i) deposition, (ii) rotating and (iii) evaporating step. Self-assembly of AuNRs@SiO$_2$ at water/hexane interface was formed by the addition of ethanol and the hexane evaporated (bottom row). The inset represented photographs of AuNRs@SiO$_2$ solution (left) and the AuNRs@SiO$_2$ monolayer formed at an air/water interface.*
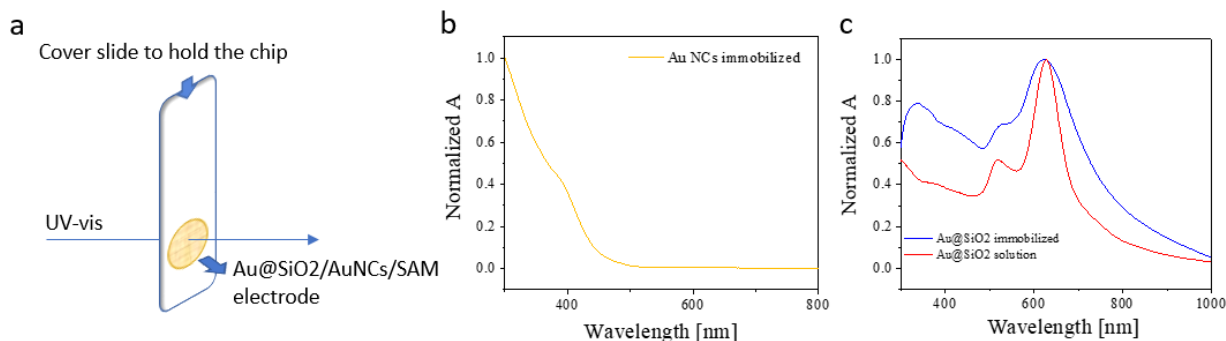
Figure 4-6. *Absorption measurement of AuNCs and AuNRs@SiO$_2$/AuNCs/SAM electrode. (a) A sketch of the absorption measurement of PEC electrode. (b-c) The normalized absorption spectra of immobilized AuNCs (b) and AuNRs@SiO$_2$ (c) on chip in comparison with those in solution.*
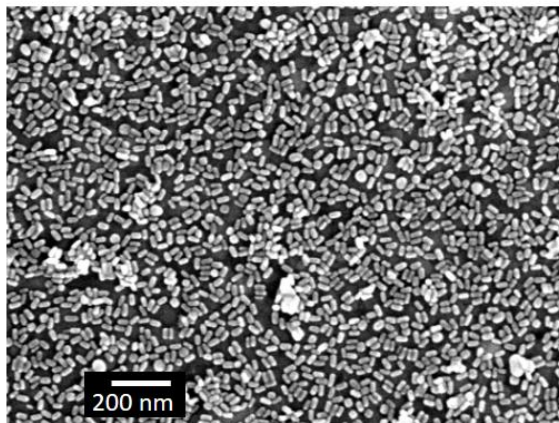
Figure 4-7. SEM image of ePEC sensor. The SEM image of this figure was recorded by Department of Chemistry, University of Hamburg.

A model diagram of the ePEC platform is shown in **Figure 4-8**. This platform consisted of two parts: the first part is a traditional PEC platform based on semiconductor or nanocluster on an Au electrode with a SAM as insulator;[68] the other part is a layer of AuNRs@SiO$_2$, which enhances the photocurrent of the PEC. In a traditional PEC, AuNCs are used as photoelectrocatalyst to induce photocurrent upon light illumination, as they have a similar bandgap structures to the one of the QDs.[68] The PEC sensing mechanism for traditional PEC has been verified: without light illumination, the insulating SAM prevents the electron transfer between the Au electrode and the analyst in the solution, and no photocurrent can be observed in this case. Upon light illumination, the light induces the charge separation within the AuNCs to form e$^-$ - h$^+$ pairs. When a negative potential is applied to the Au electrode, the electron in the Au electrode transfers through the thin insulating SAM layer into the HOMO to recombine with the photoinduced holes of Au (Kb). Also, when a positive potential is applied, the photoinduced electron of AuNCs transfers from the LUMO to the Au electrode (Ke). Analytes such as reducers (R) or oxidizers (O) in solution will react with the photo-induced holes or electrons. The electron tunneling processes among different interfaces yields to observable photocurrents.

In the ePEC sensor proposed here, plasmonic AuNRs@SiO$_2$ is introduced on the top of the AuNCs layer. The silica coating applied here is to avoid the direct touching between the An NCs and AuNRs as the direct touching would make the Au NC lose its molecular band gap structures and behave as a conductor.
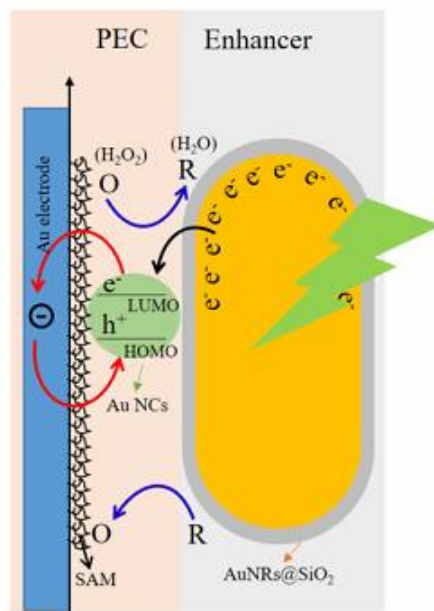
Figure 4-8. *A model diagram of the ePEC sensing system.*

To determine the plasmon enhanced PEC characteristics of the AuNRs@SiO$_2$ on AuNCs, which modifies on the Au, we tested the sensor chips under different conditions in PBS solution without H$_2$O$_2$. The modified Au electrodes are illuminated upon white light, whose photocurrent were induced under different applied potentials (E′) in the range of - 0.6 to + 0.6 V versus Ag/AgCl electrode with and without light illumination. As shown in **Figure 4-9**, anodic and cathodic background photocurrents with different amplitudes can be observed when applying different positive and negative bias potentials, respectively. In the PBS case without the addition of other effective oxidizers or reducers, the background photocurrents were arising from the redox reaction of the less active ions and dissolve oxygen in PBS solution.

The results in **Figure 4-9b** also show that the AuNRs@SiO$_2$/AuNCs/SAM/Au electrodes exhibit larger photocurrent under all applied potential than those of AuNCs/SAM/Au electrodes, suggesting that the photocurrent enhancement arises from the introduction of AuNRs. Further control experiments of the PEC measurement on the AuNRs@SiO$_2$/SAM/Au electrodes show - 3.9 nA at − 0.6 V, much smaller photocurrent amplitudes than AuNRs@SiO$_2$/AuNCs/SAM/Au (- 20.3 nA at − 0.6 V), further demonstrating that the photocurrent enhancement is not caused by the PEC process of AuNRs. In addition, the PEC properties of AuNRs/AuNCs/SAM/Au electrodes exhibite small photocurrent of - 3.6 nA (at − 0.6 V) compared to AuNCs/SAM/Au electrodes (- 10.5 nA at − 0.6 V) and AuNRs@SiO$_2$/AuNCs/SAM/Au electrodes (- 20.3 nA at − 0.6 V), implying that the silica layer is

important to avoid short circuiting and loss of photocurrent. The enhanced photocurrent is a combined effect of the AuNCs and AuNRs.

Next, to determine the underlying mechanism of the photocurrent enhancement, the photocurrent responses to various light power and light wavelength were tested on the ePEC platform. **Figure 4-10a** shows the light illumination power dependence of the photocurrent, an increase in the photocurrent with the increasing in the illumination power was observed. More importantly, the photocurrent of AuNRs@SiO$_2$/AuNCs/SAM/Au electrodes shows a super-linear dependence at high illumination power. This super-linear behavior suggests a charge-carrier driven photochemical reaction mechanism on the enhanced PEC platform (Mechanism C).[210, 222, 223] Several publications interpret a super-linear response of reaction rates to increasing light intensity as a hallmark of charge-driven chemistry.[208] In photocatalysis, the dependence of the reaction rate (v) on light intensity (I_{light}) can be described by the following relationship: $v \propto I_{light}^n$, where n is the number of the electron transfer.[223] Here, $I_{light} \propto P$ (P is the light power), since the same electrode area was used for all the measurements. We fitted our data with the equation $I_{current} = A + C*P^n$, where A is a light-independent term. The resulting curve fits well with our data and gives n = 3.1, indicating the reaction is induced by a multiple electrons transfer.

Furthermore, illumination-wavelength dependence of photocurrents was measured and the results are shown in **Figure 4-10b**. Two peaks (525 nm and 615 nm) were found in the current-wavelength curve, corresponding to the two peaks in the absorption spectrum of AuNRs@SiO$_2$. This means that the photocurrents are strongly related to the optical properties of AuNRs@SiO$_2$. Based on this dependence, the electron transfer mechanism (Mechanism C) can be further verified: since the absorption of AuNCs is placed at the wavelength of smaller than 500 nm (**Figure 4-2**), at the excitation of a wavelength more signficant than 500 nm, the AuNCs are not excited, meaning that no charge separation occurs in this case. Mechanism A and B can only enhance the charge separation but it cannot trigger the reaction. In the mechanism C, the charge separation starts from AuNRs and then transfers to the nearby AuNCs, leading to the photocurrent. Another interesting observation is that we found the photocurrent at 525 nm being larger than that at 615 nm, indicating that the strong local field does not automatically generate a high photocurrent. Similar observations have been made in previous photocurrent studies of AuNRs,[224] in which the quantum efficiency of the LSPR$_L$ mode was lower than that of the LSPR$_T$ mode.
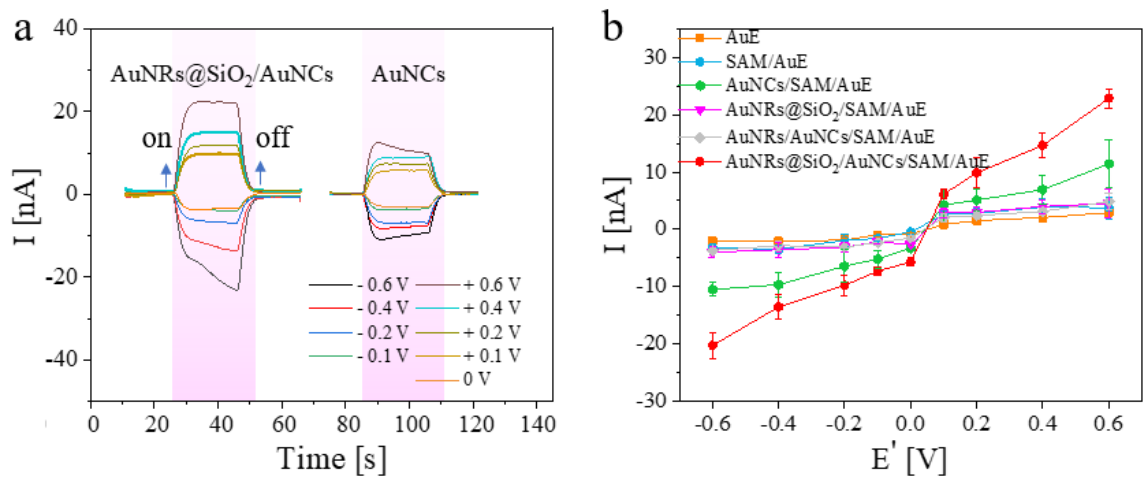
Figure 4-9. *Photocurrent of different AuNRs, AuNRs@SiO₂ and AuNCs modified Au electrode. (a) Photocurrent trace I(t) AuNCs/SAM/Au, and AuNRs@SiO₂/AuNCs/SAM/Au electrodes. (b) Photocurrent amplitude in dependent of the applied E' for Au, SAM/Au, AuNCs/SAM/Au, AuNRs@SiO₂/SAM/Au, AuNRs/AuNCs/SAM/Au and AuNRs@SiO₂/AuNCs/SAM/Au electrodes. These measurements are collected in 0.01 M PBS buffer (pH 7.4). Error bars represent the standard deviation of three measurements.*
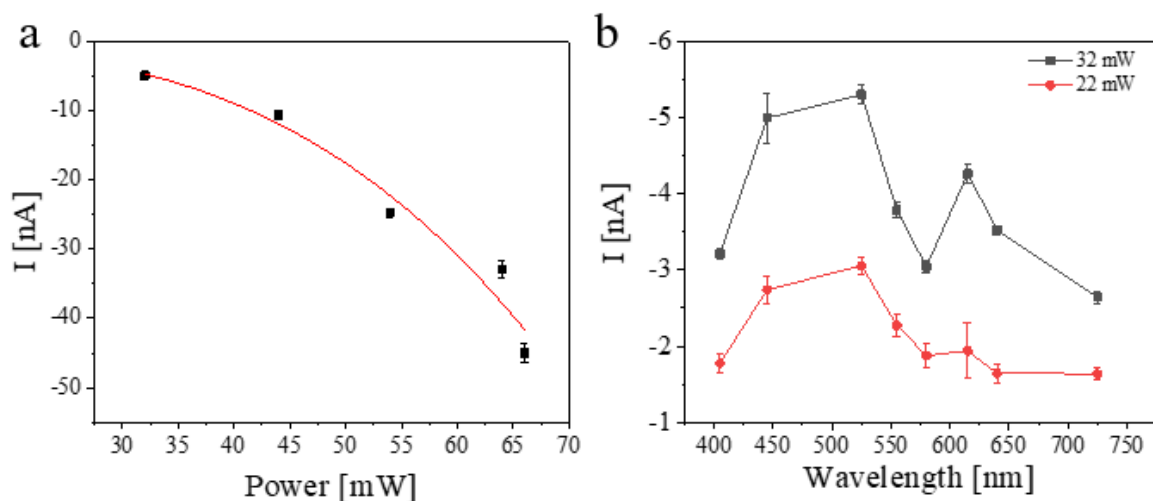
Figure 4-10. *Power-intensity dependence and wavelength dependence of AuNRs@SiO₂/AuNCs/SAM/Au electrodes. The photocurrent (I) in dependence of the power intensity of white light (a) and the different wavelengths (b). These measurements are collected in 0.01 M PBS buffer (pH 7.4) at - 0.2 V. The different wavelengths were measured by white light with different filters. The light intensity of all wavelengths was adjusted using a powermeter at a fixed power for each wavelength.*

4.2.3 AuNRs@SiO₂/AuNCs/SAM/Au sensing performances towards H₂O₂

decomposition

In order to illustrate the sensing potential of this reported ePEC sensor, H_2O_2 decomposition was chosen as a model reaction. We used the white light as an emission source and fixed the emission power at 44 mW for all measurements. A previous study indicated that H_2O_2 decomposition can be detected by the AuNCs -based PEC system under negative potential.[68] In this work, we applied different negative potentials (- 0.1, - 0.2, - 0.4 and - 0.6 V vs Ag/AgCl) on the PEC platform to probe the H_2O_2. To confirm the H_2O_2 decomposition on our AuNRs@SiO$_2$/AuNCs/SAM/Au electrodes, the photocurrent from the PEC measurements were recorded in the absence and presence of H_2O_2. As shown in **Figure 4-11**, an obvious increased photocurrent was observed after H_2O_2 infection, indicating that AuNRs@SiO$_2$/AuNCs/SAM/Au electrodes can be used to detect the H_2O_2. The negative photocurrent amplitude of the ePEC sensor increased in the presence of H_2O_2, indicating the reduction of the H_2O_2 to form H_2O. The reaction pathway can be easy to be established following the charge-transfer mechanism (**Figure 4-8**): under illumination, the photo-induced electrons, where formed from the excitation of AuNRs, transfer to the HOMO of AuNCs and then will reduce the oxidant H_2O_2 to H_2O, which is catalyzed by AuNCs; the photo-induced holes will recombine with the electrons, where from the Au electrodes. At the same illumination condition and applied potential, the number of photo-induced electrons is the same, so the photocurrents are depending on the H_2O_2 concentration. Thus we could detect the H_2O_2 concentration by measuring the enhancement photocurrent.

To demonstrate the enhancement ability of the ePEC sensor, the photocurrent traces of AuNRs@SiO$_2$/AuNCs/SAM/Au and AuNCs/SAM/Au electrodes on H_2O_2 concentration and applied potential were characterized. As shown in **Figure 4-12**, the sensing sensitivity increased with the applied potential increasing both for ePEC and PEC electrode, and the best limit of detection (LOD) is 9.1 µM at - 0.6 V for ePEC sensor (**Figure 4-12a**). This is because a higher potential indicates a greater ability to separate the electron-hole pairs. More importantly, it can be seen that at all potentials for all concentrations, the photocurrents observed from ePEC sensor are much larger than of the traditional PEC sensor, such as at - 0.6 V, the LOD of ePEC is almost 9.3 times higher than the PEC of 84.2 µM, indicating the obvious enhancement of out ePEC platform (**Figure 4-12b**). The enhancement in photocurrent suggests the sensing activity is enhanced by introducing plasmonic metals.
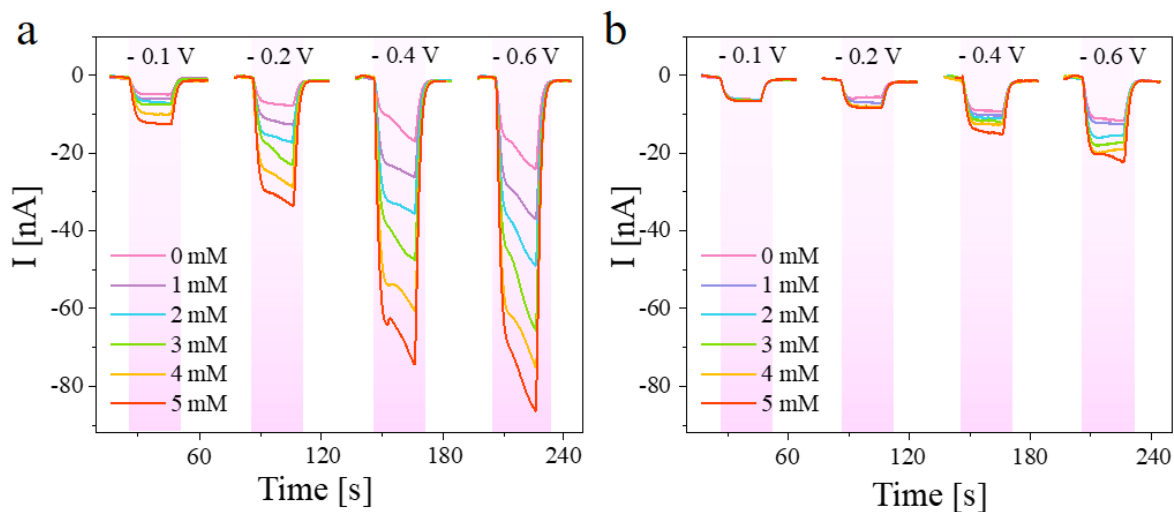
Figure 4-11. *Photocurrent trace I(t) of AuNRs@SiO₂/AuNCs/SAM/Au (a) and AuNCs/SAM/Au (b) electrodes for sensing H₂O₂. Different applied E' of - 0.1, - 0.2, - 0.4, - 0.6 V in the presence of increased H₂O₂ concentration. These measurements are collected in 0.01 M PBS buffer (pH 7.4).*
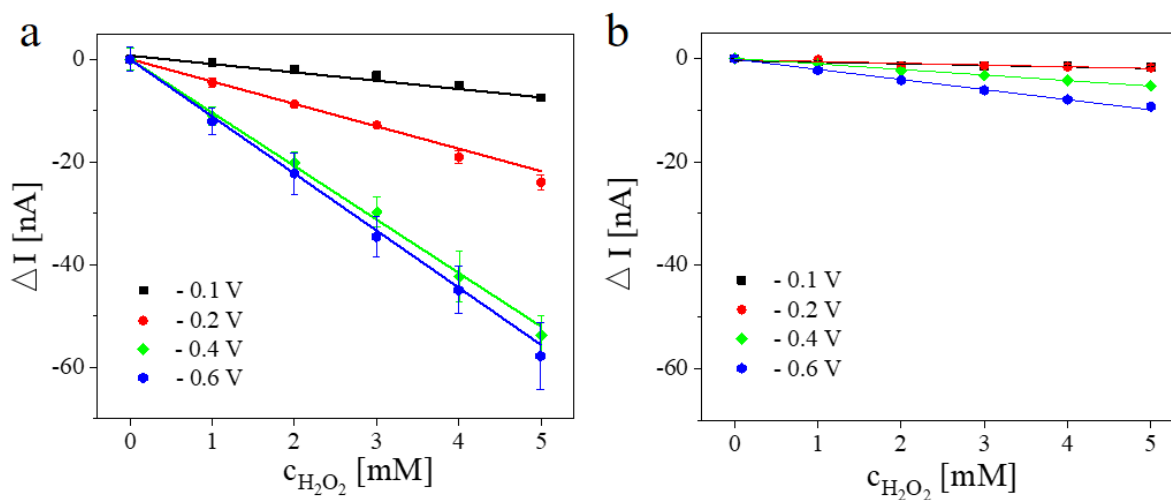
Figure 4-12. *The dependence of increased photocurrent (I) of AuNRs@SiO₂/AuNCs/SAM/Au (a) and AuNCs/SAM/Au (b) electrodes on H₂O₂ concentration and applied E'. These measurements are collected in 0.01 M PBS buffer (pH 7.4). Error bars represent the standard deviation of three measurements.*

5 Conclusion and outlook

Noble metal NCs (such as Pt, AuNCs.) possess unique physical and chemical properties, making them competitive candidates in a wide application field, such as electrocatalysis, photo(electro)chemical, energy conversion, nanomedicine. This thesis focuses on the synthesis of noble metal NCs materials and their applications in catalysis, electrocatalysis, enzyme mimics, photoelectrochemical analysis and others. The main contents and conclusions of the research are as follows:

1. We synthesized ligand-free PtNCs by using the template of ZIF-8, denoted as PtNCs@ZIF-8. From the EM images, the homogeneous distribution of PtNCs was observed with an average core diameter of $d_c = 1.86 \pm 0.20$ nm. Meanwhile, the shifts of the high-resolution XPS spectra of N 1s and Zn 2p, and the FTIR spectra were confirmed the interaction of PtNCs and ZIF-8 template. We can predict the PtNCs formation mechanisms, in which the unsaturated Zn and free N^- extremities on the external surface of ZIF-8 or at defects can hold the Pt precursor ($PtCl_4^-$) where NC nucleation initiates during the *in situ* reductions. In the meantime, when optimizing the parameter during the synthesis, the concentration of the $PtCl_4^-$ influences the distribution of PtNCs in ZIF-8. To evaluate the catalytic potential of this catalyst, the reduction reaction upon the catalytic 4-NP was applied, the mass activity parameter and activation energy of which was be 1.29×10^2 s^{-1} g^{-1}, and $E_a = 15.1$ kJ mol^{-1}, respectively, indicating the high catalytic activity compared to those of previous reports. Furthermore, HER tests show that Pt-2@ZIF-8 have a much small E_η of 1.4 mV and larger SA, MA parameters compared to other Pt-based catalysts, suggesting the better HER activity of our catalysts. We speculate that the high catalytic performance maybe due to the smaller size, ligand-free of PtNCs. In addition, ORR catalytic performance of Pt@ZIF-2 was also carried out, showing a similar Tafel slope in comparison with the commercial 20 wt.% Pt/C catalyst. Moreover, these PtNCs can be extracted to both aqueous and non-aqueous solvents. This study and finding provides a rapid synthesis method to prepare efficient catalyst and offer avenues to obtain homogenous PtNCs for further applications.

2. Based on the previous research, we prepared a PtAg alloy with the previously modified method. Two different protocols of (I) co-reduction (II) Pt-guided methods were applied to obtain larger PtAg NPs ($d_c = 9.10 \pm 2.31$ nm) and smaller PtAgNCs ($d_c = 1.78 \pm 0.12$ nm) in ZIF-8, respectively, confirmed by EM images. Further characterization of PXRD further indicated that the non-visible, additional features in PtAgNCs case were probably due to the incorporation of PtAgNCs with Pr-imidazole groups of ZIF-8, unlike the PtAgNPs case formed outside of the ZIF-8 with intact peaks compared with those of pristine ZIF-8. This is consistent with the TEM and FTIR results. Furthermore, enzyme mimicking properties of both PtAgNPs and PtAgNCs catalysts were investigated by the oxidation of OPD in the presence of H_2O_2, decomposition of H_2O_2, and the oxidation of TMB in the presence of dissolved oxygen, representing POD- ,

CAT- and OD-like activities, respectively. These findings show that the PtAgNCs possess more efficient enzyme-mimicking properties than those of PtAgNPs, pure Pt@ZIF-8 and other nanozyme catalyst reported previously, further indicating the enhanced catalytic performance may originate from the synergistic effect from the addition of Ag element. Further mechanism studies showed that the nature of the enzyme mimics behaviors of PtAgNCs may be due to their ability to accelerate the electron-transfer process between the substrates and H_2O_2 or dissolved O_2.

3. We demonstrated a plasmon-enhanced PEC sensing platform of AuNCs based on AuNRs as an enhancer to sensor H_2O_2. The enhanced PEC platform (ePEC) was built in a layer by layer method, and its PEC performance was tested for revealing the enhancement phenomenon at the different potentials in PBS solution. We observed a larger photocurrent enhancement after the enhancer (AuNRs@SiO$_2$) introduction and verified that the enhancement mechanism results from energetic changer transfer from the AuNRs to the nearby AuNCs by measuring the response of photocurrents to light power and wavelength dependent. More importantly, compared to traditional PEC method, the reported ePEC platform presents enhanced sensing ability toward H_2O_2, suggesting a strategy that using the plasmon of the plasmonic metals to enhance the sensing ability of the PEC sensors. To offer more proof for the sensing possibility of ePEC sensor, we are going to measure other redox species such as catechol, ferrocene or Ru-hexamine complexes. which are also important for biosensing and biochemical applications.

In summary, we conducted a systematic study related to the synthesis of noble metal NCs (Pt, PtAg, and Au) and the applications in the areas of catalyst, electrocatalysis, enzyme mimics as well as photoelectrochemistry. The small size PtNCs in ZIF-8 not only exhibit improved catalytic properties but also reduce the cost of the Pt-based catalyst. The alloy PtAgNCs show advanced enzyme mimics performance. The plasmon enhanced PEC sensing properties were investigated on AuNCs-based sensor incorporated with AuNRs@SiO$_2$, showing the potential of sensing H_2O_2. In future research work, while exploring the maximal photocurrent with different silica thickness of AuNRs@SiO$_2$, it is necessary to figure out the plasmon enhanced mechanism. In the meanwhile, thetheoretical experiment was also carried out for further mechanism investigation. Once it is clear, the various use of the plasmon-enhanced AuNCs sensor can go further.

6 Appendix

6.1 Materials

Zinc nitrate hexahydrate (Zn(NO$_3$)$_2$·6H$_2$O, 99%), 2-methyl imidazole (2-MeIM, 98%), chloroplatinic acid hexahydrate (H$_2$PtCl$_6$·6H$_2$O, 99%), silver nitrate (AgNO$_3$, ≥ 99%), sodium borohydride (NaBH$_4$, > 98%), sodium hydroxide (NaOH, > 98%), glutathione (GSH), dodecanethiol (DDT, ≥ 98%), dichloromethane (DCM, ≥ 99.8%), dimethyl sulfoxide (DMSO, > 98%), tetrahydrofuran (THF, ≥ 99.9%), chloroform (CHCl$_3$, ≥ 99.5%), N,N-dimethylformamide (DMF, ≥ 99.8%)，o-phenylenediamine (OPD, 98%), 3,3′,5,5′-tetramethyl benzidine (TMB, > 99%), catalase (CAT), tri-sodium citrate dihydrate (99%), citric acid (99.5%), acetic acid (HAc, ≥ 99%), monosodium phosphate (NaH$_2$PO$_4$, ≥ 99%), disodium hydrogen phosphate (Na$_2$HPO$_4$, ≥ 99%), sulfuric acid (H$_2$SO$_4$, 95-98%), sodium acetate (NaAc, ≥ 99%), terephthalic acid (TA, 98%), and hydroethidine (HE, ≥ 95%), 1,4-benzenedithiol (BDT, 99%), (3-Aminopropyl) trimethoxysilane (APTMS, 99%), cetrimonium bromide (CTAB, ≥ 98%), ascorbic acid (AA, ≥ 99%), sodium salicylate (≥ 99.5%), sodium silicate (Na$_2$SiO$_3$, 27%), hexane (anhydrous, 95%), gold(III) chloride hydrate (HAuCl$_4$·xH$_2$O, 99.995%), tetraethyl orthosilicate (TEOS, 98%) and Nafion solution (5 wt.%) were purchased from Sigma-Aldrich. Potassium tetrachloroplatinate (II) (K$_2$PtCl$_4$, ≥ 99.9%) was obtained from Alfa Aesar. Methanol (anhydrous, 98%), ethanol (≥ 99.8%), hydrochloric acid (HCl, 37%), nitric acid (HNO$_3$, 70%), perchloric acid (HClO$_4$, ~ 70%), acetone (≥ 99.9%), hydrogen peroxide (H$_2$O$_2$, 30% in H$_2$O) and toluene (≥ 99.8%) were obtained from Carl Roth. 0.01 M pH 7.4 Phosphate-buffered saline (PBS) was purchased from ThermoFischer. Carbon black BP 2000 was purchased from Asian-Pacific Specialty Chemicals Kuala Lumpur. Cover glasses (12 mm, round) were purchased form VWR. All chemicals were used as received and without any further purification. Before the nanoparticles synthesis, all glassware and stirrer bars were cleaned carefully in aqua regia (3:1 *v/v* HCl:HNO$_3$) solution and then rinsed thoroughly with Milli-Q water before use. All the aqueous solutions were prepared by using deionized Milli-Q water (18.2 MΩ).

6.2 Instrument

The successful preparation of different NCs, NCs/NPs@ZIF-8, NRs, as well as their functional modification was discussed in this work, confirmed by using various spectroscopic measurements.

The size and morphology of different samples used in this work are measured using TEM (Philips CM 300 UT, JEOL JEM 1011 (100 kV), and JEM 2200 FS). JEM 2200 FS is a versatile TEM equipped with a scan generator, which also enables scanning transmission electron microscopy (STEM) studies, that is, it can be used in high-resolution imaging of both TEM and STEM modes. Elemental analysis was recorded via energy-dispersive X-ray spectroscopy (EDS) with an energy dispersive X-ray detector at 200 kV

accelerating voltage. All TEM samples were prepared by placing a drop of the final diluted suspension on a carbon-coated copper grid (300 - 400 mesh square) and were left to dry in the air. SEM images of the PEC sensor were measured by using LEO 1550 (Zeiss, 30 kV).

X-ray photoelectron spectroscopy (XPS) analysis of NCs/NPs@ZIF-8were measured by an AXIS Ultra DLD (Kratos Company) with a monochromic Al X-ray source.

Porosity parameters of NCs@ZIF-8 and ZIF-8 were measured by N_2 adsorption-desorption at 77 K curves obtained from Quantachrome Autosorb-iQ Instrument.

TGA analysis was carried out simultaneously with N_2 atmosphere using a DSC/TGA SDT 650 (TA Instrument). For this purpose, ca. 2.5 mg of each sample was filled into a clean alumina crucible and was heated in the N_2 flow with a ramp rate of 10 °C min^{-1} from 25 – 900 °C.

FTIR spectra of these materials were carried out on an Agilent Cary 630 FTIR at 0.4 cm^{-1} resolution by using a diamond detector for the range of 4000 – 650 cm^{-1}.

The Powder X-Ray diffraction (PXRD) experiments were conducted with Powder Diffractometer Panalytical MPD X'Pert (Philips) using Cu $K\alpha$ as radiation (0.154056 nm) in the 2θ range of 5-60°with scanning rate of 0.0334225°/s.

The ultraviolet-visible (UV-vis) spectroscopy was used to measure the extinction spectrum of the samples, recorded with an Agilent 8453 UV-vis spectrophotometer. This spectral range of the light source varies from 190 to 1100 nm. The UV-vis absorption spectra were an used to confirm the successful synthesis of materials. Take the example of AuNRs in the third part, the well-defined surface plasmonic resonance of the AuNRs can tell a good synthesis. On the other hand, UV-vis spectra allow the quantitative analysis, as the concentration of analytes is directly proportional to the obtained absorption.

Fluorescence spectra were and a Fluorolog fluorescence spectrophotometer equipped with a 450 W Xe-lamp (FL3-22, Horiba Jobin Yvon Inc.), using 10 mm path length quartz cuvettes. To confirm the successful preparation of AuNCs (excited at 365 nm and emitted at ca. 605 nm) and the mechanism study of nanozyme, the corresponding fluorescence spectra were recorded.

The zeta potential measurements of AuNRs and NCs were performed via a Malvern Zetasizer Nanoparticle analyzer (ZEN 3600) instrument.

6.3　Experimental Design

6.3.1　Template-based synthesis of ligand-free PtNCs for efficient catalysis and their versatile release studies

6.3.1.1　Template-assisted synthesis of PtNCs

First, stock solutions are prepared before synthesis. For ZIF-8, 471.305 mg of $Zn(NO_3)_2 \cdot 6H_2O$ and 795.95 mg of 2-MeIM are dissolved in 15 mL MeOH to obtain 105.62 mM Zn^{2+} and 646.33 mM 2-MeIM. For PtNCs, H_2PtCl_6 stock solution of 25 mM is prepared in Milli-Q water.

Then, 2 mL of Zn^{2+}/MeOH is added in a 10 mL glass vial, followed by dropwise addition of 2-MeIM/MeOH (2 mL) under vigorous stirring at 1500 rpm. After a few min, the colorless mixture changes to milky white, suggesting the successful formation of ZIF-8 consistent with the previous reports.[37, 89, 96] One hour later, proper volume (0.333, 1.332, 1.998, and 2.664 mL, separately) of H_2PtCl_6 aqueous solution (25 mM) is introduced to the mixture obtaining the pale-yellow mixture. After another 1 h under vigorously stirring, 0.682 mL of freshly prepared aqueous $NaBH_4$ (500 mM) was quickly added to the mixture, which can quickly initiate the reduction of metal ions. After ca. 3 min, the color of mixture changed to dark grey, which indicated the formation of PtNCs@ZIF-8. The reaction continued for 1 h to warrant for the homogeneity of the reaction. Thereafter, the as-synthesized PtNCs@ZIF-8 was purified by centrifugation (at 5000 rpm for 10 min), then removed unreacted residues in the supernatant and washed with fresh methanol. Then, the centrifuge-wash process is repeated at least two times to purify the obtained PtNCs@ZIF-8. The obtained PtNCs@ZIF-8 precipitate was left drying in air at room temperature for at least 24 h, after which the powder sample was kept for further use. It should be noted that the as-prepared PtNCs@ZIF-8 with the four different volumes (0.333, 1.332, 1.998, and 2.664 mL, separately) of Pt precursors was denoted as Pt-1, Pt-2, Pt-3 and Pt-4@ZIF-8, respectively.

6.3.1.2　Catalysis of 4-NP reduction studies

The reduction of 4-NP was chosen as a model reaction. In a typical process, 0.2 mL 4-NP (1 mM) and 0.2 mL freshly prepared $NaBH_4$ was mixed with 2.06 mL Milli-Q water. After vigorous shaking for 10 s, 0.04 mL of Pt-2@ZIF-8 was injected into the mixture. Then the mixture was shaked for another 10 s before the reduction started.

For all measurements, the concentration of $NaBH_4$ is kept at 0.024 M. The process of the reduction was monitored by collecting the continuous absorption spectra at 400 nm as a function of time at 1 min intervals. For the kinetic study, the different concentrations of platinum C_{Pt} (0.579 0.959, 1.904, 3.246, and

4.474 mg L^{-1}, respectively) were investigated. For activation energy study, the final concentration of 4-NP was kept at 0.08 M, while four different temperatures of 290, 295, 300 and 305 K were applied.

Conversion yield (Y$_{4-AP}$) of 4-NPA anion to 4-AP in presence and absence of catalyst was calculated as follows:

$$Y_{AP} = (A_{400,max} - A_{400,max})/A_{400,max} \qquad \text{6-1}$$

The rate constant (k) was calculated based on equation (6-2) as the pseudo first-order kinetic mechanism in the following:

$$\ln(c/c_0) = -\text{kt} \qquad \text{6-2}$$

in which the c_0 and c are proportional to the original and the real-time absorption A at $\lambda = 400$ nm (which linearly depends on the 4-NP concentration), respectively, while k and t is the rate constant and the reaction time, respectively.[225]

Furthermore, the mass activity parameter (k') was calculated based on the equation for a quantitative comparison (6-3),

$$k' = k/m \qquad \text{6-3}$$

where m is the total mass of the catalyst.

The Arrhenius equation, which is an empirical parameter for all chemical reactions, reflects energy needed for a reaction to occur

$$k = A' \cdot e^{-Ea/RT} \qquad \text{6-4}$$

where A' is the pre-exponential factor (A' was used here instead of A to avoid the confusion with the symbol of absorbance), k is the rate constant of the reaction at temperature T (in Kelvin), and R is the universal gas constant.

6.3.1.3 Electrochemical catalytic studies

6.3.1.3.1 Hydrogen evolution reaction (HER) test

The carbon ink for HER measurements was prepared in the following process: 4 mg mL^{-1} PtNCs@ZIF-8/MeOH catalyst solution was obtained under ultrasonication. To achieve the ink, 200 μL of PtNCs@ZIF-8/MeOH (4 mg mL^{-1}), 5 mg of carbon black, 50 μL of a 5 wt.% Nafion solution in ethanol, and 750 μL of MeOH was added in a plastic vial under ultrasonication to obtain well-dispersed catalyst ink (0.8 mg/mL ink). A 10 μL aliquot of the catalyst ink was spread onto the surface of the rotating disk electrode. Control experiments were carried out with a commercially available 20 wt.% Pt/C catalyst (Johnson-Matthey), nominally 20 wt.% on carbon black (E-TEK). The 20 wt.% Pt/C catalyst ink was prepared by mixing 2 mg of catalyst, 50 μL of a 5 wt.% Nafion solution in ethanol, and 950 μL of MeOH, obtaining 2 mg mL^{-1} Pt/C ink. Then, a 10 μL aliquot of the platinum ink was dropped on the glassy carbon rotating disk electrode in the same way as done with the PtNCs@ZIF-8 catalyst. Before measurements, the electrolyte was purged with N$_2$ for 30 min to remove the oxygen in the electrolyte. CV of the prepared PtNCs@ZIF-8 catalyst was conducted first in N$_2$-saturated acidic condition (0.1 M HClO$_4$) in the potential region from - 0.2 to 1 V at a sweep rate of 50 mV s^{-1} until the CVs stayed unchanged. The polarization curves for HER were carried out with a scan rate of 5 mV s^{-1}. CVs were conducted between - 0.3 and 0 V versus RHE at 100 mV s^{-1} for 4,000 times to investigate the ADT properties.

6.3.1.3.2 Nernst equation

In this work, the applied potential E' was measured versus the Ag/AgCl electrode, which can be converted to reversible hydrogen electrode (RHE) based on the Nernst equation as follows:

$$E = E' + 0.059 \cdot pH + E^0_{Ag/AgCl}$$ 6-5

Here E' is the experimentally measured potential versus the Ag/AgCl reference electrode. The standard electrode potential of the Ag/AgCl electrode (E^{0}Ag/AgCl) is taken as 0.1976 V.

6.3.1.3.3 Electrochemically active surface area (ECSA) analysis

Typically, the *H- adsorption/desorption (H$_{UPD}$) peaks (0.05 - 0.35 V) on Pt was utilized to calculate the ECSA (A$_{ECSA}$) of Pt-based catalysts.[157] The specific ECSA was calculated based on the equation (6-6) as follows:

$$A_{ECSA} = \frac{Q_H}{m \times q_H}$$ 6-6

where Q$_H$ is the charge for H$_{UPD}$ (H$^+$ + e$^-$ = H$_{UPD}$) adsorption, m is the metal loading, and q$_H$ is the charge

95

required for a monolayer of hydrogen adsorption on Pt as assumed of 210 µC cm^{-2}.

6.3.1.3.4 HER intrinsic mechanism

Furthermore, Tafel plots were used to illustrate the intrinsic reaction mechanism of the HER process as a lower Tafel slope is preferred for the applicable purposes, which were derived from the LSVs by fitting the Tafel equation (6-7).[135, 226]

$$E_\eta = \beta \cdot \log(j) + \alpha \qquad\qquad 6\text{-}7$$

in which E_η is the overpotential, β is the Tafel slope, j is the current density, and α is the symmetry coefficient.[226] In general, as mentioned in the introduction section (**Table 1-2**), there are three possible principle steps for HER in an acidic medium, namely, the Volmer step, the Heyrovsky step, and the Tafel step with a Tafel slope of 116, 38 and 29 mV decade^{-1}, respectively.[61]

Volmer step:

$$H_3O^+ + e^- \rightarrow H^* + H_2O$$
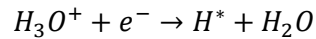
$$\beta = \frac{2.3RT}{\alpha F} \approx 116\ mV$$

Heyrovsky step:

$$H^* + H_3O^+ + e^- \rightarrow H_2 + H_2O$$
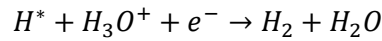
$$\beta = \frac{2.3RT}{(1+\alpha)F} \approx 38\ mV$$

Tafel step:

$$2H^* \rightarrow H_2$$
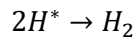
$$\beta = \frac{2.3RT}{2F} \approx 29\ mV$$

where β is Tafel slope, H* represent atoms adsorbed on the active sites of the catalysts, R is the ideal gas constant, T is the absolute temperature, $\alpha \approx 0.5$ is the symmetry coefficient, and F is the Faraday constant.

The above elementary steps lead to two mechanisms, including Volmer-Heyrovsky and Volmer-Tafel.

6.3.1.3.5 Oxygen reduction reaction (ORR) test

For the ORR analysis, LSVs were performed in O_2-saturated acidic condition (0.1 M $HClO_4$) at a scan rate of 5 mV s^{-1} using a RDE. The carbon ink for ORR was prepared as follows: 4 mg PtNCs@ZIF-8 catalyst was dispersed in 1 mL methanol under ultrasonication. Then ink was prepared by mixing 200 μL Pt-based methanol, 5 mg of carbon black, 50 μL of a 5 wt.% Nafion solution in methanol, and 750 μL of methanol in a plastic vial under ultrasonication. A 10-μL aliquot of the carbon ink was dropped on the surface of the glassy carbon rotating disk electrode, yielding an approximate catalyst loading of 0.006 mg cm^{-2} or 4 μg$_{Pt}$ cm^{-2}. Control experiments had been carried out with a commercial 20 wt.% Pt/C catalyst. The Pt/C ink was obtained by mixing 0.21 mg of catalyst, 50 μL of a 5 wt.% Nafion solution in methanol, and 950 μL of methanol. Then, a 15 μL aliquot of the platinum ink was dropped on the glassy carbon rotating disk electrode, yielding an approximate loading of 0.025 mg cm^{-2} or 5 μg$_{Pt}$ cm^{-2}.

6.3.1.3.6 Koutecky-Levich (K-L) equation

The related kinetic parameters could be calculated based on the following K-L equations:

$$\frac{1}{J} = \frac{1}{J_L} + \frac{1}{J_K} = \frac{1}{B\omega^{1/2}} + \frac{1}{J_K} \qquad\qquad 6\text{-}8$$

$$B = 0.2nFC_0(D_0)^{2/3}v^{-1/6} \qquad\qquad 6\text{-}9$$

where J is the measured current density, while J_L and J_K represent diffusion-limiting and kinetic- current densities, respectively, and ω is electrode rotation speed equation (6-8). In equation (6-9), n is the overall number of electrons transferred in oxygen reduction, F is the Faraday constant with 96485 C mol^{-1}, C_0 is the bulk concentration of O_2 (1.5 x 10^{-6} mol cm^{-3} in 0.1 M $HClO_4$), D_0 is the diffusion coefficient for O_2 in 0.1 M $HclO_4$ (2.0 x 10^{-5} cm^2 s^{-1}) and v is the kinetic viscosity of solution (0.01 cm^2 s^{-1}). The constant 0.2 is used when the unit of rotation speed remain in rpm.

6.3.1.3.7 The yield of H_2O_2

For the calculation of yields of H_2O_2 on the different catalysts, based on both ring and disk currents form RRDE, the percentage of HO_2^- generated from ORR and the electron transfer number (n) were estimated by the following equations:[50]

$$HO_2^-\% = 200 \times \frac{i_R/N}{i_D + i_R/N} \qquad\qquad 6\text{-}10$$

$$n = 4 \times \frac{i_D}{i_D + i_R/N} \qquad\qquad 6\text{-}11$$

where i_D is the disk current density, i_R is the ring current density and N is the current collection efficiency of the Pt ring disk. And N could be calculated from the reduction of $K_3Fe[CN]_6$ with 0.37. All the current densities have already been normalized to the electrode surface area.

6.3.1.4 Release of PtNCs from ZIF-8

In this work, releasing PtNCs into aqueous and non-aqueous conditions was studied. For the aqueous case, the as-synthesized Pt-2@ZIF-8 (10 mg) was added to 10 mL MeOH before the release process, followed by 5 min bath sonication to achieve 1 mg/mL Pt-2@ZIF-8/MeOH mixture. Initially, 1 mL Pt-2@ZIF-8/MeOH was added to 20 mL glass vial, which then added 50 mL of 1 mM GSH in 10 mM NaOH under vigorous stirring (1500 rpm) for 20 min. The obtained PtNC@GSH@ZIF-8 was collected by centrifugation at 5000 rpm for 10 min, while the supernatant was removed (to avoid extra GSH). The release process is described as follows. The PtNC@GSH@ZIF-8 nanocomposite was redispersed in different pH aqueous solution (1 mL for each), followed by 5 min bath sonication at 480 W (I). Next, precipitate and the mixture were separated by centrifuging at 5000 rpm for 10 min, whereby aggregated particles of large size together with residual MOFs precipitated (II). Then, the supernatant was collected for further use (III). The photo of III under different pH conditions was shown in **Figure 2-20b**.

On the other hand, a similar protocol was applied using DDT instead. 50 mL DDT/MeOH (1 mM) was introduced to 1 mL Pt-2@ZIF-8 mixture solution for 20 min. After the purification, DMSO, DCM, THF, CHCl₃, DMF, and toluene, respectively, was added into the mixture, followed by sonication (I), centrifugation (II), and supernatant collection (III). The photo of III under different solvent was displayed in **Figure 2-20b**.

6.3.2 Different methodologies for the synthesis of alloy PtAgNCs for multi-enzyme mimicking studies

6.3.2.1 Synthesis of MNCs@ZIF-8 via different methods

Synthesis of ZIF-8. Typically, 1 mL of 105.62 mM Zn(NO₃)₂ /methanol was added to a 20 mL vial, while 1 mL of 646.33 mM 2-MeIM/methanol was added dropwise, which was left for 0.5 h under stirring at

1500 rpm at room temperature.

Synthesis of Pt@ZIF-8 and Ag@ZIF-8. After the synthesis of ZIF-8, 1.332 mL of 25 mM K_2PtCl_4 or $AgNO_3$ aqueous solution was added into the 2 mL ZIF-8 mixture, and stirred for 0.5 h, followed with the addition of 1 mL 500 mM freshly prepared $NaBH_4$ aqueous solution and reaction for 1 h. Then, the as-synthesized Pt@ZIF-8 or Ag@ZIF-8 was washed by centrifugation at 5000 rpm 3 times and dispersed in 3 mL methanol.

Synthesis of PtAg alloy via co-reduction method. The PtAg alloy catalysts were synthesized based on the synthesis of ZIF-8 by using a co-reduction synthesis protocol according to the previously reported method.[36] Then, proper amount of 25 mM K_2PtCl_4 and $AgNO_3$ solution was introduced into the above 2 mL ZIF-8 methanol mixture and stirred for 0.5 h, followed with the addition of 0.5 mL 500 mM freshly-prepared $NaBH_4$ aqueous solution, which was stirring for 1 h. Afterward, the as-synthesized PtAg alloy was washed by centrifugation at 5000 rpm for 3 times, and the precipitate was left drying in the air overnight for further use. These samples were characterized as the bigger size of ca. 9.1 nm, which were denoted as PtAgNPs samples. Different ratios of $AgNO_3$ to K_2PtCl_4 solution (0.5, 1, 2, 3, 3.5, 4, 4.5, and 5) was used to prepare different compositions samples, named as PtAgNPs-1, -2, -3, -4, -5, -6, -7, and -8, respectively.

Synthesis of PtAg alloy via Pt-guided strategy. The PtAgNCs catalysts were synthesized based on the as-obtained 2 mL Pt@ZIF-8 by using Pt-guided synthesis protocol. 2 µL $AgNO_3$ and 40 µL Pt^{2+} precursor was added to the above synthesized 3 mL Pt@ZIF-8. After that, 50 mL of 500 mM freshly prepared reducing agent ($NaBH_4$ in Milli-Q water) was added, stirring at 1500 rpm for 1 h. Then the mixture was washed by centrifugation at 5000 rpm with methanol 3 times, and dry for 24 h in the air. It should be noted that the obtained PtAg alloy by this method was characterized with average core diameter of ca. 1.8 nm, which were then called PtAgNCs. A series of different volumes (2, 4, 8, 16, 32, 40, and 80 µL) $AgNO_3$ and 40 µL Pt precursor was added to 1 mL Pt@ZIF-8 to prepare a series of PtAgNCs-1 to PtAgNC-7 with different Ag and Pt compositions.

6.3.2.2 Enzyme mimicking study of PtAg alloy

6.3.2.2.1 Peroxidase (POD)-like activity of PtAg alloy

The POD-like catalytic activity of PtAg alloy was evaluated upon the catalytic oxidation of OPD substrate in the presence of H_2O_2 at 37 °C. The absorbance changes of the colored product DAP from OPD were continuously recorded by UV-vis spectroscopic at 450 nm for 24 min. In a typical measurement, the mixture solution of 3 mL citric buffer contained freshly prepared OPD (0.32 mM), H_2O_2 (326.6 mM) and an equivalent Pt content of PtAgNCs (0.25 mg mL^{-1}, 20 µL) or PtAgNPs (1 mg mL^{-1}, 35 µL). Control

experiments were performed by replacing PtAg alloys with Milli-Q water, ZIF-8, Pt@ZIF-8, and Ag@ZIF-8. The pH-dependent catalytic performance of PtAg alloys was investigated in citric buffers prepared at different pHs (pH 3, 3.5, 4, 4.5, 5, 5.5 and 6). The final absorbance at 450 nm was measured after 24 min incubation of the reaction mixture solution. To investigate the effect of Pt/Ag ratios of PtAg alloys upon the catalytic efficiency, the POD-like performance of the resulting PtAg alloys prepared with different ratios of Ag and Pt precursors (synthesis protocol mentioned earlier) was examined following the typical run at 450 nm. To study the steady-state kinetic parameters of the PtAg alloys, the measurements were carried out by changing the substrate concentrations of OPD with a fixed concentration of H_2O_2, or *vice versa*.

6.3.2.2.2 Catalase (CAT)-like activity of PtAg alloy

To evaluate the CAT-like activity of PtAg alloys, a dissolved oxygen meter (Model of Extech DO210) was used to monitor the changing generation of O_2 upon the decomposition of H_2O_2. The reaction was stirred vigorously and recorded every min for 10 min at room temperature. Typically, an equivalent Pt content of 2.5 µL PtAgNCs (0.25 mg mL^{-1}) or 4.3 µL PtAgNPs (1 mg mL^{-1}) was injected into a reaction solution of 5 mL PBS buffer (pH 7) containing H_2O_2 of 750 mM to trigger the H_2O_2 decomposition reaction. Control experiments were done by replacing the PtAg alloys with the same volume of Milli-Q water, ZIF-8, Pt@ZIF-8, Ag@ZIF-8 as well as CAT (20 U mL^{-1}). The CAT-like activity of PtAgNCs was also evaluated in PBS buffers with different pH (pH 4, and 11), following the typical protocol above. The PtAg alloys with different content of Pt to Ag were further investigated. To better understand of the catalytic property of PtAg alloys, steady-state kinetic was further evaluated with various concentrations of H_2O_2 at pH 7.

6.3.2.2.3 Oxidase (OD)-like activity of PtAg alloy

The OD-like catalytic activity of PtAg alloy was evaluated upon the catalytic oxidation of TMB substrate by O_2 in the absence of H_2O_2 at 37 °C. The changing absorbance of oxTMB was continuously monitored using UV-vis spectroscopic at 652 nm. Prior to the reaction, 0.1 M NaAc-HAc buffer was bubbling under the O_2 flow for at least 1 h. In a typical measurement, 2 mL NaAc-HAc buffer was added to the cuvettes for 20 min incubation at 37 °C, followed by the addition of 40 µL TMB (2 mg mL^{-1} in DMSO) and PtAgNCs (0.25 mg mL^{-1}, 20 µL) or PtAgNPs with an equivalent Pt content. To confirm the OD-like mimics of PtAg alloys, catalytic reaction on TMB oxidation was also performed in N_2-buffer solution with the same preparing method by replacing O_2 with N_2. Control experiments were performed by replacing PtAg alloys with Milli-Q water, ZIF-8, Pt@ZIF-8, and Ag@ZIF-8. The pH-dependent catalytic performance of PtAg alloys were investigated in NaAc-HAc buffers prepared at different pHs (pH 3, 4, 5, 6, 7 and 10). The effect of Pt/Ag ratios of PtAg alloys upon the catalytic oxidation of TMB was further investigated following the

100

same protocols. To investigate steady-state kinetic, assays were carried out by changing the substrate concentrations of TMB to record the related rate of catalytic reaction at 652 nm.

6.3.2.2.4 Steady-state kinetic study

The steady-state kinetic was investigated by varying concentration of one substrate during the reaction. The relationship of the series initial reaction rates (v) and concentration of substrate [S] was found followed the Michaelis-Menten. The apparent kinetic parameter of K_m and v_{max} were calculated following the Lineweaver-Burk plots (6-12), based on the double reciprocal of the Michaelis-Menten equation:[227]

$$1/v = (K_m/v_{max}) \times (1/[S]) + 1/v_{max} \qquad 6\text{-}12$$

A lower K_m value illustrates a higher affinity and catalytic activity between the enzyme and substrate.

6.3.2.3 Mechanism study

The production of $\cdot OH$ radicals in solution was monitored by terephthalic acid (TA) as a fluorescence probe. Typically, 50 mL of 25 mM TA in NaOH (pH = 13) solution was added into the 2 mL of buffer containing 95 mM H_2O_2 and/or PtAg alloys (1, 5, 7, 10, 15, and 20 mL, respectively) for 4 h incubation in the dark. The resulting solution was detected by using a fluorescence spectrophotometer with an excitation wavelength of 315 nm, while the emission spectra were recorded in the wavelength of 425 nm.

To monitor the generation of $\cdot O_2^-$ radical, another fluorescence probe, hydroethidine (HE), was added into O_2-buffer solution to detect $\cdot O_2^-$ for the OD-like activities of PtAg alloy. Briefly, 1 mL of NaAc-HAc buffer (pH 4 and 7) was added to the cuvette, followed with the addition of 10 mL HE (5 mM) and 10 mL PtAg alloy for 2 h. The fluorescence spectra were recorded with emission spectra at 610 nm when excited at 510 nm.

To detect the production of H_2O_2 during the OD-like activity, 30 mL CAT enzyme was added to the typical solution as described above. After reaction for 24 min, the UV-vis spectra in the presence and absence of CAT enzyme in OD-like reaction solution were recorded.

6.3.3 Plasmon enhancement of AuNCs sensing with PEC platform

6.3.3.1 Synthesis of Au@GSH NCs

For Au@GSH NCs synthesis, 8 mL of 25 mM $HAuCl_4$ aqueous solution, 89 mL Milli-Q water and 3 mL of 100 mM GSH aqueous solution were mixed, stirring at 700 rpm (70 – 75 °C) under reflux for 24 h. The color of the solution was changed from darker goldish orange to colorless within 5 min, which showed yellow color for the final product.

6.3.3.2 Synthesis of Au nanorods (AuNRs)

The AuNRs were prepared through seed-mediated growth according to a previously reported method.[219] Briefly, the seed solution for AuNRs was prepared first. The CTAB (346.6 mg, 0.2 M) was dissolved in 5 mL of warm Milli-Q water (60 – 70 °C) in a 20 mL vial. The mixture was allowed to cool to 30 °C, which was mixed with a 5 mL amount of 0.5 mM $HAuCl_4$ aqueous solution. Then, a 600 µL of fresh-prepared $NaBH_4$ (10 mM) was injected into the above Au-CTAB mixture under vigorous stirring (1200 rpm) for 2 min. The mixture color changed from yellow to brownish-yellow. The seed solution was allowed for aging at room temperature for 0.5 - 2 h to be used.

The growth solution was prepared as follows. 0.9 g of CTAB and 80 mg sodium salicylate salt were dissolved in 25 mL of warm Milli-Q water (60 – 70 °C) in a 100 mL flask. The mixture was allowed to cool to 30 °C by air when it became transparent, following is the addition of 600 µL of fresh 4 mM $AgNO_3$ aqueous solution, kept undisturbed at 30 °C for 15 min. After which, 25 mL of 1 mM $HAuCl_4$ aqueous solution was added. After 15 min reaction under slow stirring (400 rpm), 100 µL of 0.064 M ascorbic acid (AA) was injected into the above mixture under vigorously stirring for 30 s until it became colorless, and finally, 80 µL of seed solution was injected into the above growth solution, which was kept stirring for 30 s and left for undisturbed at 30 °C overnight to achieve AuNRs. The axcess CTAB in obtained AuNRs solution was removed by centrifuge twice at 11000 rpm for 15 min. Then 12.5 mL Milli-Q water was added into the precipitate to obtain the final AuNRs solution to be used.

The concentration of An NRs was characterized by UV-vis spectroscopy and ICP-MS elemental analysis. According to the previous report,[228] a value of 1.2 of absorbance at 400 nm for AuNRs is corresponding to a Au^0 concentration of 0.5 mM. After each time of measurement by UV-vis and ICP-MS method, our results are in good agreement with the previous report. 5-fold diluted AuNRs was measured by UV-vis spectroscopy in 190 – 1100 nm. To prepare ICP-MS samples, generally, 10 µL 5-fold diluted AuNRs was

added to the vials, followed by the addition of 190 µL aqua regia under mild shaking for 2 h to fully digestion of AuNRs into solution. Then 1800 µL of 2 % (*v/v*) HNO$_3$ aqueous solution was added for aging overnight before ICP-MS measurements.

6.3.3.3 Preparation of silica (SiO$_2$) coating on AuNRs (AuNRs@SiO$_2$)

The 10 mL of AuNRs solution was mixed with 30 mL Milli-Q water, followed by the addition of fresh-prepared (3-Aminopropyl) trimethoxysilane (APTMS, 0.5 mM) aqueous solution under vigorously stirring for 10 min, which ensures the complete complexation of the amine groups with the AuNRs surface. Following is the addition of a 0.54 wt.% sodium silicate aqueous solution under fast stirring.[229] To obtain the thin thickness of SiO$_2$ coating, pH 10.9 of Na$_2$SiO$_3$ aqueous was introduced, and kept stirring (1 d). After the aimed coating, the AuNRs@SiO$_2$ was washed by centrifuge at 11000 rpm for 15 min, and then 2.5 mL Milli-Q water was added to make the final AuNRs@SiO$_2$ solution.

6.3.3.4 Fabrication of PEC working electrode chip

Gold electrodes (100 nm Au/ 10 nm Cr/ 150 µm glass, 144 mm^2) were cleaned by sequential ultrasonication in acetone, absolute ethanol, and Milli-Q water. Following is the modification with SAM layer of BDT (50 mM in ethanol) for 4 h. The SAM/Au chips were washed with ethanol to remove the free BDT molecules and dried in an N$_2$ flow. Then, the Au@GSH NCs were deposited on the SAM/Au chips for 5 min, and spinning was used to remove the excess solvent and obtain AuNCs/SAM/Au electrodes. The amino-modified AuNRs@SiO$_2$ were prepared by adding APTMS (1 µL) to 1 mL high concentration AuNRs@SiO$_2$ solution under shaking for 5 h at room temperature, followed with the heating at 50 ℃ for 1 h. The AuNRs@SiO$_2$-NH$_2$ were separated by centrifuge at 8000 rpm for 10 min and redispersed with Milli-Q water three times to obtain purified materials. The self-assembly AuNRs@SiO$_2$ monolayer was formed as follows: First, 1.5 mL of the as-prepared AuNRs@SiO$_2$ solution was injected into a small plastic watch glass, and then add 230 µL of hexane to form a liquid-liquid interface. Finally, 1.8 mL methanol was injected into the mixture quickly to capture the NRs to the two-phase interface. Then, the AuNRs@SiO$_2$ film were deposited to the AuNCs/SAM/Au-electrode surface through floating transfer process to fabricate AuNRs@SiO$_2$/AuNCs/SAM/Au, the ePEC sensing platform.[230]

6.3.3.5 PEC measurement

A homebuilt PEC system was used for measuring PEC signals. A detailed photograph of the set-up is shown below (**Figure 6-1**). A Faraday cage was utilized to eliminate electromagnetic interference. White light from 250 to 1100 nm by a Xe-arc lamp (Ushio, Inc., Japan) was applied, whose intensity was controlled by the power supply (LPS 220, Photon Technology International, USA). During the measurements, the applied

illuminated was controlled to 71 Hz by using an optical chopper (Scitec instruments, USA), which works as reference frequency for the lock-in measurement of the photocurrent to enhance the signal to noise ratio (SNR).[231] The PEC measurements were carried out with a potentiostat (CH Instrument CHI600E, USA) with a three-electrode system: a NR/NC modified chips as WE, an Ag/AgCl (3 M NaCl) as RE, while a Pt wire as CE. The on-/off- illumination of the WE were manually controlled by a shutter. Photocurrents were amplified and rectified with a lock-in amplifier (EG&G Model # 5210), which was used to improve the signal-to-noise ratio, and transferred to a personal computer (PC) via USB and serial ports, controlled by homebuilt LabVIEW (National Instruments, USA) software. A detailed scheme of the PEC set-up is shown in **Figure 6-2**.

A sketch of the electrochemical cell used in this work was shown in **Figure 6-3**. It should be noted that the WE was fixed sealed by an O-ring between a teflon cell and sheet by using screws. A conductive tap was used to connect the WE and potentiostat to record the generated photocurrents. The hole size of the cell was 6 mm in diameter, which was used as spot size under illumination, with illuminated surface area A_{chip} of ca. 0.28 cm^2.

A Xe-arc lamp was utilized as the white light source (250 – 1100 nm), which can be filtered to obtain different monochromatic light by using different optical filters as following: 405 ± 10 nm (BrightLine), 445 ± 50 nm (CarlZeiss), 525 ± 50 nm (CarlZeiss), $530 – 585$ nm (CarlZeiss), 580 ± 25 nm (CHROMA), 605 ± 50 nm (CHROMA), 640 ± 25 nm (CHROMA), and 725 ± 50 nm (CarlZeiss). The light intensity of different wavelengths was adjusted by a photometer (FieldMaxII) before measurement.
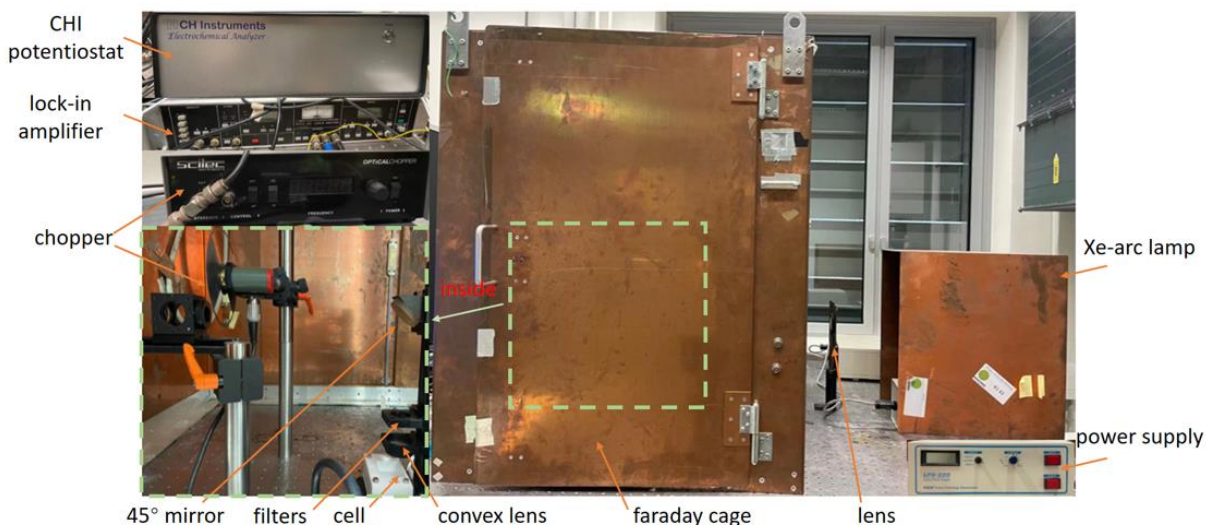
Figure 6-1. *Photography of the homebuilt PEC system in this work.*
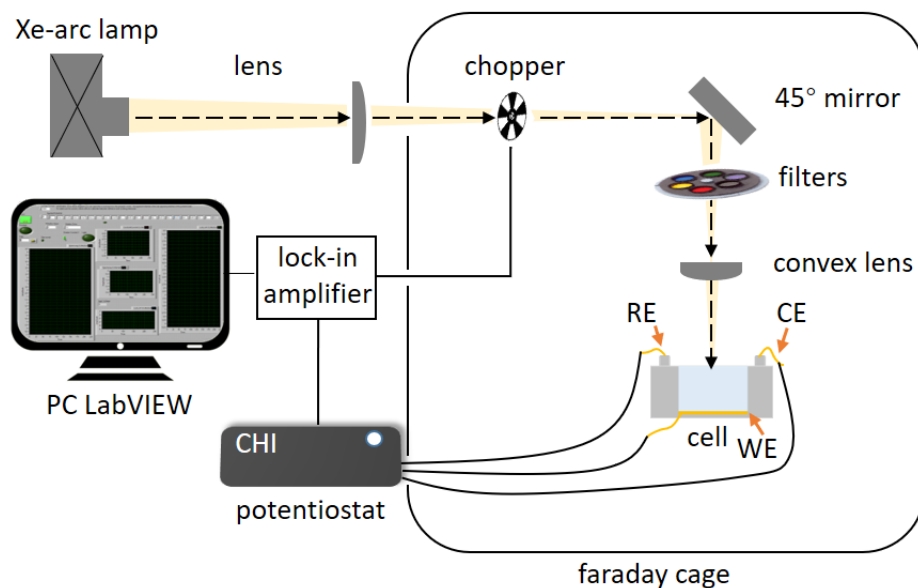
Figure 6-2. *Schematic illustration of the homebuilt PEC system. The WE was an Au electrode modified with AuNCs and AuNRs with and without silica. A Pt wire and an Ag/AgCl (3 M NaCl) worked as CE and RE, respectively.*
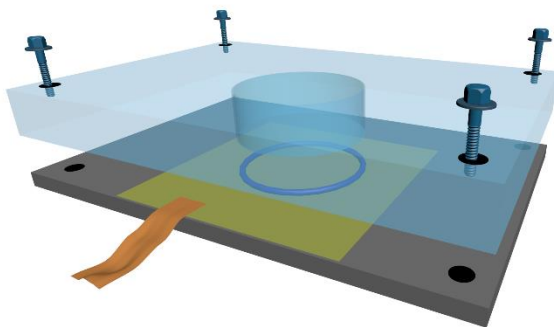
Figure 6-3. *Sketch of the electrochemical cell used for the PEC measurements.*

6.3.3.6 H$_2$O$_2$ measurements

Before the PEC measurement of H$_2$O$_2$ concentrations, the electrochemical cell, and three electrodes (WE, CE, and RE) were thoroughly rinsed with Milli-Q water and dried by flowing N$_2$. The corresponding concentration of H$_2$O$_2$ was added into the electrochemical cell for PEC measurements.

6.4 List of hazardous substances used in the work

Chemical	CAS-No.	GHS Pictogram(s)	H-Sentences (Hazard)	P-Sentences (Precaution)
$Zn(NO_3)_2 \cdot 6H_2O$	10196-18-6	danger	H272-H302-H315-H319-H335-H410	P210 – P220 – P273 – P301 + P312 – P302 + P352 – P305 + P351 + P338
2-MeIM	693-98-1	danger	H302-H314 - H351-H360Df	P260 – P280-P301+ P312-P303+ P361 + P353 – P304 + P340 + P310 – P305 + P351 + P338
$H_2PtCl_6 \cdot 6 H_2O$	18497-13-7	danger	H301-H314-H317-H334	P260 – P270 – P280 – P303 +P361 + P353 – P304 + P340 + P310 – P305+ P351+ P338
$NaBH_4$	16940-66-2	danger	H260 – H301-H314 – H360FD	P231 + P232 – P260 – P280 – P303 + P361 + P353 – P304 + P340 + P310 – P305 + P351 + P338
NaOH	1310-73-2	danger	H290-H314	P234 – P280 – P303 + P361 + P353 – P304 + P340 + P310 – P305 + P351 + P338 – P363
DCM	75-09-2	warning	H315 – H319 – H336 – H351	P201 – P202 – P261 – P302 + P352 – P305 + P351 + P338 – P308 + P313
$CHCl_3$	67-66-3	danger	H302 – H315 – H319 – H331 – H336 – H351 – H361d – H372 – H412	P201 – P273 – P301 + P312 + P330 – P302 + P352 – P304 + P340 + P311 – P308 + P313
DMF	68-12-2	danger	H226 – H312 + H332 – H319 – H360D	P210 – P280 – P303 + P361 + P353 – P304 + P340 + P312 – P305 + P351 + P338 – P308 + P313
$AgNO_3$	7761-88-8	danger	H272-H290-H314-H410	P210 – P260 – P273 – P280 – P303 + P361 + P353 – P305 + P351 + P338
HCl	7647-01-0	danger	H290-H314-H335	P234 – P261 – P271 – P280 – P303 + P361 + P353 – P305 + P351 + P338

CTAB	57-09-0	danger	H302-H315-H318-H335-H373-H410	P273 – P280 – P301 + P312 – P302 + P352 – P305 + P351 + P338 – P314
HNO_3	7697-37-2	danger	H272 – H290 – H314 – H331	P210 – P220 – P280 – P303 + P361 + P353 – P304 + P340 + P310 – P305 + P351 + P338
$HAuCl_4 \cdot x\ H_2O$	27988-77-8	danger	H290-H314-H317	P260 – P270 – P280 – P301 + P312 – P303 + P361 + P353 – P305 + P351 + P338
$HClO_4$	7601-90-3	danger	H271 – H290 - H302 – H314 – H373	P210 – P280 – P301 + P312 – P303 + P361 + P353 – P305 + P351 + P338 – P314
acetone	67-64-1	danger	H225 – H319 – H336	P210 – P233 – P240 – P241 – P242 – P305 + P351 + P338
toluene	108-88-3	danger	H225 – H304 – H315 – H336 – H361d – H373 – H412	P201 – P210 – P273 – P301 + P310 – P303 + P361 + P353 – P331
TEOS	78-10-4	warning	H226 – H319 – H332 -H335	P210 – P233 – P240 – P241 – P304 + P340 + P312 – P305 + P351 + P338
APTMS	919-30-2	danger	H302-H314-H317	P261 – P270 – P280 – P301 + P312 – P303 + P361 + P353 – P305 + P351 + P338
OPD	95-54-5	danger	H301-H312+ H332- H317-H319- H341-H351- H410	P273 – P280 – P301 + P310 – P302 + P352 + P312 – P304 + P340 + P312 – P305 + P351 + P338
H_2O_2	7722-84-1	danger	H302-H318	P264 – P270 – P280 – P301 + P312 – P305 + P351 + P338 – P501
K_2PtCl_4	10025-99-7	danger	H301 – H315 – H317 – H318 – H334	P280 – P301 + P310 + P330 – P302 + P352 – P305 + P351 + P338 + P310
hexane	110-54-3	danger	H225 – H304 – H315 – H336 – H361f – H373 – H411	P201 – P210 – P273 – P301 + P310 – P303 + P361 + P353 – P331

MeOH	67-56-1	danger	H225-H301+ H31+H331- H370	P210 – P233 – P280 – P301 + P310 – P303 + P361 + P353 – P304 + P340 + P311	
H$_2$SO$_4$	7664-93-9	warning	H290 – H314	P234 – P280 – P301 + P330 + P331 – P303 + P361 + P353 – P304 + P340 + P310 – P305 + P351 + P338	
acetic acid	64-19-7	danger	H226 – H314	P210 – P233 – P240 – P280 – P303 + P361 + P353 – P305 + P351 + P338	
DDT	112-55-0	danger	H314 – H317 – H410	P261 – P272 – P273 – P280 – P303 + P361 + P353 – P305 + P351 + P338	
THF	109-99-9	danger	H225 – H302 – H319 – H335 – H336 – H351	P201 – P202 – P210 – P301 + P312 – P305 + P351 + P338 – P308 + P313	
sodium salicylate	54-21-7	warning	H302 – H319 – H361d	P202 – P264 – P270 – P301 + P312 – P305 + P351 + P338 – P308 + P313	
Na$_2$SiO$_3$	1344-09-8	danger	H290 – H314 – H335	P234 – P261 – P271 – P280 – P303 + P361 + P353 – P305 + P351 + P338	
ethanol	64-17-5	danger	H225 – H319	P210 – P233 – P240 – P241 – P242 – P305 + P351 + P338	
GSH	70-18-8	Not hazardous substance			
DMSO	67-68-5	Not hazardous substance			
Nafion	31175-20-9	Not hazardous substance			
AA	50-81-7	Not hazardous substance			
Carbon black BP 2000		Not hazardous substance			
sodium acetate	127-09-3	Not hazardous substance			
TMB	54827-17-7	Not hazardous substance			
citric acid	77-92-9	Not hazardous substance			
NaH$_2$PO$_4$	7558-80-7	Not hazardous substance			
Na$_2$HPO$_4$	7558-79-4	Not hazardous substance			

108

BDT	624-39-5	Not hazardous substance
CAT	9001-05-2	Not hazardous substance
sodium citrate dihydrate	6132-04-3	Not hazardous substance
NaAc	127-09-3	Not hazardous substance
TA	100-21-0	Not hazardous substance
HE	104821-25-2	Not hazardous substance
PBS		Not hazardous substance

References

1.   Haruta, M.; Kobayashi, T.; Sano, H., et al., *Novel Gold Catalysts for the Oxidation of Carbon Monoxide at a Temperature far Below 0 °C.* Chemistry Letters **1987,** *16* (2), 405-408.

2.   Chakraborty, I.; Pradeep, T., *Atomically Precise Clusters of Noble Metals: Emerging Link between Atoms and Nanoparticles.* Chemical Reviews **2017,** *117* (12), 8208-8271.

3.   Tang, J.; Shi, H.; Ma, G., et al., *Ultrasmall Au and Ag Nanoclusters for Biomedical Applications: A Review.* Frontiers in Bioengineering and Biotechnology **2020,** *8* (1019), 1-12.

4.   Chakraborty, I.; Udayabhaskararao, T.; Pradeep, T., *Luminescent Sub-Nanometer Clusters for Metal Ion Sensing: A New Direction in Nanosensors.* Journal of Hazardous Materials **2012,** *211-212*, 396-403.

5.   Chakraborty, I.; Bag, S.; Landman, U., et al., *Atomically Precise Silver Clusters as New SERS Substrates.* The Journal of Physical Chemistry Letters **2013,** *4* (16), 2769-2773.

6.   Chakraborty, I.; Erusappan, J.; Govindarajan, A., et al., *Emergence of Metallicity in Silver Clusters in the 150 Atom Regime: A Study of Differently Sized Silver Clusters.* Nanoscale **2014,** *6* (14), 8024-8031.

7.   Som, A.; Chakraborty, I.; Maark, T. A., et al., *Cluster-Mediated Crossed Bilayer Precision Assemblies of 1D Nanowires.* Advanced Materials **2016,** *28* (14), 2827-2833.

8.   Jeseentharani, V.; Pugazhenthiran, N.; Mathew, A., et al., *Atomically Precise Noble Metal Clusters Harvest Visible Light to Produce Energy.* **2017,** *2* (4), 1454-1463.

9.   Chakraborty, I.; Bhuin, R. G.; Bhat, S., et al., *Blue Emitting Undecaplatinum Clusters.* Nanoscale **2014,** *6* (15), 8561-8564.

10.   Chakraborty, I.; Mahata, S.; Mitra, A., et al., *Controlled Synthesis and Characterization of the Elusive Thiolated Ag55 Cluster.* Dalton Transactions **2014,** *43* (48), 17904-17907.

11.   Bhat, S.; Chakraborty, I.; Maark, T. A., et al., *Atomically Precise and Monolayer Protected Iridium Clusters in Solution.* RSC Advances **2016,** *6* (32), 26679-26688.

12.   Chen, L.; Black, A.; Parak, W. J., et al., *Metal Nanocluster-Based Devices: Challenges and Opportunities.* Aggregate **2021,** *doi: 10.1002/agt2.132*.

13.   Fang, J.; Zhang, B.; Yao, Q., et al., *Recent Advances in the Synthesis and Catalytic Applications of Ligand-Protected, Atomically Precise Metal Nanoclusters.* Coordination Chemistry Reviews **2016,** *322*, 1-29.

14.   Maity, S.; Bain, D.; Patra, A., *An Overview on the Current Understanding of the Photophysical Properties of Metal Nanoclusters and Their Potential Applications.* Nanoscale **2019,** *11* (47), 22685-22723.

15.   Sugi, K. S.; Chakraborty, I.; Udayabhaskararao, T., et al., *Evolution of Atomically Precise Silver Clusters to Superlattice Crystals.* Particle & Particle Systems Characterization **2013,** *30* (3), 241-243.

16.   Manju, C. K.; Chakraborty, I.; Pradeep, T., *Highly Luminescent Monolayer Protected Ag56Se13S15 Clusters.* Journal of Materials Chemistry C **2016,** *4* (24), 5572-5577.

17.   Zeng, Y.; Havenridge, S.; Gharib, M., et al., *Impact of Ligands on Structural and Optical Properties of Ag29 Nanoclusters.* Journal of the American Chemical Society **2021,** *143*, 9405-9414.

18.   Baksi, A.; Schneider, E. K.; Weis, P., et al., *Linear Size Contraction of Ligand Protected Ag29 Clusters by Substituting Ag with Cu.* ACS Nano **2020,** *14* (11), 15064–15070.

19.   Ziefuss, A. R.; Steenbock, T.; Benner, D., et al., *Photoluminescence of Fully Inorganic Colloidal Gold Nanocluster and their Manipulation using Surface Charge Effects.* Advanced Materials **2021,** *33*, 2101549.

20.   Sarkar, S.; Chakraborty, I.; Panwar, M. K., et al., *Isolation and Tandem Mass Spectrometric Identification of a Stable Monolayer Protected Silver-Palladium Alloy Cluster.* Journal of Physical Chemistry Letters **2014,** *5* (21), 3757-3762.

21.   Zhang, N.; Si, Y.; Sun, Z., et al., *Rapid, Selective, and Ultrasensitive Fluorimetric Analysis of Mercury and Copper Levels in Blood Using Bimetallic Gold–Silver Nanoclusters with "Silver Effect"-Enhanced Red Fluorescence.* Analytical Chemistry **2014,** *86* (23), 11714-11721.

22.   Yong, Y.; Li, C.; Li, X., et al., *Ag7Au6 Cluster as a Potential Gas Sensor for CO, HCN, and NO Detection.* The Journal of Physical Chemistry C **2015,** *119* (13), 7534-7540.

23. Trimpalis, A.; Giannakakis, G.; Cao, S., et al., *NiAu Single Atom Alloys for the Selective Oxidation of Methacrolein with Methanol to Methyl Methacrylate.* Catalysis Today **2020,** *355*, 804-814.

24. Walsh, A. G.; Zhang, P., *Thiolate-Protected Single-Atom Alloy Nanoclusters: Correlation between Electronic Properties and Catalytic Activities.* Advanced Materials Interfaces **2021,** *8* (8), 2001342.

25. Du, Y.; Sheng, H.; Astruc, D., et al., *Atomically Precise Noble Metal Nanoclusters as Efficient Catalysts: A Bridge between Structure and Properties.* Chemical Reviews **2020,** *120* (2), 526-622.

26. Gharib, M.; Galchenko, M.; Klinke, C., et al., *Mechanistic Insights and Selected Synthetic Routes of Atomically Precise Metal Nanoclusters.* Nano Select **2021,** *2*, 831–846.

27. Chini, P., *Large metal carbonyl clusters (LMCC).* Journal of Organometallic Chemistry **1980,** *200* (1), 37-61.

28. Chakraborty, I.; Udayabhaskararao, T.; Pradeep, T., *High Temperature Nucleation and Growth of Glutathione Protected ∼Ag75 Clusters.* Chemical Communications **2012,** *48* (54), 6788-6790.

29. Chakraborty, I.; Kurashige, W.; Kanehira, K., et al., *Ag44(SeR)30: A Hollow Cage Silver Cluster with Selenolate Protection.* The Journal of Physical Chemistry Letters **2013,** *4* (19), 3351-3355.

30. Ganguly, A.; Chakraborty, I.; Udayabhaskararao, T., et al., *A Copper Cluster Protected with Phenylethanethiol.* Journal of Nanoparticle Research **2013,** *15* (4), 1522.

31. Chakraborty, I.; Udayabhaskararao, T.; Deepesh, G. K., et al., *Sunlight Mediated Synthesis and Antibacterial Properties of Monolayer Protected Silver Clusters.* Journal of Materials Chemistry B **2013,** *1* (33), 4059-4064.

32. Zhu, M.; Lanni, E.; Garg, N., et al., *Kinetically Controlled, High-Yield Synthesis of Au25 Clusters.* Journal of the American Chemical Society **2008,** *130* (4), 1138-1139.

33. Zhu, W.; Noureddine, A.; Howe, J. Y., et al., *Conversion of Metal–Organic Cage to Ligand-Free Ultrasmall Noble Metal Nanocluster Catalysts Confined within Mesoporous Silica Nanoparticle Supports.* Nano Letters **2019,** *19* (3), 1512-1519.

34. Wu, X.-Q.; Huang, D.-D.; Zhou, Z.-H., et al., *Ag-NPs Embedded in Two Novel Zn3/Zn5-Cluster-Based Metal–Organic Frameworks for Catalytic Reduction of 2/3/4-Nitrophenol.* Dalton Transactions **2017,** *46* (8), 2430-2438.

35. Xie, K.; Fu, Q.; He, Y., et al., *Synthesis of Well Dispersed Polymer Grafted Metal–Organic Framework Nanoparticles.* Chemical Communications **2015,** *51* (85), 15566-15569.

36. Chen, L.; Azeem, S.; Ruan, M., et al., *Rapid Template-Guided Ligand-Free Synthesis of Ultrasmall Pt Nanoclusters with Efficient Hydrogen Evolution Reaction Activity and Their Versatile Release.* Nano Select **2021,** *2*, 758–767.

37. Huang, Y.; Zhang, Y.; Chen, X., et al., *Bimetallic Alloy Nanocrystals Encapsulated in ZIF-8 for Synergistic Catalysis of Ethylene Oxidative Degradation.* Chemical Communications **2014,** *50* (70), 10115-10117.

38. Zhu, L.; Gharib, M.; Becker, C., et al., *Synthesis of Fluorescent Silver Nanoclusters: Introducing Bottom-Up and Top-Down Approaches to Nanochemistry in a Single Laboratory Class.* Journal of Chemical Education **2020,** *97*, 239-243.

39. White, S. L.; Banerjee, P.; Chakraborty, I., et al., *Ion Exchange Transformation of Magic-Sized Clusters.* Chemistry of Materials **2016,** *28* (22), 8391-8398.

40. Wang, S.; Song, Y.; Jin, S., et al., *Metal Exchange Method Using Au25 Nanoclusters as Templates for Alloy Nanoclusters with Atomic Precision.* Journal of the American Chemical Society **2015,** *137* (12), 4018-4021.

41. Krishnadas, K. R.; Ghosh, A.; Baksi, A., et al., *Intercluster Reactions between Au25(SR)18 and Ag44(SR)30.* Journal of the American Chemical Society **2016,** *138* (1), 140-148.

42. Zhao, S.; Riedel, M.; Patarroyo, J., et al., *Introducing Visible-Light Sensitivity into Photocatalytic CeO2 Nanoparticles by Hybrid Particle Preparation Exploiting Plasmonic Properties of Gold: Enhanced Photoelectrocatalysis Exemplified for Hydrogen Peroxide Sensing.* Nanoscale **2021,** *13*, 980-990.

43. Yang, J.; Wang, D.; Han, H., et al., *Roles of Cocatalysts in Photocatalysis and Photoelectrocatalysis.* Accounts of Chemical Research **2013,** *46* (8), 1900-1909.

44. Koh, S.; Strasser, P., *Electrocatalysis on Bimetallic Surfaces: Modifying Catalytic Reactivity for Oxygen Reduction by Voltammetric Surface Dealloying.* Journal of the American Chemical Society **2007,** *129* (42), 12624-12625.

45.   Patolsky, F.; Gabriel, T.; Willner, I., *Controlled Electrocatalysis by Microperoxidase-11 and Au-Nanoparticle Superstructures on Conductive Supports.* Journal of Electroanalytical Chemistry **1999,** *479* (1), 69-73.

46.   Katz, E.; Willner, I., *Magnetic Control of Chemical Transformations: Application for Programmed Electrocatalysis and Surface Patterning.* Electrochemistry Communications **2001,** *3* (12), 683-685.

47.   Niazov, T.; Shlyahovsky, B.; Willner, I., *Photoswitchable Electrocatalysis and Catalyzed Chemiluminescence Using Photoisomerizable Monolayer-Functionalized Surfaces and Pt Nanoparticles.* Journal of the American Chemical Society **2007,** *129* (20), 6374-6375.

48.   Liu, J.; Jiao, M.; Mei, B., et al., *Carbon-Supported Divacancy-Anchored Platinum Single-Atom Electrocatalysts with Superhigh Pt Utilization for the Oxygen Reduction Reaction.* Angewandte Chemie International Edition **2019,** *131* (4), 1175-1179.

49.   Liu, J.; Li, Y.; Wu, Z., et al., *Pt0.61Ni/C for High-Efficiency Cathode of Fuel Cells with Superhigh Platinum Utilization.* The Journal of Physical Chemistry C **2018,** *122* (26), 14691-14697.

50.   Liu, J.; Song, P.; Xu, W., *Structure-Activity Relationship of Doped-Nitrogen (N)-Based Metal-Free Active Sites on Carbon for Oxygen Reduction Reaction.* Carbon **2017,** *115*, 763-772.

51.   Zhao, S.; Li, Z.; Li, Y., et al., *BSA-AuNCs Based Enhanced Photoelectrochemical Biosensors and its Potential Use in Multichannel Detections.* Journal of Photochemistry and Photobiology A **2017,** *342*, 15-24.

52.   Chai, O. J. H.; Liu, Z.; Chen, T., et al., *Engineering Ultrasmall Metal Nanoclusters for Photocatalytic and Electrocatalytic Applications.* Nanoscale **2019,** *11* (43), 20437-20448.

53.   Hoffmann, M. R.; Martin, S. T.; Choi, W., et al., *Environmental Applications of Semiconductor Photocatalysis.* Chemical Reviews **1995,** *95* (1), 69-96.

54.   Folkesson, A.; Andersson, C.; Alvfors, P., et al., *Real Life Testing of a Hybrid PEM Fuel Cell Bus.* Journal of Power Sources **2003,** *118* (1), 349-357.

55.   Wang, C.-Y., *Fundamental Models for Fuel Cell Engineering.* Chemical Reviews **2004,** *104* (10), 4727-4766.

56.   Liu, J.; Song, P.; Ning, Z., et al., *Recent Advances in Heteroatom-Doped Metal-Free Electrocatalysts for Highly Efficient Oxygen Reduction Reaction.* Electrocatalysis **2015,** *6* (2), 132-147.

57.   Wu, J.; Yang, H., *Platinum-Based Oxygen Reduction Electrocatalysts.* Accounts of Chemical Research **2013,** *46* (8), 1848-1857.

58.   Garlyyev, B.; Kratzl, K.; Rück, M., et al., *Optimizing the Size of Platinum Nanoparticles for Enhanced Mass Activity in the Electrochemical Oxygen Reduction Reaction.* Angewandte Chemie International Edition **2019,** *58* (28), 9596-9600.

59.   Kratzl, K.; Kratky, T.; Günther, S., et al., *Generation and Stabilization of Small Platinum Clusters Pt12±x Inside a Metal–Organic Framework.* Journal of the American Chemical Society **2019,** *141* (35), 13962-13969.

60.   Chen, W.; Chen, S., *Oxygen Electroreduction Catalyzed by Gold Nanoclusters: Strong Core Size Effects.* Angewandte Chemie International Edition **2009,** *48* (24), 4386-4389.

61.   Jing, S.; Lu, J.; Yu, G., et al., *Carbon-Encapsulated WOx Hybrids as Efficient Catalysts for Hydrogen Evolution.* Advanced Materials **2018,** *30* (28), 1705979.

62.   Kwak, K.; Choi, W.; Tang, Q., et al., *A Molecule-Like PtAu24(SC6H13)18 Nanocluster as an Electrocatalyst for Hydrogen Production.* Nature Communications **2017,** *8* (1), 14723.

63.   Wang, D.; Liu, Z.-P.; Yang, W.-M., *Proton-Promoted Electron Transfer in Photocatalysis: Key Step for Photocatalytic Hydrogen Evolution on Metal/Titania Composites.* ACS Catalysis **2017,** *7* (4), 2744-2752.

64.   Wang, Y.-G.; Yoon, Y.; Glezakou, V.-A., et al., *The Role of Reducible Oxide–Metal Cluster Charge Transfer in Catalytic Processes: New Insights on the Catalytic Mechanism of CO Oxidation on Au/TiO2 from ab Initio Molecular Dynamics.* Journal of the American Chemical Society **2013,** *135* (29), 10673-10683.

65.   Zhao, S.; Völkner, J.; Riedel, M., et al., *Multiplexed Readout of Enzymatic Reactions by Means of Laterally Resolved Illumination of Quantum Dot Electrodes.* Applied Materials and Interfaces **2019,** *11*, 21830−21839.

66.   Shi, L.; Yin, Y.; Zhang, L.-C., et al., *Design and Engineering Heterojunctions for the Photoelectrochemical Monitoring of Environmental Pollutants: A Review.* Applied Catalysis B:

Environmental **2019,** *248*, 405-422.

67.   Xiao, F.-X.; Hung, S.-F.; Miao, J., et al., *Metal-Cluster-Decorated TiO2 Nanotube Arrays: A Composite Heterostructure toward Versatile Photocatalytic and Photoelectrochemical Applications.* Small **2015,** *11* (5), 554-567.

68.   Zhang, J.; Tu, L.; Zhao, S., et al., *Fluorescent Gold Nanoclusters Based Photoelectrochemical Sensors for Detection of H2O2 and Glucose.* Biosensors & Bioelectronics **2015,** *67*, 296-302.

69.   Shuang, Z.; Jun, Z.; Zhengping, L., et al., *Photoelectrochemical Determination of Hydrogen Peroxide Using a Gold Electrode Modified with Fluorescent Gold Nanoclusters and Graphene Oxide.* Microchimica Acta **2017,** *184* (3), 1-10.

70.   Zhao, W. W.; Xu, J. J.; Chen, Y. H., *Photoelectrochemical Enzymatic Biosensors.* Biosensors & Bioelectronics **2016,** *92*, 294.

71.   Huang, Y.; Ren, J.; Qu, X., *Nanozymes: Classification, Catalytic Mechanisms, Activity Regulation, and Applications.* Chemical Reviews **2019,** *119* (6), 4357-4412.

72.   Meng, X.; Zare, I.; Yan, X., et al., *Protein-protected metal nanoclusters: An Emerging Ultra-Small Nanozyme.* WIREs Nanomedicine and Nanobiotechnology **2020,** *12* (3), e1602.

73.   Gao, L.; Zhuang, J.; Nie, L., et al., *Intrinsic Peroxidase-Like Activity of Ferromagnetic Nanoparticles.* Nature Nanotechnology **2007,** *2* (9), 577.

74.   Wang, X.-X.; Wu, Q.; Shan, Z., et al., *BSA-Stabilized Au Clusters as Peroxidase Mimetics for use in Xanthine Detection.* Biosensors and Bioelectronics **2011,** *26* (8), 3614-3619.

75.   Wang, Z.; Zhang, G.; Zhong, Z., et al., *In-Situ Synthesis of Platinum Nanoclusters in Polyelectrolyte Multilayer Films.* Thin Solid Films **2018,** *660*, 59-64.

76.   Yuan, X.; Luo, Z. T.; Zhang, Q. B., et al., *Synthesis of Highly Fluorescent Metal (Ag, Au, Pt, and Cu) Nanoclusters by Electrostatically Induced Reversible Phase Transfer.* ACS Nano **2011,** *5* (11), 8800-8808.

77.   Chen, D.; Gao, S.; Ge, W., et al., *One-Step Rapid Synthesis of Fluorescent Platinum Nanoclusters for Cellular Imaging and Photothermal Treatment.* RSC Advances **2014,** *4* (76), 40141-40145.

78.   Takahashi, M.; Imaoka, T.; Hongo, Y., et al., *Formation of a Pt12 Cluster by Single-Atom Control That Leads to Enhanced Reactivity: Hydrogenation of Unreactive Olefins.* Angewandte Chemie International Edition **2013,** *52* (29), 7419-7421.

79.   Le Guével, X.; Hötzer, B.; Jung, G., et al., *Formation of Fluorescent Metal (Au, Ag) Nanoclusters Capped in Bovine Serum Albumin Followed by Fluorescence and Spectroscopy.* Journal of Physical Chemistry C **2011,** *115*, 10955-10963.

80.   Tanaka, S.-I.; Miyazaki, J.; Tiwari, D. K., et al., *Fluorescent Platinum Nanoclusters: Synthesis, Purification, Characterization, and Application to Bioimaging.* Angewandte Chemie International Edition **2011,** *50* (2), 431-435.

81.   Rodriguez, A.; Amiens, C.; Chaudret, B., et al., *Synthesis and Isolation of Cuboctahedral and Icosahedral Platinum Nanoparticles. Ligand-Dependent Structures.* Chemistry of Materials **1996,** *8* (8), 1978-1986.

82.   Chan, Y. N. C.; Craig, G. S. W.; Schrock, R. R., et al., *Synthesis of Palladium and Platinum Nanoclusters within Microphase-Separated Diblock Copolymers.* Chemistry of Materials **1992,** *4* (4), 885-894.

83.   Huang, X.; Ishitobi, H.; Inouye, Y., *Formation of Fluorescent Platinum Nanoclusters Using Hyper-Branched Polyethylenimine and Their Conjugation to Antibodies for Bio-Imaging.* RSC Advances **2016,** *6* (12), 9709-9716.

84.   Zhou, H.-C. J.; Kitagawa, S., *Metal–Organic Frameworks (MOFs).* Chemical Society Reviews **2014,** *43* (16), 5415-5418.

85.   Zhu, Q.-L.; Xu, Q., *Metal–Organic Framework Composites.* Chemical Society Reviews **2014,** *43* (16), 5468-5512.

86.   Deng, H.; Grunder, S.; Cordova, K. E., et al., *Large-Pore Apertures in a Series of Metal-Organic Frameworks.* Science **2012,** *336* (6084), 1018-1023.

87.   Carrillo-Carrion, C.; Martínez, R.; Poupard, M. F. N., et al., *Aqueous Stable Gold Nanostar/ZIF-8 Nanocomposites for Light-Triggered Release of Active Cargo Inside Living Cells.* Angewandte Chemie International Edition **2019,** *58*, 7078-7082.

88.   Dhakshinamoorthy, A.; Garcia, H., *Catalysis by Metal Nanoparticles Embedded on Metal–Organic*

Frameworks. Chemical Society Reviews **2012,** *41* (15), 5262-5284.

89.   Jiang, H.-L.; Akita, T.; Ishida, T., et al., *Synergistic Catalysis of Au@Ag Core−Shell Nanoparticles Stabilized on Metal−Organic Framework.* Journal of the American Chemical Society **2011,** *133* (5), 1304-1306.

90.   Zhan, G.; Zeng, H. C., *Synthesis and Functionalization of Oriented Metal–Organic-Framework Nanosheets: Toward a Series of 2D Catalysts.* Advanced Functional Materials **2016,** *26* (19), 3268-3281.

91.   Yadav, M.; Aijaz, A.; Xu, Q., *Highly Catalytically Active Palladium Nanoparticles Incorporated Inside Metal-Organic Framework Pores by Double Solvents Method.* Functional Materials Letters **2012,** *05* (04), 1250039.

92.   Fu, F.; Wang, C.; Wang, Q., et al., *Highly Selective and Sharp Volcano-type Synergistic Ni2Pt@ZIF-8-Catalyzed Hydrogen Evolution from Ammonia Borane Hydrolysis.* Journal of the American Chemical Society **2018,** *140* (31), 10034-10042.

93.   Wei, G.-F.; Liu, Z.-P., *Restructuring and Hydrogen Evolution on Pt Nanoparticle.* Chemical Science **2015,** *6* (2), 1485-1490.

94.   Ikeda, S.; Ishino, S.; Harada, T., et al., *Ligand-Free Platinum Nanoparticles Encapsulated in a Hollow Porous Carbon Shell as a Highly Active Heterogeneous Hydrogenation Catalyst.* Angewandte Chemie International Edition **2006,** *45* (42), 7063-7066.

95.   Zhang, D.; Gökce, B.; Barcikowski, S., *Laser Synthesis and Processing of Colloids: Fundamentals and Applications.* Chemical Reviews **2017,** *117* (5), 3990-4103.

96.   Pan, Y.; Liu, Y.; Zeng, G., et al., *Rapid Synthesis of Zeolitic Imidazolate Framework-8 (ZIF-8) Nanocrystals in an Aqueous System.* Chemical Communications **2011,** *47* (7), 2071-2073.

97.   Shen, L.; Luo, M.; Huang, L., et al., *A Clean and General Strategy To Decorate a Titanium Metal–Organic Framework with Noble-Metal Nanoparticles for Versatile Photocatalytic Applications.* Inorganic Chemistry **2015,** *54* (4), 1191-1193.

98.   Du, S.; Lu, Y.; Malladi, S. K., et al., *A Simple Approach for PtNi–MWCNT Hybrid Nanostructures as High Performance Electrocatalysts for the Oxygen Reduction Reaction.* Journal of Materials Chemistry A **2014,** *2* (3), 692-698.

99.   Jian, M.; Liu, B.; Zhang, G., et al., *Adsorptive Removal of Arsenic from Aqueous Solution by Zeolitic Imidazolate Framework-8 (ZIF-8) Nanoparticles.* Colloids and Surfaces A: Physicochemical and Engineering Aspects **2015,** *465*, 67-76.

100.   Qi, Z.; Xiao, C.; Liu, C., et al., *Sub-4 nm PtZn Intermetallic Nanoparticles for Enhanced Mass and Specific Activities in Catalytic Electrooxidation Reaction.* Journal of the American Chemical Society **2017,** *139* (13), 4762-4768.

101.   Yang, Y.; Liu, S.; Li, J., et al., *Convenient Method for Reduction of C-N Double Bonds in Oximes, Imines, and Hydrazones Using Sodium Borohydride–Raney Ni System.* Synthetic Communications **2012,** *42* (17), 2540-2554.

102.   Hu, Y.; Kazemian, H.; Rohani, S., et al., *In Situ High Pressure Study of ZIF-8 by FTIR Spectroscopy.* Chemical Communications **2011,** *47* (47), 12694-12696.

103.   Chizallet, C.; Lazare, S.; Bazer-Bachi, D., et al., *Catalysis of Transesterification by a Nonfunctionalized Metal−Organic Framework: Acido-Basicity at the External Surface of ZIF-8 Probed by FTIR and ab Initio Calculations.* Journal of the American Chemical Society **2010,** *132* (35), 12365-12377.

104.   Liu, J.; Jiao, M.; Lu, L., et al., *High Performance Platinum Single Atom Electrocatalyst for Oxygen Reduction Reaction.* Nature Communications **2017,** *8*, 15938.

105.   Cheetham, A. K.; Bennett, T. D.; Coudert, F.-X., et al., *Defects and Disorder in Metal Organic Frameworks.* Dalton Transactions **2016,** *45* (10), 4113-4126.

106.   Pang, S. H.; Han, C.; Sholl, D. S., et al., *Facet-Specific Stability of ZIF-8 in the Presence of Acid Gases Dissolved in Aqueous Solutions.* Chemistry of Materials **2016,** *28* (19), 6960-6967.

107.   Han, C.; Verploegh, R. J.; Sholl, D. S., *Assessing the Impact of Point Defects on Molecular Diffusion in ZIF-8 Using Molecular Simulations.* The Journal of Physical Chemistry Letters **2018,** *9* (14), 4037-4044.

108.   Linder-Patton, O. M.; de Prinse, T. J.; Furukawa, S., et al., *Influence of Nanoscale Structuralisation on the Catalytic Performance of ZIF-8: a Cautionary Surface Catalysis Study.* CrystEngComm **2018,** *20* (34),

4926-4934.

109.	Kubarev, A. V.; Roeffaers, M. B. J., *Surface Acid–Base Catalytic Activity of ZIF-8 Revealed by Super-Resolution Fluorescence Microscopy.* CrystEngComm **2017,** *19* (29), 4162-4165.

110.	Herves, P.; Perez-Lorenzo, M.; Liz-Marzan, L. M., et al., *Catalysis by Metallic Nanoparticles in Aqueous Solution: Model Reactions.* Chemical Society Reviews **2012,** *41* (17), 5577-5587.

111.	Esumi, K.; Isono, R.; Yoshimura, T., *Preparation of PAMAM− and PPI−Metal (Silver, Platinum, and Palladium) Nanocomposites and Their Catalytic Activities for Reduction of 4-Nitrophenol.* Langmuir **2004,** *20* (1), 237-243.

112.	Ruan, M.; Song, P.; Liu, J., et al., *Highly Efficient Regeneration of Deactivated Au/C Catalyst for 4-Nitrophenol Reduction.* The Journal of Physical Chemistry C **2017,** *121* (46), 25882-25887.

113.	Li, C.; Wang, P.; Tian, Y., et al., *Long-Range Plasmon Field and Plasmoelectric Effect on Catalysis Revealed by Shell-Thickness-Tunable Pinhole-Free Au@SiO2 Core–Shell Nanoparticles: A Case Study of p-Nitrophenol Reduction.* ACS Catalysis **2017,** *7* (8), 5391-5398.

114.	Crooks, R. M.; Zhao, M., *Dendrimer-Encapsulated Pt Nanoparticles: Synthesis, Characterization, and Applications to Catalysis.* Advanced Materials **1999,** *11* (3), 217-220.

115.	Sadeghzadeh, S. M.; Zhiani, R.; Emrani, S., *The Reduction of 4-Nitrophenol and 2-Nitroaniline by the Incorporation of Ni@Pd MNPs into Modified UiO-66-NH2 Metal–Organic Frameworks (MOFs) with Tetrathia-Azacyclopentadecane.* New Journal of Chemistry **2018,** *42* (2), 988-994.

116.	Luo, Y.; Fan, S.; Yu, W., et al., *Fabrication of Au25(SG)18–ZIF-8 Nanocomposites: A Facile Strategy to Position Au25(SG)18 Nanoclusters Inside and Outside ZIF-8.* Advanced Materials **2018,** *30* (6), 1704576.

117.	Xu, G.-W.; Wu, Y.-P.; Dong, W.-W., et al., *A Multifunctional Tb-MOF for Highly Discriminative Sensing of Eu3+/Dy3+ and as a Catalyst Support of Ag Nanoparticles.* Small **2017,** *13* (22), 1602996.

118.	Mei, Y.; Sharma, G.; Lu, Y., et al., *High Catalytic Activity of Platinum Nanoparticles Immobilized on Spherical Polyelectrolyte Brushes.* Langmuir **2005,** *21* (26), 12229-12234.

119.	Ding, Z.-D.; Wang, Y.-X.; Xi, S.-F., et al., *A Hexagonal Covalent Porphyrin Framework as an Efficient Support for Gold Nanoparticles toward Catalytic Reduction of 4-Nitrophenol.* Chemistry – A European Journal **2016,** *22* (47), 17029-17036.

120.	Huang, P.; Ma, W.; Yu, P., et al., *Dopamine-Directed In-Situ and One-Step Synthesis of Au@Ag Core–Shell Nanoparticles Immobilized to a Metal–Organic Framework for Synergistic Catalysis.* Chemistry – An Asian Journal **2016,** *11* (19), 2705-2709.

121.	Pandey, S.; Mishra, S. B., *Catalytic Reduction of p-Nitrophenol by using Platinum Nanoparticles Stabilised by Guar Gum.* Carbohydrate Polymers **2014,** *113*, 525-531.

122.	He, L.; Dumée, L. F.; Liu, D., et al., *Silver Nanoparticles Prepared by Gamma Irradiation Across Metal–Organic Framework Templates.* RSC Advances **2015,** *5* (14), 10707-10715.

123.	Liu, Y.; Jia, S.-Y.; Wu, S.-H., et al., *Synthesis of Highly Dispersed Metallic Nanoparticles Inside the Pores of MIL-101(Cr) via the New Double Solvent Method.* Catalysis Communications **2015,** *70*, 44-48.

124.	Wang, J.-S.; Jin, F.-Z.; Ma, H.-C., et al., *Au@Cu(II)-MOF: Highly Efficient Bifunctional Heterogeneous Catalyst for Successive Oxidation–Condensation Reactions.* Inorganic Chemistry **2016,** *55* (13), 6685-6691.

125.	Zhang, W.; Lu, G.; Cui, C., et al., *A Family of Metal-Organic Frameworks Exhibiting Size-Selective Catalysis with Encapsulated Noble-Metal Nanoparticles.* Advanced Materials **2014,** *26* (24), 4056-4060.

126.	Li, Z.; Zeng, H. C., *Surface and Bulk Integrations of Single-Layered Au or Ag Nanoparticles onto Designated Crystal Planes {110} or {100} of ZIF-8.* Chemistry of Materials **2013,** *25* (9), 1761-1768.

127.	Li, Z.; Zeng, H. C., *Armored MOFs: Enforcing Soft Microporous MOF Nanocrystals with Hard Mesoporous Silica.* Journal of the American Chemical Society **2014,** *136* (15), 5631-5639.

128.	Zhang, H.-X.; Liu, M.; Bu, X., et al., *Zeolitic BIF Crystal Directly Producing Noble-Metal Nanoparticles in Its Pores for Catalysis.* Scientific Reports **2014,** *4*, 3923.

129.	Dong, Z.; Le, X.; Liu, Y., et al., *Metal Organic Framework Derived Magnetic Porous Carbon Composite Supported Gold and Palladium Nanoparticles as Highly Efficient and Recyclable Catalysts for Reduction of 4-Nitrophenol and Hydrodechlorination of 4-Chlorophenol.* Journal of Materials Chemistry A **2014,** *2* (44), 18775-18785.

130.	Zhou, J.; Wang, P.; Wang, C., et al., *Versatile Core–Shell Nanoparticle@Metal–Organic Framework Nanohybrids: Exploiting Mussel-Inspired Polydopamine for Tailored Structural Integration.* ACS Nano

2015, *9* (7), 6951-6960.

131.   Ke, F.; Zhu, J.; Qiu, L.-G., et al., *Controlled Synthesis of Novel Au@MIL-100(Fe) Core–Shell Nanoparticles with Enhanced Catalytic Performance.* Chemical Communications **2013,** *49* (13), 1267-1269.

132.   Huang, D.; Wu, X.; Tian, J., et al., *Assembling of a Novel 3D Ag(I)-MOFs with Mixed Ligands Tactics: Syntheses, Crystal Structure and Catalytic Degradation of Nitrophenol.* Chinese Chemical Letters **2018,** *29* (6), 845-848.

133.   Wei, C.; Xu, Z. J., *The Comprehensive Understanding of as an Evaluation Parameter for Electrochemical Water Splitting.* Small Methods **2018,** *2* (11), 1800168.

134.   Yu, J.; Guo, Y.; She, S., et al., *Bigger is Surprisingly Better: Agglomerates of Larger RuP Nanoparticles Outperform Benchmark Pt Nanocatalysts for the Hydrogen Evolution Reaction.* Advanced Materials **2018,** *30* (39), 1800047.

135.   Voiry, D.; Chhowalla, M.; Gogotsi, Y., et al., *Best Practices for Reporting Electrocatalytic Performance of Nanomaterials.* ACS Nano **2018,** *12* (10), 9635-9638.

136.   Chen, Z.; Wu, R.; Liu, Y., et al., *Ultrafine Co Nanoparticles Encapsulated in Carbon-Nanotubes-Grafted Graphene Sheets as Advanced Electrocatalysts for the Hydrogen Evolution Reaction.* Advanced Materials **2018,** *30* (30), 1802011.

137.   Bigall, N. C.; Hartling, T.; Klose, M., et al., *Monodisperse Platinum Nanospheres with Adjustable Diameters from 10 to 100 nm: Synthesis and Distinct Optical Properties.* Nano Letters **2008,** *8* (12), 4588-4592.

138.   Dablemont, C.; Lang, P.; Mangeney, C., et al., *FTIR and XPS Study of Pt Nanoparticle Functionalization and Interaction with Alumina.* Langmuir **2008,** *24* (11), 5832-5841.

139.   Chen, Q.; Zhang, J.; Jia, Y., et al., *Wet Chemical Synthesis of Intermetallic Pt3Zn Nanocrystals via Weak Reduction Reaction Together with UPD Process and Their Excellent Electrocatalytic Performances.* Nanoscale **2014,** *6* (12), 7019-7024.

140.   Sode, A.; Li, W.; Yang, Y., et al., *Electrochemical Formation of a Pt/Zn Alloy and Its Use as a Catalyst for Oxygen Reduction Reaction in Fuel Cells.* The Journal of Physical Chemistry B **2006,** *110* (17), 8715-8722.

141.   Ying, J.; Jiang, G.; Paul Cano, Z., et al., *Nitrogen-Doped Hollow Porous Carbon Polyhedrons Embedded with Highly Dispersed Pt Nanoparticles as a Highly Efficient and Stable Hydrogen Evolution Electrocatalyst.* Nano Energy **2017,** *40*, 88-94.

142.   Wan, X.-K.; Wu, H. B.; Guan, B. Y., et al., *Confining Sub-Nanometer Pt Clusters in Hollow Mesoporous Carbon Spheres for Boosting Hydrogen Evolution Activity.* Advanced Materials **2020,** *32* (7), 1901349.

143.   Bao, X.; Gong, Y.; Chen, Y., et al., *Carbon Vacancy Defect-Activated Pt Cluster for Hydrogen Generation.* Journal of Materials Chemistry A **2019,** *7* (25), 15364-15370.

144.   Ji, J.; Zhang, Y.; Tang, L., et al., *Platinum Single-Atom and Cluster Anchored on Functionalized MWCNTs with Ultrahigh Mass Efficiency for Electrocatalytic Hydrogen Evolution.* Nano Energy **2019,** *63*, 103849.

145.   Sun, M.; Ji, J.; Hu, M., et al., *Overwhelming the Performance of Single Atoms with Atomic Clusters for Platinum-Catalyzed Hydrogen Evolution.* ACS Catalysis **2019,** *9* (9), 8213-8223.

146.   Cheng, Q.; Hu, C.; Wang, G., et al., *Carbon-Defect-Driven Electroless Deposition of Pt Atomic Clusters for Highly Efficient Hydrogen Evolution.* Journal of the American Chemical Society **2020,** *142* (12), 5594-5601.

147.   Zhang, Z.; Chen, Y.; Zhou, L., et al., *The Simplest Construction of Single-Site Catalysts by the Synergism of Micropore Trapping and Nitrogen Anchoring.* Nature Communications **2019,** *10* (1), 1657.

148.   Qiu, Y.; Wen, Z.; Jiang, C., et al., *Rational Design of Atomic Layers of Pt Anchored on Mo2C Nanorods for Efficient Hydrogen Evolution over a Wide pH Range.* Small **2019,** *15* (14), 1900014.

149.   Huang, K.; Wang, R.; Wu, H., et al., *Direct Immobilization of an Atomically Dispersed Pt Catalyst by Suppressing Heterogeneous Nucleation at −40 °C.* Journal of Materials Chemistry A **2019,** *7* (45), 25779-25784.

150.   Tian, H.; Cui, X.; Zeng, L., et al., *Oxygen Vacancy-Assisted Hydrogen Evolution Reaction of the*

Pt/WO3 Electrocatalyst. Journal of Materials Chemistry A **2019,** *7* (11), 6285-6293.

151.   Yang, L.; Cheng, D.; Xu, H., et al., *Unveiling the High-Activity Origin of Single-Atom Iron Catalysts for Oxygen Reduction Reaction.* Proceedings of the National Academy of Sciences **2018,** *115* (26), 6626-6631.

152.   Wu, Z.-S.; Yang, S.; Sun, Y., et al., *3D Nitrogen-Doped Graphene Aerogel-Supported Fe3O4 Nanoparticles as Efficient Electrocatalysts for the Oxygen Reduction Reaction.* Journal of the American Chemical Society **2012,** *134* (22), 9082-9085.

153.   Yang, L.; Su, Y.; Li, W., et al., *Fe/N/C Electrocatalysts for Oxygen Reduction Reaction in PEM Fuel Cells Using Nitrogen-Rich Ligand as Precursor.* The Journal of Physical Chemistry C **2015,** *119* (21), 11311-11319.

154.   Park, K. S.; Ni, Z.; Côté, A. P., et al., *Exceptional Chemical and Thermal Stability of Zeolitic Imidazolate Frameworks.* Proceedings of the National Academy of Sciences **2006,** *103* (27), 10186-10191.

155.   Yang, Z.; Qian, Y.; Yang, F., et al., *Investigating Adsorption/Desorption of DNA on ZIF-8 Surface by Fluorescently Labeled Oligonucleotides.* Langmuir **2019,** *35* (49), 16290-16296.

156.   Xiao-Zhen Kang; Zheng-Wei Song; Qi Shi1, et al., *Utilization of Zeolite Imidazolate Framework as an Adsorbent for the Removal of Dye from Aqueous Solution.* Asian Journal of Chemistry **2013,** *25,* 8324-8328.

157.   He, D. S.; He, D.; Wang, J., et al., *Ultrathin Icosahedral Pt-Enriched Nanocage with Excellent Oxygen Reduction Reaction Activity.* Journal of the American Chemical Society **2016,** *138* (5), 1494-1497.

158.   Wei, H.; Wang, E., *Nanomaterials with Enzyme-Like Characteristics (Nanozymes): Next-Generation Artificial Enzymes.* Chemical Society Reviews **2013,** *42* (14), 6060-6093.

159.   de Larramendi, I. R.; Ortiz-Vitoriano, N.; Acebedo, B., et al., *Pr-Doped Ceria Nanoparticles as Intermediate Temperature Ionic Conductors.* International Journal of Hydrogen Energy **2011,** *36* (17), 10981-10990.

160.   Wu, J.; Wang, X.; Wang, Q., et al., *Nanomaterials with enzyme-like characteristics (nanozymes): next-generation artificial enzymes (II).* Chemical Society Reviews **2019,** *48* (4), 1004-1076.

161.   Cao, F.; Zhang, Y.; Sun, Y., et al., *Ultrasmall Nanozymes Isolated within Porous Carbonaceous Frameworks for Synergistic Cancer Therapy: Enhanced Oxidative Damage and Reduced Energy Supply.* Chemistry of Materials **2018,** *30* (21), 7831-7839.

162.   Ballesteros, C. A. S.; Mercante, L.; Alvarenga, A., et al., *Recent Trends in Nanozymes Design: From Materials and Structures to Environmental Applications.* Materials Chemistry Frontiers **2021**.

163.   Cai, S.; Yang, R., Noble Metal-Based Nanozymes. In *Nanozymology: Connecting Biology and Nanotechnology*, Yan, X., Ed. Springer Singapore: Singapore, 2020; pp 331-365.

164.   Hu, Y.; Gao, X. J.; Zhu, Y., et al., *Nitrogen-Doped Carbon Nanomaterials as Highly Active and Specific Peroxidase Mimics.* Chemistry of Materials **2018,** *30* (18), 6431-6439.

165.   Sun, H.; Zhou, Y.; Ren, J., et al., *Carbon Nanozymes: Enzymatic Properties, Catalytic Mechanism, and Applications.* Angewandte Chemie International Edition **2018,** *57* (30), 9224-9237.

166.   Li, L.; Zhang, L.; Carmona, U., et al., *Semi-Artificial and Bioactive Ferroxidase with Nanoparticles as the Active Sites.* Chemical Communications **2014,** *50* (59), 8021-8023.

167.   Liu, J.; Jiang, X.; Wang, L., et al., *Ferroxidase-Like Activity of Au Nanorod/Pt Nanodot Structures and Implications for Cellular Oxidative Stress.* Nano Research **2015,** *8* (12), 4024-4037.

168.   Liu, J.; Hu, X.; Hou, S., et al., *Screening of Inhibitors for Oxidase Mimics of Au@Pt Nanorods by Catalytic Oxidation of OPD.* Chemical Communications **2011,** *47* (39), 10981-10983.

169.   Fan, J.; Yin, J.-J.; Ning, B., et al., *Direct Evidence for Catalase and Peroxidase Activities of Ferritin–Platinum Nanoparticles.* Biomaterials **2011,** *32* (6), 1611-1618.

170.   Zhang, Y.; Wang, F.; Liu, C., et al., *Nanozyme Decorated Metal–Organic Frameworks for Enhanced Photodynamic Therapy.* ACS Nano **2018,** *12* (1), 651-661.

171.   Zhang, P.; Wang, Y.; Chen, L., et al., *Bimetallic Nanoclusters with Strong Red Fluorescence for Sensitive Detection of Hypochlorite in Tap Water.* Microchimica Acta **2017,** *184* (10), 3781-3787.

172.   Kim, K.; Kim, K. L.; Shin, K. S., *Coreduced Pt/Ag Alloy Nanoparticles: Surface-Enhanced Raman Scattering and Electrocatalytic Activity.* The Journal of Physical Chemistry C **2011,** *115* (47), 23374-23380.

173.   Peng, Z.; You, H.; Yang, H., *An Electrochemical Approach to PtAg Alloy Nanostructures Rich in Pt at the Surface.* Advanced Functional Materials **2010,** *20* (21), 3734-3741.

174.   Song, P.; Xu, H.; Yan, B., et al., *Particle Size Effects of PtAg Nanoparticles on the Catalytic Electrooxidation of Liquid Fuels.* Inorganic Chemistry Frontiers **2018,** *5* (5), 1174-1179.

175.   Fang, C.; Zhao, J.; Zhao, G., et al., *Simultaneous Tunable Structure and Composition of PtAg Alloyed Nanocrystals as Superior Catalysts.* Nanoscale **2016,** *8* (32), 14971-14978.

176.   Jin, L.; Meng, Z.; Zhang, Y., et al., *Ultrasmall Pt Nanoclusters as Robust Peroxidase Mimics for Colorimetric Detection of Glucose in Human Serum.* ACS applied materials & interfaces **2017,** *9* (11), 10027-10033.

177.   Feng, Y.-Y.; Zhang, G.-R.; Ma, J.-H., et al., *Carbon-Supported Pt$_x$Ag Nanostructures as Cathode Catalysts for Oxygen Reduction Reaction.* Physical Chemistry Chemical Physics **2011,** *13* (9), 3863-3872.

178.   Feng, Y.-Y.; Bi, L.-X.; Liu, Z.-H., et al., *Significantly Enhanced Electrocatalytic Activity for Methanol Electro-Oxidation on Ag Oxide-Promoted PtAg/C Catalysts in Alkaline Electrolyte.* Journal of Catalysis **2012,** *290*, 18-25.

179.   Wu, J.; Xu, M.; Lei, S., et al., *High Electrocatalytic Activity and Stability of PtAg Supported on Rutile TiO2 for Methanol Oxidation.* International Journal of Hydrogen Energy **2020,** *45* (23), 12815-12821.

180.   Awadallah-F, A.; Hillman, F.; Al-Muhtaseb, S. A., et al., *On the Nanogate-Opening Pressures of Copper-Doped Zeolitic Imidazolate Framework ZIF-8 for the Adsorption of Propane, Propylene, Isobutane, and n-Butane.* Journal of Materials Science **2019,** *54* (7), 5513-5527.

181.   Zhang, W.; Liu, Y.; Lu, G., et al., *Mesoporous Metal–Organic Frameworks with Size-, Shape-, and Space-Distribution-Controlled Pore Structure.* Advanced Materials **2015,** *27* (18), 2923-2929.

182.   Chaikittisilp, W.; Hu, M.; Wang, H., et al., *Nanoporous Carbons through Direct Carbonization of a Zeolitic Imidazolate Framework for Supercapacitor Electrodes.* Chemical Communications **2012,** *48* (58), 7259-7261.

183.   Esken, D.; Turner, S.; Lebedev, O. I., et al., *Au@ZIFs: Stabilization and Encapsulation of Cavity-Size Matching Gold Clusters inside Functionalized Zeolite Imidazolate Frameworks, ZIFs.* Chemistry of Materials **2010,** *22* (23), 6393-6401.

184.   Kumar, S. V.; Bafana, A. P.; Pawar, P., et al., *High Conversion Synthesis of <10 nm Starch-Stabilized Silver Nanoparticles Using Microwave Technology.* Scientific Reports **2018,** *8* (1), 5106.

185.   Liu, X.; Li, Y.; Ban, Y., et al., *Improvement of Hydrothermal Stability of Zeolitic Imidazolate Frameworks.* Chemical Communications **2013,** *49* (80), 9140-9142.

186.   Zhao, Q.; Wang, C.; Wang, H., et al., *Synthesis of a High-Performance Low-Platinum PtAg/C Alloyed Oxygen Reduction Catalyst through the Gradual Reduction Method.* New Journal of Chemistry **2020,** *44* (9), 3728-3736.

187.   Cheng, H.; Lin, S.; Muhammad, F., et al., *Rationally Modulate the Oxidase-like Activity of Nanoceria for Self-Regulated Bioassays.* ACS Sensors **2016,** *1* (11), 1336-1343.

188.   Liu, X.; Wang, Q.; Zhao, H., et al., *BSA-Templated MnO2 Nanoparticles as both Peroxidase and Oxidase Mimics.* Analyst **2012,** *137* (19), 4552-4558.

189.   He, W.; Han, X.; Jia, H., et al., *AuPt Alloy Nanostructures with Tunable Composition and Enzyme-like Activities for Colorimetric Detection of Bisulfide.* Scientific Reports **2017,** *7* (1), 40103.

190.   Deng, H.-H.; Lin, X.-L.; Liu, Y.-H., et al., *Chitosan-Stabilized Platinum Nanoparticles as Effective Oxidase Mimics for Colorimetric Detection of Acid Phosphatase.* Nanoscale **2017,** *9* (29), 10292-10300.

191.   Cao, G.-J.; Jiang, X.; Zhang, H., et al., *Mimicking Horseradish Peroxidase and Oxidase Using Ruthenium Nanomaterials.* RSC Advances **2017,** *7* (82), 52210-52217.

192.   Su, L.; Feng, J.; Zhou, X., et al., *Colorimetric Detection of Urine Glucose Based ZnFe2O4 Magnetic Nanoparticles.* Analytical Chemistry **2012,** *84* (13), 5753-5758.

193.   Tao, Y.; Ju, E.; Ren, J., et al., *Bifunctionalized Mesoporous Silica-Supported Gold Nanoparticles: Intrinsic Oxidase and Peroxidase Catalytic Activities for Antibacterial Applications.* Advanced Materials **2015,** *27* (6), 1097-1104.

194.   Liu, J.; Meng, L.; Fei, Z., et al., *On the Origin of the Synergy between the Pt Nanoparticles and MnO2 Nanosheets in Wonton-like 3D Nanozyme Oxidase Mimics.* Biosensors and Bioelectronics **2018,** *121*, 159-165.

195.   Mu, J.; Wang, Y.; Zhao, M., et al., *Intrinsic Peroxidase-Like Activity and Catalase-Like Activity of*

Co3O4 Nanoparticles. Chemical Communications **2012,** *48* (19), 2540-2542.

196.   Yue Yang; Mei Chen; Bingzhe Wang, et al., *NIR-II Driven Plasmon-Enhanced Catalysis for a Timely Supply of Oxygen to Overcome Hypoxia-Induced Radiotherapy Tolerance.* Angewandte Chemie International Edition **2019,** *58*, 15069-15075.

197.   Liu, X.; Wu, J.; Liu, Q., et al., *Synthesis-Temperature-Regulated Multi-Enzyme-Mimicking Activities of Ceria Nanozymes.* Journal of Materials Chemistry B **2021**.

198.   Yang, H.; Xiao, J.; Su, L., et al., *Oxidase-Mimicking Activity of the Nitrogen-Doped Fe3C@C Composites.* Chemical Communications **2017,** *53* (27), 3882-3885.

199.   Ghobadi, T. G. U.; Ghobadi, A.; Özbay, E., et al., *Strategies for plasmonic hot-electron-driven photoelectrochemical water splitting.* ChemPhotoChem **2018,** *2* (3), 161-182.

200.   Zhao, C.-Q.; Zhou, J.; Wu, K.-W., et al., *Plasmonic Enhanced Gold Nanoclusters-Based Photoelectrochemical Biosensor for Sensitive Alkaline Phosphatase Activity Analysis.* Analytical Chemistry **2020,** *92* (10), 6886-6892.

201.   Lv, S.; Zhang, K.; Zhou, Q., et al., *Plasmonic Enhanced Photoelectrochemical Aptasensor with DA F8BT/g-C3N4 Heterojunction and AuNPs on a 3D-Printed Device.* Sensors and Actuators B: Chemical **2020,** *310*, 127874.

202.   Xiao, M.; Jiang, R.; Wang, F., et al., *Plasmon-Enhanced Chemical Reactions.* Journal of Materials Chemistry A **2013,** *1* (19), 5790-5805.

203.   Baffou, G.; Quidant, R., *Nanoplasmonics for Chemistry.* Chemical Society Reviews **2014,** *43* (11), 3898-3907.

204.   Zhan, C.; Chen, X.-J.; Yi, J., et al., *From Plasmon-Enhanced Molecular Spectroscopy to Plasmon-Mediated Chemical Reactions.* Nature Reviews Chemistry **2018,** *2* (9), 216-230.

205.   Hung, W. H.; Aykol, M.; Valley, D., et al., *Plasmon Resonant Enhancement of Carbon Monoxide Catalysis.* Nano Letters **2010,** *10* (4), 1314-1318.

206.   Aslam, U.; Rao, V. G.; Chavez, S., et al., *Catalytic Conversion of Solar to Chemical Energy on Plasmonic Metal Nanostructures.* Nature Catalysis **2018,** *1* (9), 656-665.

207.   Zhang, Y.; He, S.; Guo, W., et al., *Surface-Plasmon-Driven Hot Electron Photochemistry.* Chemical Reviews **2017,** *118* (6), 2927-2954.

208.   Swearer, D. F.; Zhao, H.; Zhou, L., et al., *Heterometallic Antenna− Reactor Complexes for Photocatalysis.* Proceedings of the National Academy of Sciences **2016,** *113* (32), 8916-8920.

209.   Boerigter, C.; Campana, R.; Morabito, M., et al., *Evidence and Implications of Direct Charge Excitation as the Dominant Mechanism in Plasmon-Mediated Photocatalysis.* Nature Communications **2016,** *7* (1), 1-9.

210.   Rao, V. G.; Aslam, U.; Linic, S., *Chemical Requirement for Extracting Energetic Charge Carriers from Plasmonic Metal Nanoparticles to Perform Electron-Transfer Reactions.* Journal of the American Chemical Society **2018,** *141* (1), 643-647.

211.   Sundararaman, R.; Narang, P.; Jermyn, A. S., et al., *Theoretical Predictions for Hot-Carrier Generation from Surface plasmon Decay.* Nature Communications **2014,** *5* (1), 1-8.

212.   Brown, A. M.; Sundararaman, R.; Narang, P., et al., *Nonradiative Plasmon Decay and Hot Carrier Dynamics: Effects of Phonons, Surfaces, and Geometry.* ACS Nano **2016,** *10* (1), 957-966.

213.   Thomas, P. J.; Kulkarni, G. U.; Rao, C. N. R., *An Investigation of Two-Dimensional Arrays of Thiolized Pd Nanocrystals.* The Journal of Physical Chemistry B **2000,** *104* (34), 8138-8144.

214.   Atwater, H. A.; Polman, A., Plasmonics for improved photovoltaic devices. In *Materials for Sustainable Energy*, Co-Published with Macmillan Publishers Ltd, UK: 2010; pp 1-11.

215.   Lal, S.; Grady, N. K.; Kundu, J., et al., *Tailoring Plasmonic Substrates for Surface Enhanced Spectroscopies.* Chemical Society Reviews **2008,** *37* (5), 898-911.

216.   Langer, J.; Novikov, S. M.; Liz-Marzán, L. M., *Sensing using Plasmonic Nanostructures and Nanoparticles.* Nanotechnology **2015,** *26* (32), 322001.

217.   de Aberasturi, D. J.; Serrano-Montes, A. B.; Liz-Marzán, L. M., *Modern Applications of Plasmonic Nanoparticles: From Energy to Health.* Advanced Optical Materials **2015,** *3* (5), 602-617.

218.   Ye, X.; Zheng, C.; Chen, J., et al., *Using Binary Surfactant Mixtures To Simultaneously Improve the Dimensional Tunability and Monodispersity in the Seeded Growth of Gold Nanorods.* Nano Letters **2013,** *13* (2), 765-771.

219. Ye, X.; Jin, L.; Caglayan, H., et al., *Improved Size-Tunable Synthesis of Monodisperse Gold Nanorods through the Use of Aromatic Additives.* ACS Nano **2012,** *6* (3), 2804-2817.

220. Luo, Z.; Yuan, X.; Yu, Y., et al., *From Aggregation-Induced Emission of Au(I)–Thiolate Complexes to Ultrabright Au(0)@Au(I)–Thiolate Core–Shell Nanoclusters.* Journal of the American Chemical Society **2012,** *134* (40), 16662-16670.

221. Zhang, X.-D.; Luo, Z.; Chen, J., et al., *Ultrasmall Glutathione-Protected Gold Nanoclusters as Next Generation Radiotherapy Sensitizers with High Tumor Uptake and High Renal Clearance.* Scientific Reports **2015,** *5* (1), 8669.

222. Chen, T.; Tong, F.; Enderlein, J., et al., *Plasmon-Driven Modulation of Reaction Pathways of Individual Pt-Modified Au Nanorods.* Nano Letters **2020,** *20* (5), 3326-3330.

223. Zou, N.; Chen, G.; Mao, X., et al., *Imaging catalytic hotspots on single plasmonic nanostructures via correlated super-resolution and electron microscopy.* ACS Nano **2018,** *12* (6), 5570-5579.

224. Nishi, H.; Tatsuma, T., *Mechanistic Analysis of Plasmon-Induced Charge Separation by the use of Chemically Synthesized Gold Nanorods.* The Journal of Physical Chemistry C **2018,** *122* (4), 2330-2335.

225. Chang, G.; Luo, Y.; Qin, X., et al., *Synthesis of Pt Nanoparticles Decorated 1,5-Diaminoanthraquinone Nanofibers and Their Application Toward Catalytic Reduction of 4-Nitrophenol.* Journal of Nanoscience and Nanotechnology, **2012,** *12*, 7075-7080.

226. Li, Y.; Wang, H.; Xie, L., et al., *MoS2 Nanoparticles Grown on Graphene: An Advanced Catalyst for the Hydrogen Evolution Reaction.* Journal of the American Chemical Society **2011,** *133* (19), 7296-7299.

227. Fjellstedt, T. A.; Schlesselman, J. J., *A Simple Statistical Method for use in Kinetic Analysis based on Lineweaver-Burk Plots.* Analytical Biochemistry **1977,** *80* (1), 224-238.

228. Scarabelli, L.; Sánchez-Iglesias, A.; Pérez-Juste, J., et al., *A "Tips and Tricks" Practical Guide to the Synthesis of Gold Nanorods.* The Journal of Physical Chemistry Letters **2015,** *6* (21), 4270-4279.

229. Li, J. F.; Huang, Y. F.; Ding, Y., et al., *Shell-Isolated Nanoparticle-Enhanced Raman Spectroscopy.* Nature **2010,** *464* (7287), 392-395.

230. Shin, Y., Song, J., Kim, D., et al., *Facile Preparation of Ultrasmall Void Metallic Nanogap from Self-Assembled Gold–Silica Core–Shell Nanoparticles Monolayer via Kinetic Control.* Advanced Materials **2015，** 27(29), 4344-4350.

231. Yue, Z.; Khalid, W.; Zanella, M., et al., *Evaluation of Quantum Dots Applied as Switchable Layer in a Light-Controlled Electrochemical Sensor.* Analytical and Bioanalytical Chemistry **2010,** *396* (3), 1095-1103.

Acknowledgement

My Ph.D. study is coming to an end. At this moment, I would like to express my sincere gratitude to my supervisor, Prof. Dr. Wolfgang J. Parak, who offered me the possibility to explore interesting research for my Ph.D. in his group. I am grateful for his instructive guidance, strict requirements, advice and support during my Ph.D. His rigorous academic attitude has kept me motivated when solving scientific experiment problems.

I would like to thank my co-supervisor, Prof. Dr. Holger Lange, for kind suggestions for my Ph.D. study and thesis.

I am sincerely grateful to Dr. Indranath Chakraborty for his long-term guidance, insightful suggestions and discussion throughout my Ph.D. study. The doctoral dissertation, from topic selection, experimentation, to the writing and correction of the final dissertation, was all carried out under the care and guidance of him.

Special thanks to Dr. Neus Feliu for her care about me especially during my preganent period. She helps me a lot during my whole PhD period. I would like to thank a lot to Prof. Dr. Weilin Xu and Mr. Mingbo Ruan for the collobration and continuous support in the experiment and suggestions. I am so grateful to Prof. Dr. Dorota Koziej for her help and support in experimental operations as well as in life. Her enthusiastic lifestyle and attitude to work infects me, and it is also a role mode for me in the future work and life. And I also acknowledge Prof. Dr. Fred Lisdat for the instructive guidance of the PEC work in this thesis. I am sincerely grateful to Dr. Robert Zierold and Prof. Dr. Robert H. Blick for their help in preparing the gold thin on the glass to be used in PEC study.

I am so lucky to be supported by all the colleagues of the Biophotonik group, especially the period when I was pregnant. Great work cannot be carried out so successfully without their help to me and my son Yanxu Chen. The whole atmosphere in our group was so warm, harmonious and unforgettable. I would like to take advantage of this opportunity to thank Yanan Kang and Yang Liu, who always the first to help me out of the emergent moments whenever I was in emergent clinic, surgery and laboratory, and take care of Yanxu very well.

Besides, in the completion of this thesis, Ms. Marta Gallego Gonzalez (CIC Biomagune, Spain), Mr. Andreas Kornowski and Mr. Stefan Werner (Department of Chemistry, University of Hamburg) and

Yours sincerely,

Lizhen Chen

01.12.2021, Hamburg